NASA CR-151928
D6-75793

OBLIQUE WING TRANSONIC TRANSPORT CONFIGURATION DEVELOPMENT

FINAL REPORT

January 1977

Prepared under contract NAS2-7031 by

Preliminary Design Department
BOEING COMMERCIAL AIRPLANE COMPANY
P.O. Box 3707
Seattle, Washington 98124

for

NASA

Ames Research Center
NATIONAL AERONAUTICS AND SPACE ADMINISTRATION

1 Report No	2 Government Accession No	3 Recipient's Catalog No
NASA CR-151928		

4 Title and Subtitle	5 Report Date
OBLIQUE WING TRANSONIC TRANSPORT CONFIGURATION DEVELOPMENT	January 1977
	6 Performing Organization Code
7 Author(s)	8 Performing Organization Report No
BCAC Preliminary Design Department	D6-75793
	10 Work Unit No
9 Performing Organization Name and Address	11 Contract or Grant No
BOEING COMMERICAL AIRPLANE CO. P.O. Box 3707 Seattle, Washington 98124	NAS2-7031
	13 Type of Report and Period Covered
12 Sponsoring Agency Name and Address	Final Contractor Report
National Aeronautics and Space Administration Ames Research Center Moffet Field, California 94035	14 Sponsoring Agency Code

15 Supplementary Notes

16 Abstract

This is the third document in a series of documents that describe studies of transport aircraft designed for boom-free supersonic flight. These investigations have shown the variable sweep oblique wing to be the most efficient configuration for flight at low supersonic speeds. Use of this concept leads to a configuration that is lighter, quieter, and more fuel efficient than symmetric aircraft designed for the same mission. Aerodynamic, structural, weight, aeroelastic and flight control studies described in previous documents showed the oblique wing concept to be technically feasible.

This report describes more detailed investigations of the following topics:

- Wing planform and thickness
- Pivot design and weight estimation
- Engine cycle (bypass ratio)
- Climb, descent and reserve fuel

The knowledge gained during these studies was incorporated into a final configuration and performance, weight and balance characteristics were evaluated. Flight control requirements were reviewed and areas were identified in which further research is needed.

17 Key Words (Suggested by Author(s))	18 Distribution Statement

19 Security Classif. (of this report)	20 Security Classif. (of this page)	21 No. of Pages	22 Price*
Unclassified	Unclassified		

*For sale by the National Technical Information Service, Springfield, Virginia 22161

CONTENTS

1.0 SUMMARY 1

2.0 INTRODUCTION 6

3.0 SYMBOLS AND ABBREVIATIONS 14

4.0 WING PLANFORM STUDY 21
- 4.1 Summary 21
- 4.2 Study Description 21
- 4.3 Planform Definitions 24
- 4.4 Cruise Drag 28
  - 4.4.1 Skin Friction Drag 32
  - 4.4.2 Drag Due to Lift 32
  - 4.4.3 Wave Drag 32
- 4.5 Structural Analysis 36
- 4.6 Weights 42
- 4.7 Planform and Thickness Selection 43
- 4.8 Low-Speed Aerodynamic Characteristics 47
  - 4.8.1 Estimation Methods and Procedures 47
  - 4.8.2 High Lift System Definition 47
  - 4.8.3 Low-Speed Characteristics Summary 47

5.0 PIVOT DESIGN 54
- 5.1 Summary 54
- 5.2 Study Description 55
- 5.3 Concept Selection 56
- 5.4 Pivot Location 63
- 5.5 Design Loads 63
- 5.6 Structural Load Paths 63
- 5.7 Structural Sizing 63
- 5.8 Detailed Weight Analysis 65
- 5.9 Parametric Weight-Scaling Development 68
  - 5.9.1 Pivot-Load Scalars 69
  - 5.9.2 Airplane Parameter Scalars 69
- 5.10 Potential Problem Areas 73

6.0 ENGINE CYCLE STUDY 74
- 6.1 Summary 74
- 6.2 Study Description 74
- 6.3 Powerplant Installation Concept 75
- 6.4 Powerplant Characteristics 76
- 6.5 Baseline Airplane Size and Performance 81
- 6.6 Baseline Configuration Development 83
  - 6.6.1 Powerplant Installation 83
  - 6.6.2 Body Optimization 83

6.6.3 Balance 89
6.6.4 Tail Sizing 89
6.7 Baseline Drag and Drag Scalars 89
6.7.1 Baseline Drag 89
6.7.2 Cruise-Drag Scalars 93
6.8 Baseline Weights and Weight-Scaling Methodology 96
6.8.1 Weight-Scaling Methodology 96
6.8.2 Baseline Weights 96
6.9 Climb, Descent, and Reserve Fuel 98
6.10 Airplane Sizing and Bypass Ratio Selection 99

7.0 CLIMB, DESCENT, AND RESERVE FUEL 107
7.1 Summary 107
7.2 Study Description 107
7.3 Sweep Selection 107
7.4 Drag 108
7.5 Thrust and Fuel Consumption 114
7.6 Climb Speed Schedule and Fuel 114
7.7 Reserves 118
7.8 Descent Fuel 118

8.0 FINAL CONFIGURATION 119
8.1 Summary 119
8.2 Configuration Description 119
8.3 Configuration Development 123
8.3.1 Airplane Sizing 123
8.3.2 Body Optimization 123
8.3.3 Pivot Design and Location 123
8.3.4 Empennage and Control Surface Sizing 124
8.4 Configuration Characteristics 127
8.4.1 Low-Speed Aerodynamic Characteristics 127
8.4.2 High-Speed Aerodynamic Characteristics 130
8.4.3 Weight and Balance 132
8.4.4 Performance and Noise 136

9.0 TRADE AND SENSITIVITY STUDIES 139

10.0 EXPERIMENTAL DATA ANALYSIS 141
10.1 Data Sources 141
10.2 Optimum Sweep 141
10.3 Subsonic Drag Due to Lift 146
10.4 Supersonic Lift-Drag Ratio 148
10.5 Supersonic Drag Due to Lift 151

11.0 CONCLUSIONS AND RECOMMENDATIONS 153

12.0 REFERENCES 155

1.0 SUMMARY

Studies of transport aircraft designed for boom-free supersonic flight (M ≤ 1.2) have shown the variable sweep oblique wing to be the most efficient configuration for flight at low supersonic speeds. Use of this concept leads to a configuration that is lighter, quieter, and more fuel efficient than symmetric aircraft designed for the same mission.

Aerodynamic, structural, weight, aeroelastic, and flight control studies have been carried out in sufficient depth to show that the oblique-wing concept is technically feasible and to identify areas in which further research is needed.

This document is the third in a series of reports prepared for NASA Ames Research Center, under contract NAS2-7031.

The first study, which began in 1972, compared five design concepts having a cruise Mach number equal to 1.2. An oblique-wing configuration with variable sweep showed the highest potential and was selected for further development. This configuration had an 8:1 elliptic wing planform and four bypass ratio (BPR) 1 engines integrated into the aft body.

The second study included evaluation of twin- and three-engined aircraft and an investigation of aeroelastic effects on stability and control. The four-engined integrated powerplant installation was found to be most efficient; i.e., lightest gross weight, and slightly superior to the twin. Six degree-of-freedom response calculations identified the wing pivot location, center of gravity location, tail volume coefficient, and stability augmentation required to produce convergent response to control deflections.

The third study, described in the present report, involved design and trade studies that were incorporated into the final definition of an oblique-wing transport. The following topics were investigated:

- Wing planform and thickness
- Pivot design and weight estimation
- Engine cycle
- Climb, descent, and reserve fuel

A tapered, high aspect ratio wing planform was selected following aerodynamic, structural, and weight evaluation of several candidate planforms, each having graphite-epoxy primary structure.

Ten pivot-design concepts were evaluated and a teflon-coated turntable bearing was chosen. Sized structural layouts were prepared for the pivot and supporting structure. These drawings were used to estimate the weight of the pivot and associated structure, and to develop weight-scaling relationships.

Airplanes were configured with BPR = 1, 2, and 3 engines. BPR = 2 was selected because it led to the configuration that consumed the least fuel and had very good noise characteristics and low-speed performance.

Reserve, climb, and descent fuel requirements were calculated using a wing-sweep schedule and climb trajectory developed for the variable sweep oblique-wing aircraft.

The knowledge gained from these studies was incorporated into the final configuration, Model 5-7, shown in Figure 1. The principal characteristics and performance of this aircraft are compared to competitive designs on Table 1 and Figure 2. The single-bodied oblique wing has lower gross weight, consumes less fuel, and has low-speed performance and noise characteristics superior to the more conventional, symmetric wing configurations.

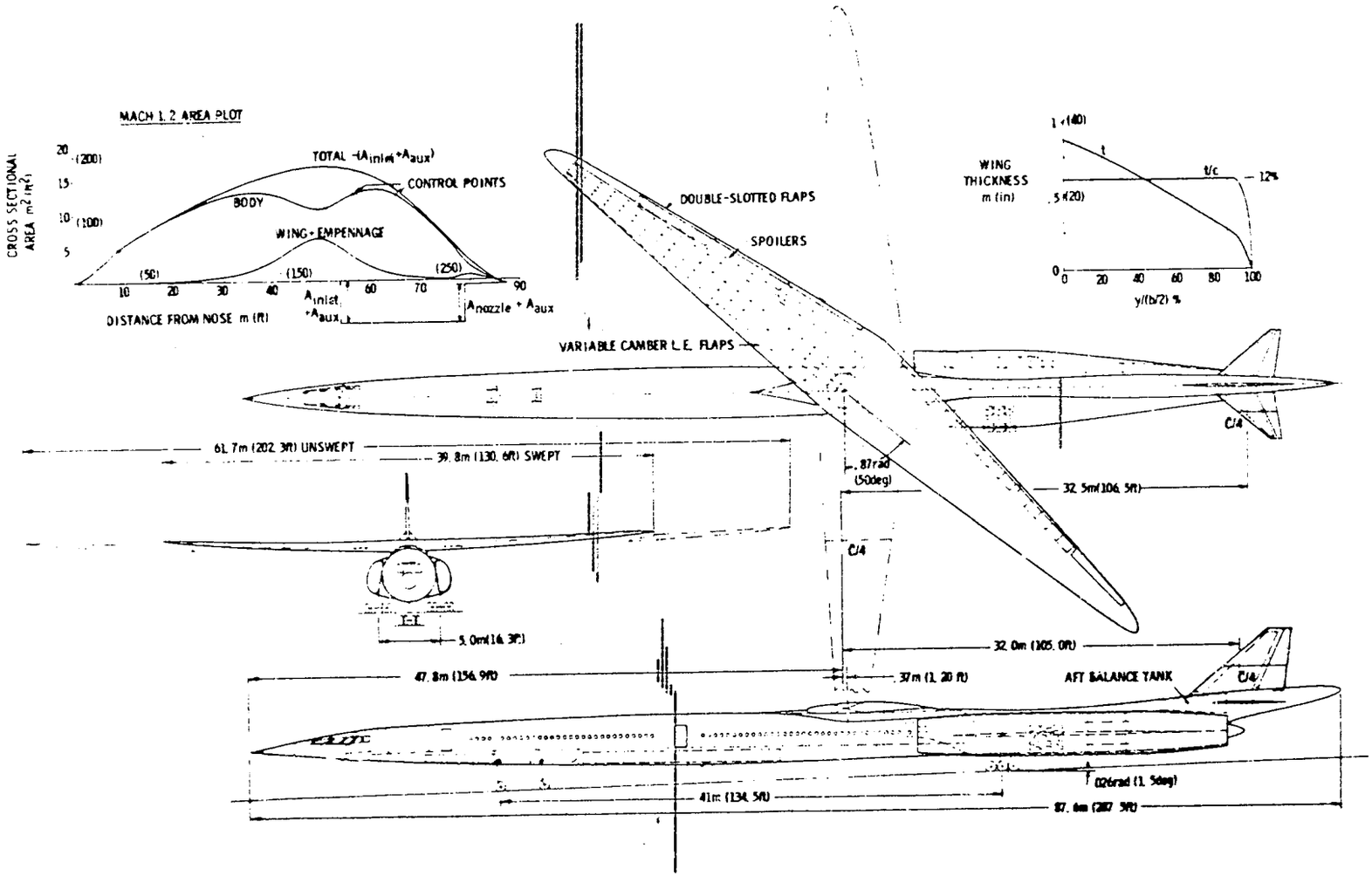

Figure 1 Oblique Wing Transport – Model 5-7

Table 1 High Transonic Speed Aircraft Characteristics and Performance

- Mach 1.2
- Payload = 18 143 kg (40 000 lb)
- Range = 5560 km (3000 nmi)
- Initial cruise altitude = 11 887 m (39 000 ft)
- Takeoff field length 3505 m (11 500 ft)
- Peripheral noise treatment *

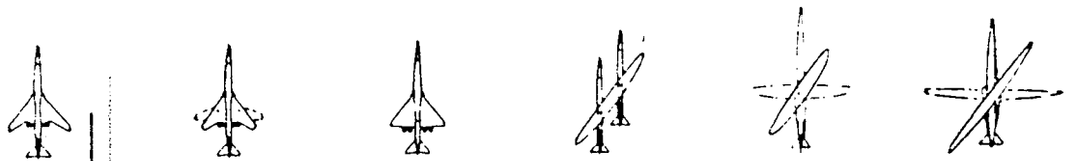

Airplane configuration	1-2a	2-2a	3-2a	4-2a	5-3a	5-7
Takeoff gross weight kg (lb)	275 283 (607 000)	388 283 (857 000)	226 796 (500 000)	280 726 (619 000)	211 828 (467 000)	194 559 (428 910)
Operating empty weight kg (lb)	122 626 (270 500)	180 726 (398 500)	103 855 (229 000)	146 804 (322 600)	113 832 (251 000)	112 523 (248 070)
Wing area m^2 (ft^2)	433.8 (4 670)	612.2 (6 590)	436.6 (4 700)	442.2 (4 760)	319.6 (3 440)	282 (3 040)
Engine thrust rating Sea level static N (lb)	284 241 (63 900)	406 123 (91 300)	216 184 (48 600)	226 859 (51 000)	156 113 (35 100)	15 677 (35 100)
Number of engines/bypass ratio	4/1	4/1	4/1	4/1	4/1	4/2
Thrust loading (T/W)	0.42	0.43	0.39	0.33	0.30	0.328
Wing loading (w/s) N/m^2 (lb/ft^2)	6 224 (130)	6 224 (130)	5 075 (106)	6 224 (130)	6 512 (136)	675 (141)
L/D cruise	8.1	8.1	8.9	10.6	12.3	13.4
Takeoff field length: max flaps m (ft)	2 438 (8 000)	1 554 (5 100)	3 505 (11 500)	2 225 (7 300)	2 179 (7 150)	2 261 (7 430)
Reduced flaps m (ft)	3 353 (11 000)	2 286 (7 500)	3 505 (11 500)	3 078 (10 100)	2 947 (9 670)	2 917 (9 560)
L/D community: reduced flaps	8.8	9.2	6.3	22	6.9	9.3
Approach speed: reduced flaps km/hr (kt)	333 (180)	296 (160)	317 (171)	261 (141)	254.5 (137.4)	269 (140)
** Community noise Δ EPNdB from FAR 36						
• Takeoff with thrust cutback at noise station	−6.0	−10.2	+1.8	−15.0	−0.4	**−15.0
• Sideline	+3.0	+ 3.5	+3.4	+ 3.1	+2.0	− 6.3
• Approach	−0.7	− 1.9	−0.5	− 2.8	−2.0	− 6.1
• Traded	+1.0	+ 1.5	+1.4	+ 1.1	0.	− 7.7

* 1976 research technology qualified for 1985 design freeze.

** Oblique wing allows thrust cutback below 50% takeoff power.

Final oblique wing configuration

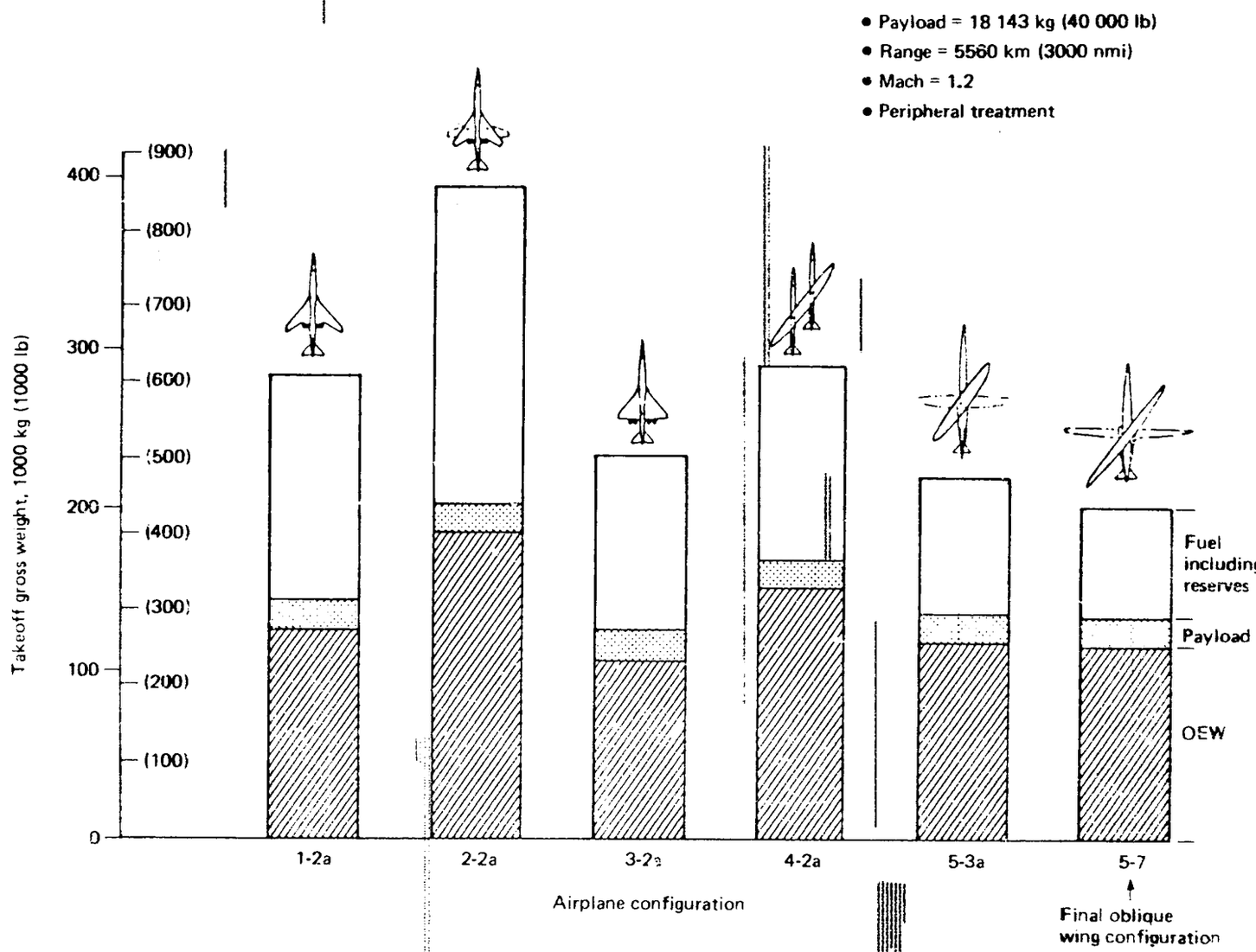

Figure 2 Gross Weight and Fuel Comparison

2.0 INTRODUCTION

This document is the final report of work accomplished at Boeing under contract NAS2-7031 (Mods. 5 and 6). It is the third in a series of reports that describe investigations of transport aircraft designed to cruise at high transonic speeds. These studies led to the definition of an oblique-wing transport configuration. The evolution of this configuration is illustrated in Figures 3, 4 , and 5.

Because of sonic boom, transport aircraft have been prevented from cruising overland at high supersonic Mach (M) numbers in the United States and some parts of the world. However, at near sonic speeds, ($M \leq 1.2$) atmospheric effects refract the shock waves generated by the airplane away from the ground, and boom-free supersonic flight is possible.

Aircraft that cruise at these high transonic speeds are of interest because, compared to conventional subsonic aircraft, they offer a considerable time saving on transcontinental flights. This interest was enhanced by advances in supercritical aerodynamics and design concepts such as the oblique wing. Consequently, in 1972, NASA Ames Research Center initiated studies of high transonic speed transport aircraft.

The first of these studies, reported in Reference 1, developed and compared the five configuration concepts (Figure 3). The single-bodied oblique wing displayed the highest performance potential. Many variants of this concept were investigated, leading to the Model 5-3 (Figure 6), ~~which has four~~ BPR = 1 engines integrated into the aft body.

Exploration of the oblique wing was continued during the second study, described in Reference 2 and outlined in Figure 4. These investigations included evaluation of twin- and three-engined installations, a climb placard study, and an investigation of aeroelastic effects on stability and control.

The third study, described in this report and outlined in Figure 5, covered the following topics:

- Wing planform selection
- Pivot design and weight estimation
- Engine cycle selection
- Climb, descent, and reserve fuel determination

The knowledge gained from all these studies was incorporated into the final configuration, Model 5-7, shown in Figure 1.

The contract technical monitor was Walter P. Nelms, NASA Ames Research Center. The work was conducted by members of the Preliminary Design department of the Boeing Commercial Airplane Company.

Technical Staff Integration	T. H. Hallstaff
Aerodynamic Analysis	T. H. Hallstaff S. E. Tolzmann R. Maier
Performance	R. L. Sullivan
Structural and Aeroelastic Analysis	J. W. Nisbet K. Kumasaka
Weights	B. Giridharadas
Configuration Development	W. F. Moore
Propulsion	H. G. Ridley
Flight Controls	P. Brubaker
Pivot Design	J. Brogan

Initial program objectives

- Synthesize 5 basic high transonic transport configuration concepts
  - Consistent technology
  - Consistent payload/range
  - Develop resulting performance and economics
- Evaluate technical feasibility of basic concepts
- Identify high risk technology areas

June 10, 1972 — Configuration initial definition — July 20, 1972 — Definition refinement

0 month — 1 month

Aerodynamic concepts

Concept no. 1 (fixed swept wing)

Concept no. 2 (variable sweep wing)

Concept no. 3 (delta wing)

Concept no. 4 (twin fuselage, yawed wing)

Concept no. 5 (single fuselage, yawed wing)

Model 4-01 Model 4-03

- First cycle configuration arrangements were defined
- Design review at NASA Ames
- Design layouts developed
  - Gross weight—272 155 kg (600 000 lb)
  - 1985 technology
  - 4 bypass ratio = 1 engine
- Mission design objectives
  - Mach = 1.2
  - Payload = 18 147 kg (40 000 lb)
  - Range = 5556 km (3000 nmi)

Model 1-2

Model 2-2

Model 3-2

Model 4-2

Model 5-2

High nacelle drag installation identified

Model 5-01 Model 5-04 Model 5-06 Model 5-07 Model 5-010

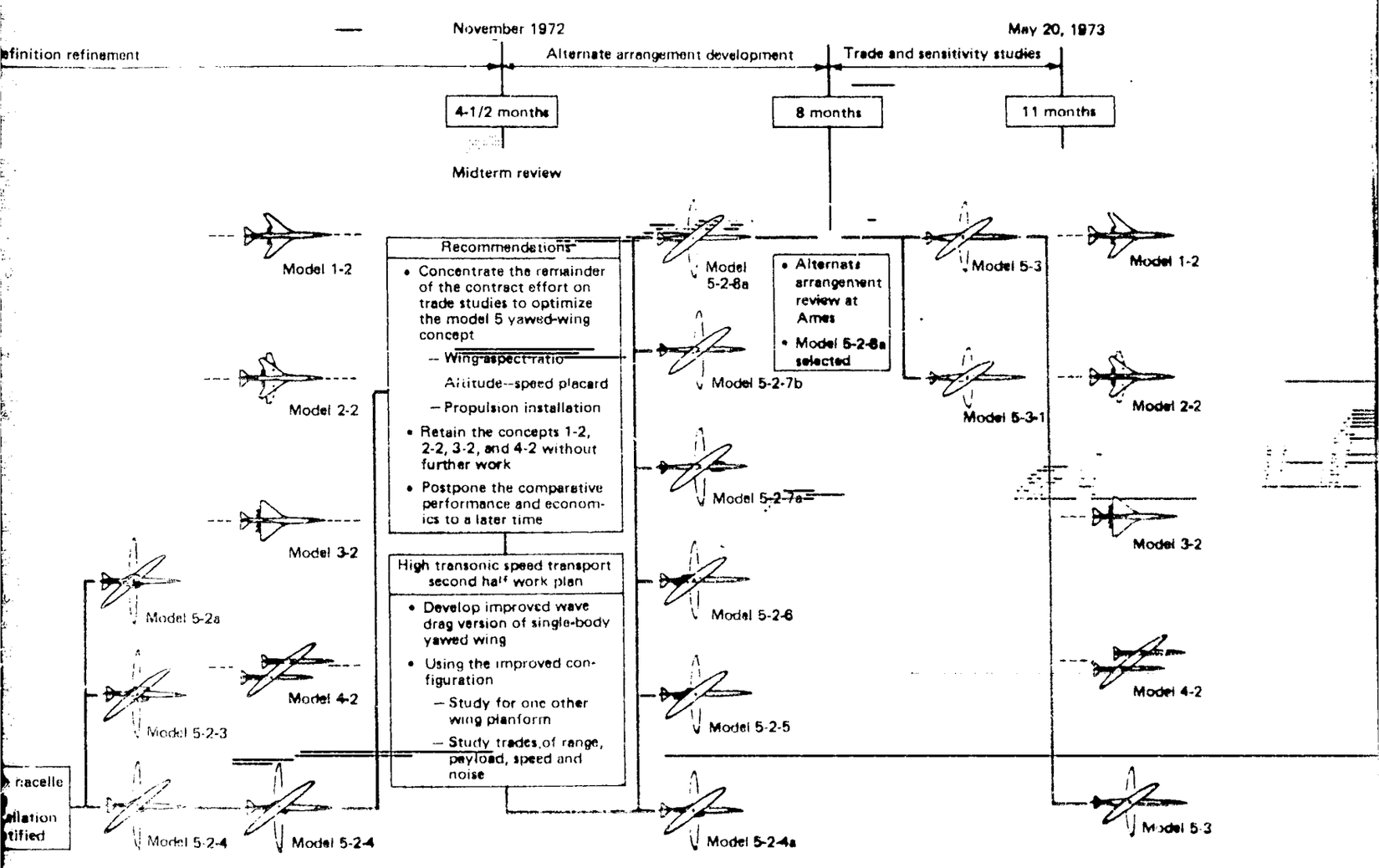

Figure 3 Configuration Evolution—Phase I

Alternate Powerplant Installations

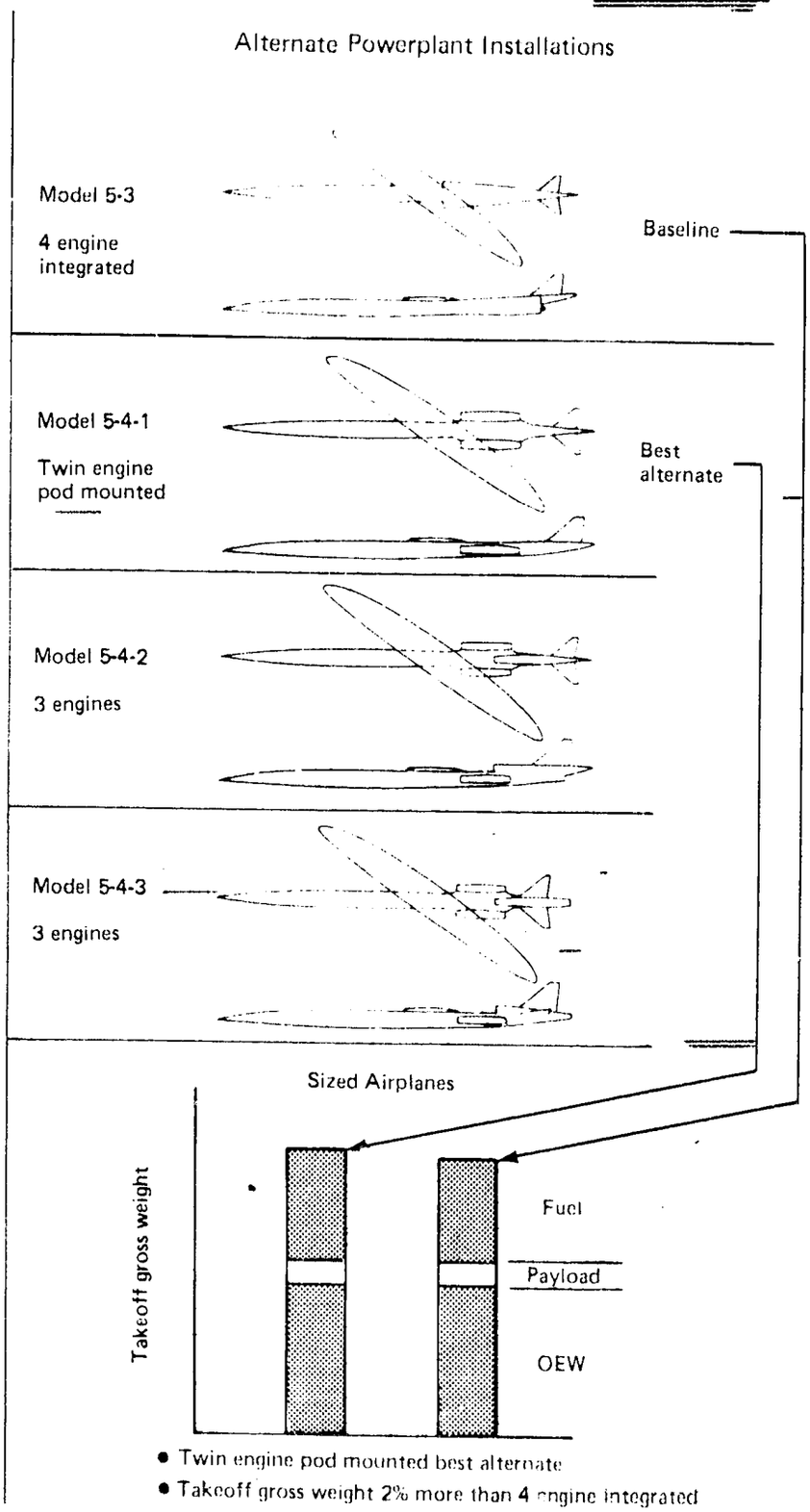

- Twin engine pod mounted best alternate
- Takeoff gross weight 2% more than 4 engine integrated

Placard Study

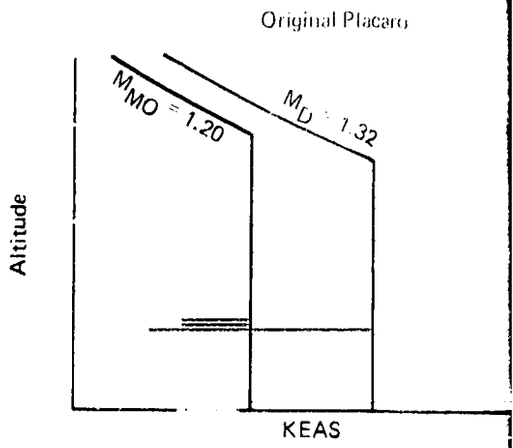

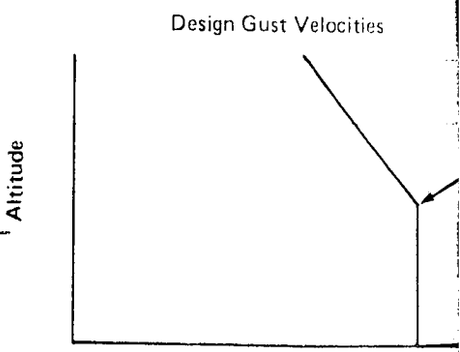

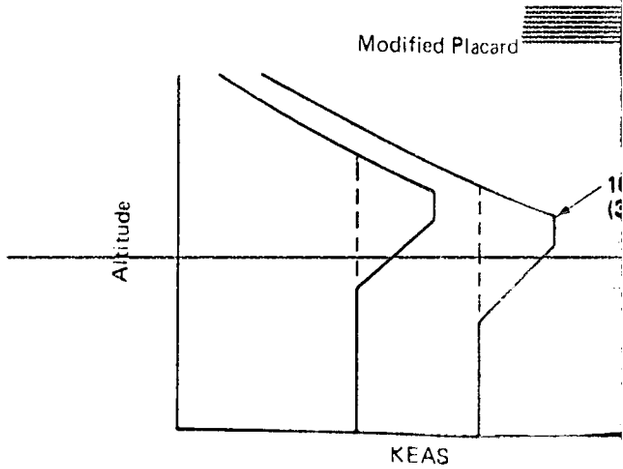

- Modified placard permits initial cruise altitude reduce to 10,363 m (34,000 ft) without st weight penalty.

FOLDOUT FRAME /

Placard Study

Original Placard

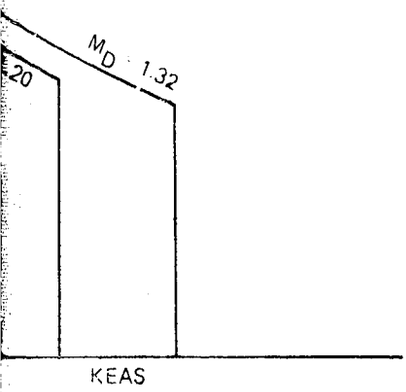

Design Gust Velocities

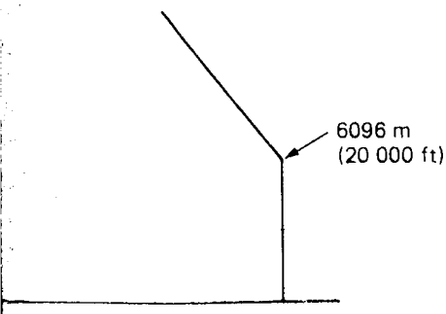

Modified Placard

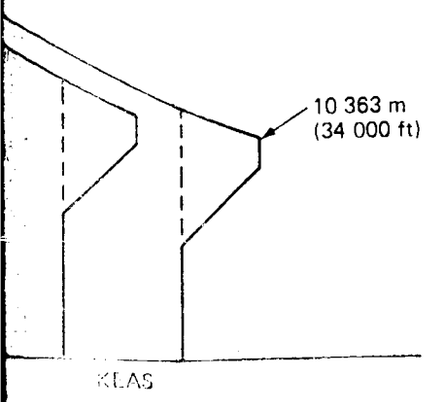

placard permits initial cruise altitude to
10 363 m (34 000 ft) without structural
nalty.

Aeroelastic Stability and Control

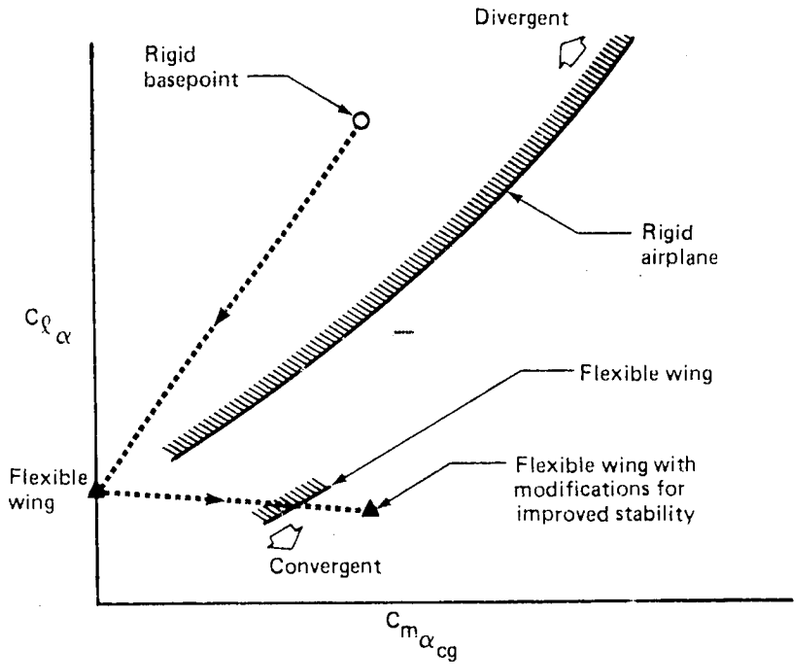

Convergent response attained by:

- Increased static margin from cg shift and stability augmentation
- Forward pivot location
- Wing flexibility

Figure 4 Configuration Evolution—Phase II

Planform Study

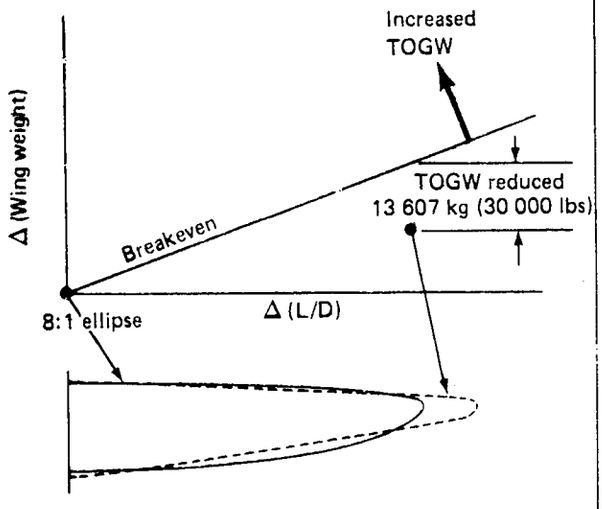

- Increase aspect ratio to 13.47
- Increase taper to 0.25
- t/c = 12% constant

Pivot Design

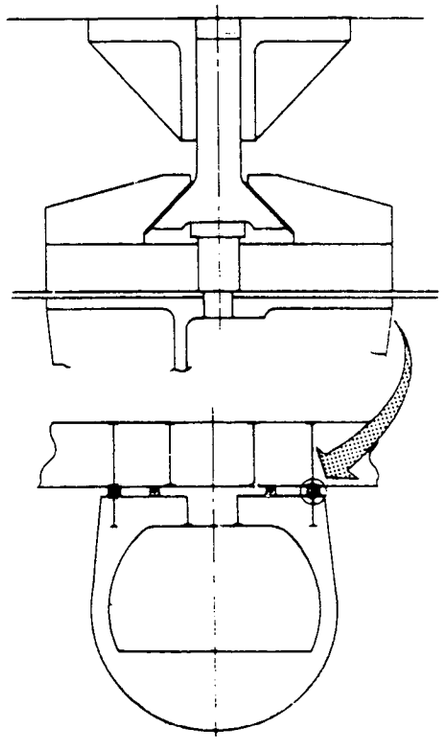

- Teflon-coated turntable bearing
- Weight estimates from sized structural layouts

Engine Cycl

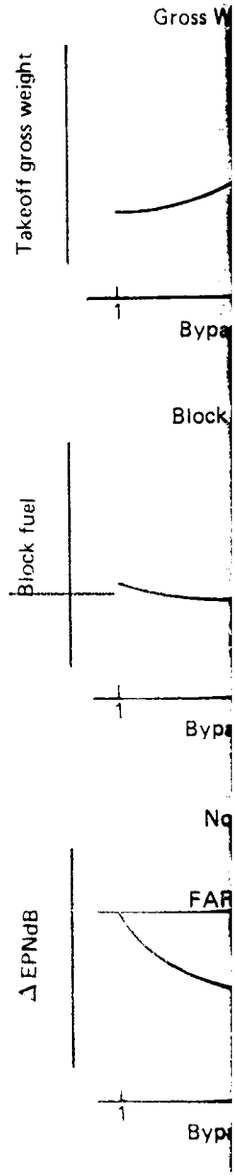

- Select bypass rati

FOLDOUT FRAME

Engine Cycle Study

Gross Weight

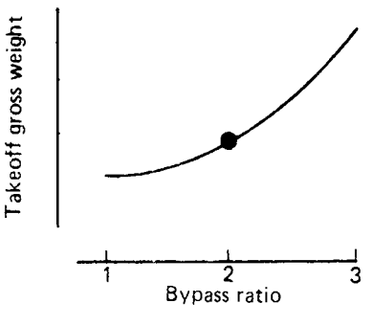

Block Fuel

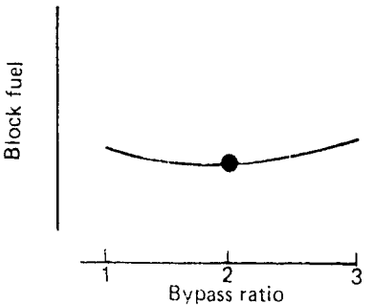

Noise

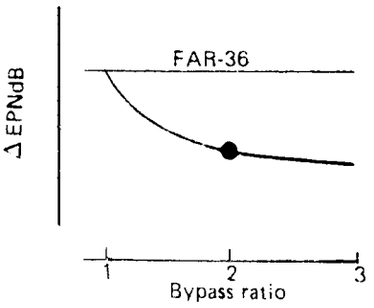

- Select bypass ratio = 2 engines

Climb, Descent and Reserve Fuel

Optimum Sweep

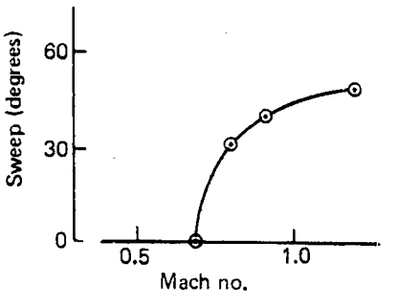

Optimum Climb Schedule

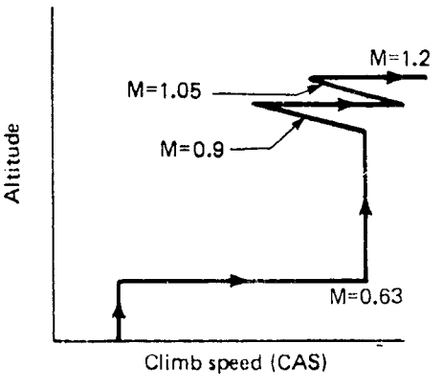

Reserves Rules

- One-hour extended cruise at M = 0.9
- Missed approach
- Alternate cruise (200 nmi)

Final Configuration

Model 5-7

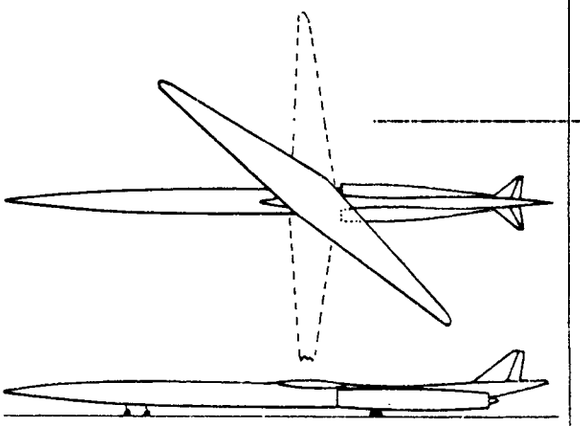

- 4 engine integrated
- Bypass ratio = 2
- Wing AR = 13.47, taper 0.25
- t/c = 12%

Figure 5 Configuration Evolution—Phase III

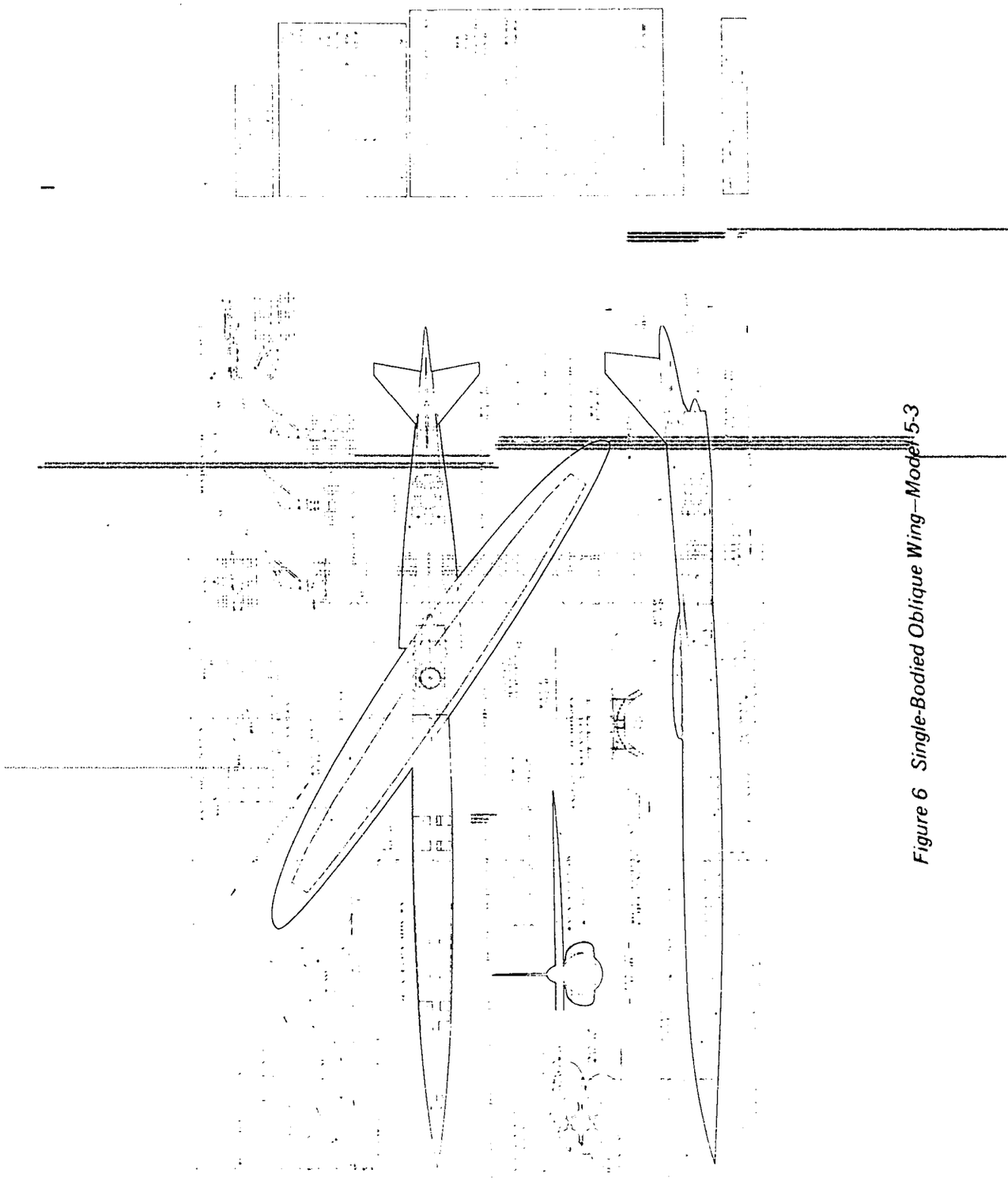

Figure 6 Single-Bodied Oblique Wing—Model 5-3

3.0 SYMBOLS AND ABBREVIATIONS

AI	inlet area
alt	altitude
a_0	two-dimensional lift curve slope
app	approach
AR	aspect ratio at zero sweep
AR(A)	swept aspect ratio
ATA	Air Transport Association
Aw	wetted area
aux	auxiliary
b	span
β	$\sqrt{M^2 - 1}$
BPR	bypass ratio
$\bar{c}$	mean aerodynamic chord
c	local chord
C_A	aft flap chord
CAS	calibrated airspeed
C'/C	Fowler motion ratio, expanded wing chord to wing chord ratio
C_D	drag coefficient
C_{D_F}	friction drag coefficient
C_{D_0}	minimum drag coefficient
C_{D_R}	roughness drag coefficient
$C_{D_{SYM}}$	minimum drag of symmetric, nonlifting configuration
C_{D_W}	wave drag coefficient

C_F	skin friction coefficient
C_F/C	trailing edge flap chord to wing chord ratio
cg	center of gravity
C_L	lift coefficient
$C_{L_{app}}$	approach lift coefficient
$C_{L_{\alpha=0}}$	lift coefficient at zero incidence
C_{LE}	leading edge flap chord
C_{L_H}	horizontal tail lift coefficient
C_{LI}	initial cruise lift coefficient
$C_{LL_{OF}}$	lift coefficient at liftoff
$C_{L_{V_2}}$	Lift coefficient at V
cm	centimeter
C_{n_β}	yawing moment due to sideslip stability derivative
const	constant
C_{PB}	base pressure coefficient
C_R	root chord
CT	leading edge thrust coefficient
deg	degrees
dia	diameter
D	drag force
e	span efficiency factor
EAS	equivalent airspeed
ell	elliptic
EPNdB	effective perceived noise level

F	net force at pivot center
FAR	Federal Aviation Regulation
Fn	net thrust
ft	feet
fwd	forward
g	acceleration due to gravity
GM	gross mass
GW	airplane gross weight
HL	hinge line
horiz	horizontal
hp	horsepower
hrs	hours
ICAC	initial cruise altitude capability
in.	inch
K	drag due to lift factor
K_1 through K_6	various constants having values identified as in text
KCAS	calibrated airspeed knots
K_E	envelope drag due to lift factor
KEAS	knots equivalent airspeed
kg	kilograms
km	kilometer
KTS	nautical miles per hour
l	characteristic length
lb	pound

lbf	pound force
lbm	pound mass
L/D	lift/drag ratio
L/D_{V_2}	lift/drag ratio at takeoff climb speed
LE	leading edge
$l_{H.25_c}$	tail arm
LRC	long-range cruise
M	Mach number
M	net moment at pivot center
LOF	liftoff
m	meters
MAC	mean aerodynamic chord (zero sweep)
matl	material
max	maximum
M_C	design cruise Mach number
M_D	design dive Mach number
min	minimum
MP	maneuver point
MTOGW	maximum takeoff gross weight
N	newton
n	load factor
nmi	nautical miles
No..no.	number
OEW	operating empty weight

opt	optimum
P	loading intensity on pivot
PTFE	teflon
rad	radian
R/C	rate of climb
RF	range factor
S	wing reference area
s	effective leading edge suction factor
SAS	stability augmentation system
sec	second
SFC	specific fuel consumption
S_H	horizontal tail area
SI	standard international
SL	sea level
SLST	sea level static thrust
SST	supersonic transport
sta	station
T^*	mean temperature
ti	titanium
t/c	thickness to chord ratio
TE	trailing edge
TOFL	takeoff field length
TOGW	takeoff gross weight
T/W	thrust to weight ratio

typ	typical
V	ultimate vertical load on the pivot–newtons (lb)
V_2	takeoff climb speed
V_{app}	approach speed
V_C	design cruise speed
V_D	design dive speed
VE	equivalent airspeed
vert	vertical
V_H	horizontal tail volume coefficient
VS	stall speed
V_V	vertical tail volume coefficient
W_1	weight of wing box structural penalty due to pivot
W_2	weight of penalty to fuselage structure due to pivot
WBN-W	(wing body nacelle)–wing
W_{BOX}	combined weight of wing box shear and bending material inclusive of nontheoretical structure, e.g., pads, fasteners
WL	waterline
W/S	wing loading
X,Y,Z	reference axes from pivot center: X positive aft; Y positive to right wing tip; Z positive upward
α	angle of attack
α_0	angle of attack at zero lift
δe	elevator deflection
δF_{TE}	trailing edge flap deflection angle
δH	stabilizer deflection

ΔP	loading intensity gradient across pivot diameter
$\ddot{\theta}$	pitch acceleration
λ_E	wing equivalent taper ratio
τ	roll time mode constant
Λ	sweep angle of wing quarter chord line
$\approx$	approximately

4.0 WING PLANFORM STUDY

4.1 SUMMARY

The purpose of this study was to determine the wing planform shape and aspect ratio (AR) best suited to the transonic oblique-wing transport. Earlier work (References 1 and 2) utilized elliptic planforms with elliptic spanwise distribution of thickness/chord ratio (t/c). In the present study, the five additional planforms shown in Figures 7 and 8 were investigated. These extended the range of the study to more highly tapered shapes and higher aspect ratios. It was anticipated that an increased taper would result in a reduction in wing weight or would reduce drag by allowing the span to be increased without an increase in wing weight.

In addition to the planform investigation, some variations in thickness/chord ratio and spanwise distribution of thickness were studied. The study was conducted on the uncycled baseline Model 5-3, whose development is described in Reference 1. This configuration has a wing area of 371.6 m^2 (4000 ft^2) and a takeoff gross weight (TOGW) equal to 226 800 kg (500 000 lb).

The major results were:

- Tapered planform 5 (AR = 13.47, λ_E = 0.25) offers the best cruise performance. This planform, with constant 12 percent thickness/chord ratio, was selected for use in subsequent studies. The use of this planform reduced the TOGW of the sized airplane by approximately 13 608 kg (30 000 lb) and block fuel by 9072 kg (20 000 lb).

- Cruise performance is improved when the spanwise distribution of thickness/chord ratio is changed from elliptic to constant. This occurs because the reduction in wing weight more than compensates for the increase in wave drag.

- Estimates based on linearized aerodynamic theory show that performance would further improve if thickness/chord ratio were increased to 14 percent or more. In practice, the maximum allowable thickness would be determined by the onset of flow separation. Reference 3, published after completion of this study, contains data that suggest that 12 percent is close to the maximum allowable value, because a significant loss in lift/drag ratio (L/D) was found when thickness increased from 12 percent to 14 percent.

4.2 STUDY DESCRIPTION

The study baseline was the oblique-wing transport Model 5-3, (Figure 6) that is described in Reference 1. The cruise (M = 1.2) lift/drag ratio of this configuration was evaluated both with the baseline elliptic wing and with each study wing. The study wings were analyzed at sweep angles between 0.79 rad (45°) and 1.05 rad (60°), so that the optimum sweep angle could be determined.

The size of the wing structural members was determined by an analysis that included both strength and stiffness requirements.

8:1 Elliptic Wing

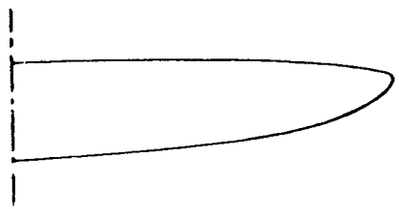

AR = 10.2 λ_E = 0.571
b/b_{ell} = 1.0

Tapered Planform No. 1

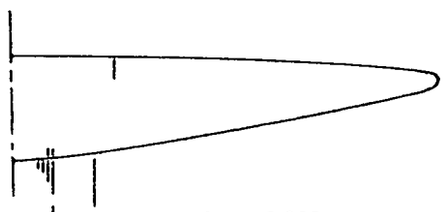

AR = 12.3 λ_E = 0.328
b/b_{ell} = 1.1

Tapered Planform No. 2

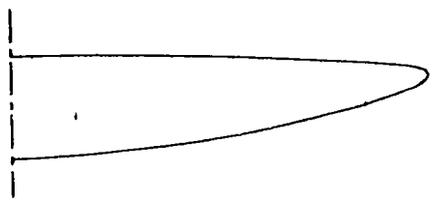

AR = 11.25 λ_E = 0.436
b/b_{ell} = 1.05

Tapered Planform No. 3

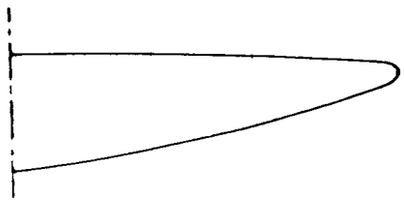

AR = 10.2 λ_E = 0.328
b/b_{ell} = 1.0

Tapered Planform No. 4

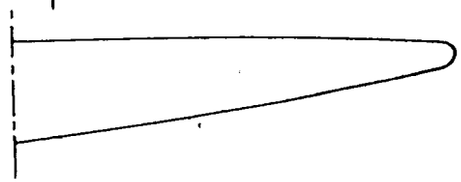

AR = 13.47 λ_E = 0.328
b/b_{ell} = 1.15

Tapered Planform No. 5

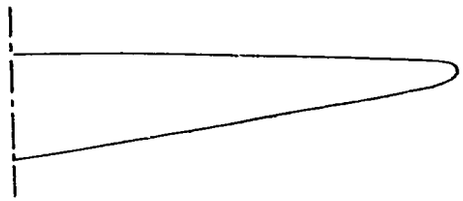

AR = 13.471 λ_E = 0.250
b/b_{ell} = 1.15

Note: $\lambda_E = \frac{2S}{bc_{root}} - 1$

Figure 7 Study Planforms

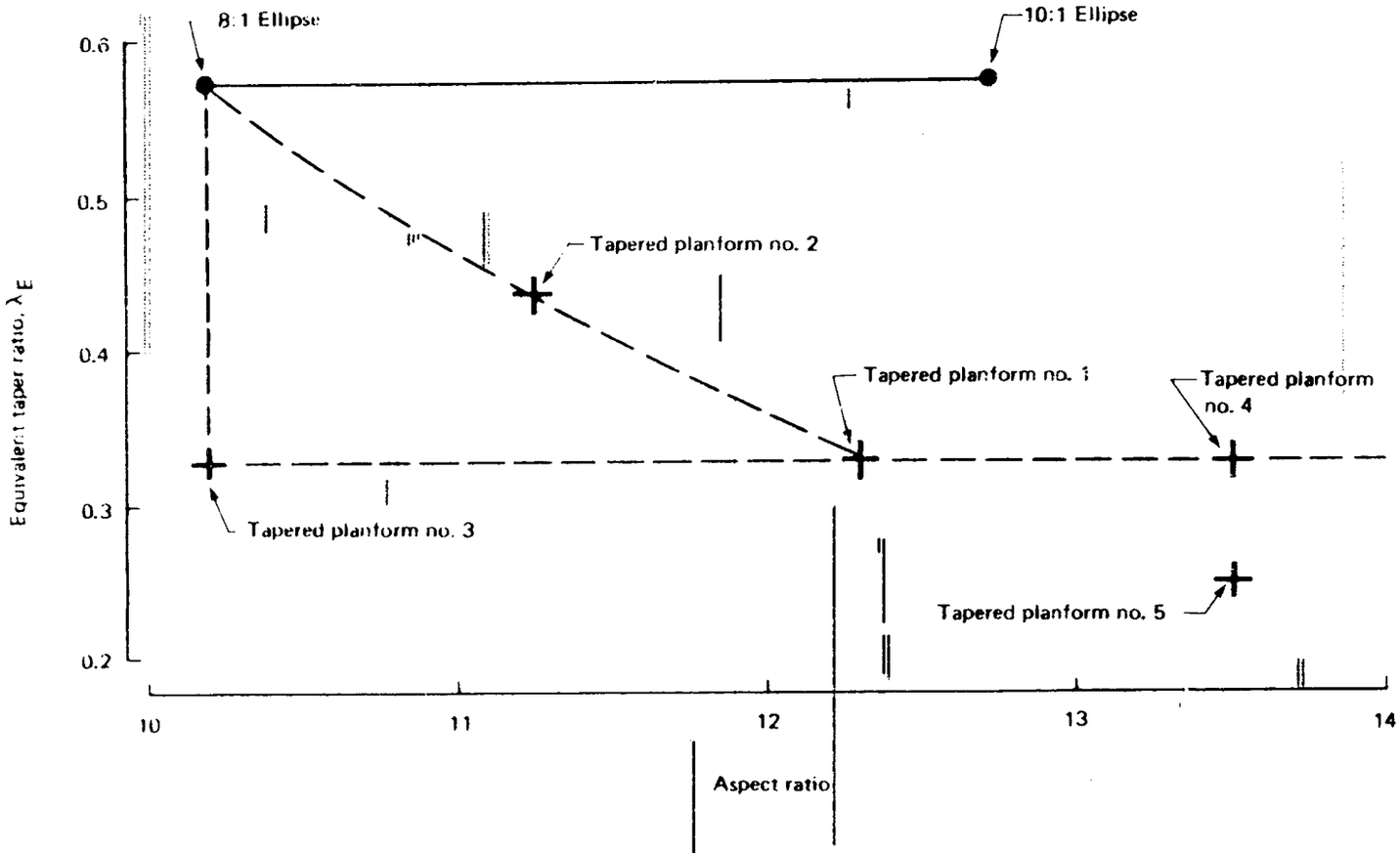

Figure 8 Aspect Ratio and Taper Ratio Variations

Using the theoretical wing-box weights from structural analysis, wing weights for all planforms were calculated by allowing for nonoptimum structure, leading edges (LE), and trailing edges (TE).

The best planform was selected by comparing the change in cruise performance, relative to the baseline, using trade factors derived from earlier studies.

Finally, the low-speed characteristics of the selected wing were evaluated and compared to the basepoint elliptic planform.

These analyses are described in Sections 4.3 to 4.7.

4.3 PLANFORM DEFINITIONS

The study planforms are defined in Figures 9 to 13, and are compared to the baseline 8:1 ellipse. The derivation of these planforms is described below.

The span of planform 1 was made 10 percent greater than the baseline 8:1 ellipse. A new spanwise distribution of chord was then found using the approach described in Reference 4, which gives minimum induced drag while maintaining lift and root bending moment equal to that of the baseline ellipse. The planform was then modified slightly to increase the chord near the wing tip while maintaining constant area (Figure 14).

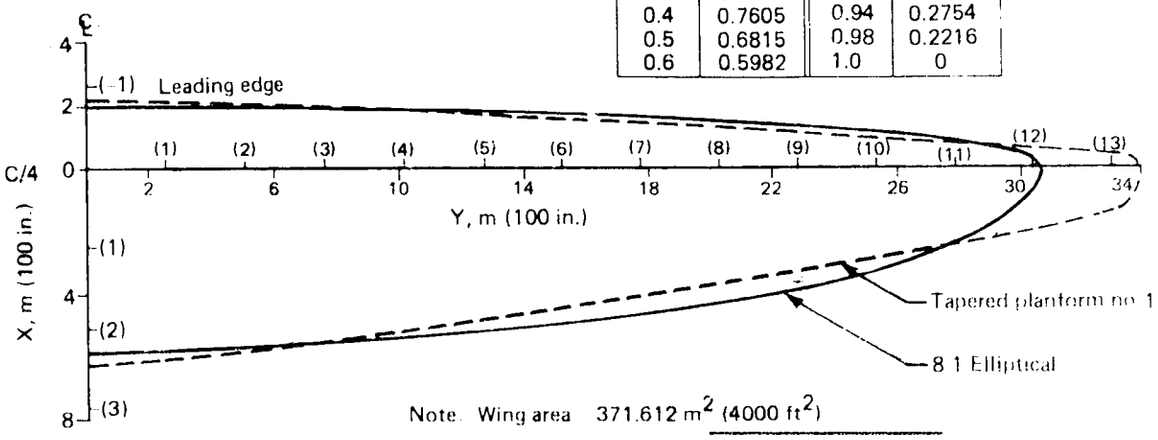

Figure 9 Tapered Planform No. 1

$2y/b$	C/C_R	$2y/b$	C/C_R
0	1.0	0.6363	0.6635
0.0786	0.9905	0.7856	0.4762
0.1571	0.9714	0.8641	0.3746
0.3142	0.9079	0.9427	0.2714
0.3928	0.8571	0.9819	0.2159
0.4713	0.80	0.9898	0.1873
0.6284	0.6698	1.0	0

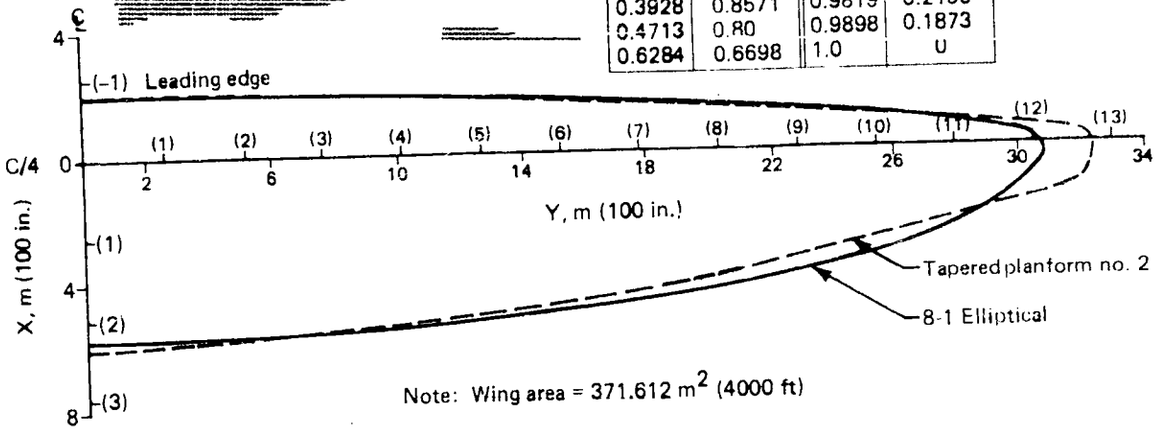

Note: Wing area = 371.612 m^2 (4000 ft)

Figure 10 Tapered Planform No. 2

$2y/b$	C/C_R	$2y/b$	C/C_R
0	1.0	0.6	0.5984
0.1	0.9564	0.7	0.5109
0.2	0.8997	0.8	0.4187
0.3	0.8334	0.9	0.3200
0.4	0.7605	0.98	0.2216
0.5	0.6817	1.0	0

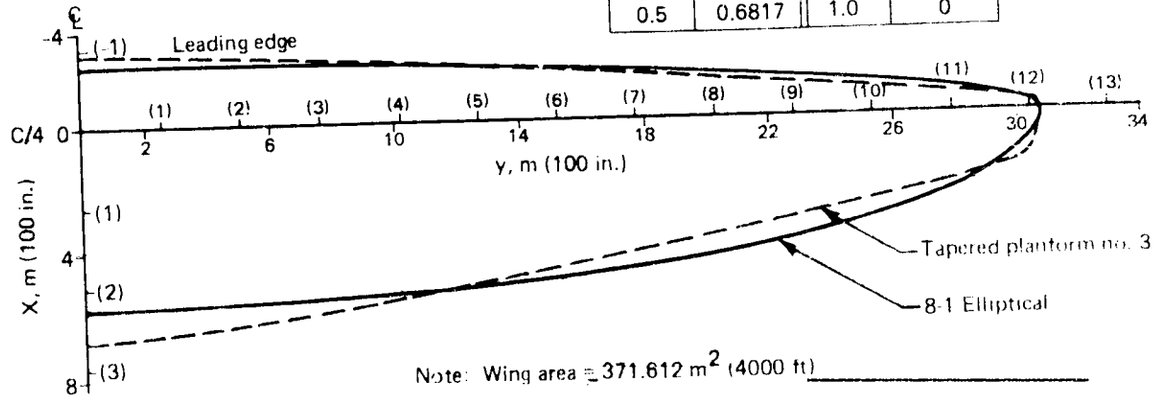

Note: Wing area = 371.612 m^2 (4000 ft)

Figure 11 Tapered Planform No. 3

$2y/b$	C/C_R	$2y/b$	C/C_R
0	1.0	0.80	0.4188
0.10	0.9564	0.90	0.3200
0.20	0.8995	0.920	0.2984
0.30	0.8335	0.940	0.2755
0.40	0.7604	0.96	0.2507
0.50	0.6817	0.980	0.2216
0.60	0.5983	1.0	0
0.70	0.5109		

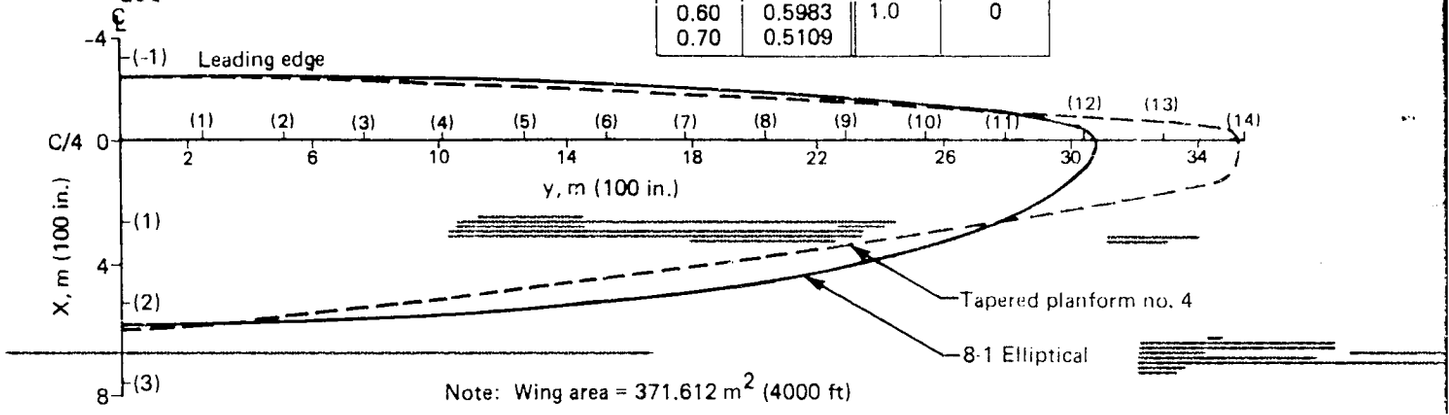

Note: Wing area = 371.612 m^2 (4000 ft)

Figure 12 Tapered Planform No. 4

$2y/b$	C/C_R	$2y/b$	C/C_R
0	1.0	0.80	0.3681
0.10	0.9419	0.90	0.2764
0.20	0.8720	0.92	0.2569
0.30	0.7957	0.94	0.2363
0.40	0.7144	0.96	0.2143
0.50	0.6301	0.98	0.1887
0.60	0.5440	1.0	0
0.70	0.4568		

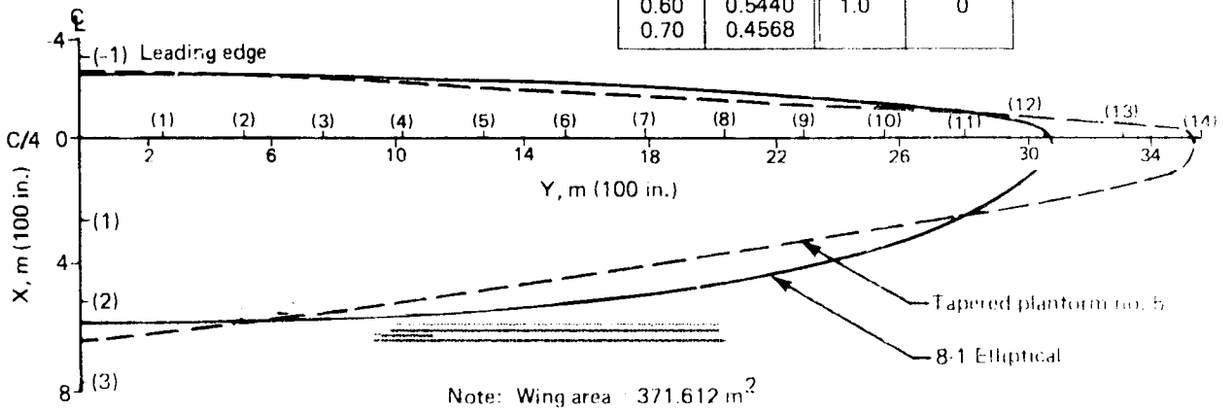

Note: Wing area = 371.612 m^2

Figure 13 Tapered Planform No. 5

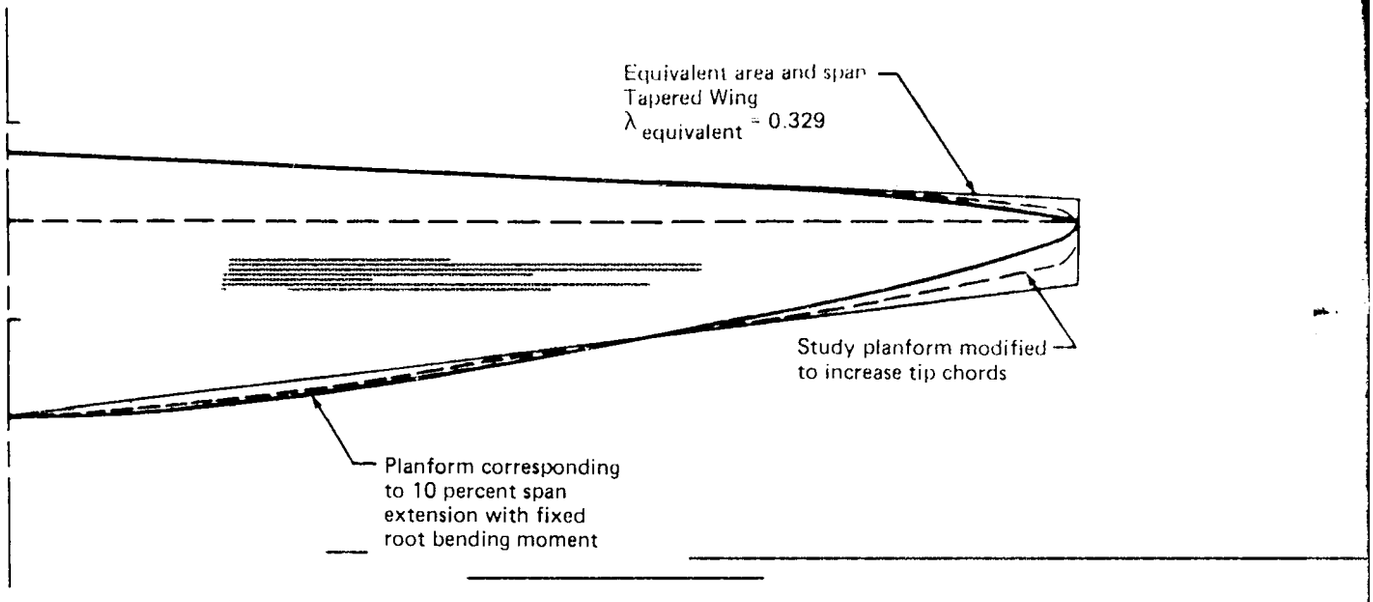

Figure 14 Tapered Wing Planform

The remaining planforms were derived by transforming planform 1 using the following expressions:

WING AREA

$$S = 372\ m^2\ (4000\ ft^2) = \frac{b_1}{2} \cdot C_{R_1} \cdot (1 + \lambda_{E_1}) = \frac{b}{2} \cdot C_R \cdot (1 + \lambda_E)$$

SPAN

$$\frac{b}{b_1} = \sqrt{\frac{AR}{AR_1}}$$

ROOT CHORD

$$\frac{C_R}{C_{R1}} = \left(\frac{1 + \lambda_{E1}}{1 + \lambda_E}\right) \cdot \frac{b_1}{b}$$

LOCAL CHORD

$$\frac{c}{C_R} = \left(\frac{c}{C_R}\right)_1 \left(1 - K \cdot \frac{2Y}{b}\right)$$

Where K is a constant related to taper ratio by

$$K \quad \left(\lambda_{E_1} \quad \lambda_E\right) \Big/ \int_0^1 \left(\frac{c}{C_R}\right)_1 \left(\frac{2Y}{b}\right) d\left(\frac{2Y}{b}\right)$$

The 25 percent chord line was held straight throughout the study.

A modified wing tip was developed for planform 5 (the selected planform), to ensure low wave drag and smooth airfoil sections at all sweep angles.

The wing tip region ($2Y/b > 0.9$) was modified as follows:

- The spanwise distribution of chord and thickness to chord ratio were redefined to be elliptical in the region $0.9 < 2Y/b < 1.0$.

- A spanwise variation of airfoil shape was defined that features a smooth variation from a subsonic section (blunt leading edge) at $2Y/b = 0.90$ to a supersonic section (sharp leading edge) for $0.98 < 2Y/b < 1.0$.

These changes ensure that the streamwise airfoil sections have sharp leading edges wherever the normal component of the free stream Mach number is supersonic, and that the wing equivalent bodies of revolution used in the wave drag calculations have zero rate of area growth at their extremities, as required by linearized theory. Figure 15 illustrates these changes by comparing planform 5 to the modified wing, designated planform 5a. The streamwise airfoil section shapes of planform 5a at several spanwise stations for a sweep angle of 0.87 rad (50°) are shown in Figure 16.

4.4 CRUISE DRAG

The method used to evaluate the effect of planform variations on total configuration cruise drag is shown in Figure 17.

Two simplifying assumptions were made:

(a) The zero-lift drag of the total configuration minus the isolated wing is not sensitive to planform variations.

(b) Drag due to lift (K_E) can be expressed as an envelope polar based on adjusted linear theory.

These assumptions allowed the total configuration drag to be compared to that of the Model 5-3 by comparing each new planform to the 8:1 ellipse. The total configuration drag was built up for each new planform at sweep angles of 0.79 (45°), 0.87 (50°) and 1.05 rads (60°), by adding the following items:

- The zero lift drag of the complete Model 5-3 minus wing (8:1 ellipse) skin friction and wave drag

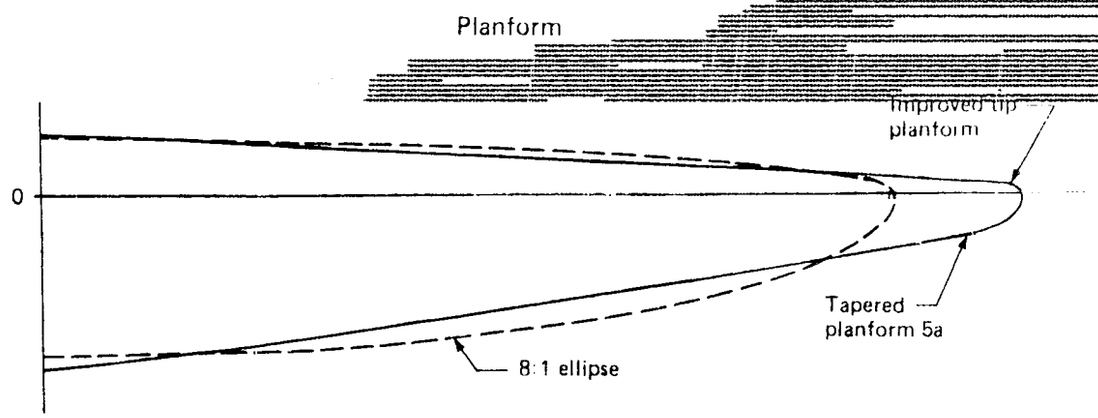

$2y/_b$	$X_{LE}/_{C_R}$	$C/_{C_R}$	$t_{max}/_C$
0	-0.25	1	0.12
0.10	-0.235	0.942	0.12
0.20	-0.218	0.872	0.12
0.30	-0.199	0.796	0.12
0.40	-0.179	0.714	0.12
0.50	-0.158	0.630	0.12
0.60	-0.136	0.544	0.12
0.70	-0.114	0.457	0.12
0.80	-0.092	0.368	0.12
0.90	-0.069	0.276	0.12
0.92	-0.064	0.255	0.1178
0.94	-0.057	0.227	0.1106
0.96	-0.048	0.191	0.0971
0.98	-0.035	0.138	0.0732
0.990	-0.025	0.099	0.0533
0.998	-0.011	0.034	0.0244
1	0	0	0

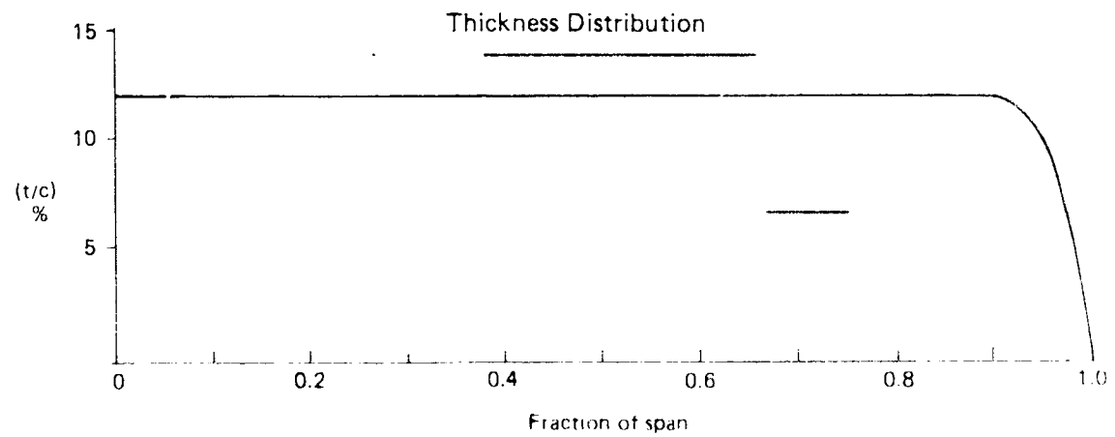

Figure 15 Selected Planform and Thickness Distribution

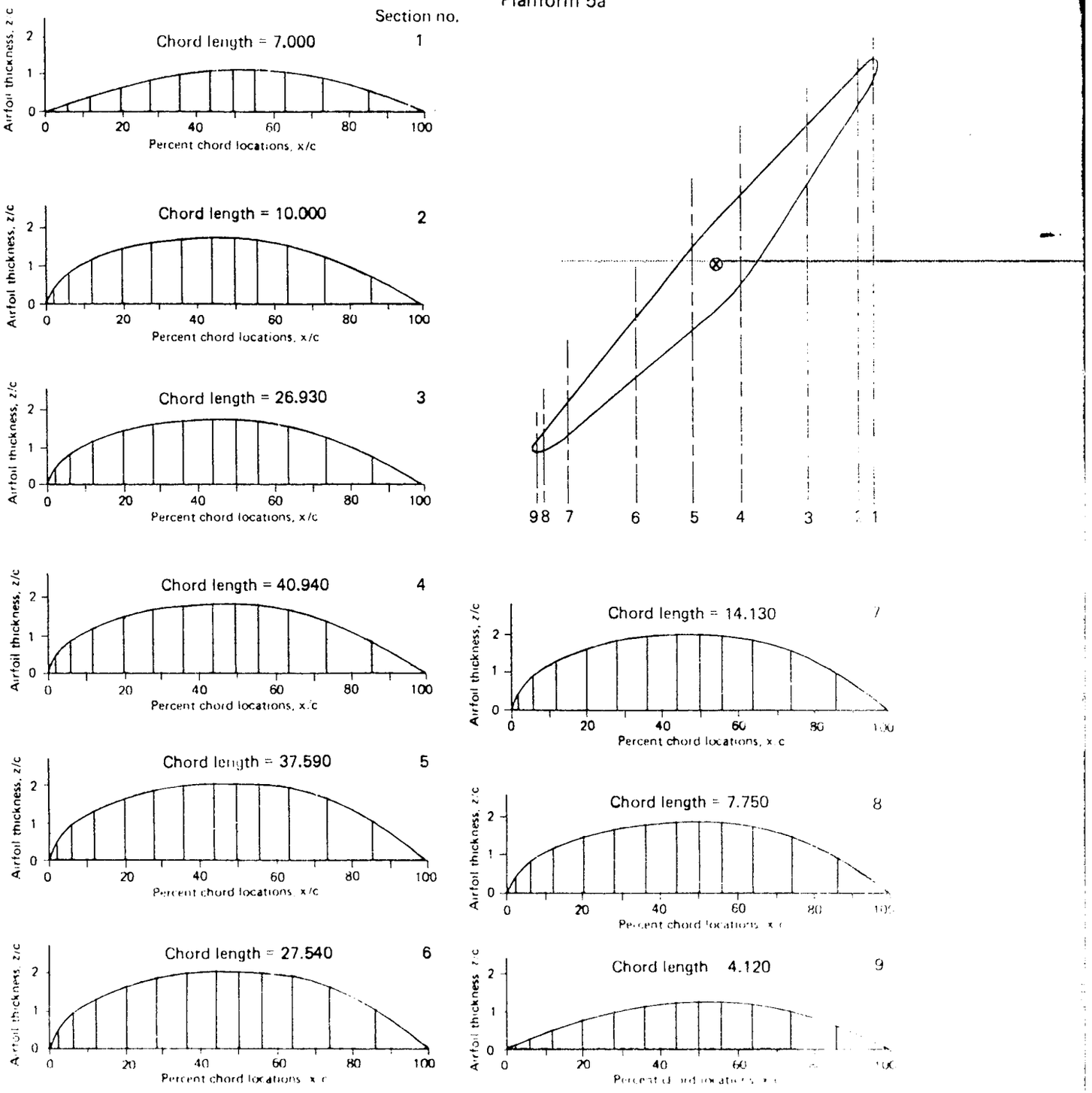

Figure 16 Streamwise Airfoil Section Shapes, $\Lambda = 0.87$ Rad (50^{0})

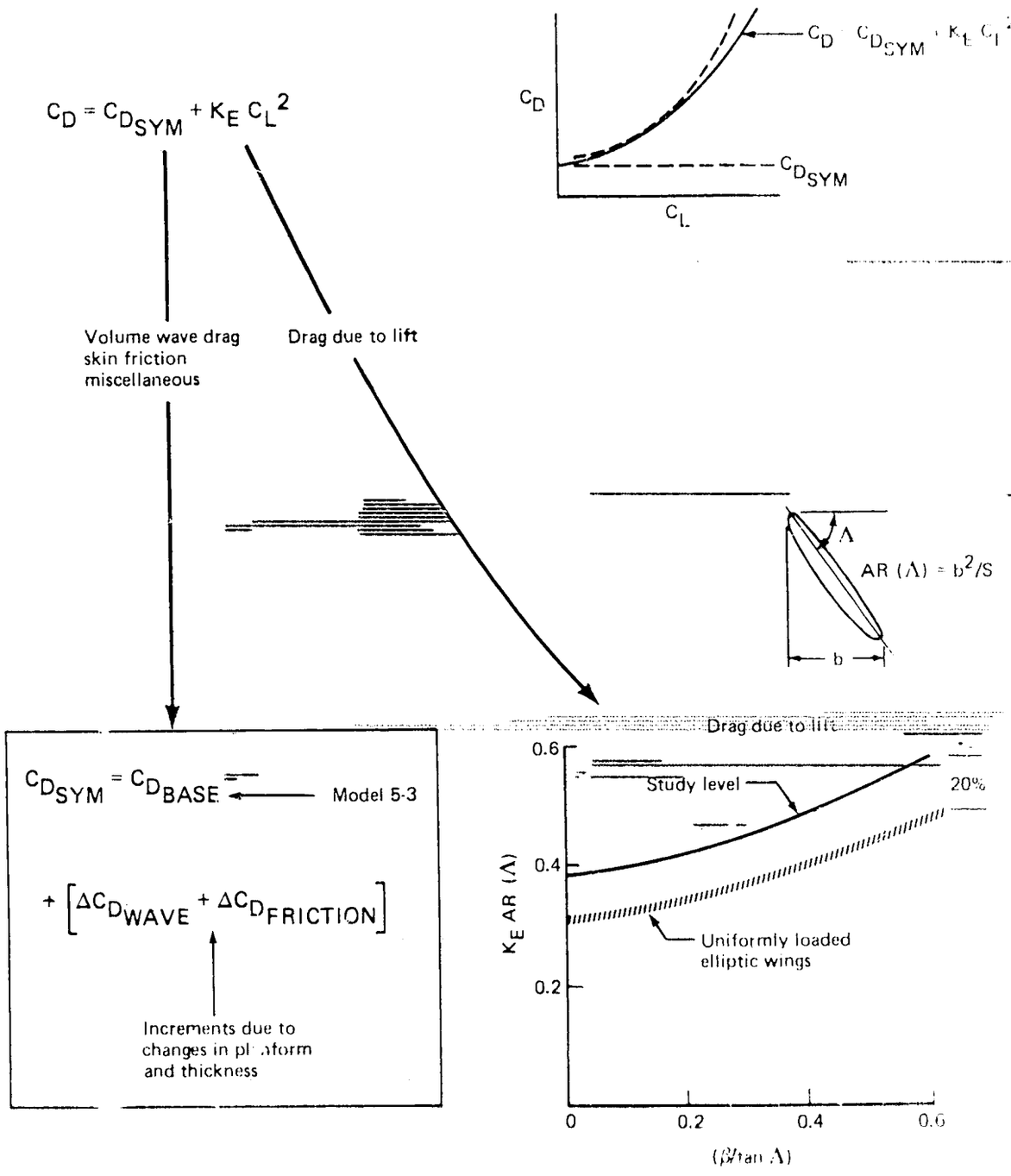

Figure 17 Planform Study – Cruise-Drag Method

- Wing skin friction and wave drag
- Drag due to lift

The first item is independent of planform, by assumption (a). The methods used to obtain friction, wave drag, and drag due to lift are described below. They are consistent with methods used in Reference 1.

4.4.1 SKIN-FRICTION DRAG

Skin-friction drag was calculated by the Sommer and Short T* method (Reference 5). The altitude was 11 887 m (39 000 ft), and the reference length for each planform and sweep angle was found by dividing the planform area 372 m^2 (4000 ft^2) by the swept span.

4.4.2 DRAG DUE TO LIFT

The drag-due-to-lift factor for each planform and sweep angle was obtained by using the analytic solution for the drag due to lift of an oblique elliptical wing (Reference 6). It was found that for a given sweep angle, the product of envelope-drag-due-to-lift factor (K_L) and swept aspect ratio remained essentially constant over a range of aspect ratios corresponding to the study planforms. The $K_L AR$ versus sweep angle curve obtained was then multiplied by a factor of 1.2 to account for the fact that the analytic solution represents a theoretical optimum that is unlikely to be attained in practice. These drag-due-to-lift values are discussed further in Sections 8.4.2 and 10.0.

4.4.3 WAVE DRAG

The zero-lift wave drag of each of the planforms was calculated using the supersonic area rule. Because the available computer program is not designed to handle asymmetric configurations directly, the approach depicted in Figure 18 was used. The entire wing was positioned far enough to the right of the plane of symmetry so as not to interfere with its image that is automatically created in the available computer program. The calculated drag is therefore twice that of an isolated wing.

To avoid time-consuming lofting procedures, a 65A-BIC airfoil,* defined streamwise, was used in the analysis. In practice, a supercritical airfoil, defined normal to the leading edge, would probably be used. This is a reasonable approximation, however, since oblique-wing wave drag predicted by the supersonic area rule is not sensitive to small variations in airfoil section shape (Reference 1, Figure 58).

The results of the cruise drag analysis are summarized in Figure 19 and Table 2.

Notice that for the tapered planforms, only a small wave drag penalty occurs when changing from elliptic to constant spanwise distribution of thickness chord ratio. Structural studies described in Section 4.5, showed that this change produced a significant weight saving. Therefore, the remaining planforms were analyzed only with constant thickness chord ratio.

*NACA 65 Thickness Distribution with Increased Depth Aft of 50 Percent Chord

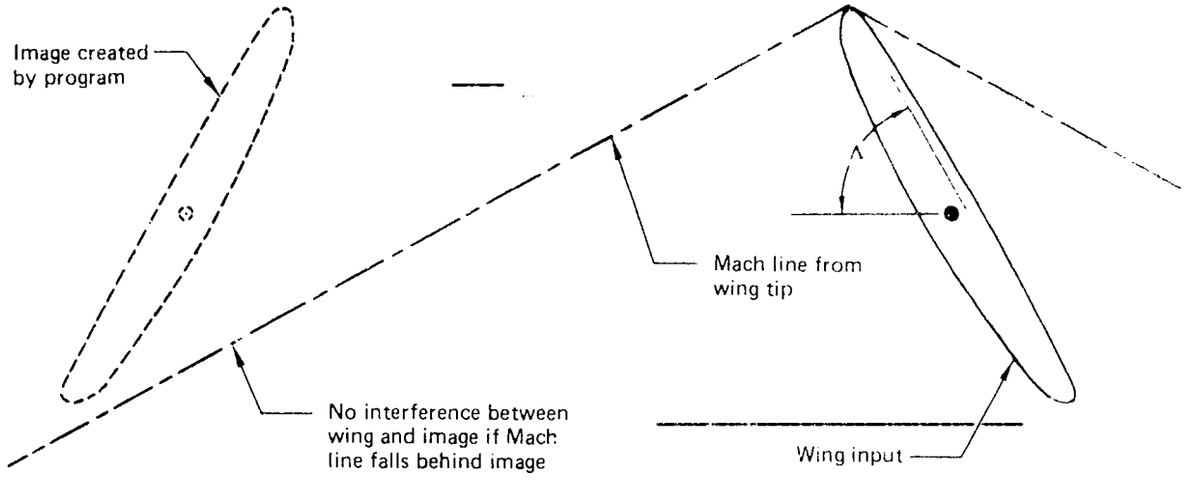

Figure 18 Oblique Wing Wave Drag Analysis

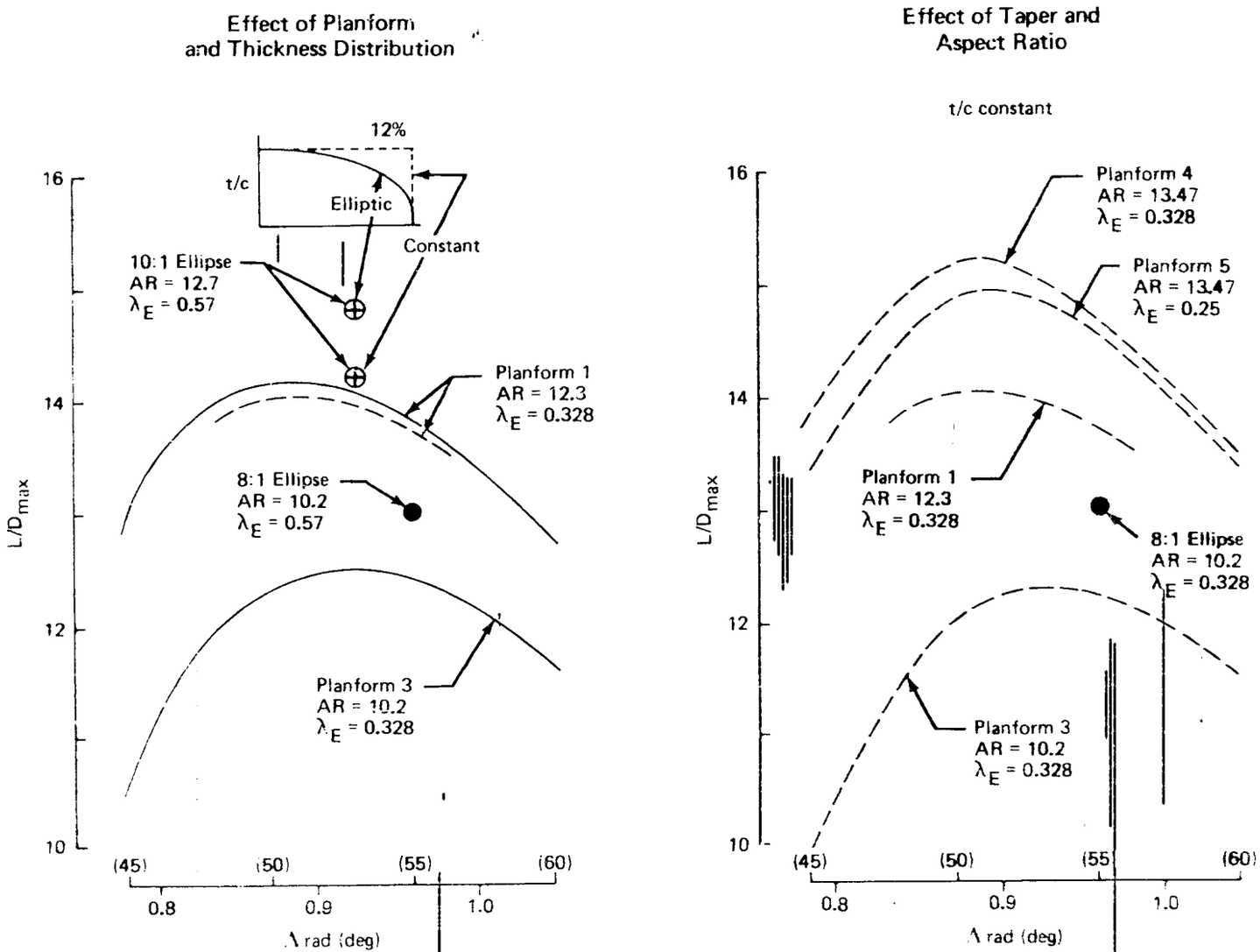

Figure 19 Planform Study–Cruise Lift/Drag Ratio

Table 2 Tapered Planform Sweep Optimization

Drag Buildup

Configuration	Sweep rad (deg)	Wing wave drag ell	Wing wave drag const	Wing skin friction	Body, tail, powerplant, interference*	C_{D_0} ell	C_{D_0} const	K_1	L/D_{max} ell	L/D_{max} const
Planform no. 1	0.79 (45)	0.00791		0.00390	0.00703	0.01884		0.078	13.01	
	0.87 (50)	0.00295	0.00335	0.00390		0.01388	0.01428	0.089	14.19	14.03
	0.96 (55)	0.00142	0.00163	0.00386		0.01231	0.01252	0.106	13.84	13.73
	1.05 (60)	0.00091		0.00378		0.01172		0.131	12.76	
Planform no. 2	0.79 (45)	0.00951		0.00394		0.02048		0.0863	11.89	
	0.87 (50)	0.00348		0.00390		0.01441		0.0967	13.39	
	0.96 (55)	0.00161		0.00384		0.01248		0.1137	13.27	
	1.05 (60)	0.00090		0.00376		0.01169		0.1426	12.25	
Planform no. 3	0.79 (45)	0.01279	0.01574	0.00392		0.02374	0.02669	0.094	10.58	9.98
	0.87 (50)	0.00473	0.00549	0.00388		0.01564	0.01640	0.105	12.34	12.05
	0.96 (55)	0.00236	0.00274	0.00380		0.01319	0.01357	0.123	12.41	12.24
	1.05 (60)	0.00140	0.00168	0.00375		0.01218	0.01246	0.152	11.62	11.49
8:1 ellipse	0.96 (55)	0.00163		0.00379		0.01245		0.120	12.94	
10 1 ellipse	0.93 (53)	0.00118	0.00225	0.00388		0.01209	0.01316	0.094	14.83	14.22
Model 5 3 with tapered planform no. 4	0.79 (45)		0.00696	0.0040			0.01799	0.072		13.89
	0.87 (50)		0.00248	0.00394			0.01345	0.081		15.14
	0.96 (55)		0.00118	0.00390			0.01211	0.096		14.05
	1.05 (60)		0.00067	0.00382			0.01152	0.122		13.45
Model 5-3 with tapered planform no. 5	0.79 (45)		0.00827	0.00400			0.01930	0.0725		13.37
	0.87 (50)		0.00294	0.00394			0.01391	0.0817		14.53
	0.96 (55)		0.00140	0.00390			0.01233	0.0960		14.53
	1.05 (60)		0.00079	0.00382	0.00703		0.01164	0.1205		13.36

*Based on Single Body Yawed-Wing Model S_{REF} 371.6m^2 (4000 ft^2)

● ell elliptic spanwise distribution of t/c ● const t/c constant over span ● t/c 12% at root

4.5 STRUCTURAL ANALYSIS

The results of an analysis to determine the theoretical structural material required for elliptic and tapered wing planforms are discussed in this section. The weight of the remaining nonoptimum and secondary structure that has to be added to the theoretical structure to obtain the total wing weight is discussed in the next section. The results of the structural and weight analysis are summarized in Table 3.

The wings, shown on Figures 9 to 13, were pivoted about 50 percent root chord at body station 58.9 m (2320 in.) on the Model 5-3 fuselage (Figure 6).

The wings were constructed of honeycomb with graphite-epoxy face sheets. Structural material properties and allowable stresses were taken from Reference 1.

The design criteria were consistent with the previous oblique-wing studies. Figure 20 shows the structural design speed placard that was developed as described in Reference 2. Previous analyses (Reference 1) indicated that a reasonable approximation to the structural weight of the wing would result from sizing the structure to the more stringent of the following conditions:

- Gust and maneuver loads at zero yaw angle
- Aeroelastic stability with the wing yawed to $\pi/4$ rad (45°)

The gust loads were analyzed for the airplane at its maximum zero fuel weight at 6096 m (20 000 ft) altitude and 180 m/sec (350 KT) equivalent air speed (EAS). The 2.5 acceleration-due-to-gravity (g) maneuver loads were analyzed for the airplane at its maximum gross weight at 4877 m (16 000 ft) altitude and 216 m/sec (420 KT) equivalent air speed. The minimum divergence speed for an oblique wing occurs at a yaw angle of $\pi/4$ rad (45°). At $\pi/4$ rad (45°) yaw, the wing lift curve slope is a maximum at Mach 1.0. Hence, aeroelastic instabilities are most likely to occur at a yaw angle of $\pi/4$ rad (45°) and Mach 1.0. Figure 20 shows that the Mach 1.0 line intersects the flutter and divergence requirements line at 271 m/sec (527 KT) equivalent air speed. This speed was used as the minimum aeroelastic stability clearance speed.

Table 3 shows the theoretical skin and spar weight required for graphite-epoxy wings that satisfy both strength and aeroelastic stability requirements. Only tapered wing number 1 with the elliptic thickness/cord ratio distribution required material for stability in addition to that required for strength. A comparison of the weights of tapered planform 3 to the 8:1 elliptic wing shows that tapered wings are lighter than elliptic wings of the same aspect ratio.

Changing from a thickness/chord ratio that has an elliptic spanwise variation to one that is constant at 12 percent reduced the theoretical structural material required for tapered planform 1 by 16 percent. Figure 21 shows a comparison of the theoretical material cross-section area and bending stiffness on the two thickness/chord ratio variations. On the wing with the elliptic thickness/chord ratio variation, surface material was added to the strength sized structure to increase the stiffness for aeroelastic stability. The stiffness of the

Table 3 Summary of Wing Weights

Wing planform	Spanwise thickness distribution	Aspect ratio	Equivalent taper ratio	Wing area m^2 (ft^2)	Span m (ft)	Mean aerodynamic chord m (ft)	Airplane max takeoff weight kg (lb)	Theoretical spar weight kg (lb)	[2] Theoretical skin weight kg (lb)	[3] Total wing weight kg (lb)
8:1 Elliptic	Elliptic	10.20	0.571	371.6 (4000)	61.56 (202.0)	6.55 (21.50)	226 796 (500 000)	715.9 (1576)	21 480 (47 350)	36 990 (81 550)
10:1 Elliptic	Elliptic	12.73	0.571		68.79 (225.7)	5.84 (19.17)		856.4 (1888)	33 300 (73 410)	51 950 (114 520)
Tapered No. 1	Elliptic	12.30	0.328		67.67 (222.0)	6.49 (21.29)		748.0 (1649)	27 020 (59 570)	43 960 (96 920)
Tapered No. 1	Constant t/c = 0.12	12.30	0.328		67.67 (222.0)	6.49 (21.29)		820.1 (1808)	22 480 (49 570)	38 380 (84 620)
Tapered No. 2	Elliptic	11.25	0.436		64.68 (212.2)	6.40 (21.00)		852.8 (1880)	23 120 (50 970)	37 900 (83 560)
Tapered No. 3	Elliptic	10.20	0.328		61.56 (202.0)	7.14 (23.42)		597.8 (1318)	19 930 (43 940)	34 920 (76 980)
Tapered No. 4	Constant t/c = 0.12	13.50	0.328		70.74 (232.1)	6.21 (20.37)		880.0 (1940)	26 340 (58 060)	43 270 (95 400)
Tapered No. 5	Constant t/c = 0.12	13.50	0.250		70.74 (232.1)	5.92 (19.41)		845.1 (1863)	24 680 (54 420)	41 080 (90 750)
Tapered No. 4	Constant t/c = 0.14	13.50	0.328		70.74 (232.1)	6.21 (20.37)		893.6 (1970)	21 520 (47 440)	37 270 (82 160)
Tapered No. 5	Constant t/c = 0.14	13.50	0.250		70.74 (232.1)	5.92 (19.41)		863.6 (1904)	20 190 (44 500)	35 560 (78 400)
Tapered No. 5	Constant t/c = 0.10	13.50	0.250		70.74 (232.1)	5.92 (19.41)		860.9 (1898)	32 690 (72 060)	51 180 (112 840)
Tapered No. 5a	[1]	13.50	0.250		70.74 (232.1)	5.92 (19.41)		839.2 (1850)	24 620 (54 260)	41 070 (90 540)
Tapered No. 5a		13.50	0.250		70.74 (232.1)	5.92 (19.41)	208 652 (460 000)	818.7 (1805)	23 940 (52 770)	40 200 (88 620)
Tapered No. 5a		13.50	0.250		70.74 (232.1)	5.92 (19.41)	190 509 (420 000)	797.4 (1758)	23 280 (51 320)	39 350 (86 750)
Tapered No. 5a		13.50	0.250	315.9 (3400)	65.23 (214.0)	5.46 (17.90)	208 652 (460 000)	689.5 (1520)	20 370 (44 900)	35 580 (78 420)

[1] t/c = 0.12 constant inboard of = 0.9, t/c elliptic outboard of = 0.9

[2] Theoretical spar and skin weights from structural analysis

[3] Total wing weight, including nonoptimum wing box structure, wing box ribs, pivot and pivot structure, leading and trailing edges

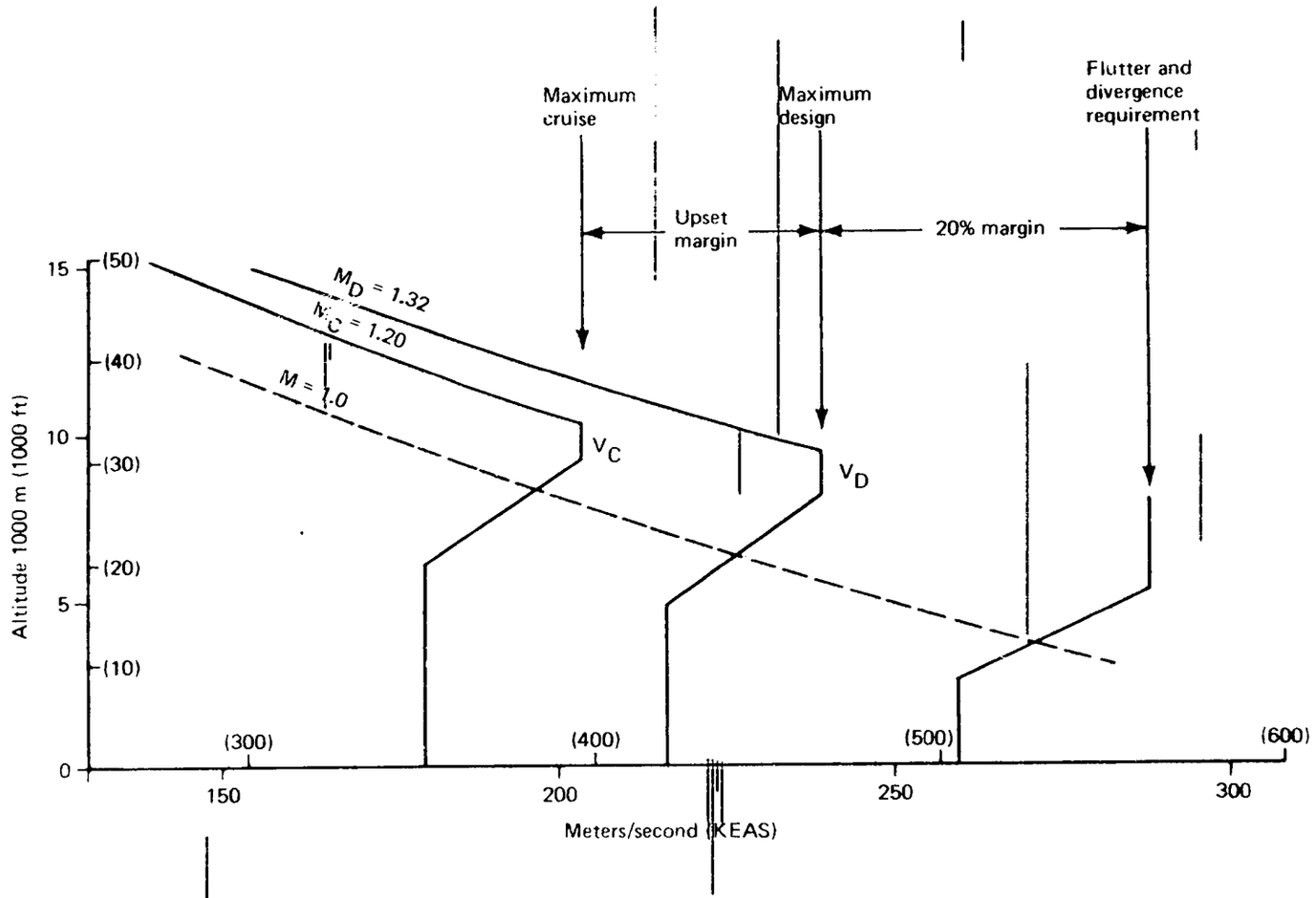

Figure 20 Structural Design Speed Placard

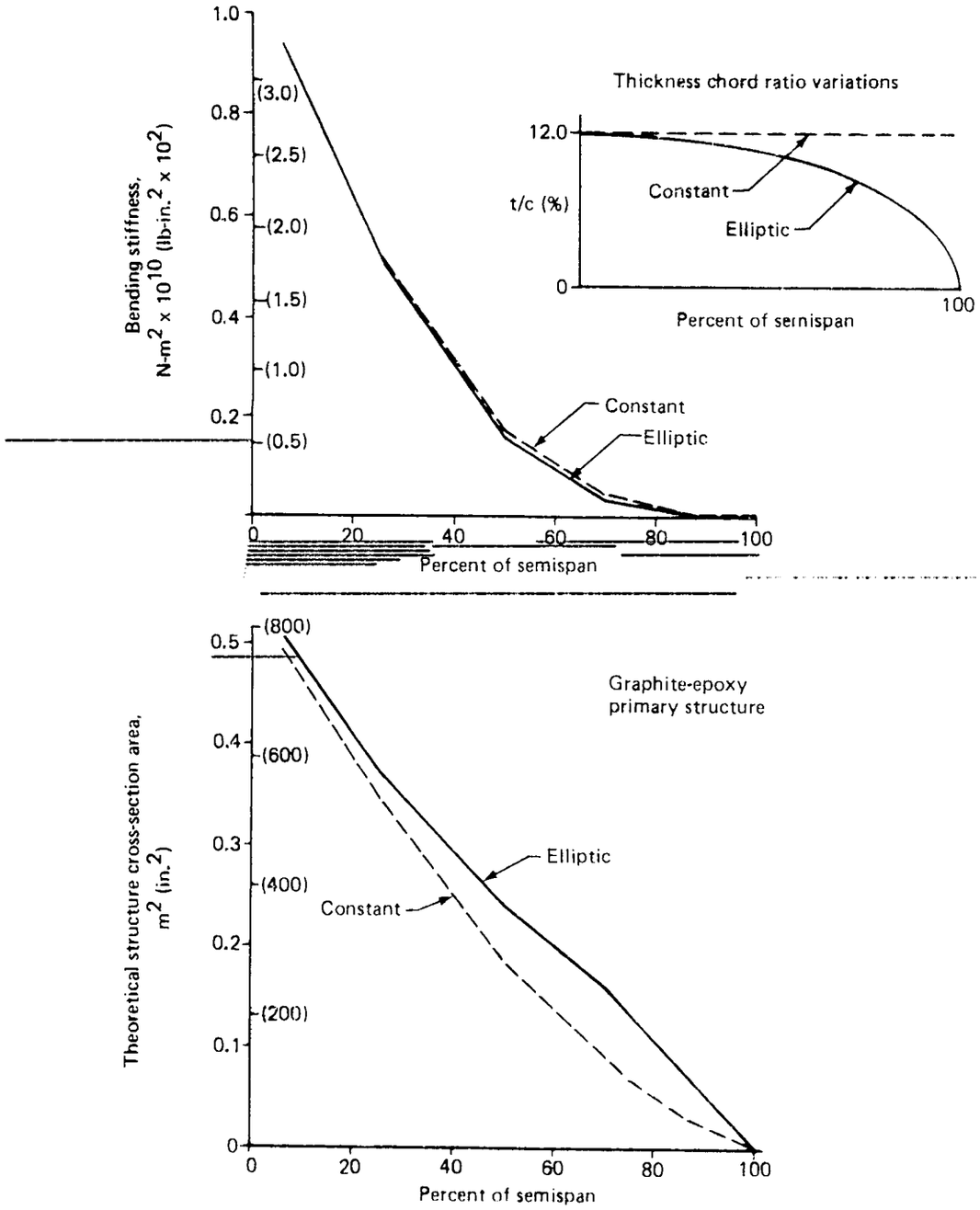

Figure 21 *Effect of Spanwise Thickness Distribution on Stiffness and Structure Material*

two wings is nearly the same even though there is substantially less material in the wing with a constant thickness/chord ratio.

Planforms 4 and 5 were used to evaluate the effect of wing thickness and taper on the theoretical structural weight. The results of this evaluation are shown in Figure 22.

Wings with planform 5a were analyzed with maximum airplane gross weights (GW) of 226 800 kg (500 000 lb), 20 870 kg (460 000 lb), and 190 500 kg (420 000 lb) to determine the variation of theoretical structural material weight with gross weight. At a gross weight of 20 870 kg (400 000 lb), a wing with a planform similar to planform 5a but scaled down to an area of 315.9 m^2 (3400 ft^2) was analyzed to determine the variation in theoretical structural material weight with wing area. These results are presented in Figure 23.

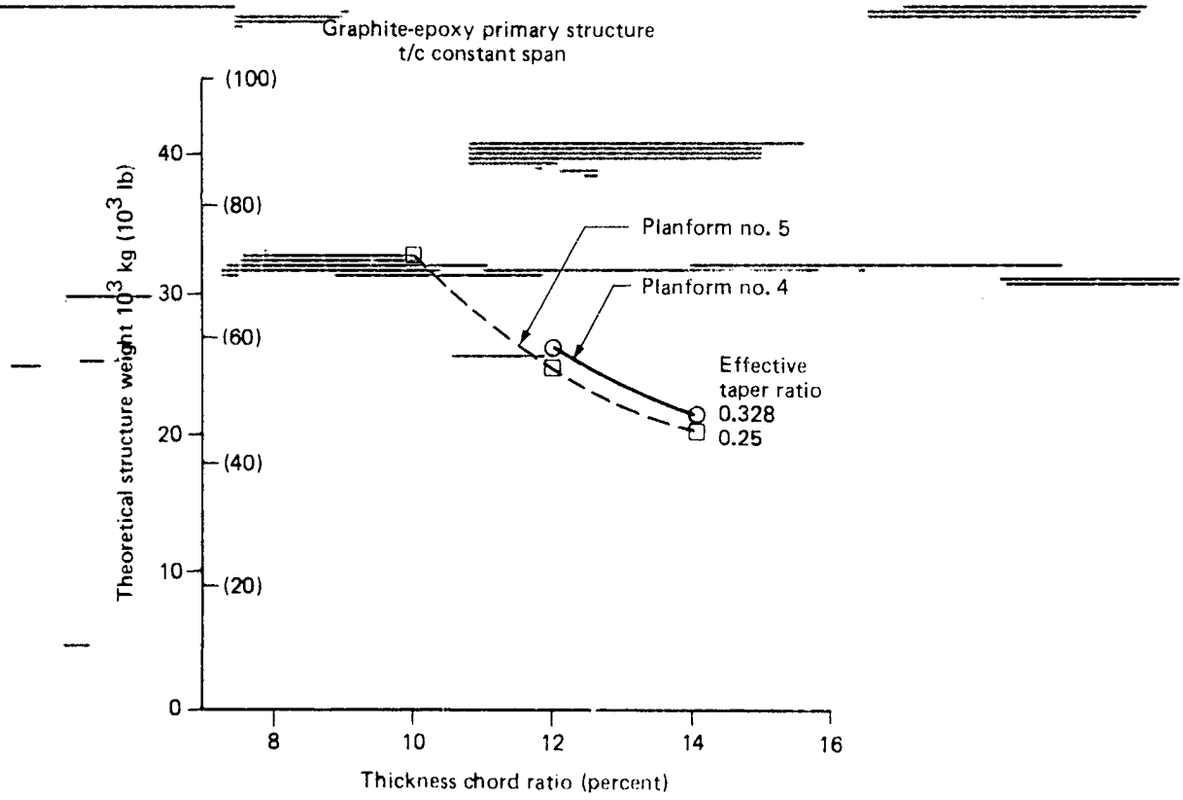

Figure 22 Effect of Wing Thickness and Taper on Structure Weight

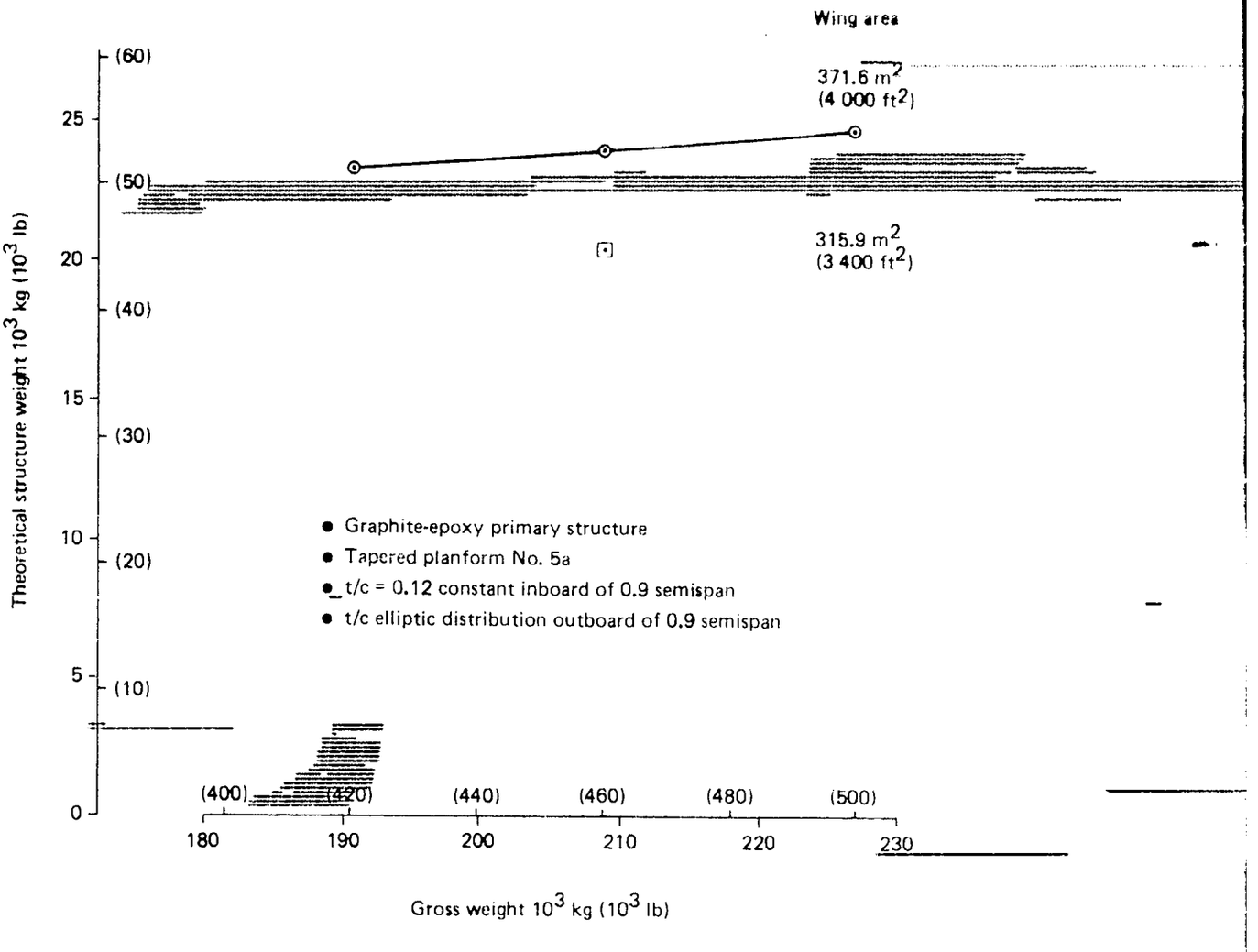

Figure 23 *Effect of Gross Weight and Wing Area on Structure Weight*

4.6 WEIGHTS

Table 3 shows the wing geometric characteristics and weights corresponding to the planforms described in Section 4.2. Detailed structural analysis on the wing box outlined in Section 4.5 provided the theoretical weights from which total wing weights were developed by accounting for the following components:

(a) Nonoptimum wing-box structure such as pad-ups, splices, fasteners, etc.

(b) Wing-box ribs, pivot, and pivot structure

(c) Leading and trailing edges inclusive of both fixed and movable surfaces

The weight of components (b) and (c) remained constant for all the wings analyzed at the same value as that of the Model 5-3 (Reference 1) because the gross weights and wing areas were identical. Weight of component (a) was dependent on the wing-box structural weight and therefore varied with planform changes.

The weight distribution of two of the oblique-wing planforms was compared to that of a 747 wing. Table 4 shows this comparison in terms of unit weights based on total wing area. In spite of the fact that the oblique wings are constructed of graphite-epoxy, they have significantly greater unit weights than the aluminum 747 wing. This is primarily due to the theoretical wing box weight.

The theoretical box weight is dependent on the wing-box thickness distribution, the external loads and the structural material. Figure 24 shows the weight distribution of theoretical structure over the wing semispan. The large weight difference between the 747 and the

Table 4 Wing Weight Breakdown

	Unit weight, kg/m^2 (lb/ft^2)		
	Wing planform		747
	8:1 elliptic	Tapered no.5a	
Theoretical wing box	59.5 (12.2)	68.4 (14.0)	41.5 (8.5)
Nonoptimum (25% for graphite-epoxy)	15.1 (3.1)	17.1 (3.5)	6.3 (1.3)
Bulkhead and pivot	8.8 (1.8)	8.8 (1.8)	
Ribs	3.9 (0.8)	3.9 (0.8)	8.8 (1.8)
Leading and trailing edges	12.2 (2.5)	12.2 (2.5)	21.2 (4.4)
Total wing	99.5 (20.4)	110.4 (22.6)	77.8 (16.0)

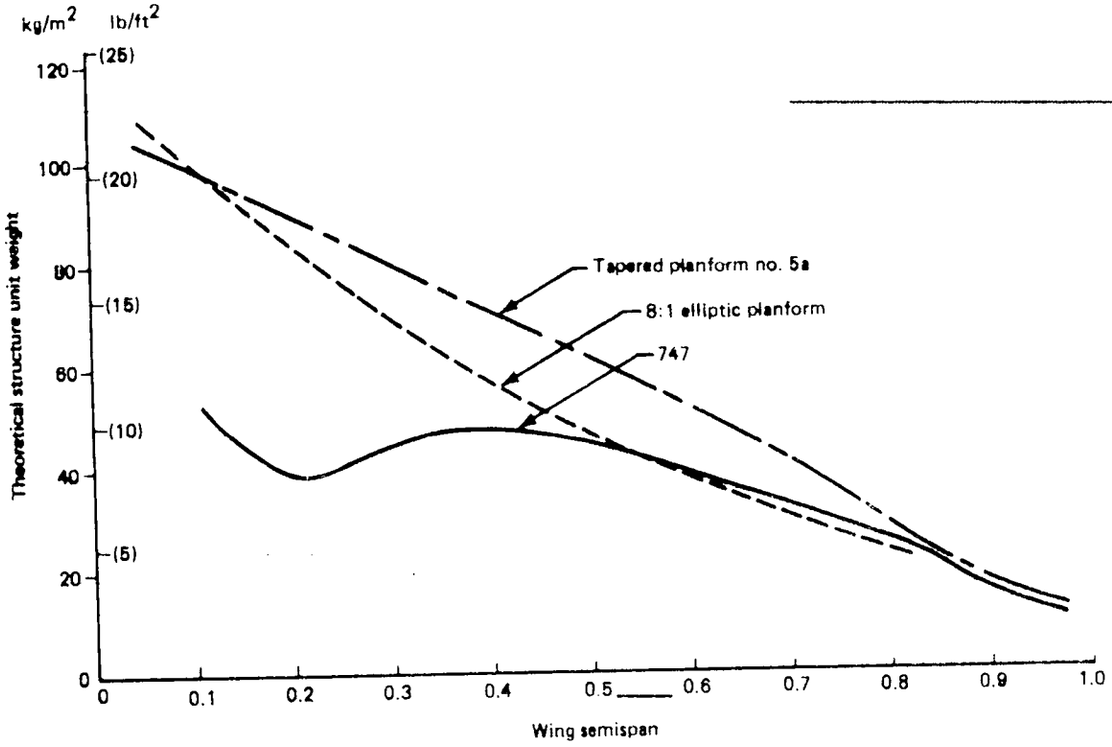

Figure 24 Wing Theoretical Weight Distribution

oblique-wing planforms in the inboard portion of the wing is due to a large increase in the 747 wing thickness as it is faired into the body. The 747 wing thickness increases nearly 170 percent between 50 percent semispan and the side of the body. The corresponding oblique-wing thickness increase is approximately 30 percent for the 8:1 elliptic planform and approximately 50 percent for the tapered planform number 5a.

It is informative to compare theoretical wing weights on the basis of a ratio of wing semispan to average thickness. Such a comparison is shown on Figure 25 for all of the planform study wings. Also shown on this plot are the effects of differences in external loads and structural material between the 747 and the oblique-wing planforms. The 747 external loads are relieved by the wing-mounted engines and by the aeroelastic characteristics of a fixed sweep angle

4.7 PLANFORM AND THICKNESS SELECTION

Weight drag trades derived from Reference 1 showed that, at fixed range, 5560 km (3000 nmi), a 454 kg (1000 lb) increase in empty weight requires TOGW to increase by 1361 kg (3000 lb) and that a unit increase in lift drag ratio permits TOGW to be reduced by 12 973 kg (28 600 lb

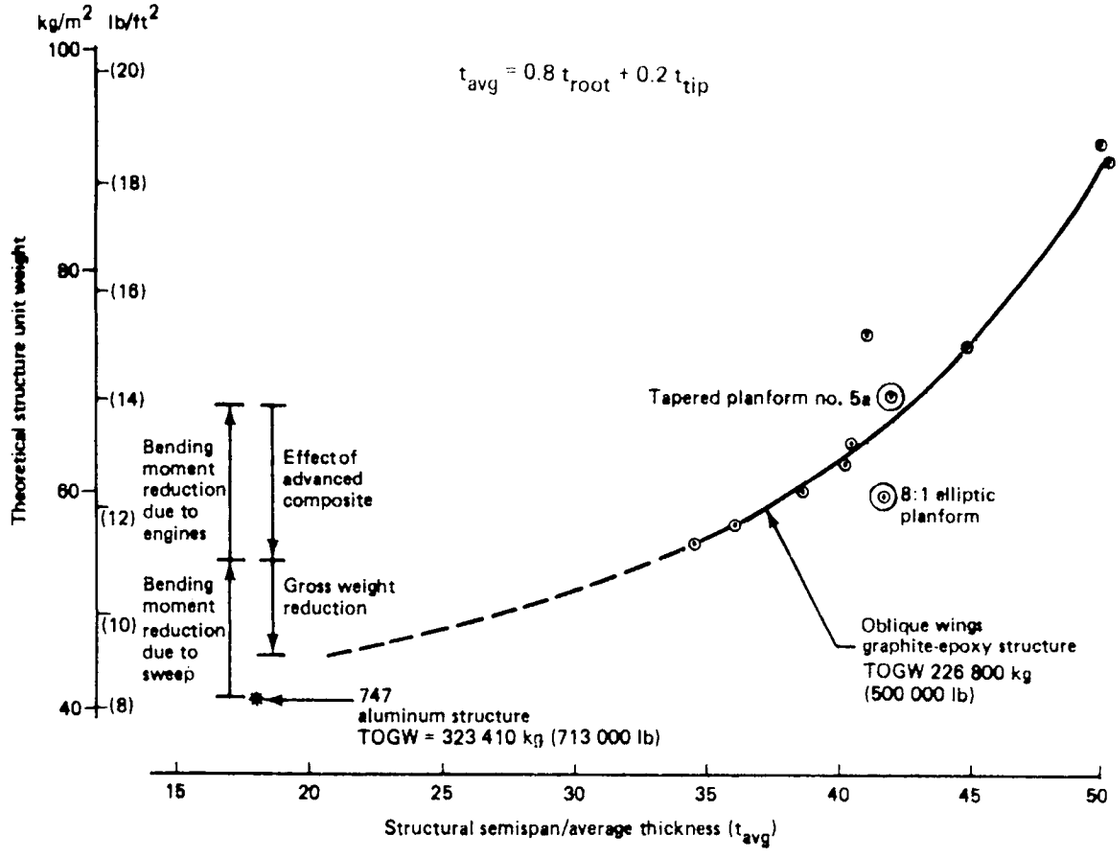

Figure 25 Theoretical Structural Weight Comparison

These factors were used to construct Figures 26 and 27, which show incremental wing weight and lift drag ratio, compared to lines of constant incremental TOGW. Points that lie below the breakeven line (ΔTOGW = 0) represent wings that have better cruise performance than the basepoint 8:1 ellipse.

Figure 26 shows that planform 5, with constant thickness chord ratio, is most efficient, leading to TOGW approximately 13 608 kg (30 000 lb) lower than the basepoint. This wing was selected for use in subsequent studies.

Figure 26 also illustrates the effect of spanwise distribution of thickness chord ratio. In the case of planform 1, changing from elliptic to constant thickness chord ratio reduced wing weight significantly, with only a small loss in lift drag ratio. TOGW would be reduced by approximately 13 608 kg (30 000 lb).

Figure 27 shows the effect of variations in wing thickness chord ratio. In the case of planform 5, increasing thickness from 12 percent to 14 percent could reduce TOGW by an additional

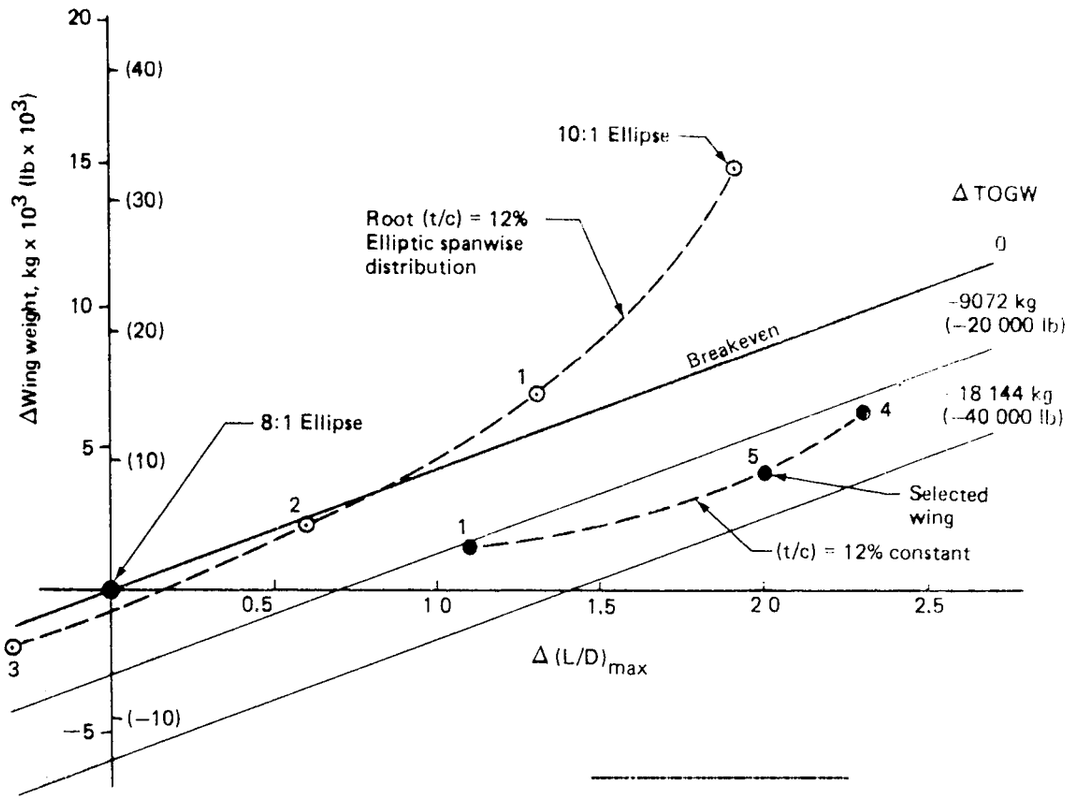

Planform	Aspect ratio	Equivalent taper ratio
8:1 Ellipse	10.2	0.571
10:1 Ellipse	12.73	0.571
1	12.3	0.328
2	11.25	0.436
3	10.2	0.328
4	13.47	0.328
5	13.47	0.25

Figure 26 Effect of Planform and Thickness Distribution on TOGW

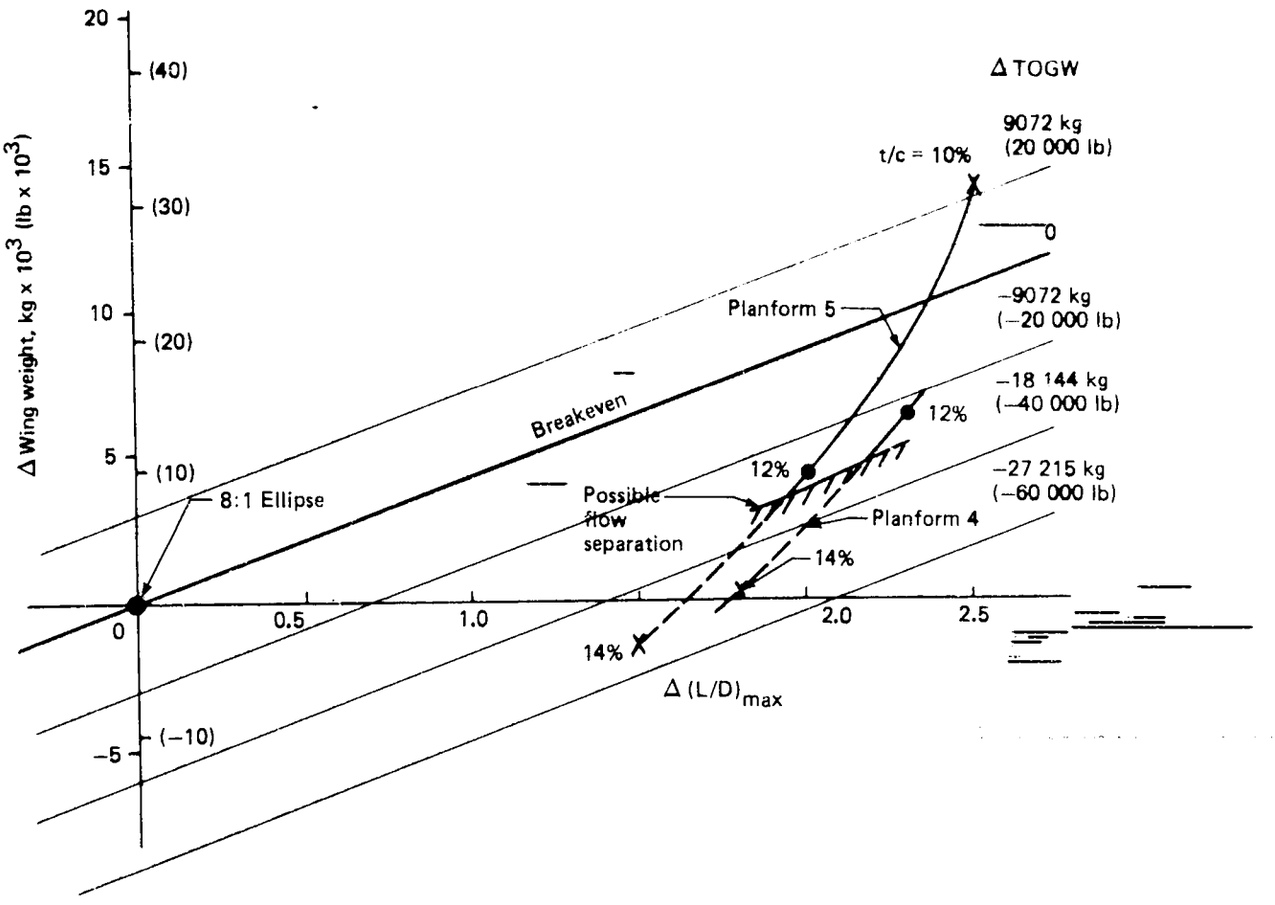

Planform	Aspect ratio	Equivalent taper ratio
4	13.47	0.328
5	13.47	0.25

Figure 27 Effect of Thickness/Chord Ratio on TOGW

11 340 kg (25 000 lb), provided drags based on linearized theory are valid. In practice the maximum allowable thickness will be determined by the onset of flow separation. Reference 3, published after completion of this study, contains data that suggest that 12 percent is close to the maximum, since a significant loss in lift drag ratio was found when thickness was increased from 12 percent to 14 percent. The airfoils used in this test were conventional NACA 4-digit series; it is possible that a well designed supercritical airfoil could permit thickness to increase, with corresponding improvements in performance.

Figure 28 shows a baseline [TOGW 226 796 kg (500 000 lb), uncycled] configuration designated Model 5-6, incorporating the new planform 5a.

4.8 LOW-SPEED AERODYNAMIC CHARACTERISTICS

4.8.1 ESTIMATION METHODS AND PROCEDURES

The low-speed aerodynamic characteristics of the new planform were predicted by methods described in Reference 1, which are based on theoretical results adjusted by flight test and wind tunnel data.

4.8.2 HIGH-LIFT SYSTEM DEFINITION

Wing planform and flap system geometry for Models 5-6 and 5-3 are summarized in Table 5. The leading and trailing edge flap systems used on the Model 5-6 are of the type used on the Model 5-3 (Reference 1). The leading edge device is a variable camber Krueger flap, while the trailing edge flap is a main-aft double-slotted Fowler arrangement. The Fowler motion of the trailing edge flap is constant for all deflection angles.

4.8.3 LOW-SPEED CHARACTERISTICS SUMMARY

Comparisons of the low-speed aerodynamic data for Model 5-6 and Model 5-3 in terms of second segment lift drag ratio (L/D_{V_2}) versus lift coefficient ($C_{L_{V_2}}$) and landing approach lift drag ratio (L/D_{app}) versus lift coefficient ($C_{L_{app}}$) are shown in Figure 29. The improvement in lift drag ratio of the Model 5-6 is due to increased aspect ratio. A detailed discussion of low-speed performance is given in Section 8.4.

4.9 PERFORMANCE

Tables 6 and 7 compare the major characteristics of a sized airplane using the selected planform 5a (designated Model 5-6a) with the Model 5-3a (Reference 1), which has an S-t elliptic planform.

The sizing procedure used was similar to that described in Reference 1 and in Section 6.0 of this report.

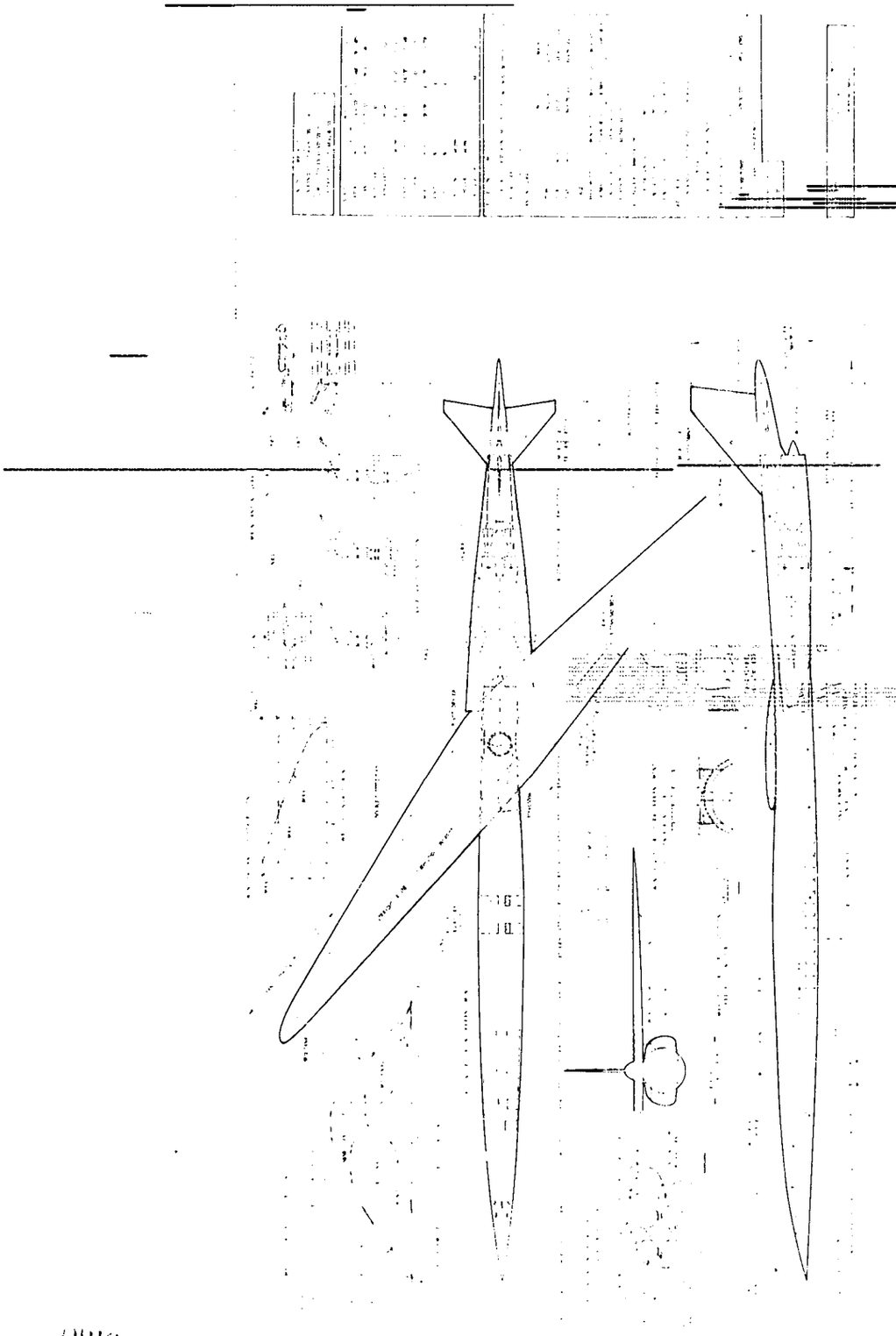

Figure 28 General Arrangement—Model 5-6

Table 5 Wing Planform and Flap System Parameters

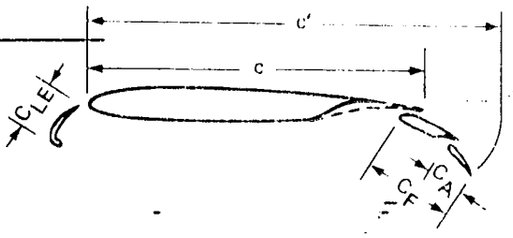

	Configuration	5-3	5 6
Wing	Wing planform shape	8:1 Ellipse	Tapered
	Sweep, $\Lambda c/_4$, rad (deg)	0 (0)	0 (0)
	Aspect ratio, AR (unswept)	10.18	13.47
	Taper ratio, λ_E	0.571	0.250
TE Flaps	Type	Double-slotted Fowler flap	Double-slotted Fowler flap
	Flap chord ratio, $C_F/_C$	0.25	0.25
	Fowler motion ratio, $c'/_c$	1.20	1.20
	Flap span, Y/2b	0.066 to 0.733	0.057 to 0.733
	Aft flap chord ratio, $C_A/_{C_F}$	0.40	0.40
LE Flaps	Type	Variable camber Krueger flap	Variable camber Krueger flap
	Flap chord ratio, $C_{LE}/_C$	0.15	0.15
	Flap span, Y/2b	0.066 to 0.92	0.057 to 0.92
	LE deflection, δ_{LE}, rad (deg)	0.87 (50)	0.87 (50)

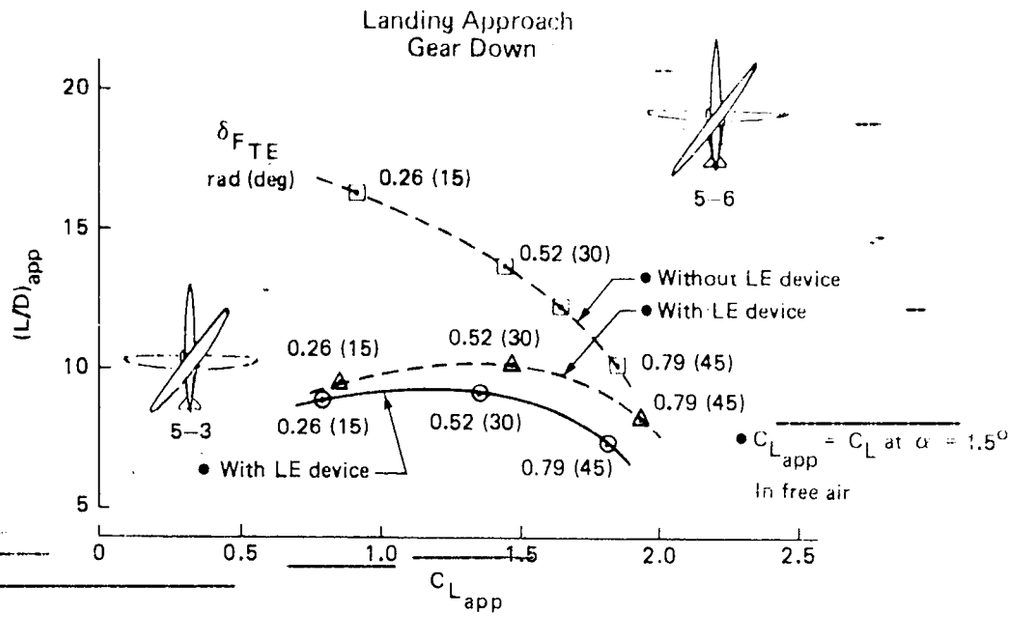

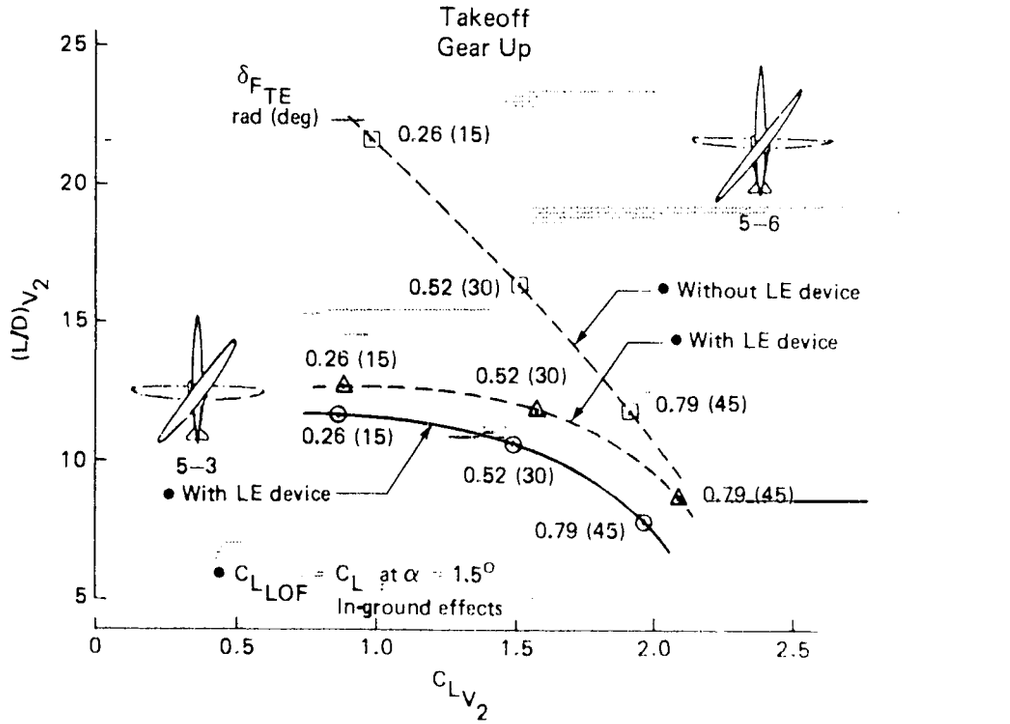

Figure 29 Low-Speed Aerodynamic Data Comparison

Table 6 Comparison of Model 5-3a and Model 5-6a Sized Airplane Characteristics

Item		Original Planform		Revised Planform	
		5-3a 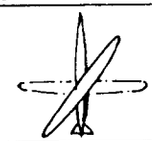		5-6a 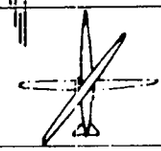	
Weight	Payload (15%/85% mix), kg (lb)	18 144	(40 000)	18 144	(40 000)
	Range, km (nmi)	5 556	(3 000)	5 556	(3 000)
	Design Mach number	1.2			
	TOGW, kg (lb)	211 828	(467 000)	194 550	(428 910)
Fuselage	Body length, m (ft)	87.63	(287.5)	87.63	(287.5)
	Cabin length, m (ft)	43.98	(144.3)	43.98	(144.3)
	Min/max diameter m/m (in./in.)	3.556/4.064	(140/160)	3.556/4.115	(140/162)
	Min/max abreast seating	4/6		4/6	
	Min/max no. of aisles	1/1		1/1	
Wing	Area, m^2 (ft^2)	319.6	(3 440)	282.4	(3 040)
	Aspect ratio	10.2	(Unyawed)	13.47	
	C/4 sweep, rad (deg)	0.96	(55)	0.87	(50)
	Thickness ratio, root/tip, %	12.0/0		12.0/0	
	Taper ratio	8:1 ellipse		0.25	
	Wing C/4 location on body, % body length	56		54.6	
Empennage	Horizontal tail area, m^2 (ft^2)	27.4	(295)	20.0	(215)
	Aspect ratio	2.5		2.6	
	LE sweep, rad (deg)	0.87	(50)	0.87	(50)
	Thickness ratio, root/tip, %	4.0/4.0		4.0/4.0	
	Taper ratio	0.2		0.2	
	Vertical tail area, m^2 (ft^2)	25.5	(275)	23.3	(251)
	Aspect ratio	1.11		1.11	
	LE sweep, rad (deg)	0.87	(50)		
	Thickness ratio, root/tip %	3.5/3.5		3.5/3.5	
	Taper ratio	0.254		0.254	
Propulsion	Type/BPR	ATSA 1.20 1-3000-16/1		ATSA 1.20 2-3000-16/1	
	Number of engines/location	4/aft body		4/aft body	
	Static thrust/engine SL 305k (90 deg f) N (lbf)	156 133	(35 100)	156 577	(35 200)

Table 7 Comparison of Sized Aircraft Performance

- Mach = 1.20
- Payload = 40 000 lb
- Range = 3 000 nmi
- Takeoff field length ≤ 11 500 ft
- Peripheral noise treatment *

		Model 5-3a Original planform	Model 5-6a Revised planform
TOGW	kg (lb)	211 828 (467 000)	197 585 (435 600)
OEW	kg (lb)	113 852 (251 000)	109 724 (241 900)
S	m^2 (sq ft)	3 440	2 900
SLST	kg (lb)	15 921 (35 100)	13 154 (29 000)
Block fuel	kg (lb)	64 864 (143 000)	55 701 (122 800)
Reserves	kg (lb)	15 876 (35 000)	14 832 (32 700)
No. of engines/BPR		4/1	4/1
Thrust loading (T/W)		0.30	0.27
Wing loading (W/S)	N/m^2 (lb/sq ft)	6 512 (136)	7 182 (150)
ICAC	m^2 (ft)	11 887 (39 000)	11 887 (39 000)
RF	km (nmi)	15 872 (8 570)	17 705 (9 560)
Cruise altitude	m (ft)	12 497 (41 000)	12 497 (41 000)
L/D (cruise)		12.3	13.8
L/D (max)			14.2
C_L at L/D max		0.29	0.43
C_L at (cruise)		0.30	0.34
TOFL: Max flaps, ft		7 150	9 290
Reduced flaps, ft		9 670	11 500
C_L (max flaps)		With LE 1 95	Without LE 1.90
C_L (reduced flaps)		With LE 1.46	Without LE 1.55
L/D community noise reduced flaps (V_{app} + 5.14 m/s (10 KTS))		8.3	9.25
Approach speed: Max flaps KEAS		124.4	127.9
With LE C_L (max flaps) at 1.3VS		With LE 1.80	With LE 1.95
Reduced flaps KEAS		137.4	141.2
With LE C_L (reduced flaps)		With LE 1.48	With LE 1.60
Community noise: EPNdB *			
From FAR 36			
Takeoff with thrust cutback at noise station		−0.4	−3.8
Sideline 648 m (0.35 nmi)		+2.0	+1.5
Approach		−2.0	−2.7
Traded		0	−0.5

* 1976 research technology qualified for 1985 design freeze

The higher aspect ratio wing of the Model 5-6a produces major performance improvements, namely:

- TOGW reduced by 14 061 kg (31 000 lb)
- Block fuel reduced by 9072 kg (20 000 lb)
- Takeoff field length (TOFL) reduced by 640 m (2100 ft)

Data presented for the Model 5-6a are approximate because it represented an intermediate step toward the development of the final configuration, and only a single sizing cycle was conducted. Weight and drag estimates were not refined and questions of airplane balance and control surface sizing were not addressed.

5.0 PIVOT DESIGN

5.1 SUMMARY

The objective of this study was to design and weigh a practical pivot, and develop weight-scaling rules to be used in future design synthesis.

A number of pivot-bearing concepts were reviewed and the most promising, the teflon-coated turntable bearing (Figure 30), was selected for more detailed design, structural, and weight analysis. The advantages and disadvantages of this design are summarized below.

Advantages	Disadvantages
Fail-safe	Inspection difficult
Light weight	
No large holes in wing or body	
Minimum wing/body gap	
Good producibility features	
Adjustable	
Self-lubricating	

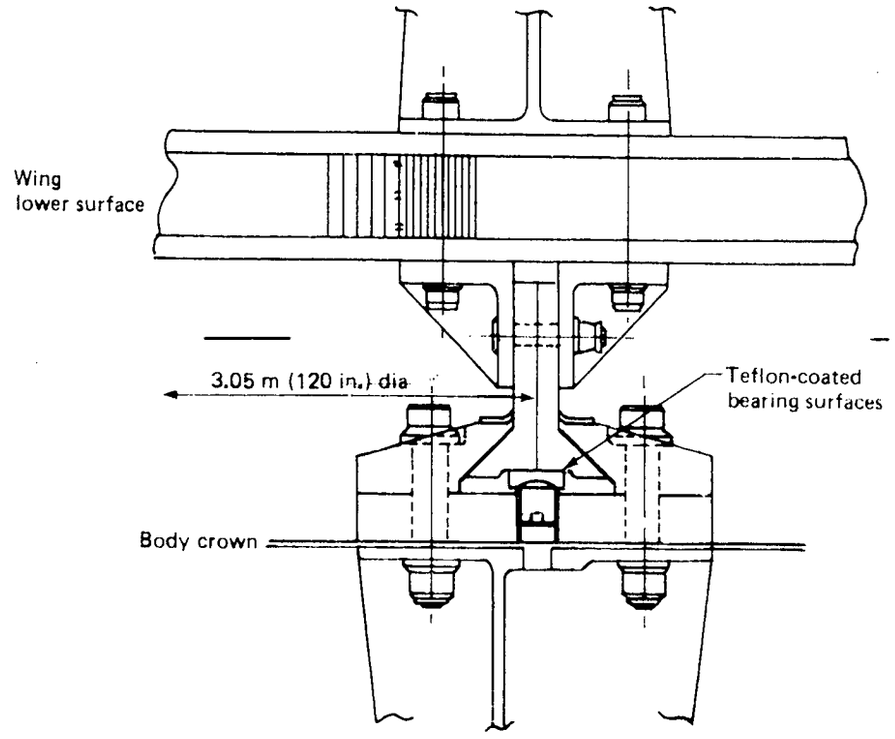

Figure 30 Teflon-Coated Turntable Bearing

Pivot weights based on this analysis are shown in Figure 31. The weight resulting from the design is 42 percent lower than earlier estimates used in Model 5-3 development. Reference

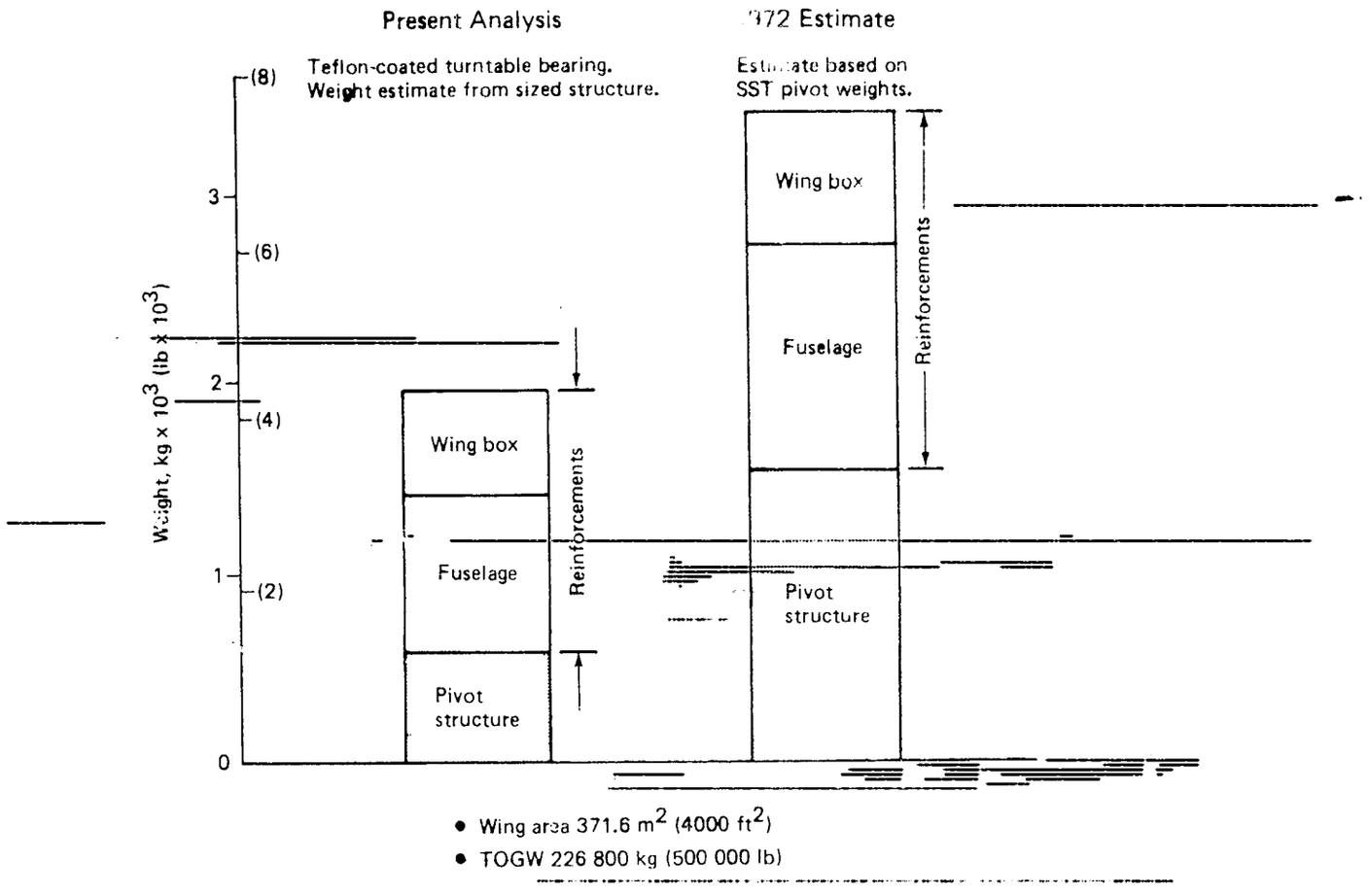

Figure 31 Pivot Weights

5.2 STUDY DESCRIPTION

The airplane configuration used for this study was the Model 5-6. (Figure 28) that utilizes the wing planform developed during the study described in Section 4.0. This uncycled baseline configuration has TOGW = 226 796 kg (500 000 lb) and wing area of 371.6 m^2 (4000 ft^2).

Design objectives were established and 10 pivot concepts were evaluated relative to these objectives. Three turntable-type designs were subjected to more detailed examination and one, the teflon-coated turntable bearing, was selected as the final design.

The loads carried by the pivot were estimated, wing and body load paths were identified, and sized structural layouts were prepared. The weight of the pivot and supporting structure was estimated and weight-scaling rules were developed. Potential problem areas were identified and recommendations for future research were prepared.

5.3 CONCEPT SELECTION

The following objectives were established for the pivot design:

- Wing rotation 0 – 0.96 rads (0 – 55°)
- Fail-safe structure
- Wing actuation, dual system
- Systems access through pivot
- Minimum wing/body gap

The 10 design concepts shown in Figure 32 were evaluated, and the results are summarized in Table 8.

Three turntable-type bearings, shown in Figures 33, 34, and 35, satisfied the design objectives. These large diameter, shallow bearings that rely on the support of the wing and body for strength and stiffness, minimize the wing-body gap and permit the wing panels and body structure to remain intact.

The teflon-coated turntable bearing (Figures 30 and 35) was considered most satisfactory and was selected as the final design. This bearing is constructed from concentric rings that are split vertically to provide dual load paths. The annulus construction also permits electrical, hydraulic, and fuel lines to pass through the center of the bearing. Wing sweep position is controlled by twin screw jacks located within the pivot annulus (Figure 35, details BB and CC). This design has the following desirable features:

- Fail-safe. Limit load can be carried by either inner or outer rings alone.
- High load capacity. The bearing relies on surface contact rather than line contact, as is the case with roller bearings, allowing a higher load capacity for a given weight.
- No false brinelling.
- No lubrication required. The teflon (PTFE) coating on the bearing surfaces is self-lubricating.
- Adjustable. The bearing is adjustable for fit and wear.

Bearing	Description
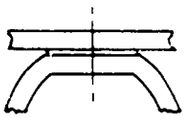	Slew ring bearing "Rotek series 10 000" Outer race attached to wing Inner race attached to body
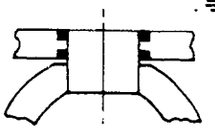	Body-mounted shaft Thrust and radial bearings
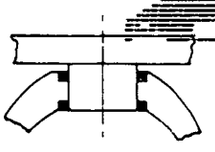	Wing-mounted shaft Thrust and radial bearings
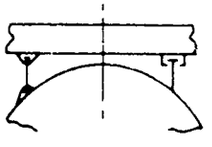	Link and carriage
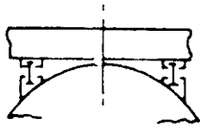	Double rail and carriage

Bearing	Description
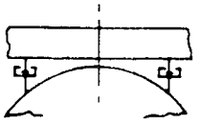	Circular track and multiple carriages (8)
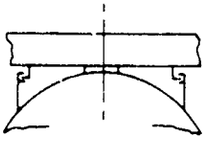	Center pivot and end journal 1
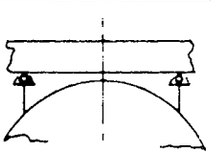	Hydraulic lock bearing
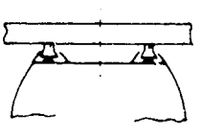	Turntable bearing Teflon-coated surfaces Fail-safe features 1
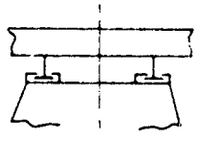	Turntable bearing Wire race type Fail-safe features 1

1 Selected for study

Figure 32 Pivot Design Concepts

Table 8 Bearing Concept Type Selection

Bearing number	Type	Eliminated	Selected
1	'Rotek' series 10 000 commercial	Poor load path in bearing	
2	Cantilevered post in body	Poor load path in wing	
3	Cantilevered post in wing	Poor load path in body	
4	Link and carriage	Concentrated loads Fail-safety difficult	
5	Double rail and carriage	Large wing/body gap multiple parts	
6	Circular track and multiple carriages (8)	Large wing/body gap multiple parts	
7	Center pivot and end journal		Compatible with joint criteria
8	Hydraulic lock bearing	Requires long-term development	
9	Turntable bearing Teflon-coated surfaces		Compatible with joint criteria
10	Turntable bearing Wire race type		Compatible with joint criteria

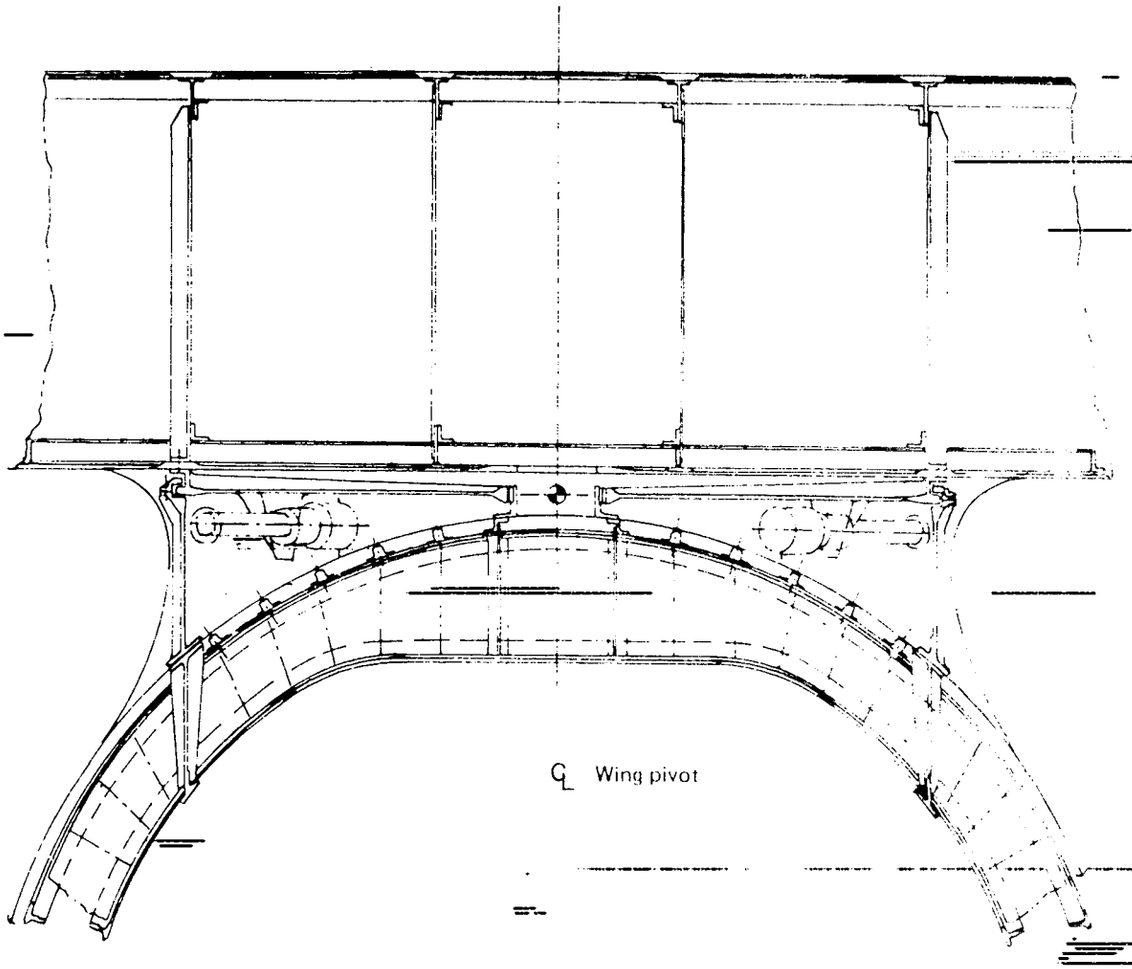

Figure 33 Center Pivot and End Journal Bearing (No. 7)

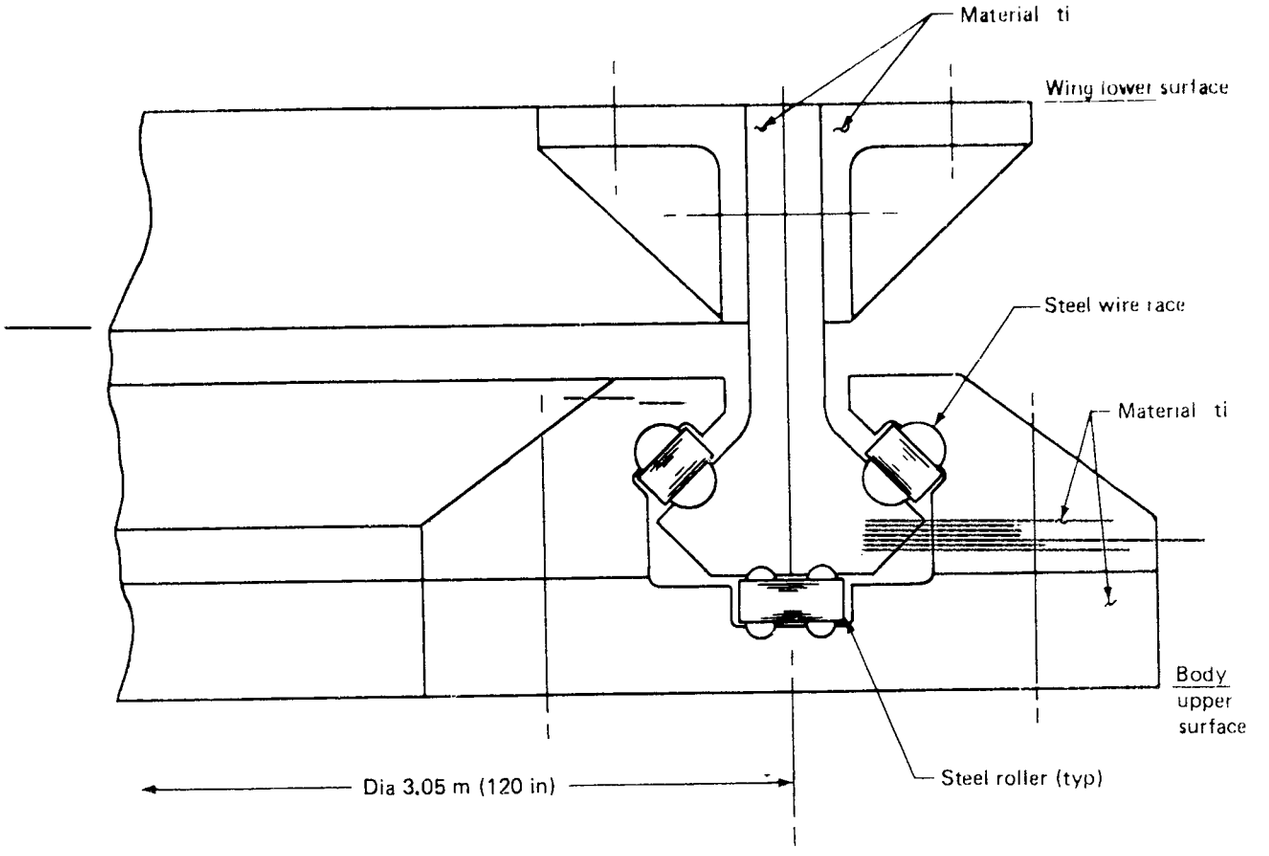

Figure 34 Wire Race Type Bearing (No. 10)

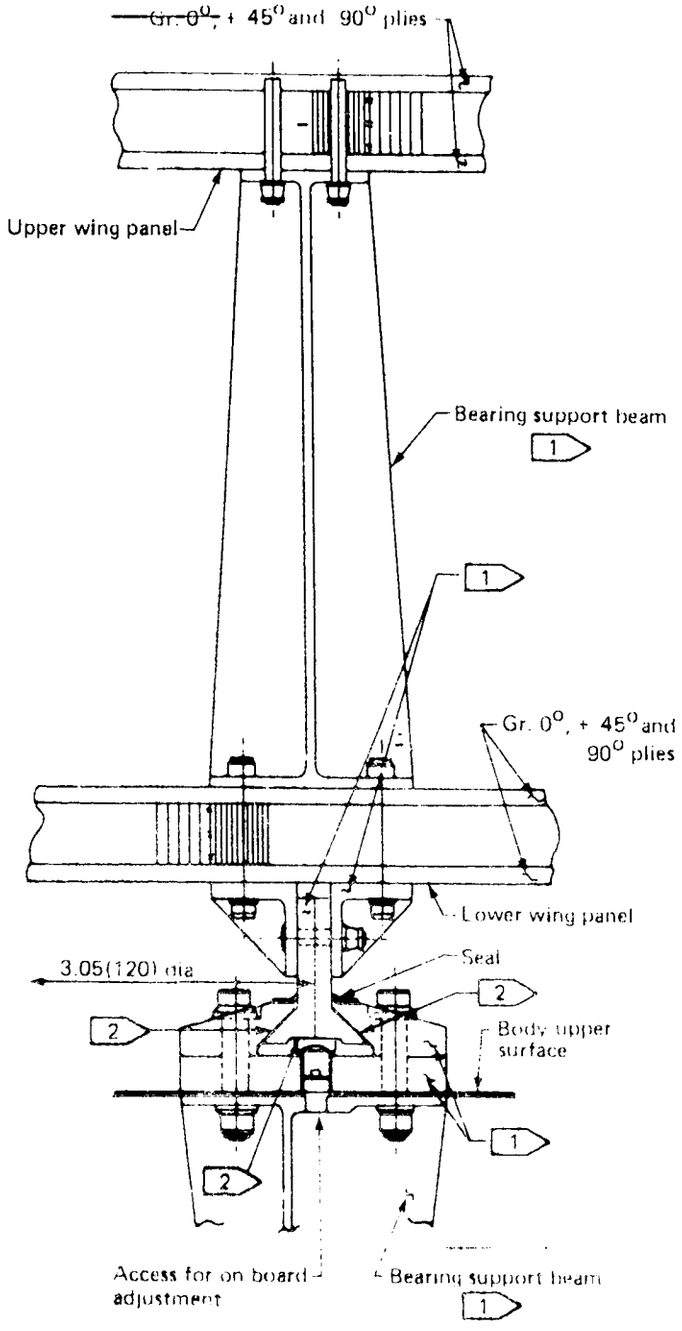

Detail I

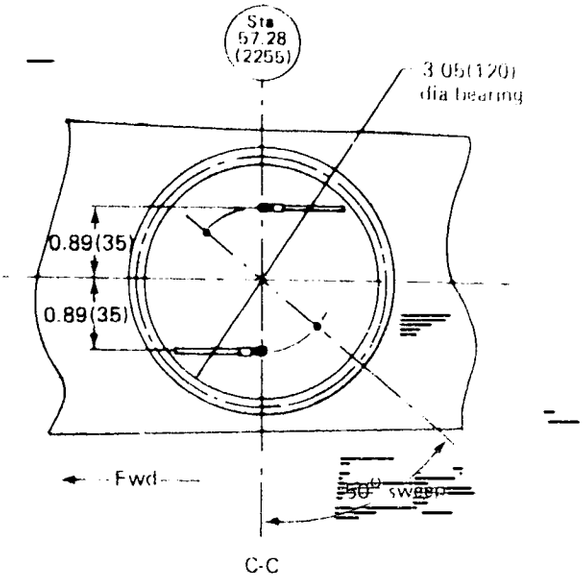

C-C

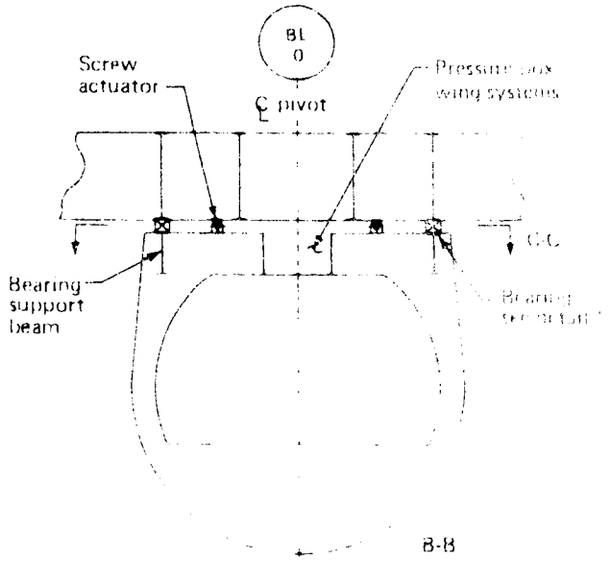

B-B

FOLDOUT FRAME

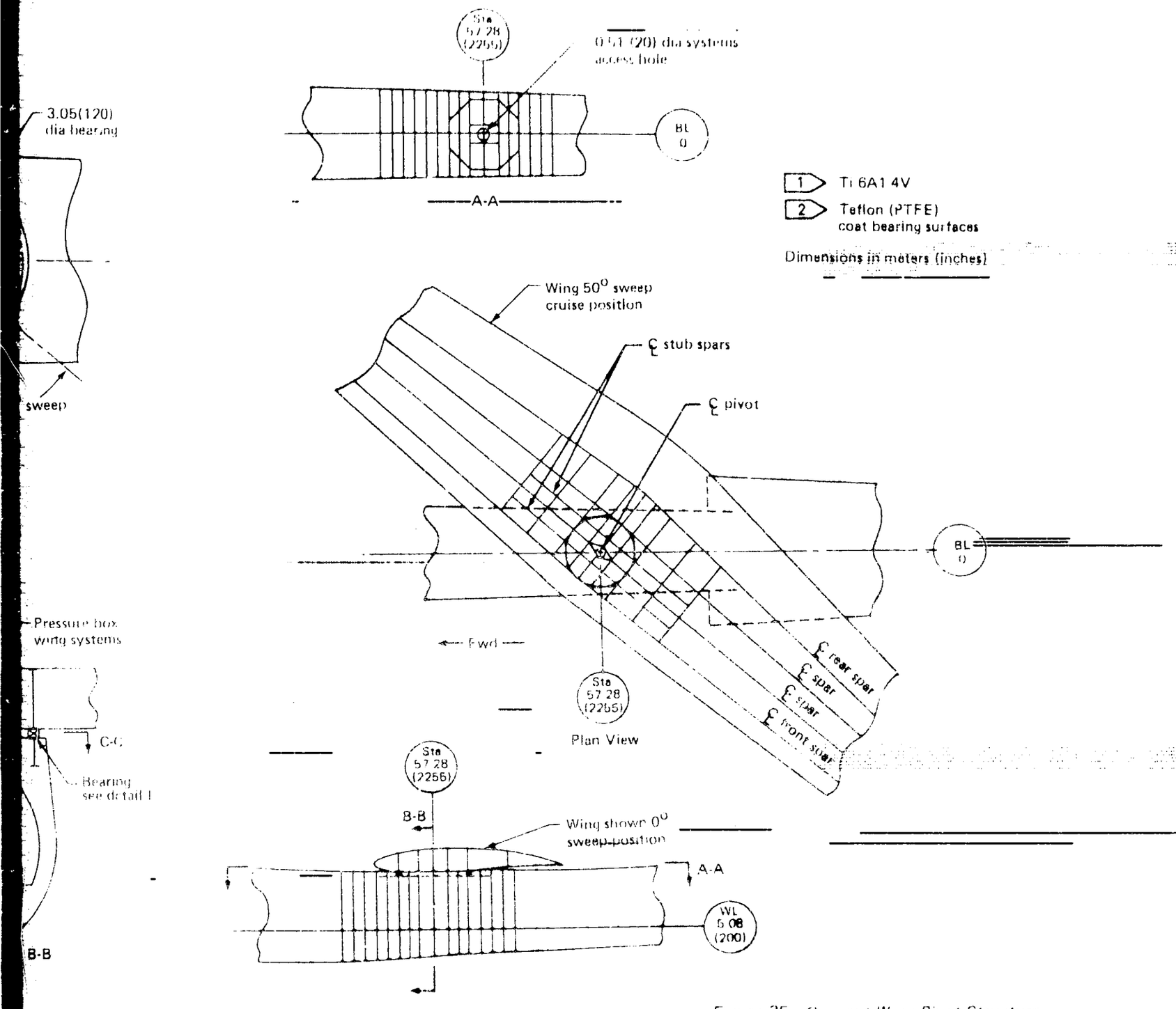

Figure 35 Concept Wing Pivot Structure (Model 5.6)

5.4 PIVOT LOCATION

The following factors were considered when selecting the location of the pivot relative to the wing and body.

The pivot was located as far forward on the wing root chord as possible, consistent with structural constraints (Figure 35). This places the pivot near the wing aerodynamic center, reducing the pitching moment carried through the pivot, and permits the forward member of the bearing support grid to be located at the front spar. The bearing diameter is 3.05 m (120 in.), thus placing the pivot center at 30 percent wing root chord. Forward location of the pivot also reduces the aerodynamic pitch roll coupling. The pivot was located on the body at station 57.28 m (2255 in.), which maintains the same wing body relationship as the Model 5 6 at zero sweep.

5.5 DESIGN LOADS

Eight load cases were considered for the analysis and preliminary sizing of the pivot and supporting structure. A description of the load cases and the associated loads is given in Table 9.

5.6 STRUCTURAL LOAD PATHS

The pivot, wing support structure, and body support structure for the oblique wing should transfer all loads from the wing into the fuselage efficiently, and permit large relative motions between the wing and body. To do so, the structures must provide good load paths for all loading conditions without having excessively hard spots that could potentially lead to racking problems.

The ability of the wing to distribute the incoming loads around the pivot, and the ability of the fuselage pivot support structure to redistribute the loads from the pivot into the body frames were considerations in meeting the above criteria. Figure 35 shows the selected structural arrangement that consists of an octagonal grid utilizing spar and rib structure. The pivot structure itself provides the load transfer between the wing and body structures. This link was made as direct as possible to avoid eccentricities in the load transfer between wing and fuselage.

5.7 STRUCTURAL SIZING

The pivot and pivot support structure is titanium (6Al-4V) except for the wing skins, which are composite. The bearing surfaces of the pivot are coated with PTFE (teflon). Static strength, stiffness, relative stiffness, and fail-safety were the primary considerations in the sizing of the various structures.

The requirement of a movable wing imposes relative deflection limitations across the bearing. It was assumed that racking of the bearing would be avoided at relative displacement of 1.27 cm (0.5 in.) across the bearing diameter.

Table 9 Design Load Cases

						Operational loads limit			Design loads ultimate					
Condition	λ rad (deg)	Altitude m (ft)	V_E m/sec (KEAS)	GW 10^3 kg (10^3 lbm)	n	Fz 10^3 N (10^3 lbf)	Mx 10^6 Nm (10^6 in. lbf)	My 10^6 Nm (10^6 in. lbf)	Fx 10^3 N (10^3 lbf)	Fy 10^3 N (10^3 lbf)	Fz 10^3 N (10^3 lbf)	Mx 10^6 Nm (10^6 in. lbf)	My 10^6 Nm (10^6 in. lbf)	Mz 10^6 Nm (10^6 in. lbf)
Level flight	0	0	180 (350)	227 (500)	1.2	1317 (296)	±0.113 (±1.0)	2.147 (19)						
Level flight	0.79 (45)*	0	180 (350)	227 (500)	1.2	1317 (296)	±0.113 (±1.0)	1.582 (14)						
Gust	0	6 096 (20 000)	180 (350)	150 (330)	3.9				0	0	7215 (1622)	±0.678 (±6)	5.65 (50)	0
Gust	0.79 (45)*	6 096 (20 000)	180 (350)	150 (330)	3.9				0	0	7215 (1622)	±0.678 (±6)	3.95 (35)	0
One-gear land	0	0		181 (400)	1.5				0	0	752 (169)	±3.16 (±28)	0	0
Ground turn	0	0		227 (500)	1.0				0	±974 (±219)	−1944 (−437)	0	0	0
Braked roll	0	0		227 (500)	1.0				−1557 (−350)	0	−1944 (−437)	0	0	0
Fin gust	0.79 (45)*	6 096 (20 000)	180 (350)	227 (500)	1.0				0	±133 (±30)	1495 (336)	±0.79 (±7)	±0.565 (±5)	±0.452 (±4)

* Right wing forward

Pivot, plan view

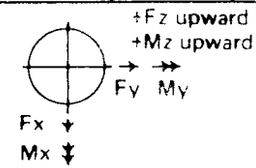

As mentioned in Section 5.6, the ability of the wing to distribute loads around the pivot and the ability of the fuselage pivot support structure to redistribute the loads from the pivot into the body frames is important to the nature of the load transfer within the wing, pivot, and fuselage system. This relative stiffness problem was handled in both the wing and fuselage structure by making load paths to and from the pivot as direct as possible and by preventing any load points around the perimeter of the pivot from being excessively hard or soft in a relative sense.

The fail-safe criteria applied was that the airplane must be able to survive limit load after the failure of a principal structural member. Thus, for example, the skin-spar chord distribution of material must be such that if a wing panel fails, the structure with the failed panel can still survive limit load. Similar arguments were applied to elements of the pivot structure.

The scope of the effort did not permit a highly detailed (computer-aided) stress analysis or a recycling of loads through the structures. Hence, the structural sizes shown in Figures 36, 37, and 38 must be considered as preliminary only.

5.8 DETAILED WEIGHT ANALYSIS

Weight analysis of the pivot structure was based on the structural details discussed in Section 5.7. The weight impact of a pivoting wing on the total airplane can be divided into three components:

- Reinforcements to the wing-box structure resulting from load redistribution requirements to transfer design loads to the pivot and fuselage (W_1)
- Weight of the pivot structure itself (W_2)
- Reinforcements to the fuselage structure in the region of the wing body interface to sustain pivot-imposed loads and limit deflection and or twisting across the pivot structure (W_3)

The magnitude of the above weight increments based on a gross weight of 226 796 kg (500 000 lb) and a wing area of 371.6 m^2 (4000 ft^2) provides a comparison with penalties previously estimated for Model 5-3, and is shown below. These penalties are 42 percent lower than earlier estimates used in Model 5-3 development.

Item	Weights based on sized structure		Previously estimated weights for Model 5-3	
	kg	(lb)	kg	(lb)
Wing box structural reinforcements	580	(1279)	888	(1516)
Pivot structure	551	(1214)	1542	(3400)
Fuselage structure	863	(1903)	1203	(2652)
Total (per airplane)	1994	(4396)	3433	(7568)

• TOGW 226 796 kg (500 000 lb) • Wing Area 371.6 m^2 (4000 ft^2)

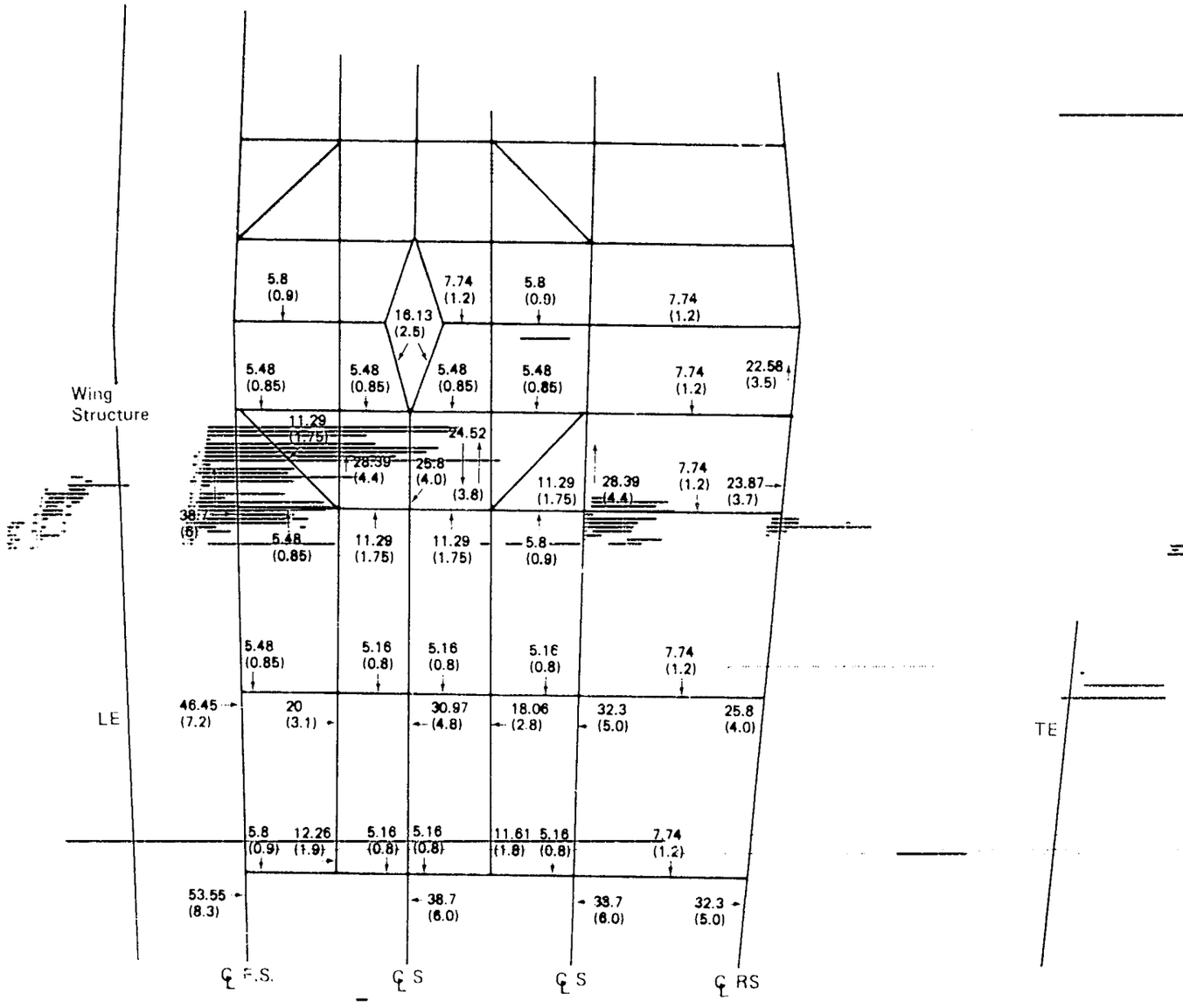

Note. The numbers are sized spar cap areas in cm^2 ($in.^2$)

Figure 36 Wing Structure Cap Areas

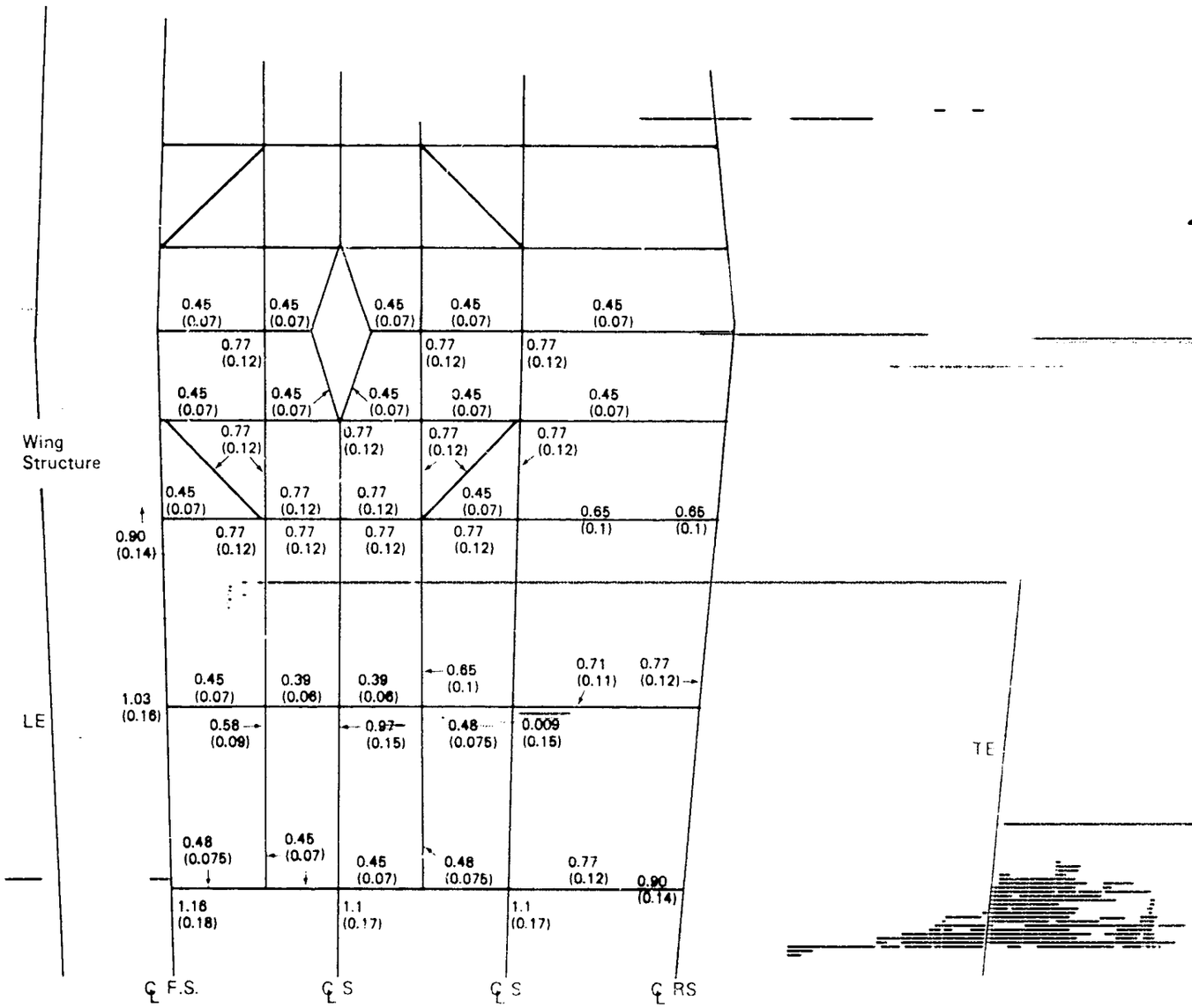

Gussets on octagon ring are 0.059 cm (0.15 in.) at 10.16 cm (4 in.) spacing

Note: The numbers are sized spar web gages in cm (in.)

Figure 37 Wing Structure Web Gages

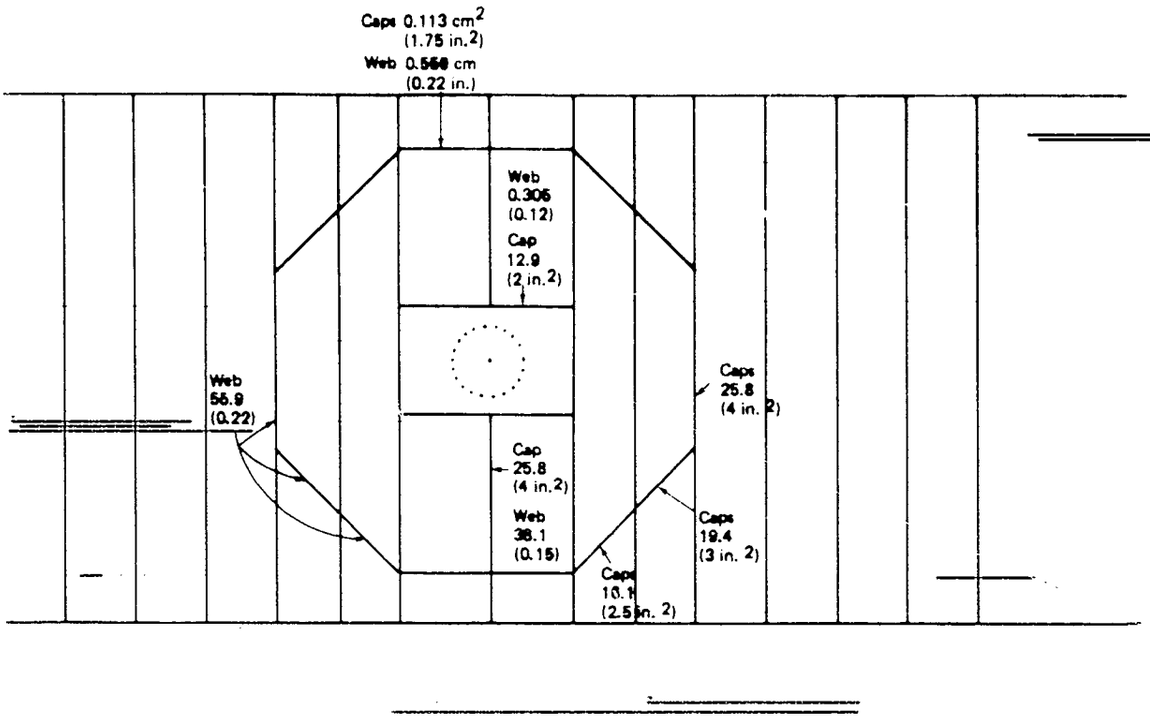

Gussets on octagon ring are 0.059 (0.15 in.) at 10.16 cm (4 in.) spacing

Ring gages in cm (in.)
Cap areas in cm2 (in.2)

Figure 38 Body Ring Gages and Cap Areas

5.9 PARAMETRIC WEIGHT-SCALING DEVELOPMENT

As indicated in Section 5.8, the pivot weight penalty consisted of three components, each of which is a function of a unique design parameter(s). Weight-scaling rules were developed at two levels of detail, in terms of pivot parameters and in terms of airplane parameters. The airplane-parameter relationships permit evaluations of pivot-related weights during scaling over regimes normally associated with performance sizing. The pivot-parameter scalars allow evaluation of pivot weights over a wider regime of size and loading. This allows study of the oblique-wing concept to be applied to other missions and configurations.

5.9.1 PIVOT-LOAD SCALARS

The weight of the reinforcing wing-box structure (Figure 39) is dependent on the vertical force carried by the pivot and can be expressed as:

$$W_1 = K_1 V$$

The constant K_1 has the following values:

$$K_1 = 80.41 \times 10^{-6} \text{ kg/N } (788.53 \times 10^{-6} \text{ lb/lb})$$

The weight of the pivot structure (Figure 40) is a function of the vertical load and moment carried by the pivot, given by:

$$W_2 = K_2 V + \frac{K_3 M}{D}$$

The constants K_2 and K_3 have the following values:

$$K_2 = 24.982 \times 10^{-6} \text{ kg/N } (244.99 \times 10^{-6} \text{ lb/lb})$$

$$K_3 = 199.9 \times 10^{-6} \text{ kg/N } (1960 \times 10^{-6} \text{ lb/lb})$$

The weight of reinforcements to the fuselage structure is proportional to the vertical force carried by the pivot (Figure 41).

$$W_3 = K_3 (V)$$

The constant K_4 has the following values:

$$K_4 = 119.64 \times 10^{-6} \text{ kg/N } (1173.24 \times 10^{-6} \text{ lb/lb})$$

These relationships are valid only under the following conditions:

- Pivot diameter is not less than 80 percent of fuselage width.
- Wing construction is 4-spar with composite skins and titanium pivot support structure.
- The ratio of pivot diameter to wing chord is approximately 35 percent, and the pivot covers approximately 60-65 percent of the main structural box, so that the current wing spar, rib, and pivot structural arrangement may be used.

5.9.2 AIRPLANE PARAMETER SCALARS

Pivot weight penalties W_1 and W_2 are included in the wing and W_3 in the body. The penalties comprise a very small portion of their respective functional item weights and therefore do not significantly impact scaling behavior of the wing and body when scaled over parametric limits associated with normal performance sizing.

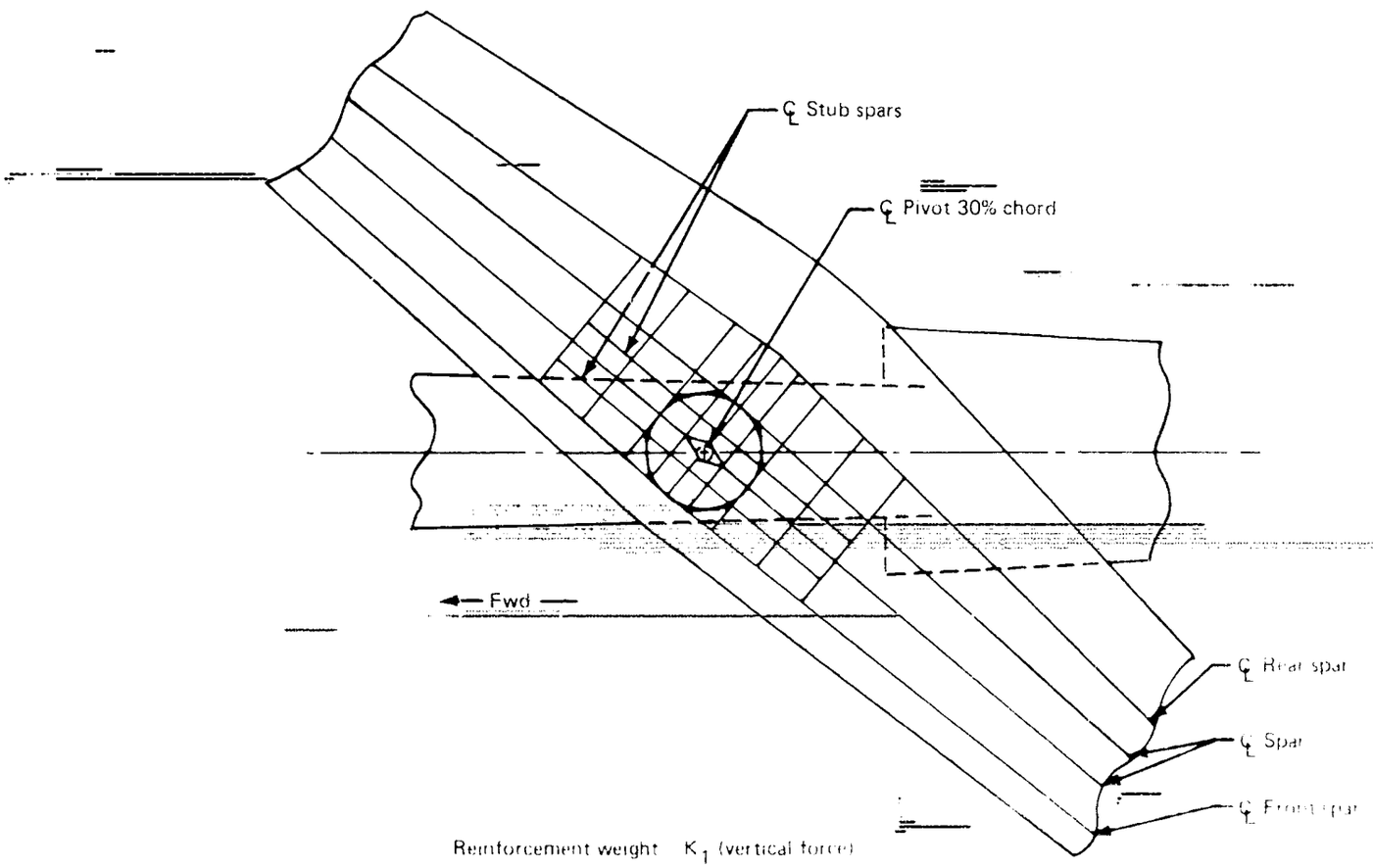

Reinforcement weight K_1 (vertical force)

K_1 80.41×10^{-6} kg/N (788.53×10^{-6} lb/lb)

Figure 39 Wing Reinforcements

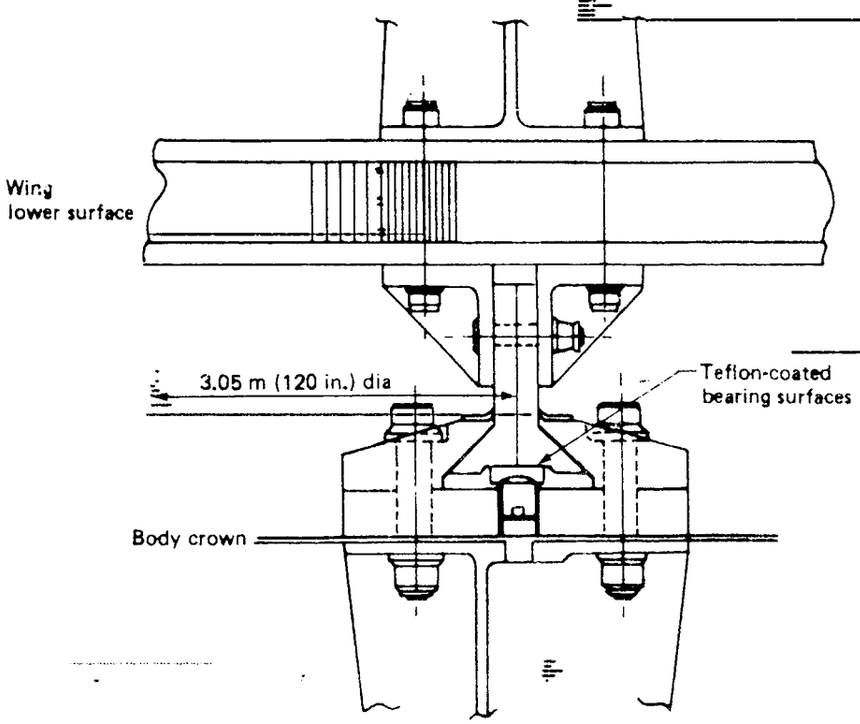

$$\text{Bearing weight} = K_2\,(\text{vertical force}) + K_3\left(\frac{\text{pitching moment}}{\text{pivot diameter}}\right)$$

$K_2 = 24.982 \times 10^{-6}$ kg/N $(244.99 \times 10^{-6}$ lb/lb$)$

$K_3 = 199.9 \times 10^{-6}$ kg/N $(1960 \times 10^{-6}$ lb/lb$)$

Figure 40 Bearing Detail

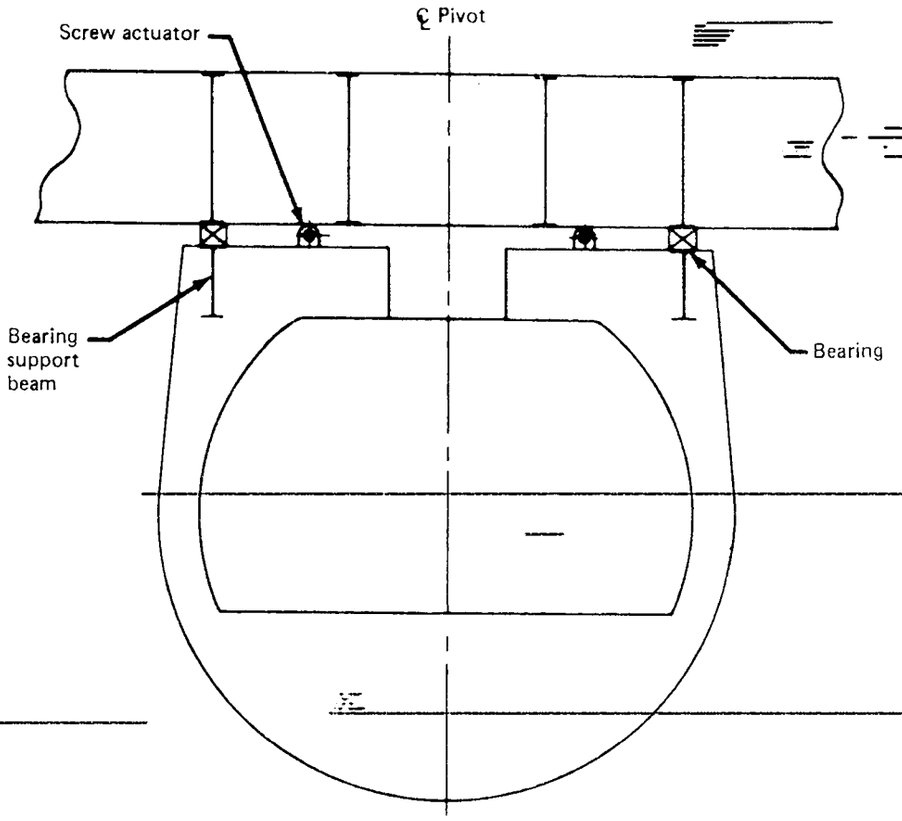

Reinforcement weight = K_4 (vertical force)

K_4 = 119.64 x 10^{-6} $kg/_N$ (1173.24 x 10^{-6} $lb/_{lb}$)

Figure 41 Fuselage Reinforcement

The wing weight (hence W_1 and W_2) is a function of wing loading and wing area and the body weight (hence W_3) varies with airplane gross weight.

The equation describing behavior of pivot weight penalty included in the wing during airplane scaling can be written as:

$$(W_1 + W_2) = K_4 (W/S)^{0.2454} (S)^{1.046}$$

$K_4 = 0.48\ (0.13)$

The remaining pivot penalty included in the body scales as:

$$W_3 = K_5 + (7.967 \times 10^{-4})\ (GW - K_6)$$

$K_5 = 863.2\ (1903)$

$K_6 = 226\ 796\ (500\ 000)$

5.10 POTENTIAL PROBLEM AREAS

(a) The effect of relative deflections of the wing, body, and bearing structure on the static and dynamic capability of the bearing.

(b) Bonding of the PTFE strip to the metal bearing rings.

6.0 ENGINE CYCLE STUDY

6.1 SUMMARY

The purpose of this study was to determine the engine cycle characteristics best suited to the oblique-wing transonic transport. Some cycle characteristics (pressure ratio, turbine inlet temperature, etc.) already had been selected following studies described in Reference 1. The present study, therefore, concentrated on selection of the optimum bypass ratio (BPR).

Airplanes with engines of BPR = 1, 2, and 3 were configured using the wing selected during the planform study (Section 4.0).

Data obtained from the pivot design study (Section 5.0) and the climb and reserve fuel calculations (Section 7.0) were incorporated, and two sizing cycles were completed, leading to sized airplanes whose major characteristics are given below.

		BPR					
		1		2		3	
TOGW	kg (lb)	192 427	(424 230)	194 550	(428 910)	202 710	(446 900)
OEW	kg (lb)	109 098	(240 520)	112 523	(248 070)	118 524	(261 300)
S	m^2 (ft^2)	285	(3 070)	282	(3 040)	288	(3 100)
Block fuel	kg (lb)	53 479	(117 900)	52 526	(115 800)	54 340	(119 800)
Community noise:							
EPNdB from FAR 36 traded		−0.1		−6.4		−7.0	

The airplane with BPR = 2 engines was selected as the final design, because although it has slightly higher TOGW than BPR = 1, fuel consumption, low-speed performance, and noise are improved. The final configuration with BPR = 2 engines is described in Section 8.0.

6.2 STUDY DESCRIPTION

The first phase of the study was a brief investigation to select the powerplant installation concept to be used. A comparison of twin-engined strut-mounted and four-engined integrated installations led to selection of the four-engined installation for use during the remainder of the study.

First estimates of weight and drag were made and preliminary airplane selection charts were prepared. First-cycle sizes were selected for airplanes with BPR = 1, 2, and 3 engines. Configuration drawings were prepared for each bypass ratio. Powerplant and duct installations were laid out, the optimum body area distribution was determined, and the airplane balance and control surface sizing were checked. These configurations became new baselines from which final airplane sizing was determined.

A second-cycle drag and weight analysis was carried out and final airplane selection charts were prepared, incorporating data from the pivot design study and the climb and reserve calculations described in Sections 5.0 and 7.0. Using these charts, final airplane sizes were determined at each bypass ratio, leading to selection of BPR = 2 engines for the final configuration.

6.3 POWERPLANT INSTALLATION CONCEPT

Before beginning the bypass ratio study, a brief investigation was conducted to select the type of powerplant installation.

Earlier studies, described in Reference 2, had shown the four-engined integrated installation to have slightly superior performance to the twin-engined, strut-mounted type when BPR = 1 engines were used. The purpose of the present investigation was to select the installation concept likely to have the best performance with engines of higher bypass ratio.

The procedure (illustrated in Table 10) was to compare twin- and four-engined airplanes having equal TOGW, wing area, and total cruise thrust using range as a figure of merit.

Table 10 Powerplant Installation Concept Selection

Approach: Compare range of twin- and four-engined installations for fixed airplane size

I. Fix airplane characteristics
- TOGW = 197 585 kg (435 600 lb)
- Wing area = 269.4 m^2 (2900 ft^2)
- Cruise thrust = 13 717 kg (30 240 lb) (total)
- Wing aspect ratio 13.47 ($\Lambda_{0.25}$)

II. Size engines for given cruise thrust

BPR	1	2	3
Total SLST kg (lb)	51 029 (112 500)	56 427 (124 400)	61 979 (136 640)

III. Prepare powerplant sketches for twin- and four-engine installations (Figures 42 and 43)

IV. Evaluate differences between installation concepts (Figure 44)
- Weight
- Drag
- Fuel consumption

V. Convert to range increments (Figure 44)

$\frac{\Delta(\text{Range})}{\Delta(\text{OEW})}$ 0.1233 km/kg (= 0.0302 nmi/lb) $\frac{\Delta(\text{Range})}{\Delta(\text{L/D})}$ 363 km/unit (196 nmi/unit)

$\frac{\Delta(\text{Range})}{\Delta(\text{SFC} \times 2\%)}$ 45.56 km (24.6 nmi)

Engines having BPR = 1, 2, and 3 were sized for given cruise thrust. Sketches of the powerplant installations were prepared (Figures 42 and 43), and body area distributions were developed to minimize cruise drag. Weight and drag increments were estimated, taking the four-engined configuration with BPR = 1 engines as the basepoint.

The installed cruise thrust and specific fuel consumption was found for each ~~configuration~~, taking account of the increased losses in the long ducts of the four-engined installation. An approximate estimate was made of the change in reserve fuel requirements with increasing bypass ratio.

~~Trade factors (Table 10), derived from the Breguet range equation, were used to convert~~ weight, drag, and fuel consumption increments to ~~range~~ (Figure 44). These are combined in Figure 45 to ~~show~~ the effect of bypass ratio on the cruise range of twin- and four-engined installations.

The range of the twin-engined installation decreases continuously with bypass ratio, while the four-engined installation reaches maximum range near BPR = 2.

The four-engined integrated installation therefore was selected for use during the remainder of the study.

Notice that the final results of the bypass ratio study showed that the TOGW of mission-sized, four-engined airplanes increased with bypass ratio. Thus it is likely that the advantage of the four-engined configuration relative to the twin is less than indicated by this brief study. Future development of the oblique-wing transport should include a more thorough examination of the pod-mounted engine installation, since it will probably be easier to develop than the more complex integrated design.

6.4 POWERPLANT CHARACTERISTICS

The engine performance, size, and weight characteristics were obtained from a computerized advanced transonic subsonic parametric engine family. The uninstalled engine data are identical to that used in Reference 1. Installation effects include losses caused by the increased inlet and exhaust system length required for the four-engined integrated arrangement.

Bypass ratios of 1, 2, and 3 were studied. For each of these, a design overall pressure ratio of 16 and a maximum turbine entry temperature of 1670° K (3000° R) was selected. Engine component technology is representative of the mid-1980 time period. Each engine incorporates peripheral lining in the fan duct and an internal mixer for the fan and primary gas streams.

Auxiliary engine inlet doors are provided for operation during takeoff. The inlet geometry is fixed during all other operations. The exhaust nozzles have a fixed throat area and a variable exit area.

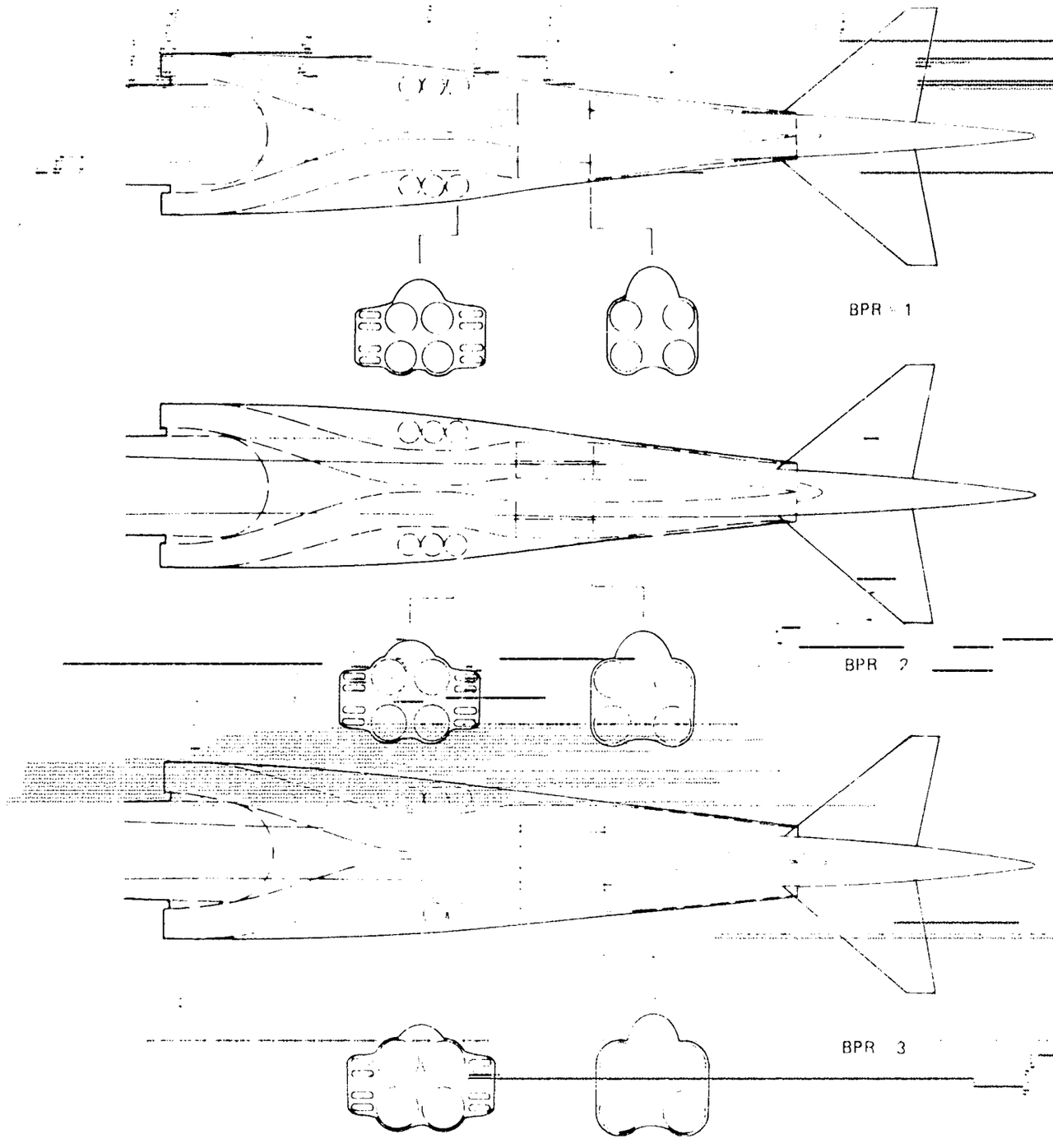

Figure 42 Four-Engined Integrated Installation

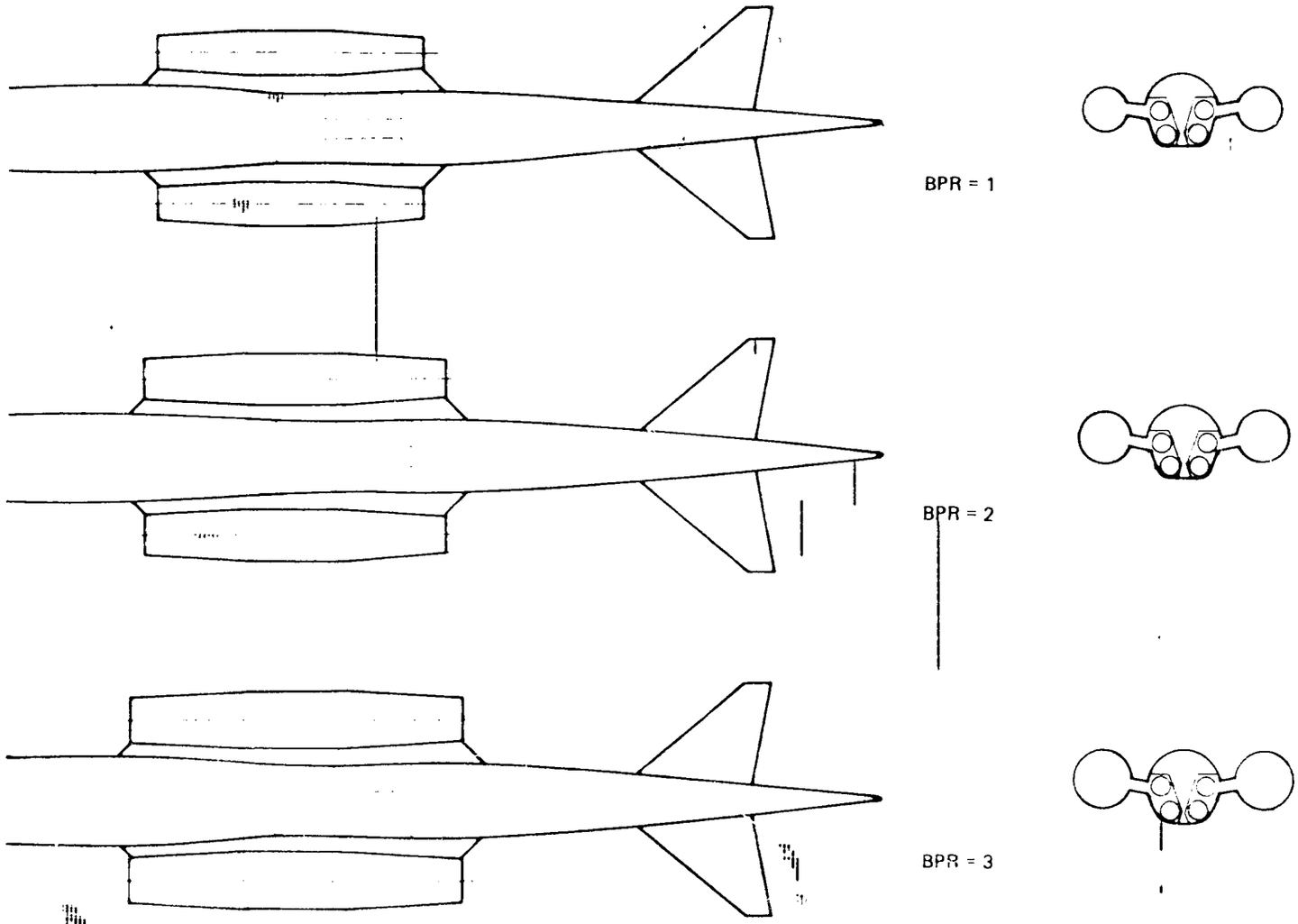

Figure 43 Twin-Engined Installation

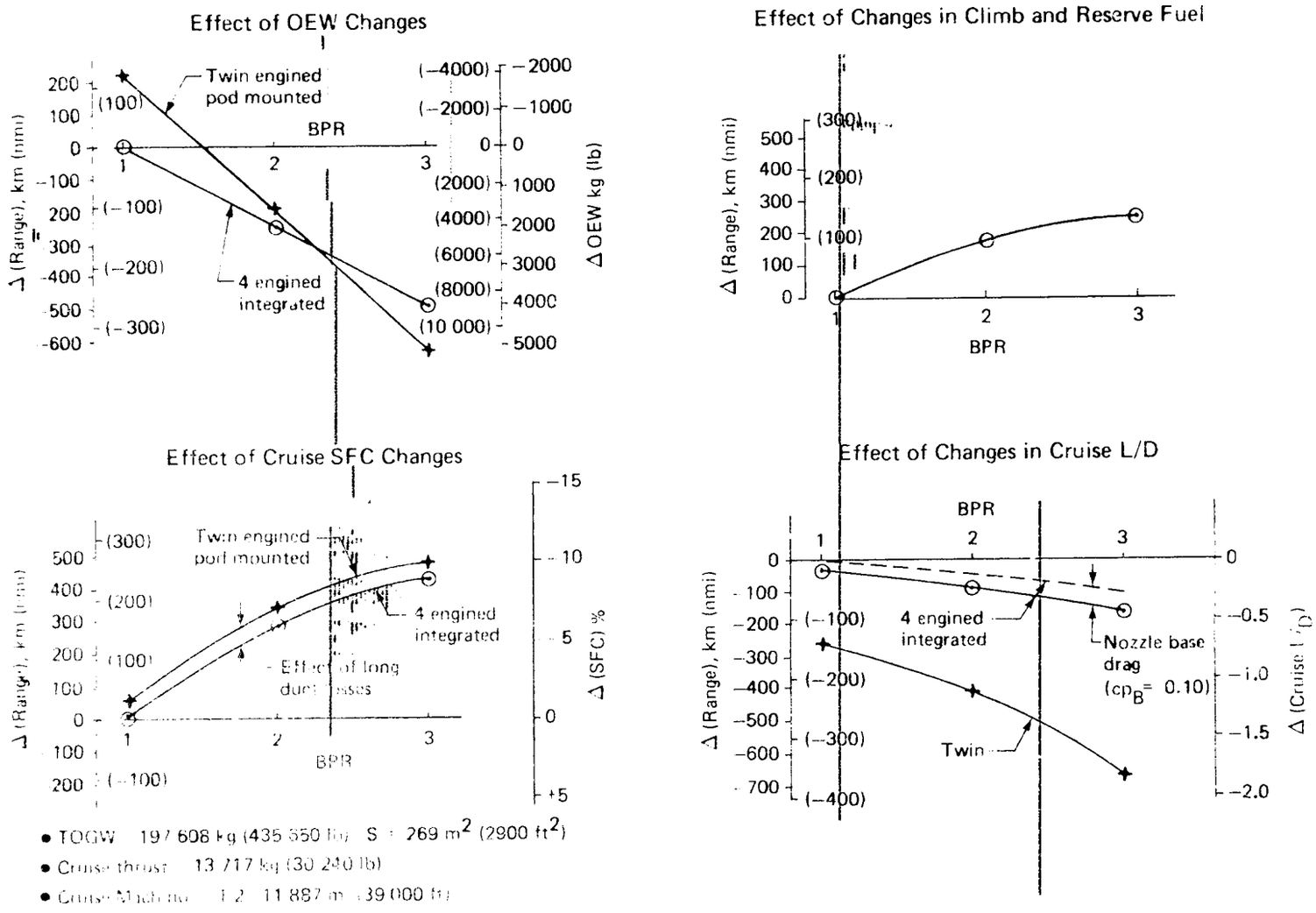

- TOGW 197 608 kg (435 550 lb) S = 269 m^2 (2900 ft^2)
- Cruise thrust 13 717 kg (30 240 lb)
- Cruise Mach no. 0.8 11 887 m (39 000 ft)

Figure 42 Effect of Bypass Ratio on Twin- and Four-Engined Installations

Cruise Range Comparison

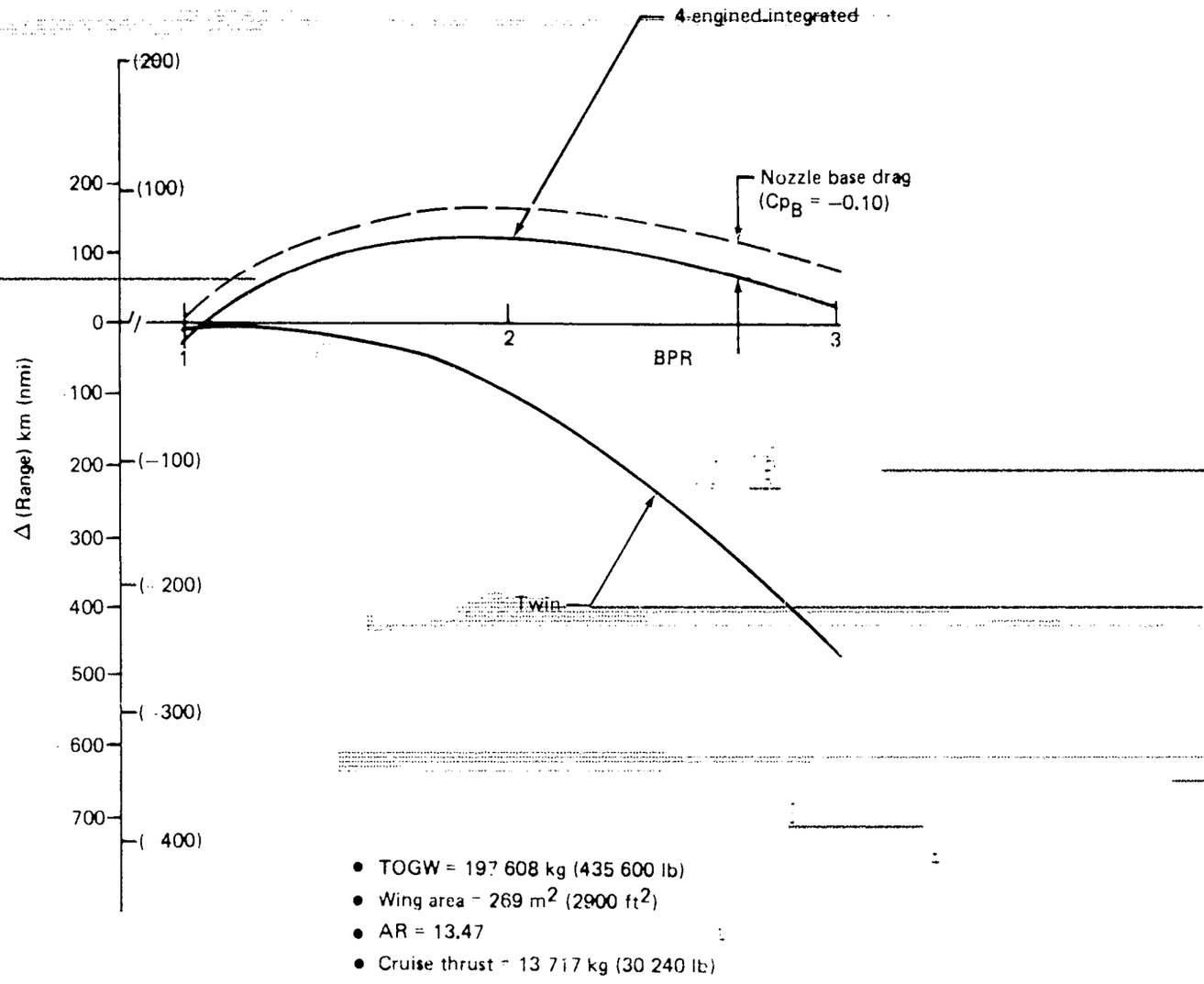

- TOGW = 197 608 kg (435 600 lb)
- Wing area = 269 m^2 (2900 ft^2)
- AR = 13.47
- Cruise thrust = 13 717 kg (30 240 lb)

Figure 45 Cruise Range Comparison

The installed performance reflects losses due to the reduced inlet recovery and increased exhaust system pressure loss of the four-engined integrated installation, relative to a pod-mounted installation. The magnitude of this performance loss is shown below.

BPR	$\frac{\Delta \text{Thrust}}{\text{Thrust}}$ (1)	$\frac{\Delta \text{SFC}}{\text{SFC}}$ (1)
[illegible]	-3.6%	1.05%
2	-3.4%	1.20%
3	-3.4%	1.40%

(1) Relative to pod engines at 1.2 M cruise

The installed performance also includes the effects of 0.91 kg sec (2.0 lb sec) high pressure bleed and 48.5 kW (65 hp) power extraction, per engine. External nacelle drag is included in the airplane drag (Section 6.7).

Installed performance of the study engines during 1.2M cruise is shown in Figure 46. The cruise thrust shown is that which results when the engines are sized for a takeoff thrust rating of 178 000 N (40 000 lb). Since the thrust available for cruise decreases as the bypass ratio is increased, the sized airplanes require correspondingly larger engines and greater propulsion system weight, as shown in Section 6.8.

6.5 BASELINE AIRPLANE SIZE AND PERFORMANCE

Data generated during the planform study (Section 4.0) and the powerplant installation study (Section 6.3) were used to make preliminary estimates of the size and performance of airplanes with BPR = 1, 2, and 3 engines. These became the baseline airplanes used in the development of the final sized configuration.

The design objectives were:

Cruise Mach number	M = 1.2
Range	5560 km (3000 nmi)
Noise goal	FAR 36
Payload	18 114 kg (40 000 lb)

These objectives are identical to those of Reference 1 except that the noise goal was relaxed to FAR 36 rather than 15 effective perceived noise level (EPNdB) below FAR 36.

The preliminary sizing procedure was the same as that described in Sections [illegible] of Reference 1. Methods used to estimate drag, weight, and fuel requirements were similar to those described in Sections 6.7 to 6.9, except that approximate values were used for climb, descent, and reserve fuel, because the more accurate data from Section 5.0 and 7.0 were not available.

- M = 1.2
- 12 190 m (40 000 ft)
- Standard day
- Maximum cruise thrust
- Takeoff thrust 178 000 N (40 000 lb)

- Overall pressure ratio = 16
- Turbine entry temperature 1670° k (3000° r)
- 1985 technology, peripheral lining

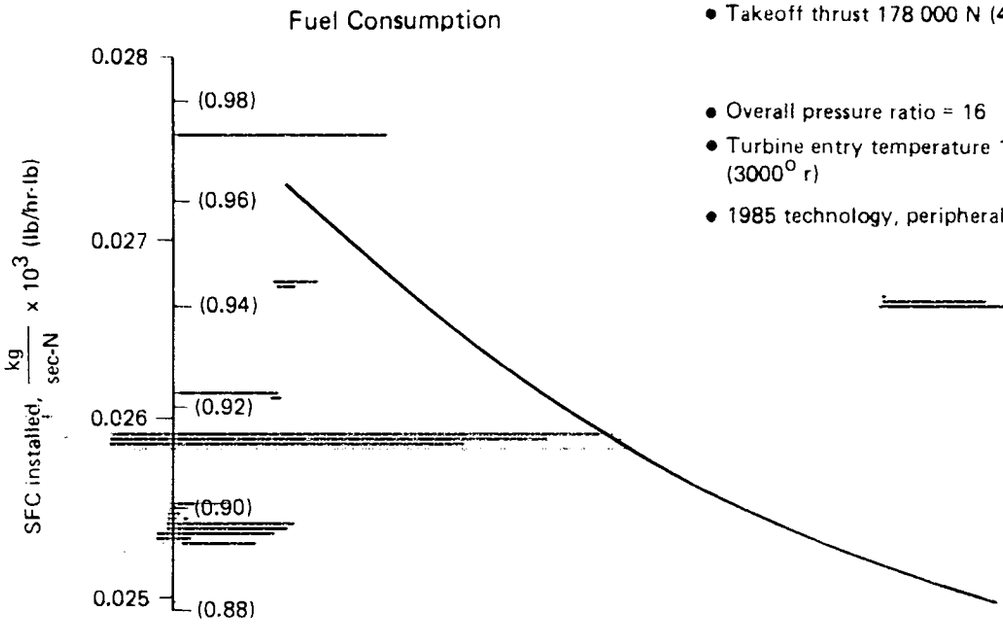

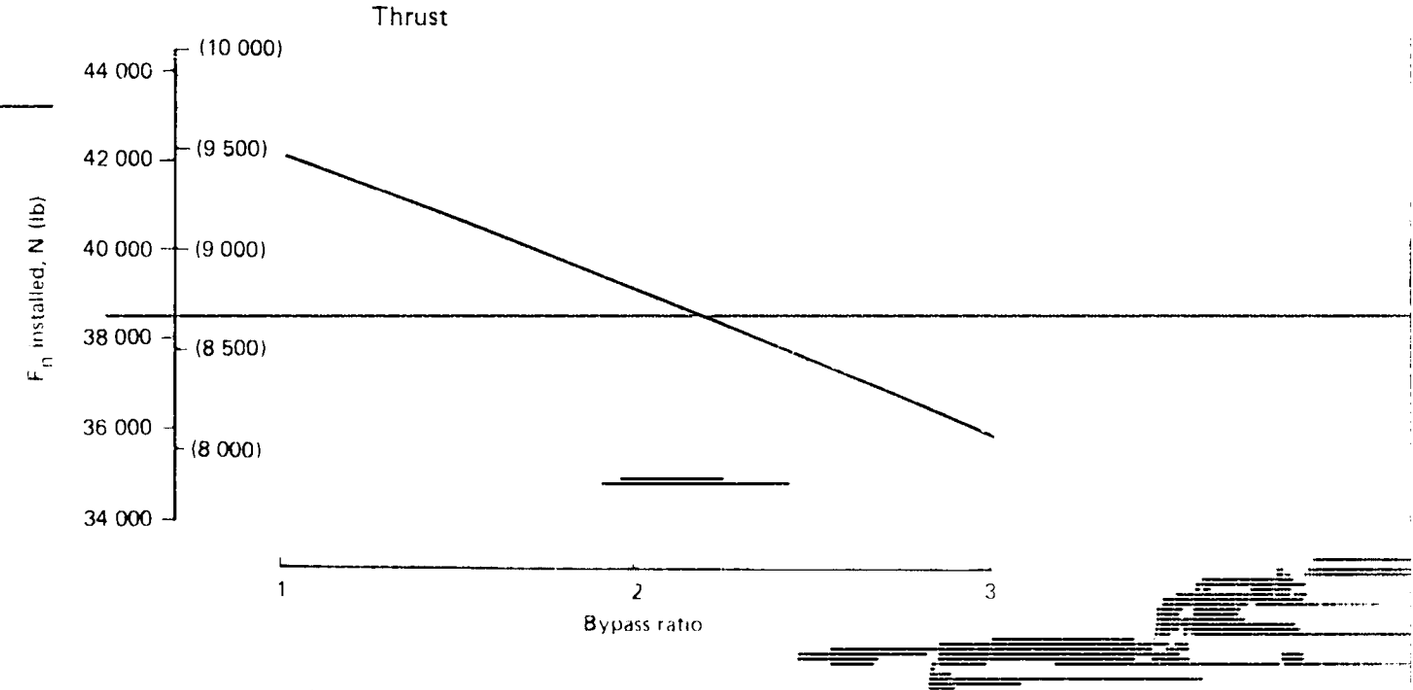

Figure 46 Engine Characteristics

The results of this preliminary analysis are given in the table below which gives the principal parameters that define the three baseline airplanes described in the following section.

		BPR					
		1		2		3	
TOGW	kg (lb)	197 313	(435 000)	193 684	(427 000)	195 498	(431 000)
S	m^2 (ft^2)	291	(3 130)	277	(2 980)	277	(2 980)
Block fuel	kg (lb)	54 885	(121 000)	52 163	(115 000)	52 163	(115 000)
W/S	N/m^2 (lb/ft^2)	656	(139)	685	(143)	694	(145)
T/W		0.29		0.33		0.36	
SLST	N (lb) engine	141 720	(31 860)	154 264	(34 680)	172 502	(38 780)

6.6 BASELINE CONFIGURATION DEVELOPMENT

6.6.1 POWERPLANT INSTALLATION

The different bypass ratios used for the baseline airplanes resulted in different engine sizes, which in turn resulted in different aft fuselage layouts.

The guidelines followed in laying out the engines, ducts, and landing gears are shown in Figure 47.

The duct area aft of the diffuser section was maintained at the fan area to keep the duct flow velocity below M = 0.5. The duct bend radius was limited to a minimum of six times the duct radius, based on experience gained during the 727 program. A clearance of 13 cm (5 in.) was maintained between the duct inner envelope and the rear cabin bulkhead, and the landing gear and the airplane centerline to allow room for duct structure.

The engine centerlines were placed to allow 81 cm (32 in.) between the engine [illegible]. The inlets were placed to allow 30 cm (12 in.) between the inboard lip and the fuselage boundary layer diversion. The boundary layer air that does not flow into the [illegible] auxiliary inlet is diverted downwards under the ducts; the boundary layer [illegible] length-to-height ratio of 2.5. The engine nozzle ducts are the minimum length [illegible] boattail.

As expected, the larger engines (the higher bypass ratios) [illegible] aft-body sections with greater cross-sectional areas as [illegible] Table 11 and the configuration drawings, Figures 48, 49, and 50.

6.6.2 BODY OPTIMIZATION

Seven cross-section control points were used to define an optimum area-ruled [illegible] airplane.

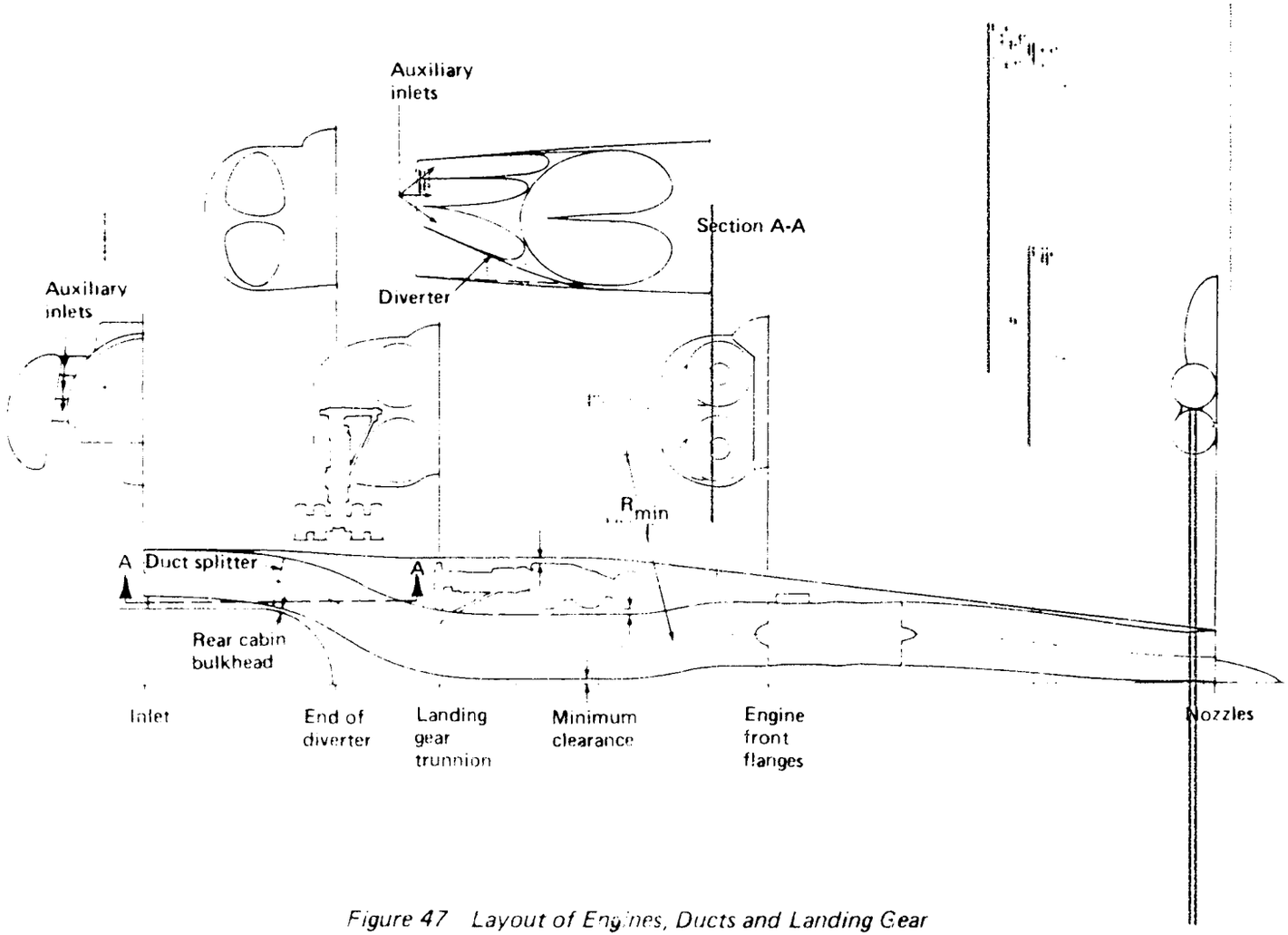

Figure 47 Layout of Engines, Ducts and Landing Gear

Table 11 Bypass Ratio Study Airplanes

	BPR 1		BPR 2		BPR 3	
TOGW kg (lb)	197 430	(435 250)	193 570	(426 750)	195 680	(431 400)
Payload No. passengers	190		190		190	
kg (lb)	18 150	(40 000)	(18 150	(40 000)	18 150	(40 000)
OEW kg (lb)	111 890	(246 680)	112 850	(241 800)	116 700	(257 280)
Wing area m^2 (ft^2)	290.9	(3131)	277.2	(2984)	276.4	(2975)
Wing span m (ft)	62.6	(205.4)	61.1	(200.5)	61.0	(200.2)
Aspect ratio	13.47		13.47		13.47	
Wing MAC m(ft)	5.37	(17.63)	5.24	(17.20)	5.23	(17.18)
C/4 sweep (cruise) rad (deg)	0.87	(50)	0.87	(50)	0.87	(50)
$\bar{V}_H$	0.44		0.44		0.44	
Horizontal tail arm m(ft)	33.0	(108.3)	32.4	(106.4)	31.7	(103.9)
Horizontal tail area m^2 (ft^2)	21.7	(234)	20.3	(218)	20.2	(217)
Horizontal tail aspect ratio	2.6		2.6		2.6	
Horizontal tail taper ratio	0.2		0.2		0.2	
Horizontal tail LE sweep rad (deg)	0.87	(50)	0.87	(50)	0.87	(50)
Horizontal tail t/c %	4		4		4	
$\bar{V}_V$	0.043		0.043		0.043	
Vertical tail area m^2 (ft^2)	25.5	(275)	23.7	(255)	23.5	(253)
Vertical tail arm m (ft)	32.57	(106.8)	32.0	(105.0)	31.2	(102.5)
Vertical tail aspect ratio	1.11		1.11		1.11	
Vertical tail taper ratio	0.254		0.254		0.254	
Vertical tail LE sweep rad (deg)	0.87	(50)	0.87	(50)	0.87	(50)
Vertical tail t/c %	3.5		3.5		3.5	
Engine thrust N (lbf)	141 700	(31 850)	154 250	(34 680)	172 500	(38 780)
Engine diameter m(ft)	1.26	(4.15)	1.48	(4.85)	1.70	(5.57)
Engine length m(ft)	2.85	(9.37)	3.10	(10.17)	3.40	(11.16)
Pivot location from nose m(ft)	49.1	(161.2)	49.6	(162.8)	50.4	(165.4)
End of cabin from nose m(ft)	58.3	(191.2)	58.3	(191.2)	58.3	(191.2)
Engine front flange from nose m(ft)	67.2	(220.5)	67.5	(221.6)	67.9	(222.8)
Inlet plane from nose m(ft)	54.1	(177.4)	53.8	(176.4)	53.3	(175.0)
Nozzle plane from nose m(ft)	77.2	(253.3)	78.8	(258.4)	80.4	(263.7)
Length, inlet to nozzle m(ft)	23.1	(75.9)	25.0	(81.9)	27.1	(88.9)
Inlet area m^2 (ft^2)	3.7	(40)	5.1	(55)	6.8	(73)
[illegible] area m^2 (ft^2)	1.0	(11)	1.0	(11)	1.0	(11)
Max [illegible] body cross-section area [illegible] m^2 (ft^2)	12.3	(132)	13.0	(140)	15.1	(162)

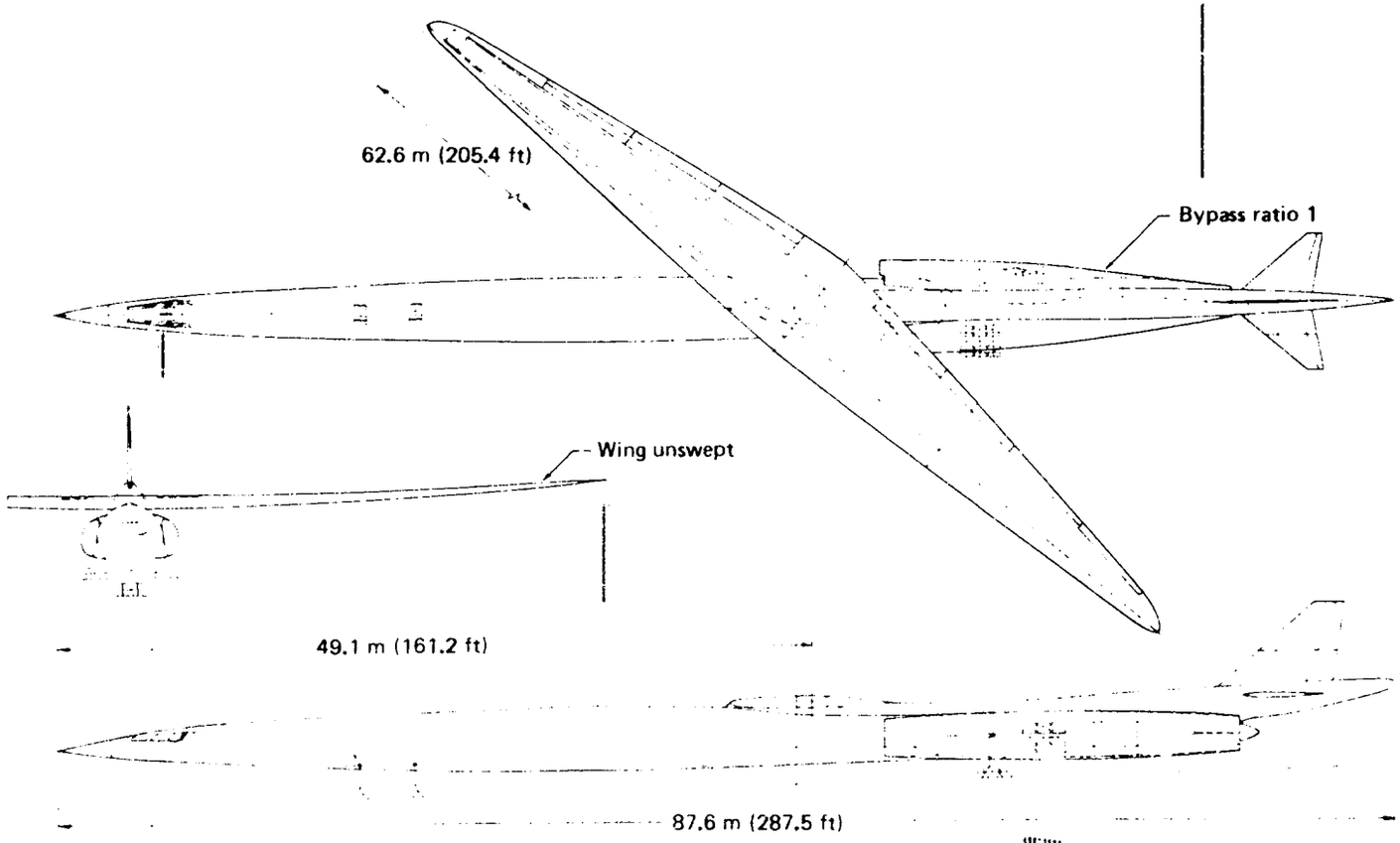

Figure 48 Baseline Airplane Bypass Ratio = 1

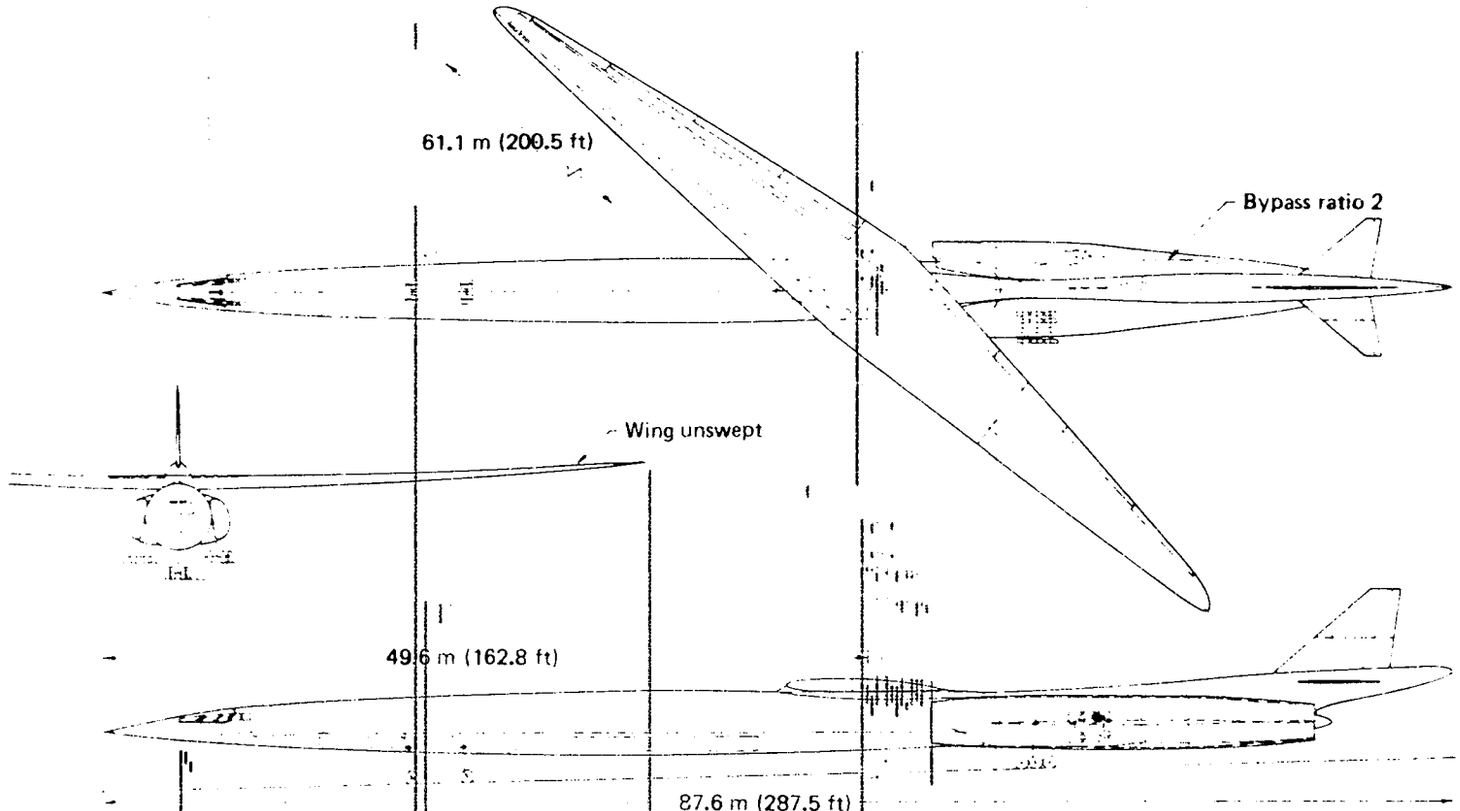

Figure 49 Baseline Airplane Bypass Ratio = 2

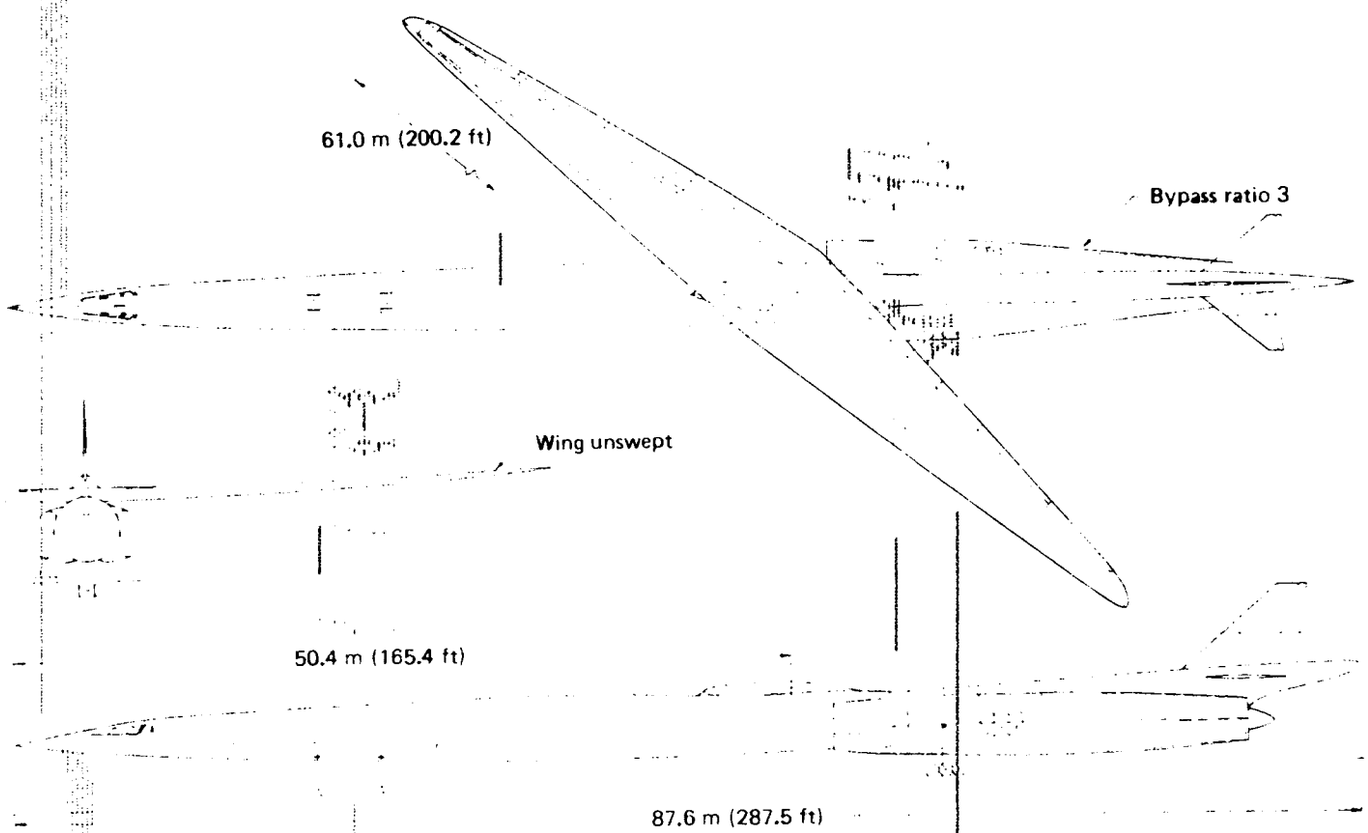

Figure 50 Baseline Airplane Bypass Ratio = 3

Four control points were independent of the engine size. These were at the nose, the flight deck, the pivot location, and the tail (the pivot control point depends indirectly on engine size as the pivot location changes with the aircraft balance which is influenced by engine size and location).

Three additional cross-sectional area control points were identified in the integrated engine aft-body section. These include one near the end of the inlet diverter, one at the landing gear truck (stowed), and one on the engine nozzle boattail. In some cases, one or more of these constraints were removed, as the resulting cross-sectional area was greater than the minimum required.

The area plots for the three baseline airplanes are shown in Figure 51.

6.6.3 BALANCE

Preliminary performance evaluation (Section 6.5) yielded configurations at bypass ratios 2 and 3 with varying engine and powerplant dimensions. Because all of these airplanes had aft engines, their balance was critically dependent on the weight of the powerplant installation, requiring a detailed analysis at each bypass ratio to ensure accurate positioning of the wing on the body. The small mean aerodynamic cord (MAC) lengths associated with these high aspect ratio wings made the airplane balance extremely sensitive to wing location.

The operating empty weight (OEW) center of gravity (cg) for all three bypass ratios was located aft of the aft center of gravity limit determined by stability and control considerations. This implied that a forward water ballast tank would be required at all bypass ratios for partial payloads or for ferry missions. Therefore, balance considerations were not a factor in bypass ratio selection.

Forward balance requirements and fuel management philosophy are identical to that previously discussed for the 5-3 configuration (Reference 1, p. 189).

6.6.4 TAIL SIZING

The horizontal and vertical tail volume coefficients chosen for the baseline development were those used in a previous study of a similar configuration (Reference 21). A review of the 5-3 configuration discussed in Section 8.3.4 shows that these values remain valid.

6.7 BASELINE DRAG AND DRAG SCALARS

6.7.1 BASELINE DRAG

The cruise drag characteristics of the three baseline airplanes are summarized in Table 11, while Table 12 contains the detailed drag buildup.

The following items contribute to cruise drag:

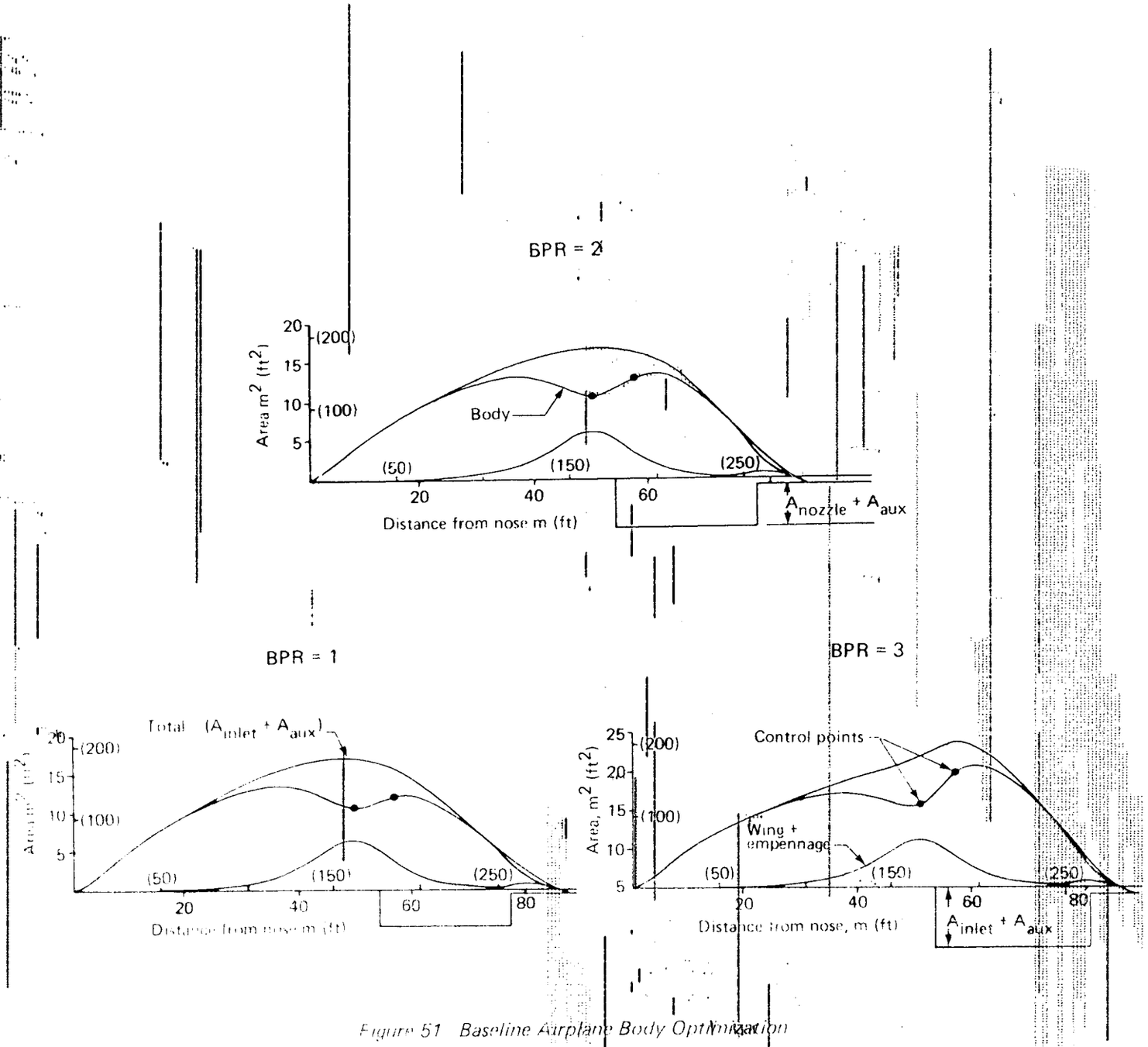

Figure 51 Baseline Airplane Body Optimization

M = 1.2 Λ = 50° 39 000 ft

Zero Lift Drag

Bypass ratio	1	2	3
	$C_D \times 10^4$		
Wave drag	46.0	49.6	54.2
Skin friction	92.7	97.6	100.5
Miscellaneous* items	12.0	13.1	13.9
Total	150.7	160.3	168.6

Envelope Drag Polars

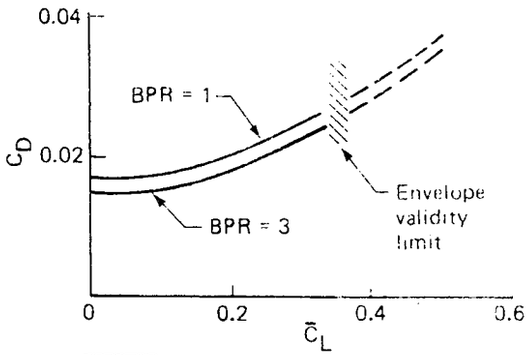

Drag Due to Lift

Envelope factor

$K_E = 0.0829$

Maximum Lift/Drag Ratio

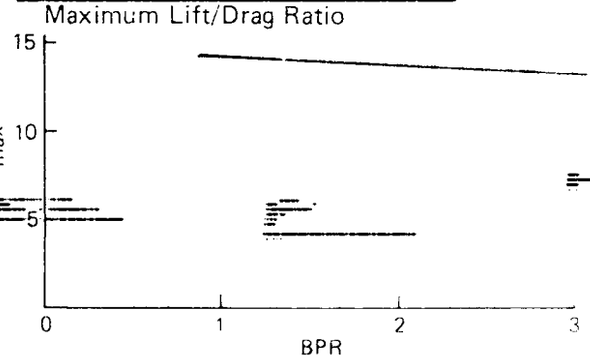

*Roughness, base drag, boundary layer inlets
**Envelope values

Figure 52 Baseline Airplane Cruise Drag

Table 12 Baseline Airplane Drag Buildup

M 1.2 11 887.2 m (39 000 ft) Λ 0.87 rad (50 deg)

Friction and roughness

Component	BPR 1 S = 291 m^2 (3130 ft^2)				BPR 2 S = 277 m^2 (2980 ft^2)				BPR 3 S = 277 m^2 (2980 ft^2)			
	$A_{W/S}$	ℓ m (ft)	C_{D_F} x 10^4	C_{D_R} x 10^4	A_{W/S_W}	ℓ m (ft)	C_{D_F} x 10^4	C_{D_R} x 10^4	$A_{W/S}$	ℓ m (ft)	C_{D_F} x 10^4	C_{D_R} x 10^4
Wing	1.964	7.2 (23.7)	39.3	3.0	1.964	7.0 (23.1)	39.5	3.0	1.964	7.0 (23.1)	39.5	3.0
Body-nacelle	3.30	87.8 (288.0)	46.7	5.0	3.63	87.8 (288)	51.4	5.4	3.82	87.8 (288)	54.1	5.7
Vertical tail	0.166	4.7 (15.5)	3.5	0.2	0.164	4.6 (15.0)	3.5	0.2	0.168	4.6 (15.2)	3.6	0.2
Horizontal tail	0.141	3.0 (10.0)	3.2	0.2	0.140	3.0 (9.8)	3.2	0.2	0.144	3.0 (9.9)	3.3	0.2
Total	5.571		92.7	8.4	5.898		97.6	8.8	6.096		100.5	9.1

Wave and miscellaneous drag

Component	C_{D_W} x 10^4	C_D base x 10^4	C_D aux inlet x 10^4		C_{D_W} x 10^4	C_D base x 10^4	C_D aux inlet x 10^4		C_{D_W} x 10^4	C_D base x 10^4	C_D aux inlet x 10^4	Notes
Wing	29.3				29.3				29.3			Isolated wing
Body-nacelle	7.8	1.2	2.4		11.3	1.8	2.5		15.9	2.3	2.5	(Wing-body nacelle) wing
Vertical tail	4.22				4.17				4.27			(Body, nacelle tail)
Horizontal tail	4.65				4.82				4.75			(Body-nacelle)
Total	49.6				53.9				59.0			
$C_{D_{SYM}}$	150.7				160.3				168.6			

Lift/drag ratio

L/D_{max}	14.2	13.7	13.3

Envelope drag due to lift factor K_E 0.0829

- Skin Friction and Roughness

  Turbulent skin friction was calculated using the method described in Reference 5. Roughness drag includes the effect of such surface imperfections as fasteners, access doors, joints, and larger protuberances such as antennae. Roughness drag was estimated using data obtained during the national supersonic transport (SST) program.

- Wave Drag

  Wave drag was calculated using supersonic area rule techniques as described in Reference 1. The body/nacelle area distribution was designed to minimize cruise drag, as described in Section 6.6.2.

- Base and Auxiliary Inlet Drag

  Base area exists between the clustered exhaust nozzles beneath the aft body. An estimate of the associated drag has been made by applying a pressure coefficient to this area of -0.1, derived from data for bodies of revolution.

  The auxiliary inlet captures boundary-layer air that is ducted to nozzles mounted aft of the wing trailing edge. A conventional diverter does not appear to be practical because boundary-layer air deflected upwards would be forced to flow through the narrow channel between the body and the wing lower surface. Boundary-layer air deflected downward is handled by a conventional diverter. The drag of the diverter, inlet, and associated ducting has been estimated using methods described in Reference 7. Experimental data would be desirable to obtain more accurate estimates of the auxiliary inlet and base drag.

- Drag Due to Lift

  Drag due to lift was given by the envelope equation,

  $$\Delta C_{D_{LIFT}} = K_E C_L^{\ 2} \quad \text{with} \quad K_E = 0.0829$$

  obtained as described in Section 4.3. This form is appropriate for baseline airplane drag polars that are used during final airplane sizing, when design lift coefficient has not been established.

- Trim Drag

  Cruise drag has not been penalized for trim.

Sections 7.4 and 8.4 contain a more complete discussion of trim drag and drag due to lift.

6.7.2 CRUISE-DRAG SCALARS

The cruise-drag buildup given in the preceding section applies to the baseline airplanes described in Section 6.6. The process of resizing these baseline airplanes to achieve the design

range requires scaling laws, permitting the baseline airplane drag to be adjusted for small changes in powerplant size, wing, and empennage area.

The drag-due-to-lift factor (K_E) is independent of wing area so that scaling relationships are needed only for the components of zero-lift drag. These relationships were derived as described below.

The airplane was divided into the following components:

- Body/nacelle, including interference
- Wing
- Horizontal tail
- Vertical tail

The arrangement of the passenger compartment is fixed, so that the lines and area distribution of the body/nacelle are determined almost entirely by the duct radius (Section 6.6.1), that is directly related to inlet area. Engine bypass ratio has only a minor influence on body/nacelle shape, so that the body/nacelle drag is a function of inlet area and is not directly dependent on bypass ratio. This relationship permitted the derivation of laws relating body/nacelle drag to powerplant size, without analyzing configurations having a range of powerplant sizes at each bypass ratio.

Figure 53 shows that the drag of the three optimized baseline configurations is a near linear function of inlet area. Thus, the rate of change of body/nacelle drag with powerplant size is given by

$$\frac{d\,(D/q)}{d\,(SLST)} = \frac{d\,(D/q)}{d\,A_I} \Big/ \frac{d\,(SLST)}{d\,A_I}$$

The rate of change of body/nacelle drag with inlet area $\left[d\,(D/q)/d\,A_I\right]$ is shown in Figure 53. The rate of change of reference thrust with inlet area $\left[d\,(SLST)/d\,A_I\right]$ is a function of bypass ratio, obtained from powerplant data.

The resulting body/nacelle drag scaling relationships are given in Figure 53.

The zero-lift drag of the wing, horizontal, and vertical tails take the form

$$\frac{d}{q} = \left\{ C_{D_W} + C_{D_F} \right\} S$$

Where S is the component planform area, C_{D_W} and C_{D_F} are wave and skin friction drag coefficients based upon S.

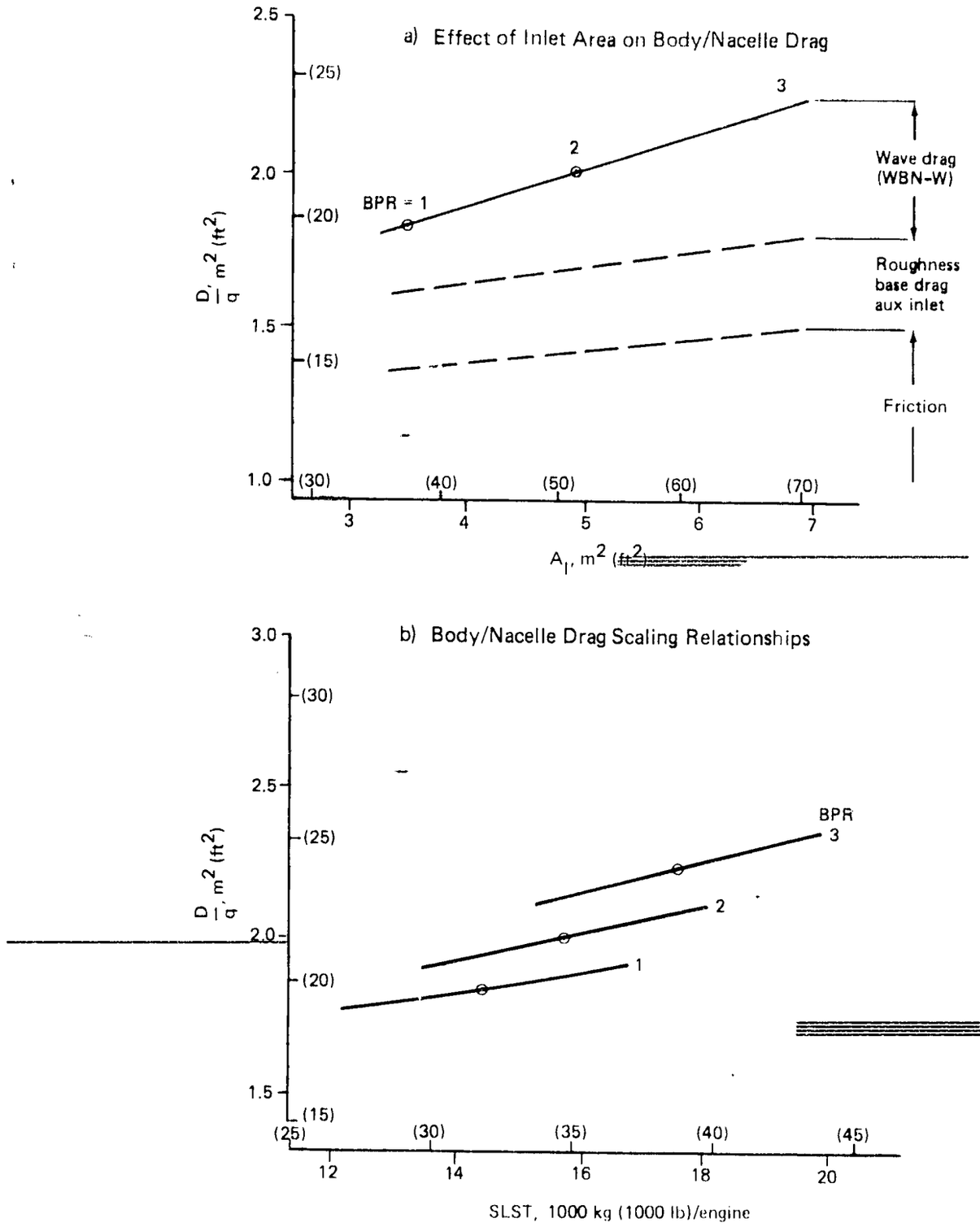

Figure 53 Effect of Powerplant Size on Cruise Drag

The effect of small variations of component area on drag are therefore given by

$$\frac{d(D/q)}{dS} = C_{D_W} + C_{D_F} + \left(\frac{AW}{S}\right)\left(\frac{\ell}{2}\right)\left(\frac{dC_f}{d\ell}\right)$$

(A_W/S) is the component wetted area ratio and ℓ is the component characteristic length.

This expression leads to the drag scalars tabulated below

Component	Wing	Horizontal and vertical tails
$\frac{d(D/q)}{dS}$	0.0066	0.0103

6.8 BASELINE WEIGHTS AND WEIGHT-SCALING METHODOLOGY

6.8.1 WEIGHT-SCALING METHODOLOGY

Weight scaling involves interrelationships between component weights and design parameters; e.g., gross weight, wing area, and engine thrust that can be expressed in terms of partial derivatives, as shown in Figure 54. These weight sensitivities were developed for the oblique-wing airplanes in recognition of their specific configuration characteristics. This enabled development of a consistent set of airplane operating empty weights that were required as inputs to mission sizing analyses.

Since a constant payload was maintained throughout the study, the primary weight effects of variations in gross weight, wing area, and engine thrust were limited to the airplane structure, surface controls, and propulsion-related items. Payload-related weight, such as fixed equipment, customer options, and standard and operational items remained unchanged.

6.8.2 BASELINE WEIGHTS

Table 13 contains a list of weights, by functional item, for the baseline airplanes shown on Figures 48, 49, and 50. As can be noted, the principal reason for relative OEW differences can be found in the weight of propulsion systems (influenced by engine size) and structure (due to gross weight and wing area differences). Section 8.4.2 contains a detailed weight statement of the BPR = 2 airplane that was selected at the conclusion of these studies.

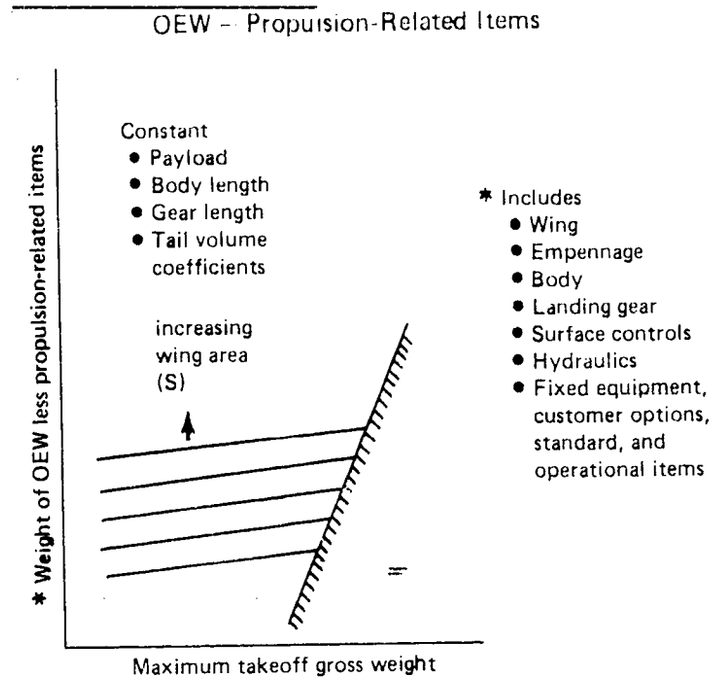

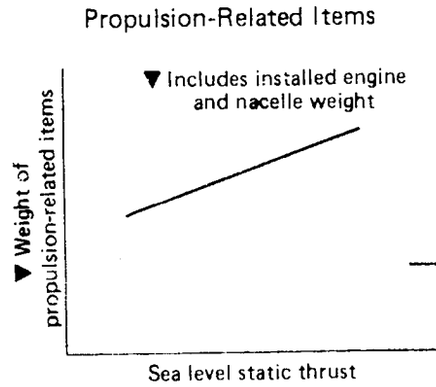

$$dW = \underbrace{\frac{\partial W}{\partial MTOGW}\,dMTOGW + \frac{\partial W}{\partial S}\,dS}_{\text{* OEW less propulsion items}} + \underbrace{\frac{\partial W}{\partial SLST}\,dSLST}_{\text{▼ Propulsion-related items}}$$

Figure 54 Parametric Representation of the Weight-Scaling Data

Table 13 Baseline Airplane Weights

Functional item	BPR 1 kg (lb)	BPR 2 kg (lb)	BPR 3 kg (lb)
Structure	72 350 (159 510)	74 120 (163 400)	77 760 (171 430)
Propulsion system	10 060 (22 180)	11 660 (25 720)	13 850 (30 530)
Fixed equipment	20 320 (44 800)	20 380 (44 920)	20 520 (45 240)
Standard and operational items including customer options	6 360 (14 030)	6 360 (14 030)	6 360 (14 030)
OEW	109 090 (240 520)	112 520 (248 070)	118 490 (261 230)

6.9 CLIMB, DESCENT, AND RESERVE FUEL

The results of climb, descent and reserve fuel calculations ar summarized below.

	Climb			Descent			Reserves
BPR	Time (hrs)	Distance km (nmi)	Fuel % TOGW	Time (hrs)	Distance km (nmi)	Fuel % TOGW	Fuel % TOGW
1	0.396	357 (193)	3.98	0.4	314 (170)	0.4	6.5
2	0.380	343 (185)	3.59	0.4	314 (170)	0.4	6.3
3	0.328	294 (159)	2.99	0.4	314 (170)	0.4	6.3

The analysis leading to these results is described in Section 7.0.

The reserve fuel was calculated using the following rules:

- One-hour extended cruise at M = 0.9
- Missed approach (2 minutes at maximum takeoff power)
- Climb, cruise, and descent to 370.6 km (200 nmi) alternate

The 1-hour extended cruise and cruise-to-alternate was calculated at the specific range at best-cruise altitude. Exchanging 45 minutes at end-of-cruise altitude and cruise Mach (FAR 25) in place of the 1-hour extended cruise at Mach 0.9 and best-cruise altitude resulted in only a slight increase in reserve fuel requirements. It should be noted that under FAR reserve rules, the 370.6 km (200 nmi) alternate could be considerably shorter in distance should one exist for

a given flight. Speeds below Mach 0.8 were thought to be incompatible with other air traffic and above Mach 0.9, specific range begins to deteriorate. The fuel mileage between Mach 0.8 and 0.9 is nearly constant.

The 1967 Air Transport Association (ATA) Domestic Reserve Rules were chosen for being comparable to present FAR rules and because no new transonic reserve rules have been formulated.

6.10 AIRPLANE SIZING AND BYPASS RATIO SELECTION

Design selection charts for configurations with BPR = 1, 2, and 3 engines are shown in Figures 55, 56, and 57.

Point design airplanes were selected at the intersection of the wing fuel volume limit line and the maximum cruise lift coefficient line (CL = 0.35), that lies very close to minimum block fuel and gross weight. These selection charts are based on aerodynamic, performance, and weight and balance analysis of the three baseline airplanes described in Section 6.5. Pivot weights and weight scalars are taken from the results of the pivot design study (Section 5.0).

Characteristics and performance of the selected point designs are given in Table 14 and Figures 58, 59, and 60. Bypass ratio = 2 engines were selected for the final configuration because they lead to the lowest fuel consumption and have good noise characteristics.

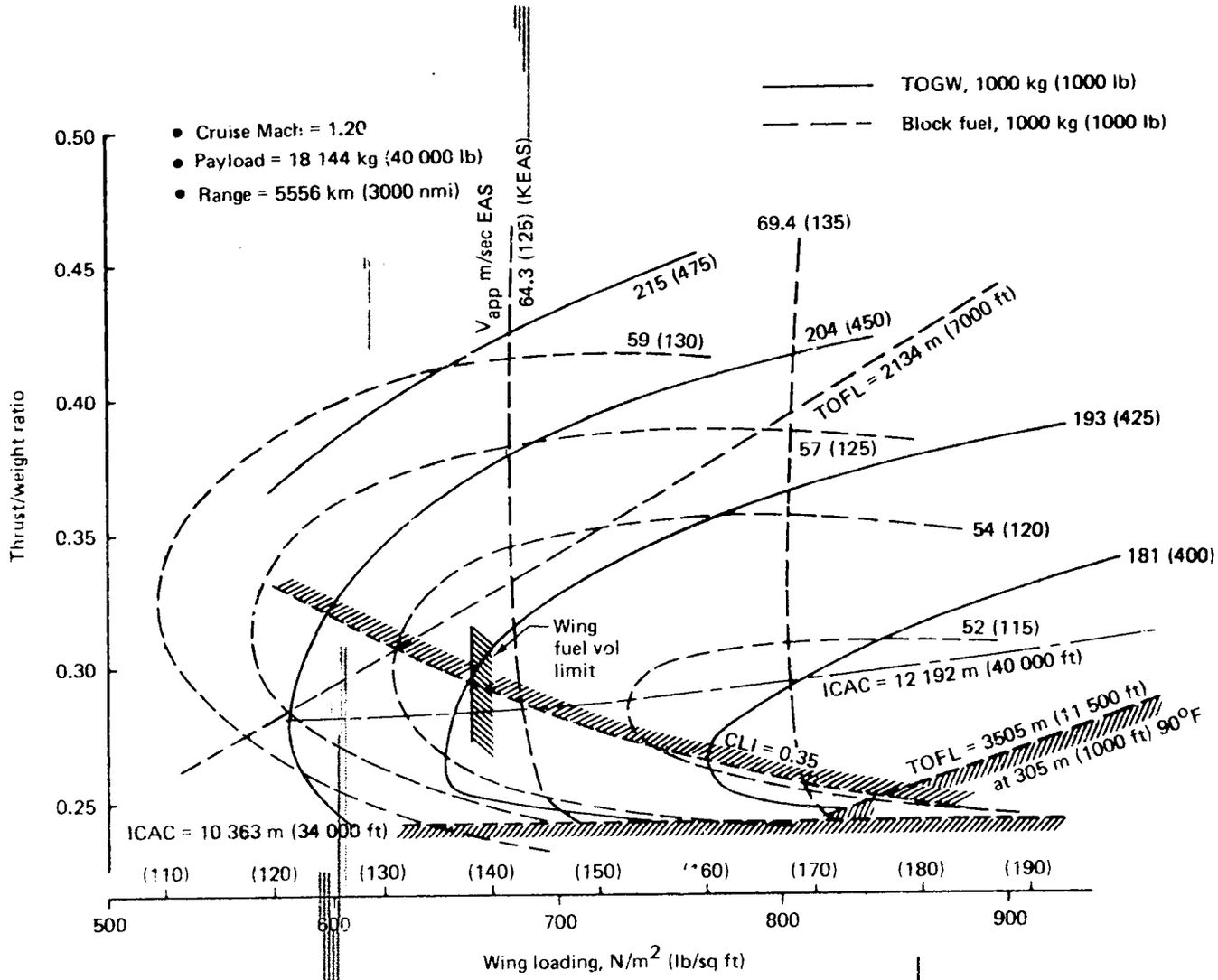

Figure 55 Design Selection Chart BPR = 1

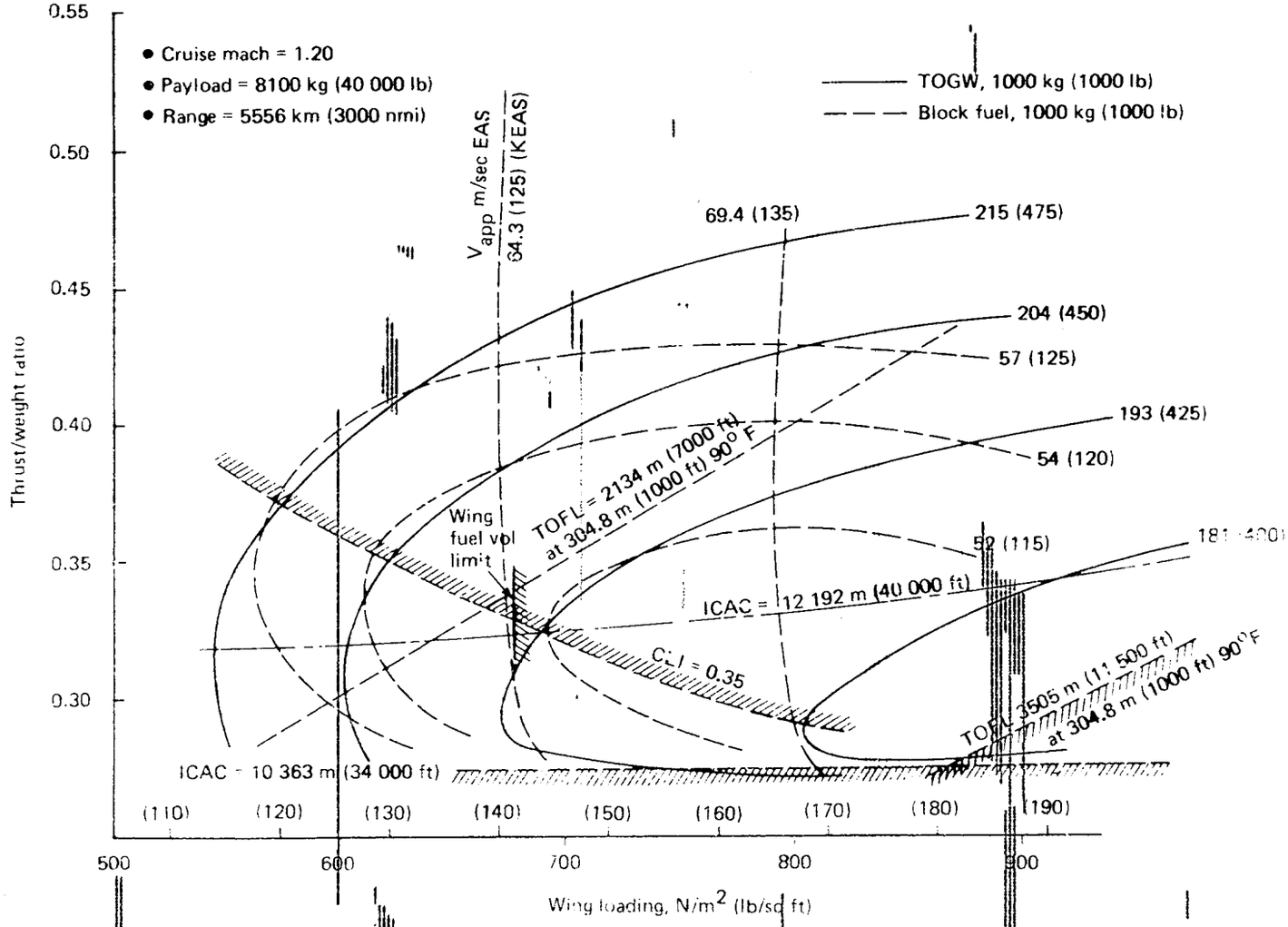

Figure 56 Design Selection Chart BPR = 2

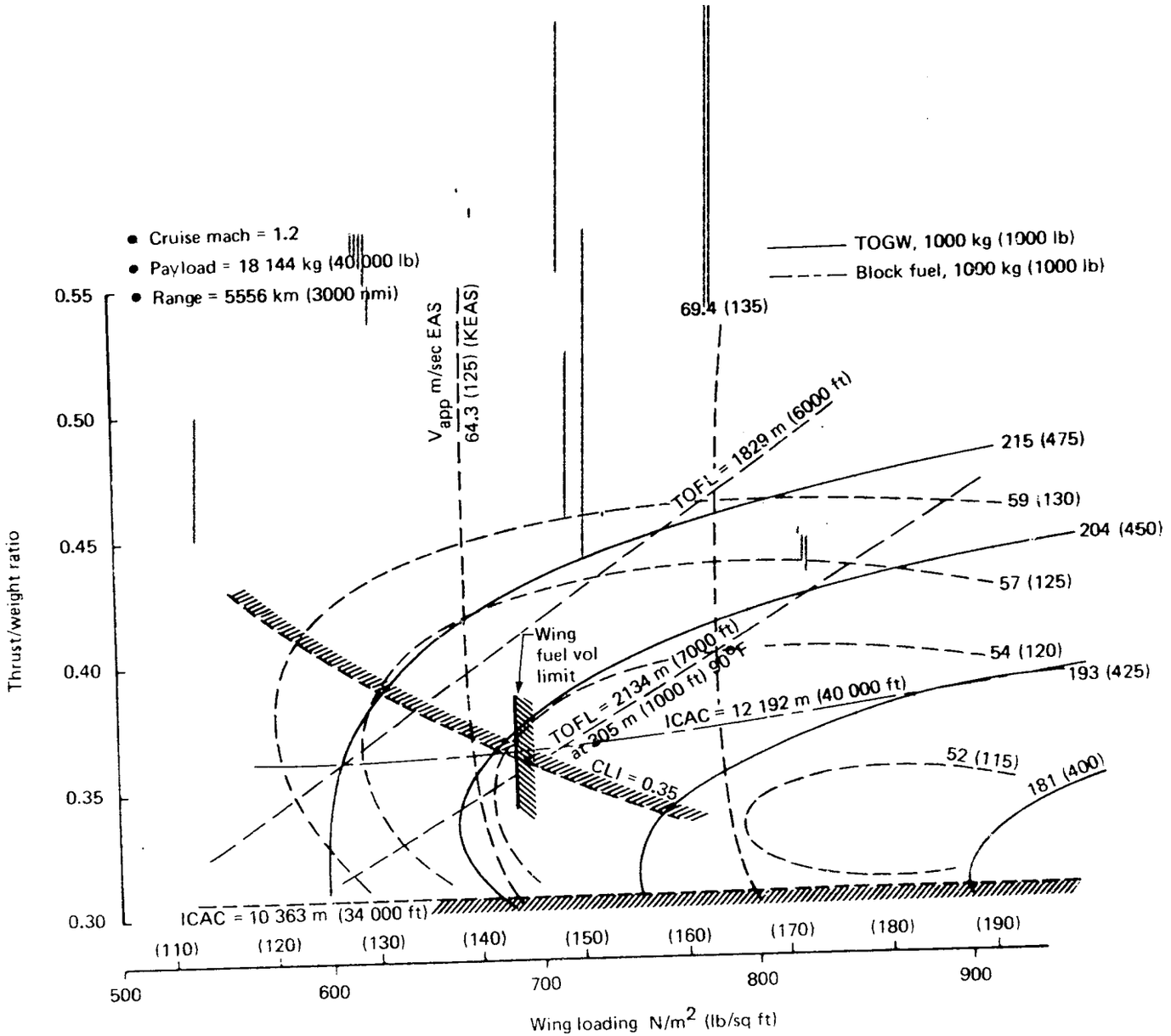

Figure 57 Design Selection Chart BPR = 3

Table 14 Effect of Bypass Ratio on Sized Aircraft Performance

- Mach 1.20
- Payload = 18 144 kg (40 000 lb)
- Range = 5556 km (3000 nmi)
- Peripheral noise treatment*

	BPR 1	BPR 2	BPR 3
TOGW kg (lb)	192 427 (424 230)	194 550 (428 910)	202 710 (446 500)
OEW kg (lb)	109 098 (240 520)	112 523 (248 070)	118 524 (261 300)
S m^2 (ft^2)	285 (3 070)	282 (3 040)	288 (3 100)
SLST kg (lb)	14 152 (31 200)	15 966 (35 200)	18 325 (40 400)
Block fuel kg (lb)	53 479 (117 900)	52 526 (115 800)	54 340 (119 800)
Reserves kg (lb)	12 510 (27 580)	12 247 (27 000)	12 791 (28 200)
No. of engines/BPR	4/1	4/2	4/3
Thrust loading (T/W)	0.294	0.328	0.362
Wing loading (W/S) N/m^2 (lb/sq ft)	661 (138)	675 (141)	689 (144)
ICAC m (ft)	12 466 (40 900)	12 344 (40 500)	12 131 (39 800)
Cruise alt m (ft)	13 076 (42 900)	12 954 (42 500)	12 741 (41 800)
RF m (NAM)	18 150 (9 800)	18 705 (10 100)	18 705 (10 100)
$SFC_{(cruise)}$ kg/N-S x 10^{-5} (lb/hr/lb)	2.7334 (0.965)	2.5776 (0.910)	2.4926 (0.880)
L/D (cruise)	13.7	13.4	12.9
L/D (max)	14.1	13.7	13.4
C_L at L/D max	0.43	0.43	0.44
C_L at (cruise)	0.34	0.34	0.34
TOFL: at 305 m (1000 ft) 305 k (90^O)			
Max flaps, m (ft)	2 359 (7 740)	2 201 (7 220)	2 079 (6 820)
Reduced flaps, m (ft)	3 365 (11 040)	3 139 (10 300)	2 969 (9 740)
C_L (max flaps)	Without LE 1.90	1.90	1.90
C_L (reduced flaps)	Without LE 1.35	1.35	1.35
L/D community noise reduced flaps (V_{app} + 5.1 m/s (10 kts))	9.3	9.3	9.3
Approach speed:			
Max flaps m/s EAS (KEAS)	63.3 (123.0)	64.4 (125.1)	65.1 (126.6)
With LE C_L (max flaps) at 1.3 Vs	1.95	1.95	1.95
Reduced flaps m/s EAS (KEAS)	72.0 (140)	72.0 (140)	72.0 (140)
With LE C_L (reduced flaps)	1.51	1.56	1.60
Community noise: EPNdB*			
From FAR 36			
Takeoff with thrust cutback at noise station	2.6	**11.4	**15.6
Sideline 648.2 m (0.35 nmi)	11.9	6.3	11.1
Approach	2.1	4.4	5.0
Traded	0.1	6.4	7.0

*1976 research technology qualified for 1985 design freeze

**Oblique wing allows thrust cutback below 50 percent takeoff power

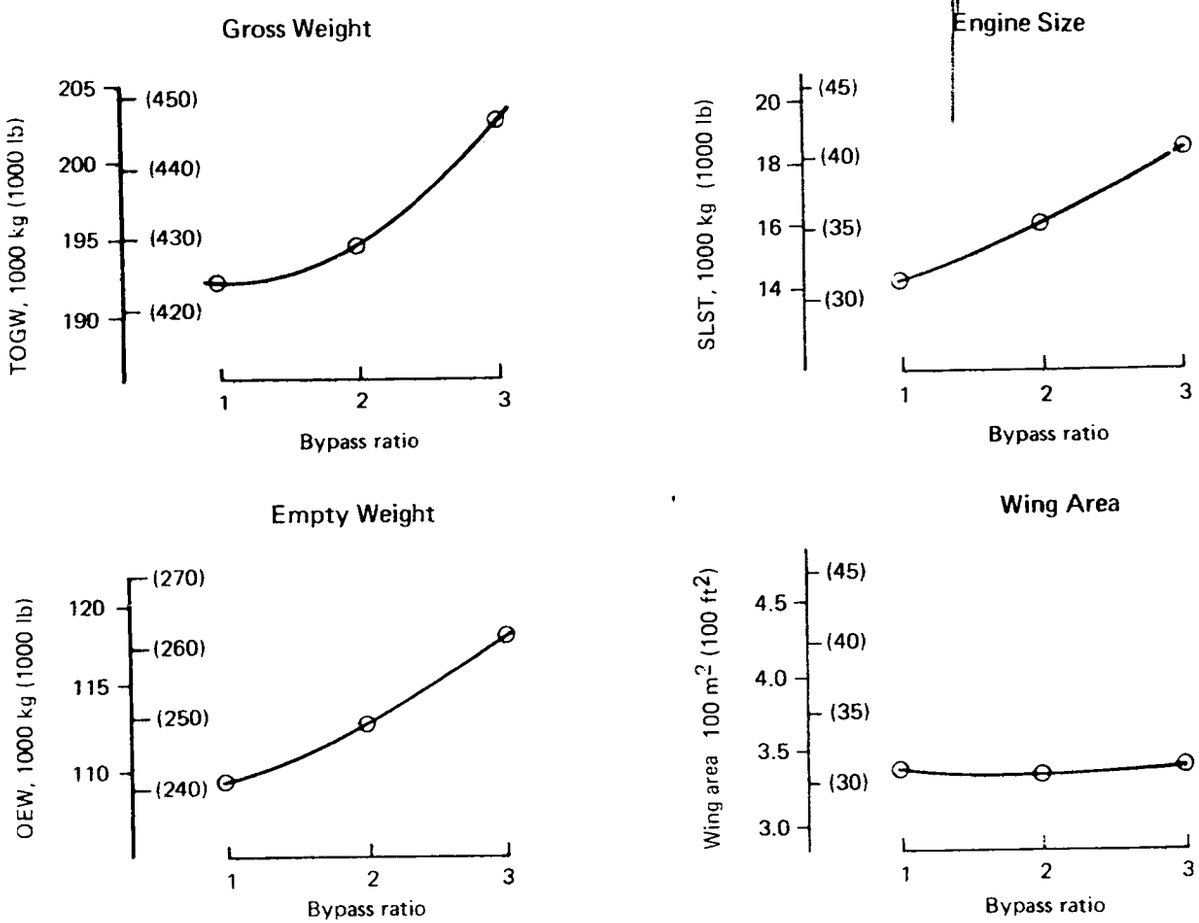

- Cruise Mach no. = 1.2
- Range 5560 km (3000 nmi)
- Payload 18 144 kg (40 000 lb)
- Peripheral noise treatment (1976 research technology qualified for 1985 design freeze)

Figure 58 Size and Weight Trades

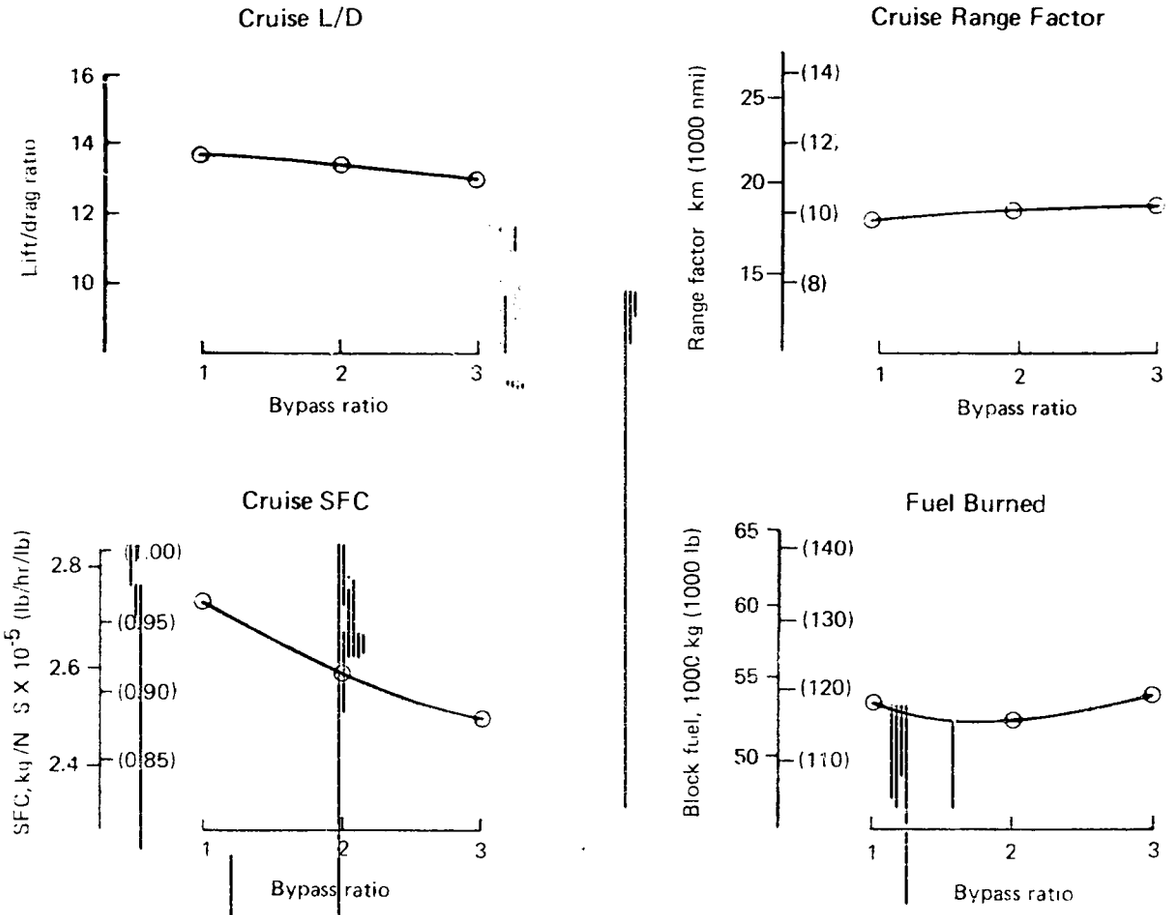

- Cruise Mach no. = 1.2
- Range 5560 km (3000 nmi)
- Payload 18 144 kg (40 000 lb)
- Peripheral noise treatment (1976 research technology qualified for 1985 design freeze)

Figure 59 Cruise Performance Comparison

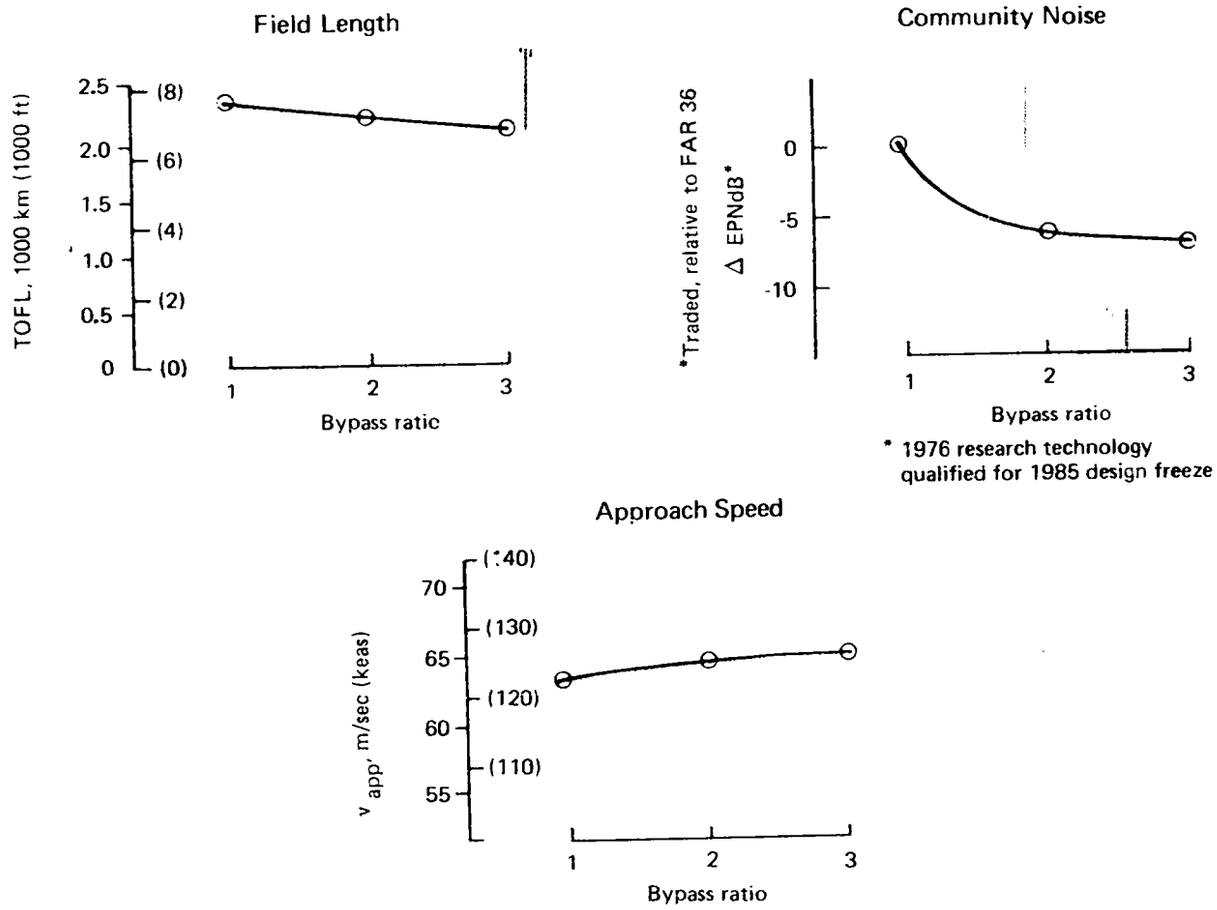

- Cruise Mach no. = 1.2
- Range 5560 km (3000 nmi)
- Payload 18 144 kg (40 000 lb)
- Peripheral noise treatment (1976 research technology qualified for 1985 design freeze)

Figure 60 Low-Speed Performance

7.0 CLIMB, DESCENT, AND RESERVE FUEL

7.1 SUMMARY

During previous studies, (Reference 1), the fuel required for climb, descent, and reserves had been estimated using SST experience as a guide. Detailed calculations had not been conducted. The objective of the study described here was to evaluate these fuel requirements more accurately, using thrust, fuel consumption, and drag data appropriate for the yawed oblique wing.

The results of these calculations were applied to the bypass ratio study (Section 6.0) and are summarized in Section 6.9.

7.2 STUDY DESCRIPTION

Major advantages of the yawed oblique-wing concept are that sweep may be varied to minimize drag at each flight condition and that the large wing span gives excellent lift/drag ratios at low and transonic speeds.

The first phase of this study, therefore, was to select the sweep angles that give maximum lift/drag ratio for the Mach number attained during climb and subsonic cruise. Sweep selection and drag estimates were based on experimental data, as described in Sections 7.3 and 7.4.

Section 7.5 contains typical engine thrust and fuel consumption characteristics for subsonic conditions.

Selection of the climb speed schedule and climb fuel calculations are described in Section 7.6, while reserve and descent fuel calculations are described in Sections 7.7 and 7.8.

Detailed climb calculations were conducted only for the BPR = 2 engines, which preliminary estimates (Section 6.5) showed to be the most likely choice for the final configuration. Estimates for BPR = 1 and 3 were made by applying increments to the BPR = 2 data, based on knowledge of the relative drag, thrust, and fuel consumption characteristics of the three baseline configurations described in Section 6.6.

7.3 SWEEP SELECTION

The following wing sweep angles were used during climb and subsonic cruise.

M	0 ⟶ 0.68	0.8	0.9
Λ	0	0.61 rad (35°)	0.92 rad (41°)

They were selected following an analysis of experimental data described in Section 10.0, which showed that maximum lift/drag ratio is attained when:

$$M \cos \Lambda \approx 0.68$$

7.4 DRAG

Figure 61 shows predicted drag polars at M = 0.5, 0.8 and 0.9 for the baseline configuration with BPR = 2 engines.

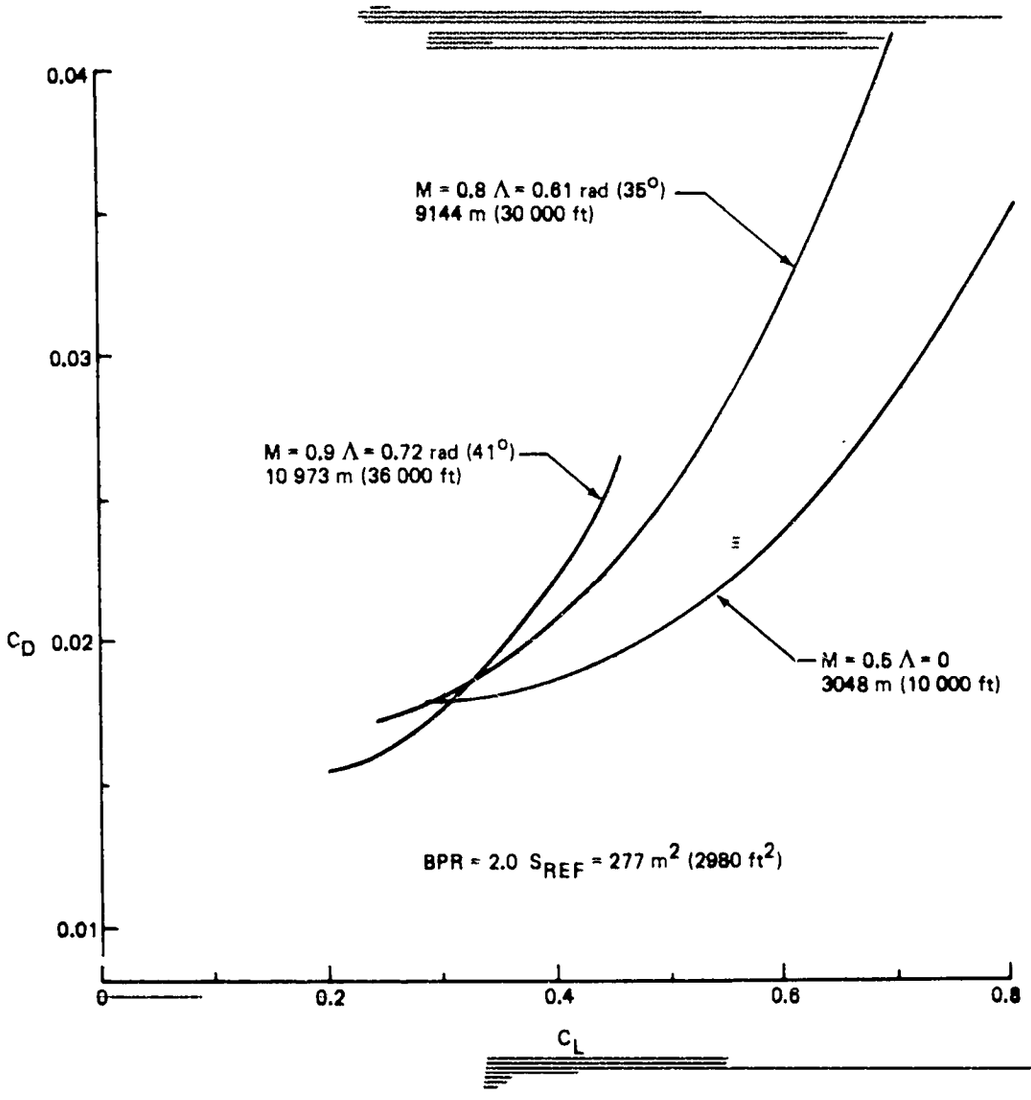

Figure 61 Oblique Wing Baseline Subsonic Drag

The drag polars have the form

$$C_D = C_{D_{SYM}} + \Delta C_{D_{TRIM}} + \Delta C_{D_{LIFT}}$$

$C_{D_{SYM}}$: Friction, profile, roughness, miscellaneous

$\Delta C_{D_{TRIM}}$: Trim

$\Delta C_{D_{LIFT}}$: Drag due to lift

Tables 15, 16 and 17 give details of the drag buildup at BPR = 2 and increments to change the data to BPR = 1 and 3.

Drag due to lift was estimated using the leading edge suction approach described in Reference 8 which gives

where

$$\Delta C_{D_{Lift}} = \left\{ C_L \frac{\text{Tan}\,(\alpha-\alpha_0) - s}{} \left[C_L \text{Tan}\,(\alpha-\alpha_0) - \left(\overline{C_L{}^2}/\pi AR \right) \right] \right\}$$

$$\alpha - \alpha_0 = \left(C_L / C_{L_\alpha} \right)$$

Lift slope (C_{L_α}) and the effective leading edge suction factor(s) were derived from experimental data, as described in Section 10.0.

Trim drag was included at M = 0.5, A = 0 with the center of gravity at 26 percent $\bar{c}$ and the estimated values of C_{M_o} and wing body aerodynamic center shown below

	C_{M_o}
Wing	−0.097
Body	−0.026
Total	−0.123

	Aerodynamic center (%$\bar{c}$)
Wing	26
Body	−11
Total	15

Wing C_{M_o} and aerodynamic center were estimated using test data for NACA 4-digit series airfoils. Body effects were predicted using slender body theory.

No trim drag has been included when at M = 0.8, M = 0.9, or during supersonic cruise. When the wing is swept back, C_{M_o} depends strongly upon the upward curvature (dihedral) built into the wing at zero sweep. A wide range of C_{M_o} can be obtained with negligable increase in drag due to lift; in addition, cruise cg can be adjusted by fuel transfer. In consequence, it should be possible to obtain minimum (negative) trim drag in cruise and very small penalties during climb and subsonic cruise. Figure 62 summarizes these results and shows that the oblique-wing subsonic lift drag ratios are a little higher than conventional aircraft having equivalent span and wetted area.

Table 15 Oblique Wing Subsonic Drag Mach No. 0.5

SLST 141 898 N (31 900 lb/engine) Alt 3048 m (10 000 ft) Sweep 0 rad (0 deg) S_{REF} 277 m^2 (2980 ft^2)

BPR 2

Zero Lift Drag Buildup

Component	Friction				Profile		Miscellaneous $\Delta C_D \times 10^4$	
	Aw/S	ℓ m (ft)	C_F	$C_{D_F} \times 10^4$	Form factor	$\Delta C_D \times 10^4$		
Wing	1.964	4.5 (14.9)	0.00231	45.4	0.33	15.1	Roughness	4.2
Body Nacelles	3.63	87.8 (288)	0.00153	55.5	0.02	0.9	Body upsweep base aux inlet	0.8 1.8 2.0
Horizontal	0.14	3.0 (9.8)	0.00245	3.4	0.03	0.1		
Vertical	0.16	4.6 (15.0)	0.00230	3.7	0.03	0.1		
Total	108.0				16.2			8.8
$C_{D_{SYM}} = 133.0 \times 10^{-4}$								

Effect of Bypass Ratio

BPR	1	2	3
$\Delta C_{D_{SYM}} \times 10^4$	−6.6	0	5.5
$C_{D_{SYM}} \times 10^4$	126.4	133.0	136.5

Drag Polar

		C_L	0.3	0.4	0.5	0.6	0.7	0.8
		s	0.86	0.955	0.97	0.97	0.95	0.93
		$\Delta C_{D_{lift}}$	39.8	48.4	70.1	101.0	152.0	217.5
		$\Delta C_{D_{trim}}$	6.0	5.0	4.1	3.2	2.5	1.7
BPR	2	C_D	178.8	186.4	207.2	237.2	287.5	352.2
		L/D	16.8	21.5	24.1	25.3	24.3	22.7
	1	L/D	17.4	22.2	24.9	26.0	24.9	23.1
	3	L/D	16.3	20.8	23.5	24.7	23.9	22.4

Table 16 Oblique Wing Subsonic Drag Mach No. 0.8

SLST = 141 898 N (31 900 lb/engine) Alt 9144 m (30 000 ft) Sweep 0.61 rad (35 deg) S_{REF} 277 m^2 (2980 ft^2)

BPR 2

Zero Lift Drag Buildup

Component	Friction				Profile		Miscellaneous $\Delta C_D \times 10^4$	
	Aw/S	ℓ m (ft)	C_F	$C_{D_F} \times 10^4$	Form factor	$\Delta C_D \times 10^4$		
Wing	1.964	5.5 (18.2)	0.00222	43.6	0.183	8.0	Roughness	6.3
Body Nacelles	3.63	87.8 (288)	0.00152	55.2	0.017	0.9	Body upsweep Base Aux inlet	0.8 1.8 2.0
Horizontal	0.14	3.0 (9.8)	0.00244	3.4	0.03	0.1		
Vertical	0.16	4.6 (15.0)	0.00228	3.6	0.03	0.1		
Total	105.8				9.1			10.9
$C_{D_{SYM}} = 125.8 \times 10^{-4}$								

Effect of Bypass Ratio

BPR	1	2	3
$\Delta C_{D_{SYM}} \times 10^4$	-6.6	0	5.5
$C_{D_{SYM}} \times 10^4$	119.2	125.8	131.3

Drag Polar

		C_L	0.25	0.3	0.4	0.5	0.6	0.7
		s	0.76	0.855	0.905	0.902	0.885	0.85
		$\Delta C_{D_{lift}}$	46.6	52.9	81.2	127.9	194.5	287.7
		$\Delta C_{D_{trim}}$	0	0	0	0	0	0
BPR	2	C_D	172.4	178.7	207.0	253.7	320.3	413.5
		L/D	14.5	16.8	19.3	19.7	18.7	16.9
	1	L/D	15.1	17.4	20.0	20.2	19.1	17.2
	3	L/D	14.1	16.3	18.8	19.3	18.4	16.7

Table 17 Oblique Wing Subsonic Drag Mach No. 0.9

SLST 141 898 N (31 900 lb/engine) Alt 10 973 m (36 000 ft) Sweep 0.72 rad (41 deg) S_{REF} 277 m^2 (2980 ft^2)

BPR = 2

Zero Lift Drag Buildup

Component	Friction				Profile		Miscellaneous $\Delta C_D \times 10^4$	
	Aw/S	ℓ m (ft)	C_F	$C_{D_F} \times 10^4$	Form factor	$\Delta C_D \times 10^4$		
Wing	1.964	6.0 (19.7)	0.00220	43.2	0.143	6.2	Roughness	6.3
Body Nacelles	3.63	87.8 (288.0)	0.00152	55.2	0.017	0.9	Body upsweep Base Aux inlet	0.8 1.8 2.0
Horizontal	0.14	3.0 (9.8)	0.00244	3.4	0.03	0.1		
Vertical	0.16	4.6 (15.0)	0.00228	3.6	0.03	0.1		
Total	105.4				7.3			10.9
$C_{D_{SYM}} = 123.6 \times 10^{-4}$								

Effect of Bypass Ratio

BPR	1	2	3
$\Delta C_{D_{SYM}}$	−6.6	0	5.5
$C_{D_{SYM}}$	117.0	123.6	129.1

Drag Polar

		C_L	0.2	0.25	0.3	0.35	0.4	0.45
		s	0.8	0.89	0.90	0.895	0.88	0.86
		$\Delta C_{D_{lift}}$	30.7	38.0	53.2	73.5	100.2	133.9
		$\Delta C_{D_{trim}}$	0	0	0	0	0	0
BPR	2	C_D	154.3	161.6	176.8	197.1	223.8	257.5
	2	L/D	13.0	15.5	17.0	17.8	17.9	17.5
	1	L/D	13.5	16.1	17.6	18.4	18.4	17.9
	3	L/D	12.5	15.0	16.5	17.3	17.4	17.1

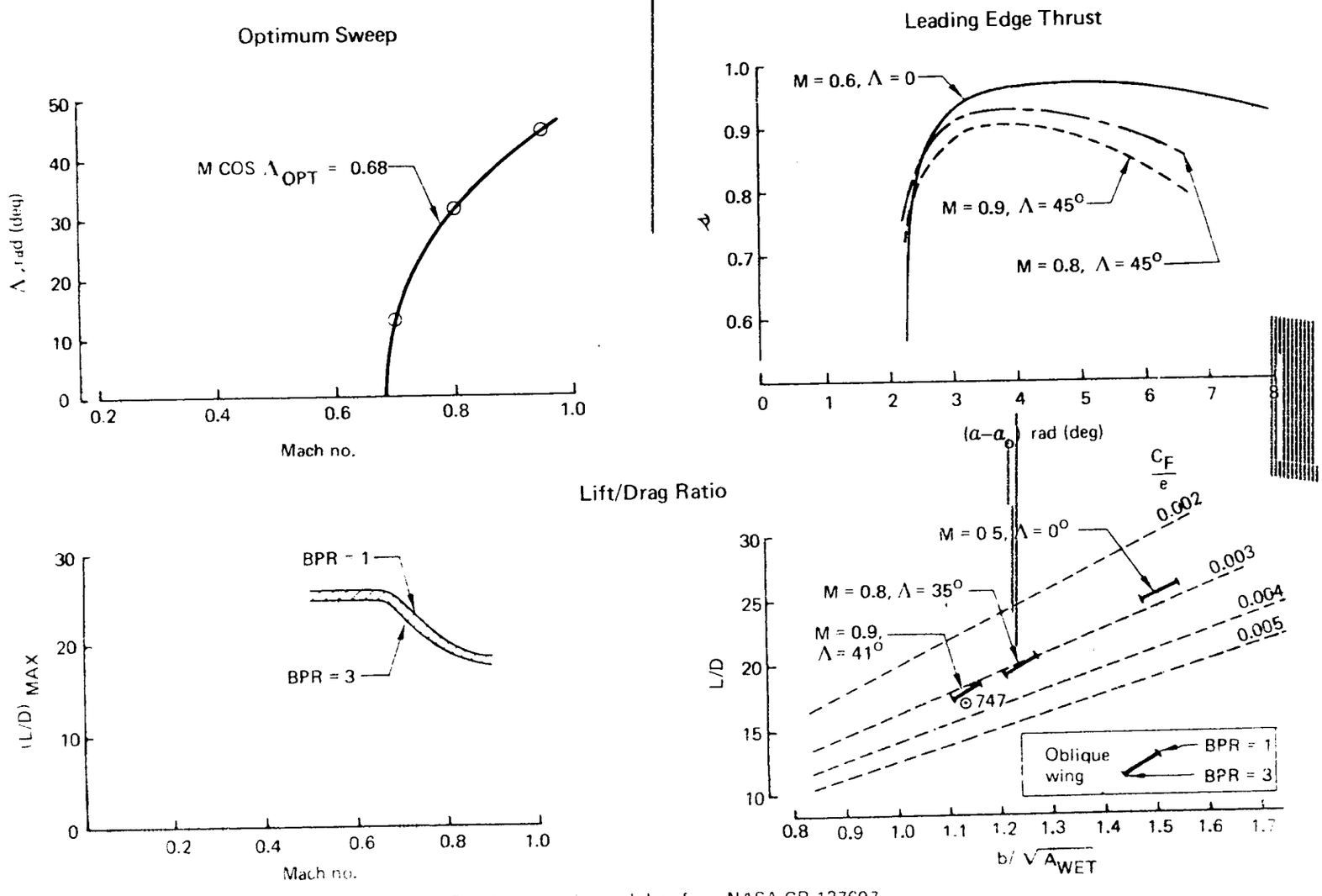

Based on experimental data from NASA CR 137697

Figure 62 Subsonic Drag

7.5 THRUST AND FUEL CONSUMPTION

Figure 63 shows typical off-design thrust and fuel consumption data for BPR = 2 engines, and also illustrates the effect of changes in bypass ratio. Engine characteristics are discussed more fully in Section 6.4.

7.6 CLIMB SPEED SCHEDULE AND FUEL

The climb speed schedule was chosen to meet the following criteria:

- Minimum block fuel
- Maintain 152 m/min (500 ft/min) rate of climb at end of climb altitude
- Maintain velocities below structural design speed placard
- Maintain familiar operational techniques

An automatic Mach number/wing sweep positioning system was assumed to maintain near maximum lift/drag ratio during climb, following the sweep schedule given in Section 7.3.

Several combinations of constant calibrated airspeeds and climb Mach numbers were compared to determine the best climb schedule. The schedule chosen is shown in Figure 64.

The rate of climb capability and operational lift/drag ratio of the baseline airplane with BPR = 2 engines is shown in Figure 65.

Climb performance was evaluated for calibrated airspeeds between 200 and 400 KCAS and altitudes from sea level to 12 172 m (40 000 ft). It was found that 350 KCAS was near maximum rate of climb for all altitudes when climbing at constant calibrated airspeed. Two constant Mach number climb segments are used above 8992 m (29 500 ft), to:

(a) Maintain optimum rate of climb (R/C) capability

(b) Maintain flyable instrument reference speeds to ease pilot workload

(c) Keep overall block fuel at a minimum while maintaining good end-of-climb performance; i.e., R/C and time to accelerate to cruise Mach

A summary of the climb distance, time, and fuel burned follows:

BPR	Time (hours)	Distance km (nmi)	Fuel (% TOGW)
1	0.396	357 (193)	3.98
2	0.380	343 (185)	3.59
3	0.328	294 (159)	2.99

Note • Installed thrust and SFC data have been corrected for inlet, duct and nozzle losses, bleed, power extraction, mixing, spillage and acoustic lining

• Thrust data apply to reference engine having 177 929 N (40 000 lb) uninstalled SLST

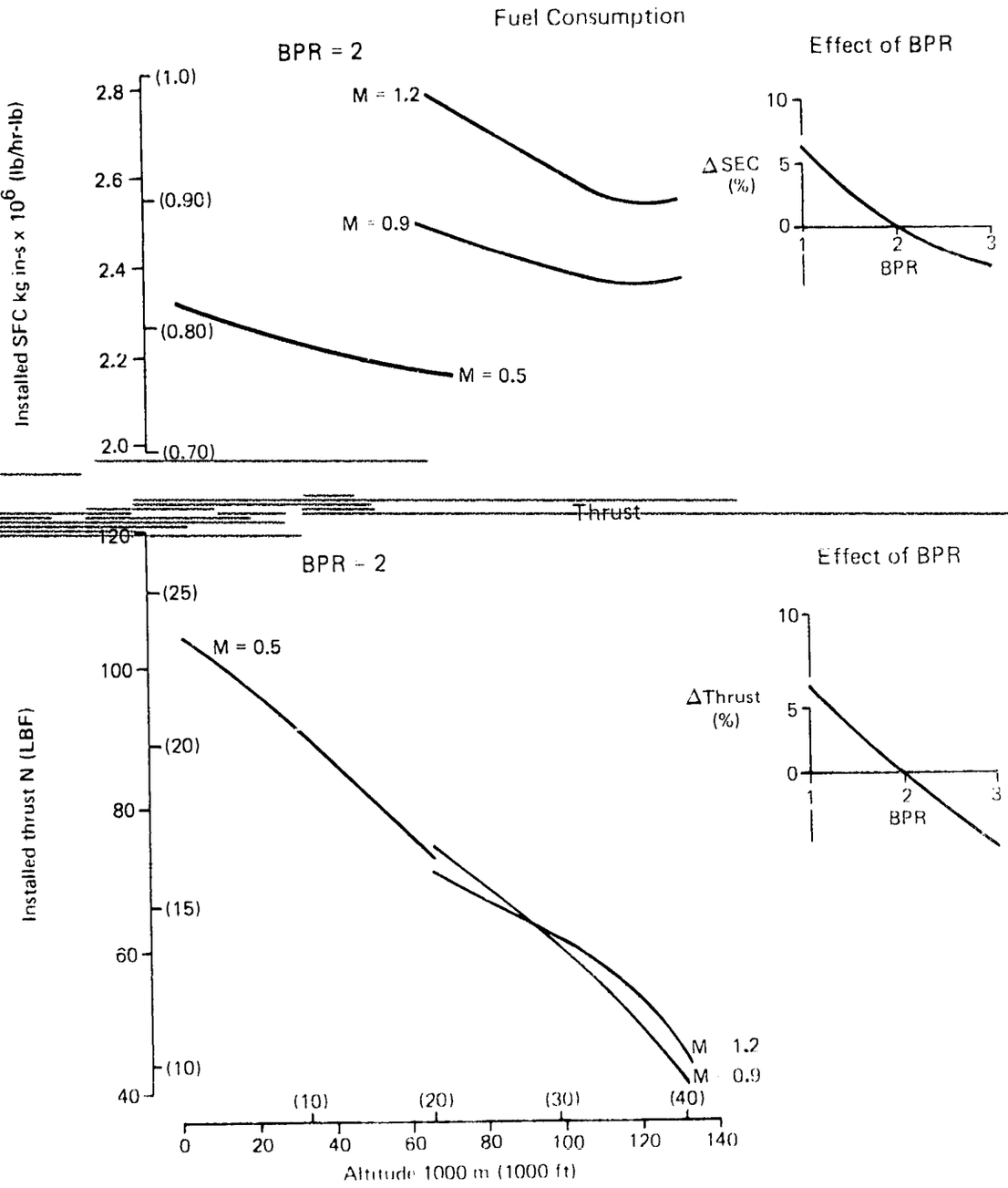

Figure 63 Off-Design Powerplant Characteristics

- Best schedule chosen from several combinations of constant calibrated airspeed and climb Mach numbers

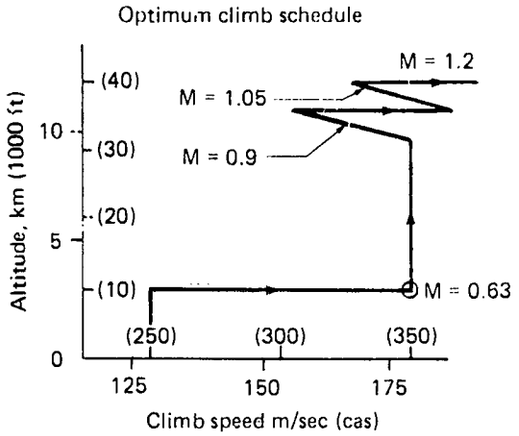

457 m (1500 ft)–3048 m (10 000 ft)		at 129 m/sec (250 kcas)
3048 m (10 000 ft)	accelerate to	180 m/sec (350 kcas)
3048 m (10 000 ft)–8992 m (29 500 ft)		at 180 m/sec (350 kcas)
8992 m (29 500 ft)–11 000 m (36 089 ft)		at Mach 0.90
11 000 (36 089 ft)	accelerate to	Mach 1.05
11 000 m (36 089 ft)–12 192 m (40 000 ft)		at Mach 1.05
12 192 m (40 000 ft)	accelerate to	Mach 1.20

Figure 64 Climb Speed Schedule

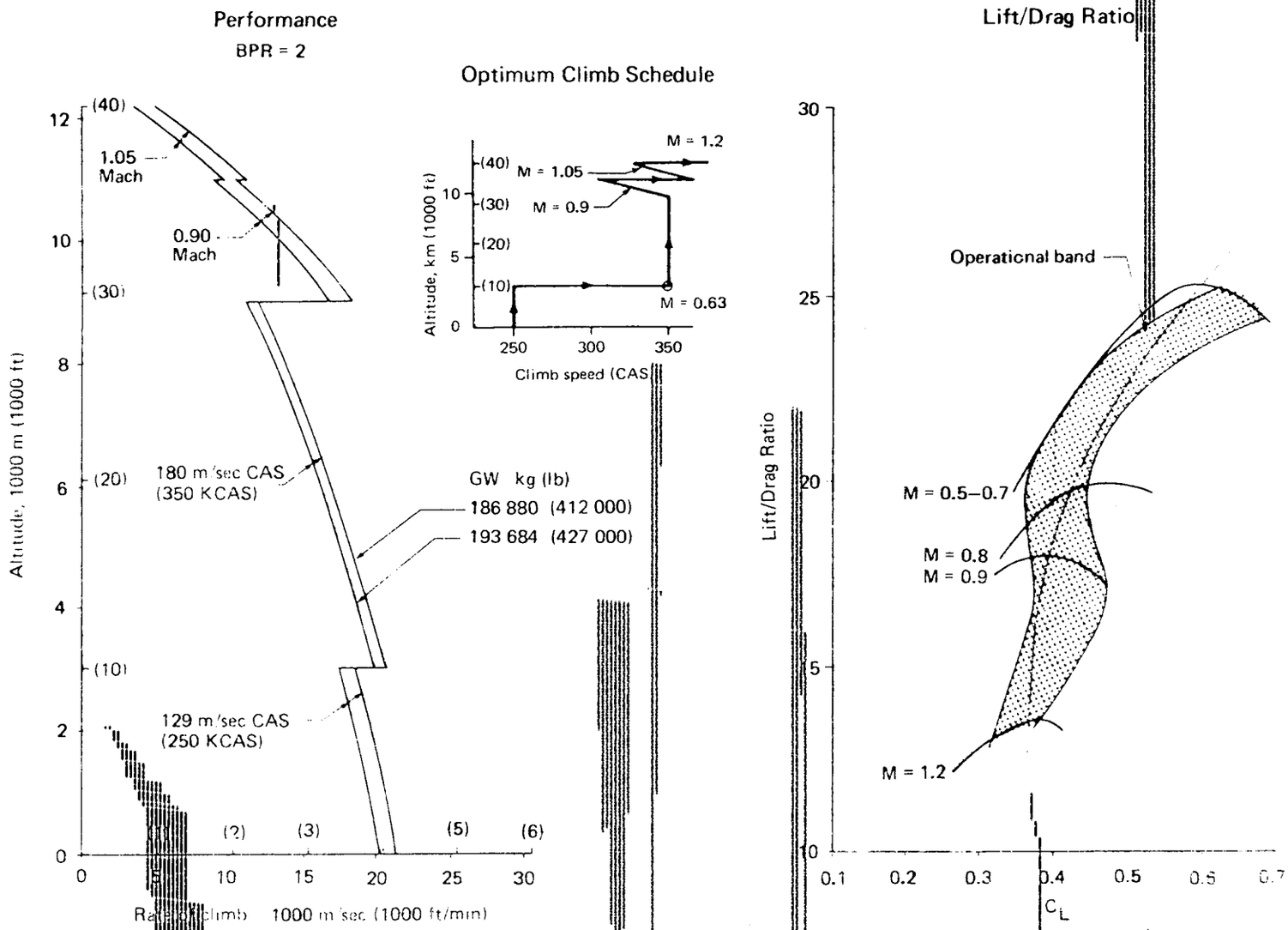

Figure 65 Climb Performance BPR = 2

7.7 RESERVES

The reserve fuel was calculated using the following rules:

- One-hour extended cruise at M 0.9
- Missed approach (2 minutes at maximum takeoff power)
- Climb, cruise, and descent to 370 km (200 nmi) alternate

The 1-hour extended cruise and cruise-to-alternate was calculated at the specific range at best-cruise altitude. Exchanging 45 minutes at end-of-cruise altitude and cruise Mach (FAR 25) in place of the 1-hour extended cruise at Mach 0.9 and best-cruise altitude resulted in only a slight increase in reserve fuel requirements. It should be noted that under FAR reserve rules the 370 km (200 nmi) alternate could be considerably shorter in distance should one exist for a given flight. Speeds below Mach 0.8 were thought to be incompatible with other air traffic and above Mach 0.9 specific range begins to deteriorate. The fuel mileage is nearly constant at Mach number between 0.8 and 0.9.

The 1967 ATA Domestic Reserve Rules were chosen for being comparable to present FAR rules and because no new transonic reserve rules have been formulated.

A summary of the resulting reserve fuel requirements follows.

BPR	Reserve fuel % TOGW
1	6.5
2	6.3
3	6.3

7.8 DESCENT FUEL

Descent is conducted with the engines at part power and idle thrust. Since the idle fuel consumption of the study engines is not well established, the fuel burned during descent was estimated to be 0.4 percent of TOGW, based on SST experience. This is the same quantity used during early oblique-wing studies described in Reference 1.

8.0 FINAL CONFIGURATION

8.1 SUMMARY

The final configuration incorporates the knowledge gained during early oblique-wing studies (References 1 and 2), and those described in Sections 4, 5, 6, and 7 of this report.

The configuration with BPR = 2 engines, developed during the engine cycle study, was selected as the starting point for the final configuration, as described in Section 6.10. The aerodynamic characteristics, weight, balance, and flight control requirements were reviewed and refined, leading to the final configuration, designated Model 5-7, shown in Figure 66. The performance and noise of the Model 5-7 were evaluated and are summarized in Table 18.

8.2 CONFIGURATION DESCRIPTION

The final configuration, designated Model 5-7, is shown in Figure 66. Its characteristics are summarized on Table 19. It is based on the Model 5-3 of Reference 1, having a high wing and four BPR = 2 engines integrated into the aft body. It is nearly identical to the baseline BPR = 2 airplane of Section 6.6.1.

The wing has an area of 282.5 m^2 (3040 ft^2), an aspect ratio of 13.47, with planform as in Section 4. It has leading edge variable camber flaps, and double-slotted trailing edge flaps (Figure 67); roll control is by tip ailerons, augmented by spoilers.

The pivot has a diameter of 2.67 m (105 in.) and is located at 30 percent of the root chord.

The turbofan powerplants (BPR = 2) are fed by pitot inlets alongside the aft fuselage. The intake ducts curve around behind the aft cabin bulkhead and between the landing gear bays, and were laid out as described in Section 6.6-1. The empennage consists of a fixed swept fin with a conventional rudder, and an all-moving horizontal tail with a geared elevator. The tail is supported from the engine mount structure.

The landing gear is of the bicycle type; i.e., the airplane does not rotate about the aft gear at takeoff. Instead, the static ground attitude is chosen for liftoff. The rear gear consists of two side-by-side twelve-wheeled trucks that retract into bays behind the powerplant inlets. The front gears consist of two tandem single-axle four-wheeled trucks that retract into bays underneath the cabin floor. Approximately 70 percent of the gross weight is supported by the rear gear, and 30 percent by the front. Details of the gear design are given in Reference 1.

The passenger cabin holds 190 passengers [28 first class at 102 cm (40 in.), and 162 tourist at 86 cm (34 in.) pitch] with single aisle, four-, five-, and six-abreast seating. The cabin ends immediately behind the engine intakes with a hemispherical bulkhead.

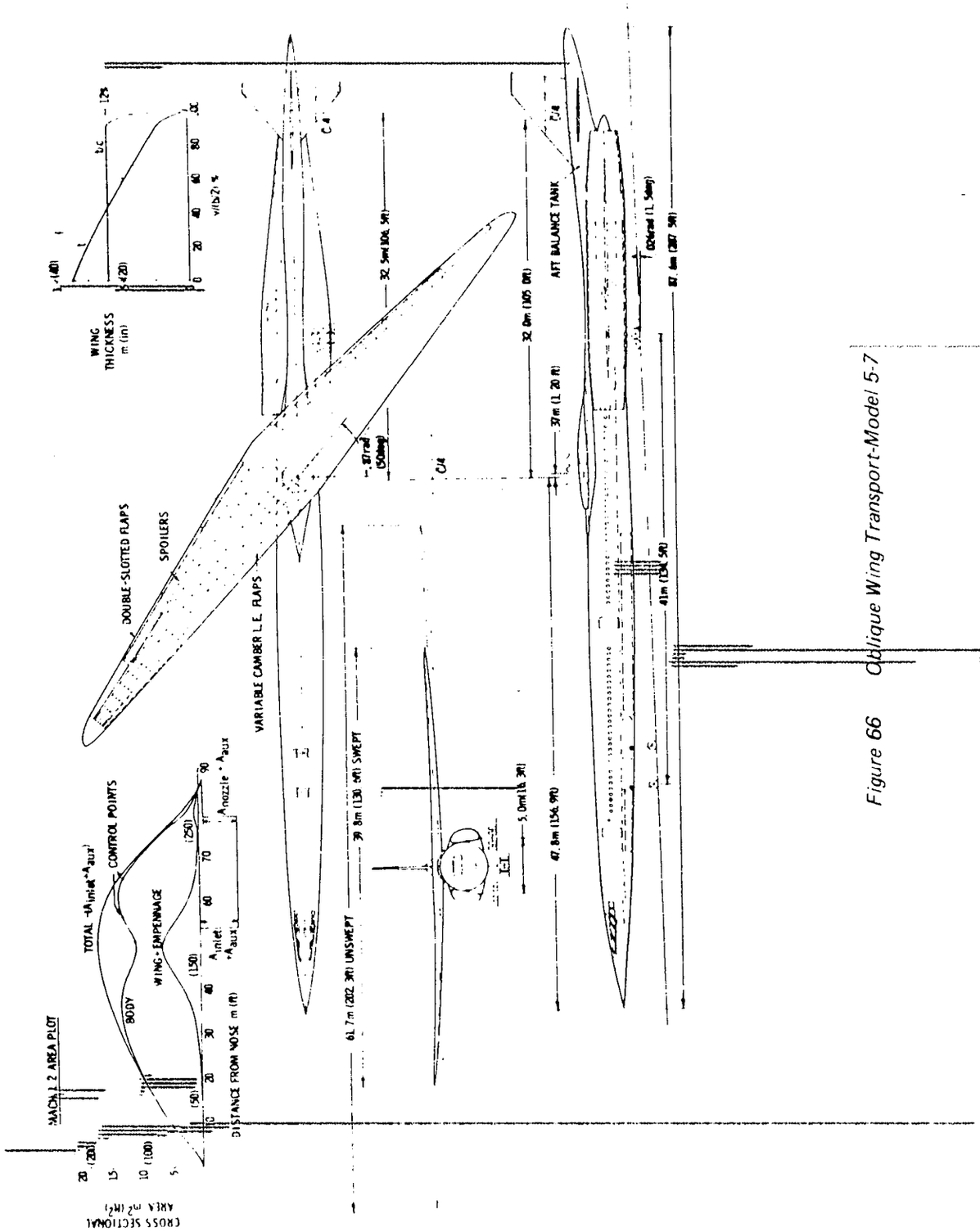

Figure 66 Oblique Wing Transport-Model 5-7

Table 18 Model 5-7 Performance and Noise

- Cruise Mach no. 1.2
- Payload 18 144 kg (40 000 lb)
- BPR = 2
- Range 5556 km (3000 nmi)
- Peripheral noise treatment*

TOGW	kg (lb)	194 550	(428 910)
OEW	kg (lb)	112 523	(248 070)
S	m^2 (ft^2)	282	(3 040)
SLST	kg (lb)	15 966	(35 200)
Block fuel	kg (lb)	52 526	(115 800)
Reserves	kg (lb)	12 247	(27 000)
No. of engines/BPR		4/2	
Thrust loading (T/W)		0.328	
Wing loading (W/S)	N/m^2 (lb/ft^2)	675	(141)
ICAC	m (ft)	12 344	(40 500)
Cruise alt	m (ft)	12 954	(42 500)
RF	km (NAM)	18 705	(10 100)
$SFC_{(cruise)}$	kg/N-S x 10^{-5} (lb/hr/lb)	2.5776	(0.910)
L/D (cruise)		13.47	
L/D (max)		13.7	
C_L at L/D max		0.43	
C_L at (cruise)		0.34	
TOFL: 305 m (1000 ft) 305K (90°F)			
Max flaps	m (ft)	2 265	(7 430)
Reduced flaps	m (ft)	2 917	(9 570)
C_L (max flaps)		1.85	
C_L (reduced flaps)		1.45	
L/D community noise reduced flaps (V_{app} + 5.1 m/s (10 kts))		9.3	
Approach speed:			
Max flaps m/s EAS (KEAS)		63.6	(123.6)
With LE C_L (max flaps) at 1.3 Vs		2.00	
Reduced flaps (m/s EAS (KEAS))		72.0	(140)
With LE C_L (reduced flaps)		1.56	
Community noise: EPNdB*			
From FAR part 36			
Takeoff with thrust cutback at noise station		** 15.0	
Sideline 6.48.2 m (0.35 nmi)		6.3	
Approach		6.1	
Traded		7.7	

*1976 research technology qualified for 1985 design freeze

**Oblique wing allows thrust cutback below 50 percent takeoff power

Table 19 Model 5-7 Characteristics

	Model 5-7
TOGW kg (lb)	194 550 (428 910)
Payload kg (lb)	18 144 (40 000)
OEW kg (lb)	112 850 (248 070)
Fuel capacity	
Wing	59 600 (131 400)
Body	6 800 (15 000)
Wing area m^2 (ft^2)	282.6 (3040)
Span m (ft)	61.7 (202.3)
MAC m (ft)	5.29 (17.37)
Aspect ratio	13.47
Taper ratio	0.25
Quarter chord sweep rad (deg)	0.87 (50)
t/c (root/tip) %	12
Pivot location from nose m (ft)	48.2 (158.1)
C/4 location from nose m (ft)	47.8 (156.9)
Horizontal tail V_H	0.44
Arm m (ft)	32.5 (106.5)
Area (exposed) m^2 (ft^2)	20.2 (218)
Span m (ft)	8.8 (28.7)
MAC m (ft)	3.21 (10.53)
Aspect ratio	2.6
Taper ratio	0.20
LE sweep rad (deg)	0.87 (50)
t/c %	4.0
Vertical tail V_V	0.043
Arm m (ft)	0 (105.0)
Area m^2 (ft^2)	23.4 (252)
Span m (ft)	5.1 (16.7)
MAC m (ft)	5.14 (16.85)
Aspect ratio	1.11
Taper ratio	0.254
LE sweep rad (deg)	0.87 (50)
t/c %	3.5
Body payload	190 passengers (28 1st/162 tourist) 29.7 m^3 (1050 ft^3) cargo
Length m (ft)	87.6 (287 ft)
Cabin length m (ft)	44.0 (144.5)
Diameter max/min m (in.)	4.11 (162)/3.55 (140)
Powerplants	4 x ATSA 1.20 2-3000-16/2
Bypass ratio	2
Thrust N (lbf)	156 600 (35 200)
Diameter m (ft)	1.49 (4.87)
Length m (ft)	3.00 (9.85)
Length, inlet to nozzle m (ft)	17.5 (57.3)
Landing gear	
Tires m (in.)	0.87 x 0.28 (34 x 11)
Aft trucks	2 x 12 tire–3 axle
Size m (in.)	1.88 x 1.23 (71 x 54)
Tread m (ft)	5.0 (16.3)
Fwd trucks	2 x 4 tire–1 axle
Size	1.27 (50)
Wheel base m (ft)	41.0 (134.5)
Ground attitude rad (deg) nose up	0.026 (1.5)

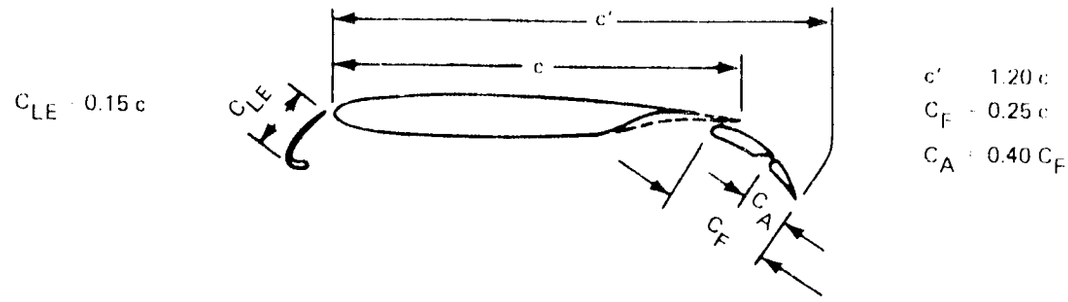

Leading edge flap

- Variable camber Kruger flap
- δ_{LE}, rad (deg) 0.87 (50)

Trailing edge flap

- Double-slotted Fowler flap
- Span, Y/2b = 0.057 to 0.733
- Max $\delta_{F_{TE}}$, rad (deg) 0.78 (45)

Figure 67 Model 5--7 Flap System

8.3 CONFIGURATION DEVELOPMENT

8.3.1 AIRPLANE SIZING

The airplane TOGW, wing area, and powerplant size were selected as described in Section 6.10.

8.3.2 BODY OPTIMIZATION

The cross-sectional area distribution of the Model 5-7 fuselage was optimized using the procedure explained in Section 6.6.2. In this case, the control point on the nozzle boattail was not used, as its minimum area requirement was satisfied by the body resulting from the other six control points.

The area plot for the Model 5-7 is shown in the configuration drawing, Figure 66.

8.3.3 PIVOT DESIGN AND LOCATION

The pivot bearing and support structure is similar to that shown in Figure 30, scaled to the smaller wing area of the Model 5- 7.

The pivot is located at 30 percent wing root chord. The reasons for this choice of location are stated in Section 5.4.

8.3.4 EMPENNAGE AND CONTROL SURFACE SIZING

This study is summarized in Figure 68. The horizontal and vertical tail sizing and roll control capability of the Model 5-7 were reviewed. The horizontal and vertical tail volume coefficients (V) established during earlier studies (References 1 and 2) were found to be adequate and were retained. It was necessary to add spoilers to provide satisfactory roll control.

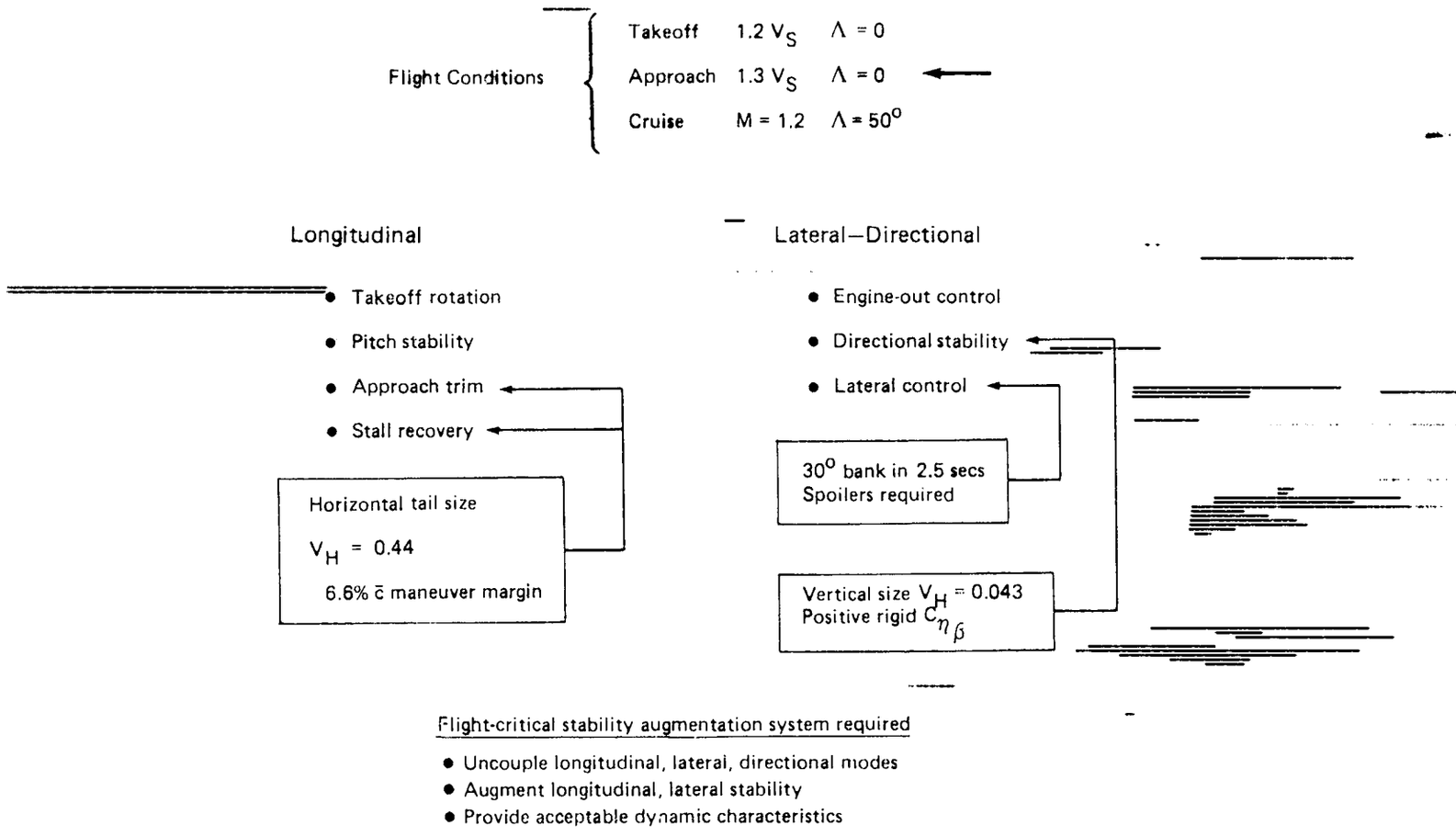

Figure 68 Control Surface Sizing

Horizontal Tail

The horizontal tail size was chosen considering the items listed below:

- Takeoff Rotation: Because of geometry limitations, it was not possible to rotate the airplane for takeoff. Instead the airplane will fly-off at taxi attitude similar to a B-52. This method of takeoff only requires the horizontal tail to trim this attitude in ground effect and is not demanding on the horizontal tail size.

- Approach Trim: The horizontal tail for this study is defined as a controlled stabilizer with a geared elevator, similar to the B-2707-300 SST. A maximum C_{L_H} 1.4 was assumed for forward cg trim calculations, which allows adequate elevator authority for maneuver

- Static Pitch Stability: Based on B-2707-300 SST simulator experience, a negative 6.6 percent MAC (A 0) maneuver margin sets the aft cg limit. This inherently unstable condition requires a flight-critical stability augmentation system (SAS). The above longitudinal static stability criteria was used in previous yawed-wing studies (References 1, and 2). A coupled roll-pitch trim system is required when the wing is yawed to take care of mistrim values introduced by wing flexibility.

- Transient Dynamics: With the wing yawed, coupled transients exist between all three axes. These transients can be induced by either pilot inputs or turbulence; i.e., a pitch input disturbs roll and yaw. A full-time stability augmentation system will be required to suppress the oscillations to an acceptable level. The augmentation system shall have the dual function of uncoupling the longitudinal, lateral, and directional mode and providing acceptable dynamic characteristics (frequency, damping, control responses). More investigations are needed into the question of uncoupling symmetric and asymmetric modes. Response calculations, carried out for an F-8 fitted with an oblique wing, showed that in this case, uncoupling would undoubtedly be needed. On the other hand, pilots have flown radio control models without augmentation. The need clearly depends on the dynamic and aerodynamic characteristics of the particular configuration. The oblique wing transport has not been studied in depth, but current opinion is that decoupling of longitudinal, lateral, and directional modes will probably be necessary.

- Stall Recovery: Recent SST studies have shown an aft cg nose-down, pitch-control requirement of $\ddot{\theta}$ -0.08 rad sec^2 evaluated at $V_{MIN.\ DEM}$. This criteria was applied at the approach stall speed in this study.

The horizontal tail sizing chart for the Model 5-7 is shown in Figure 69. The required loading range of 25 percent MAC was established as described in Section 8.4.2. The required tail volume coefficient was determined to be V 0.44. Note the aft limit is set by nose down pitch-control requirements rather than by stability limitations.

Vertical Tail

The following items were considered in determination of the vertical tail size:

- Engine-Out Control: The engine-out control is not a problem owing to the engines location near the body centerline. The vertical tail was sized by stability considerations.

- Lateral Directional Stability: Unaugmented static directional stability is assumed positive (C_{n_β} 0) throughout the flight envelope, with a flight critical lateral-directional SAS providing satisfactory stability and handling qualities.

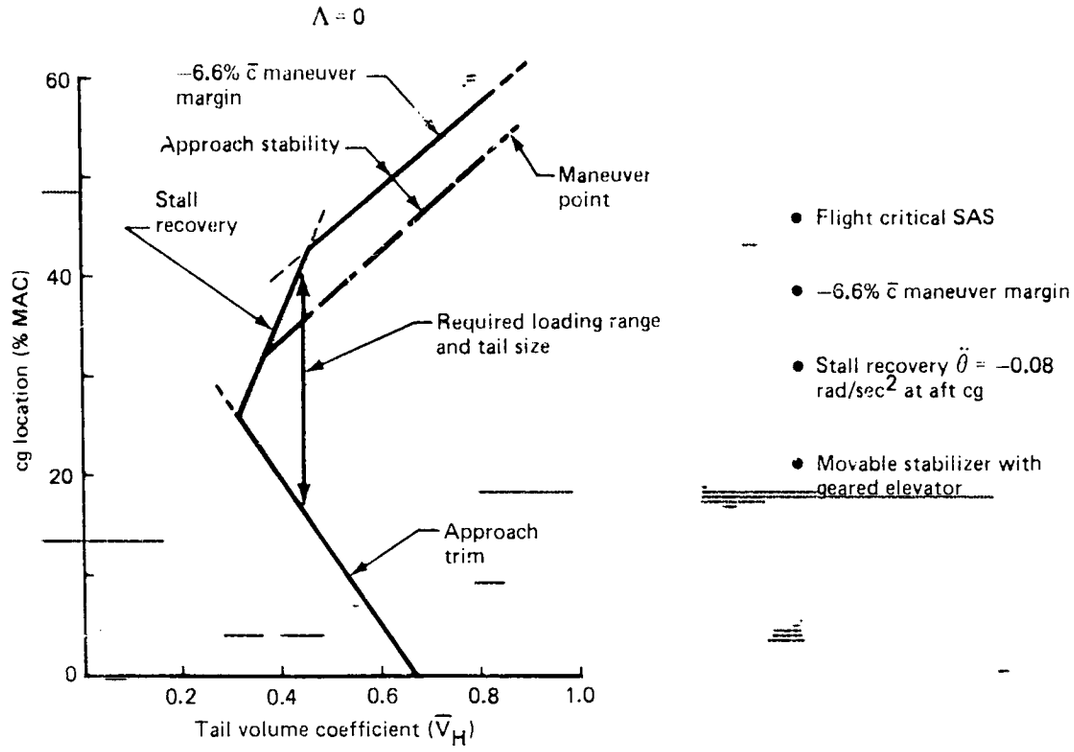

Figure 69 Horizontal Tail Sizing

Lateral Control

Using a single-degree-of-freedom roll analysis, the rolling moment coefficient required to achieve a 30° bank in 2.0 seconds at M = 1.2 cruise (Λ = 50°) was found to be C_ℓ = 0.024. At approach (Λ = 0), the required roll capability is 30° of bank in 2.5 seconds and the required rolling moment coefficient is C_ℓ = 0.110. The roll mode time constant, τ, was held below 1.4 seconds for both flight conditions.

For both the cruise and approach conditions, it was determined that ailerons provided only 25 percent of the required roll control.

Spoilers ahead of the flaps were, therefore, added to obtain satisfactory roll control at approach. Conventional spoilers have been shown to be ineffective as roll control devices for yawed wings. Other means, such as antisymmetric deflection of the trailing edge flaps, will therefore be required for high-speed roll authenticity. The spoilers will also be necessary as conventional dive brakes used for flight path control.

8.4 CONFIGURATION CHARACTERISTICS

8.4.1 LOW-SPEED AERODYNAMIC CHARACTERISTICS

The low-speed aerodynamic characteristics of the Model 5-7 are presented in Figures 70 and 71

The principal difference between this data and the results presented in Section 4 is that lift at zero incidence has been increased by 0.3. This value is based on experimental data described in Section 10, and is typical of the cambered airfoil sections likely to be used for an oblique wing. This camber lift was not included in earlier estimates.

Leading and trailing edge flaps are employed as shown in Figure 67. The leading edge flap is a 92 percent semispan tapered variable camber Krueger flap with a constant flap wing chord ratio of 0.15. The trailing edge flap is a main-aft double-slotted Fowler arrangement. Total flap/wing chord ratio is 0.25 and the aft to total flap chord ratio is 0.40. The flap extends from the side of the body outboard to 73 percent of the wing semispan, and the Fowler motion is constant for all deflection angles.

The nonrotating takeoff and landing procedures are unorthodox for transport category airplanes, but should present no operational problems because the concept has been proven on the B-47 and B-52. The leading edge flap is used only for approach and landing where the improved stall speed margins are beneficial.

Retracting the leading edge flap for takeoff and climb provides a substantial improvement in low-speed climb performance (particularly at low flap angles), and due to the nonrotating takeoff procedures used, the operating liftoff speeds are higher than the current $1.2V_S$ requirements of FAR 25 for most flap settings.

Maximum takeoff flaps, with leading flaps retracted, are restricted to 0.52 rad (30°) by the $1.2V_S$ requirements of FAR 25 (Figure 70). If takeoff field length or liftoff speed became critical, climb performance (community noise) could be traded for improved takeoff performance by deflecting the leading edge flaps.

For takeoff, the ground roll attitude is, in effect, the geometry limit, and, therefore, normal takeoffs would be performed at essentially minimum unstick speed. As shown in Figure 70, these liftoff speeds provide adequate margins, and requiring the airplane to lift off at speeds higher than minimum unstick would unnecessarily penalize takeoff performance.

Landing approach angle of attack was 0.026 rad (1.5°) for trailing edge flap deflections up to 0.61 rad (35°). For larger approach flap settings, approach attitude and lift coefficient are limited by $1.3V_S$ requirements. The landing flare maneuver for a two-point touchdown would require only a small attitude change for these approach conditions. Figure 70 shows the attitude and lift coefficient for the Model 5-7 landing configuration with the leading edge flap deflected. With the leading edge flap retracted, the approach speed for maximum flap deflection (0.79 rad (45°)) would be about 6.7 m sec (13 KT sec) faster (Figure 71)

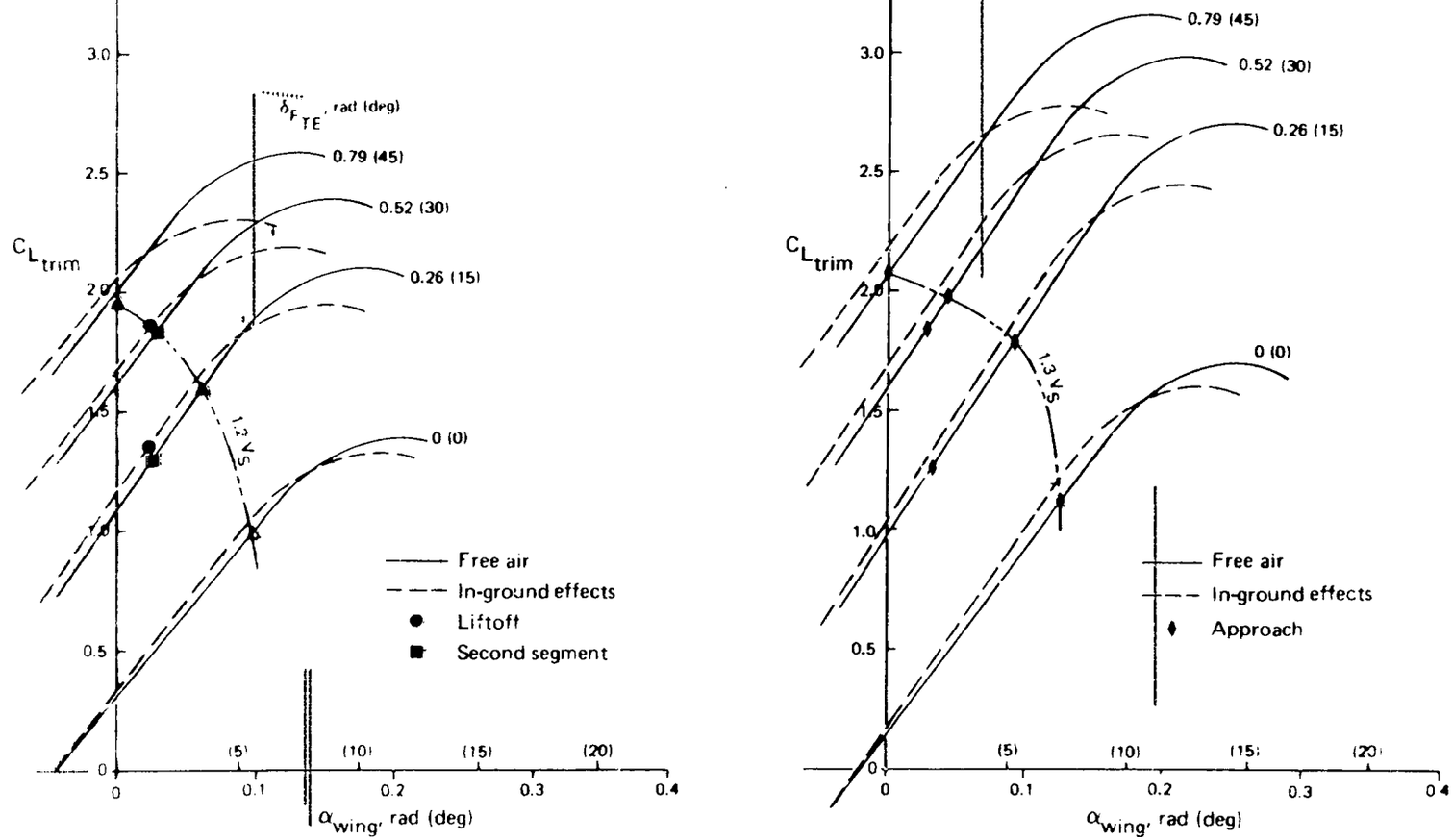

Figure 70 Model 5-7 Low-Speed Lift Characteristics

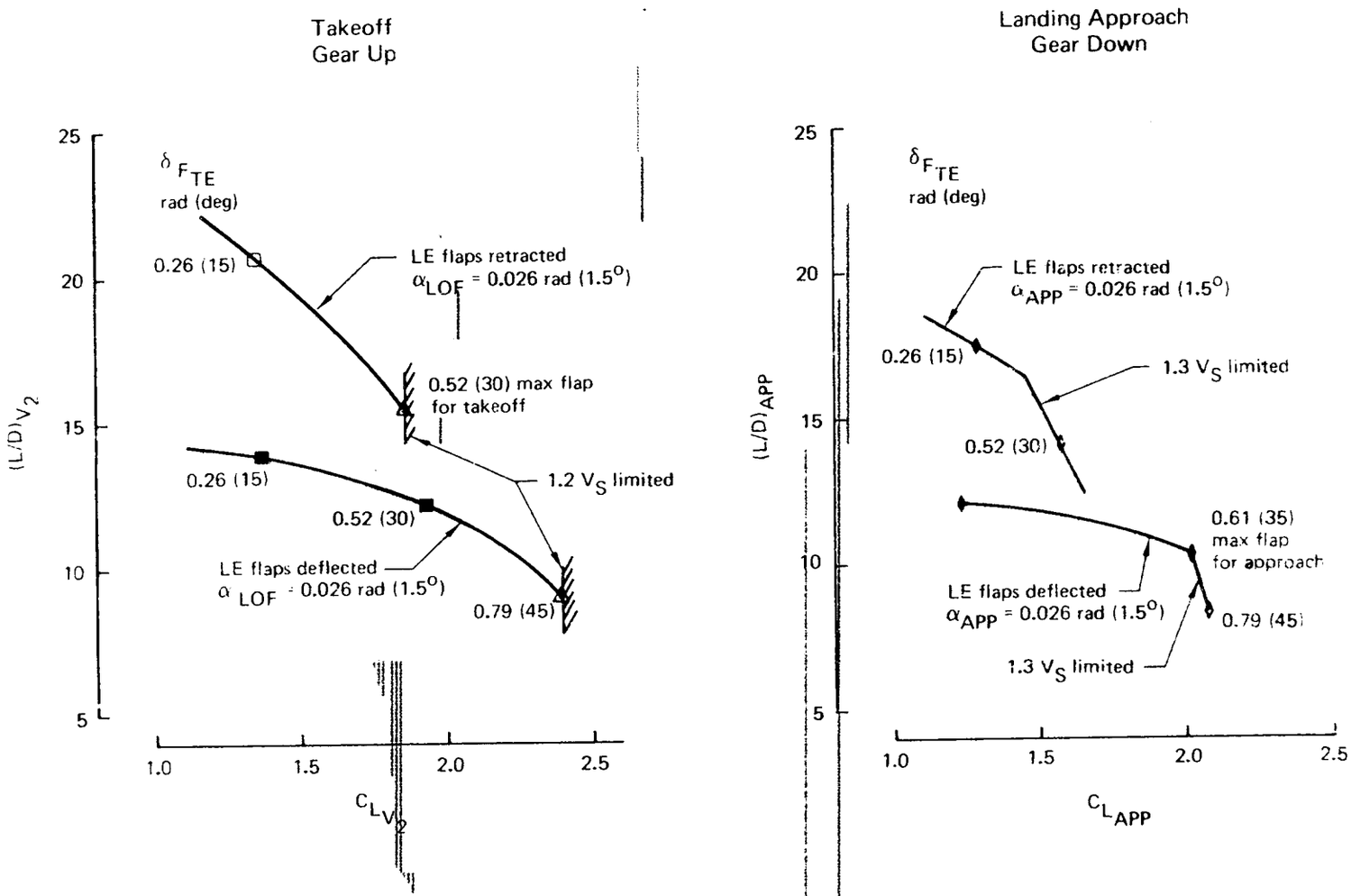

Figure 71 Takeoff and Landing Lift/Drag Ratios

The low-speed lift/drag characteristics of the Model 5-7 are presented in Figure 71. The performance calculations were based on a liftoff and landing angle of attack of 0.026 rad (1.5°), equal to the wing-incidence angle. The second segment operating point was assumed to be at the same lift coefficient as liftoff.

Although a nonrotating configuration could be certified under current Federal Aviation Regulations, a reexamination of FAR 25 is recommended, particularly with regard to the section on rotation speed, liftoff speed, and minimum unstick speed.

8.4.2 HIGH-SPEED AERODYNAMIC CHARACTERISTICS

Figure 72 shows the variation of lift/drag ratio of the Model 5-7 with Mach number, while the drag polar at supersonic cruise is given in Figure 73. Subsonic drag has been predicted using experimental data, as described in Sections 7 and 10. Supersonic cruise drag has been estimated using theoretical methods, as described below. Experimental data has not been used at supersonic speeds because results available for a wind tunnel model that resembled the Model 5-7 do not reflect the potential aerodynamic efficiency of the configuration (Section 10).

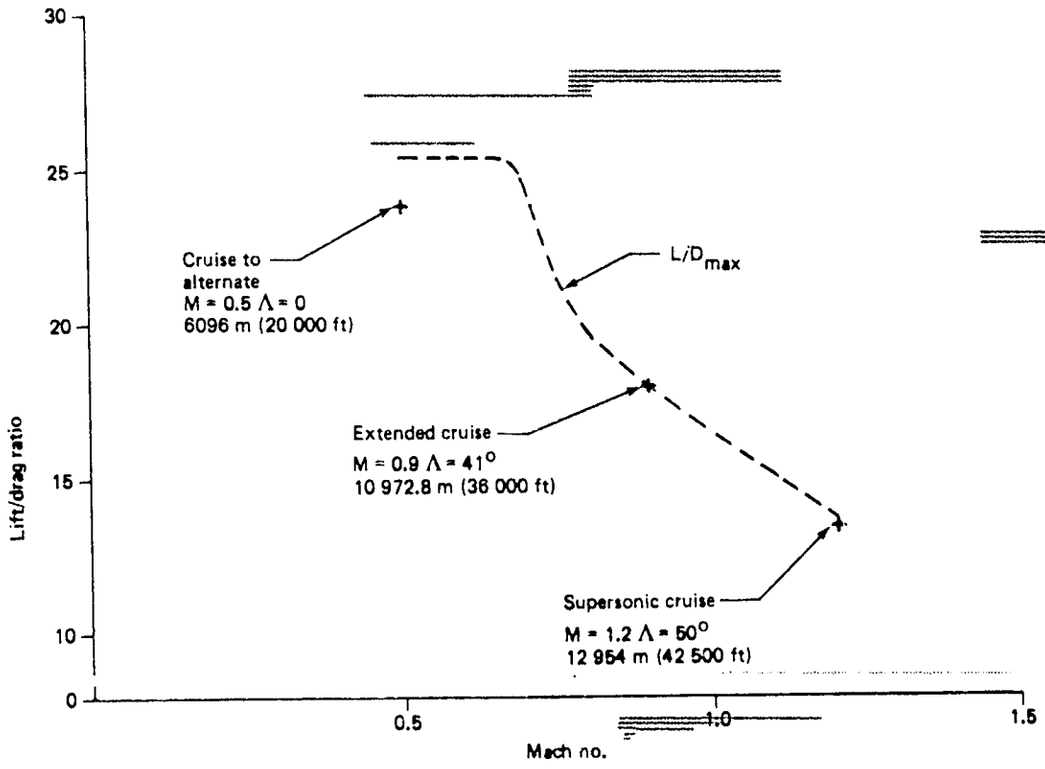

Figure 72 Lift/Drag Ratio Model 5-7

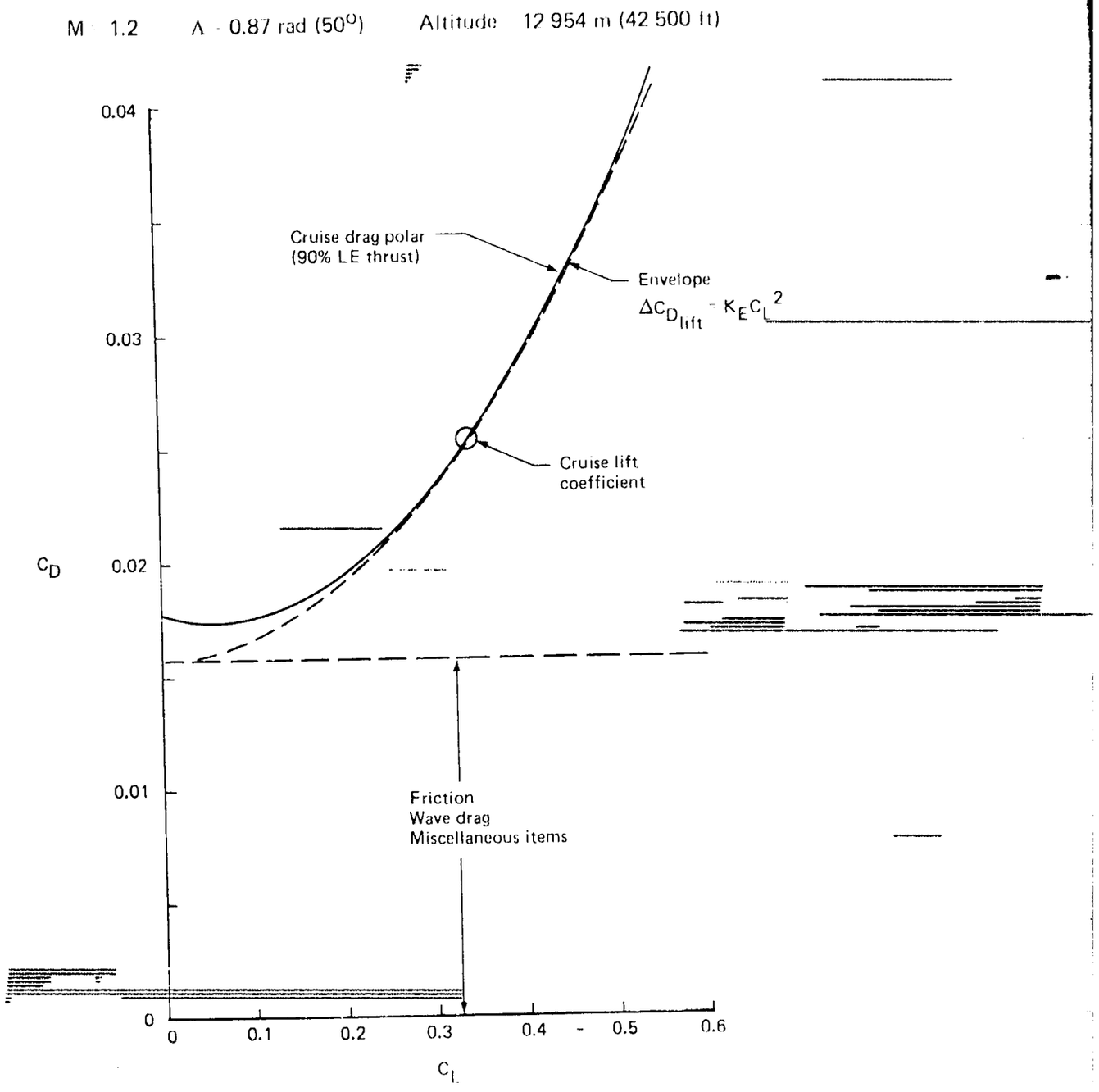

Figure 73 Cruise Drag Polar Model 5-7

The cruise drag polar of the Model 5-7 (Figure 73) is given by

$$C_D = C_{D_{SYM}} + \left[A + BC_L + KC_L^2\right]$$

$C_{D_{SYM}}$: Friction, wave drag miscellaneous items

$BC_L + KC_L^2$: Drag due to lift

where A, B, and K are constants. $C_{D_{SYM}}$ was built up as described in Section 6.7.

Drag due to lift is represented as a parabola that is tangential to the envelope at cruise lift coefficient. This condition determines the constants A and B.

The envelope-drag-due-to-lift factor (K_E) is consistent with values used in the planform study (Section 4). Figure 74 compares K_E with the theoretical minimum value for slender wings (Reference 9) and optimally loaded elliptical wings (Reference 6). Figure 74 also shows a numerical solution for the Model 5-7 wing planform obtained by the influence coefficient method described in Reference 10. The envelope values used during this study are 20 percent greater than the elliptical wing value and 15 percent greater than the numerical solution.

The polar-drag-due-to-lift factor is given by

$$K = \frac{1}{C_{L_\alpha}} - 0.9\,\frac{C_T}{C_L^2}$$

where C_{L_α} is the lift curve slope and C_T/C_L^2 the theoretical flat plate leading edge thrust force, which were derived from results of an aerodynamic influence coefficient analysis. The leading edge thrust force was calculated using a technique developed by R. M. Kulfan that is described in Reference 11. It was assumed that 90 percent of the theoretical leading edge thrust force could be attained. This assumption is supported by data presented in Section 10 and Reference 18.

No cruise trim drag penalty has been imposed. This is justified because wing drag due to lift is insensitive to center of pressure location (Reference 1, p. 88) and the aft balance tank permits flight at a wide range of cg locations. Thus, it should be possible to trim with a small up load on the horizontal tail, leading to negative trim drag.

8.4.3 WEIGHT AND BALANCE

A detailed weight statement for the Model 5-7 is given in Table 20. Figure 75 confirms the results of a balance analysis showing the airplane has acceptable loadability within the specified center of gravity range dictated by stability and control considerations. As emphasized in Section 6.6.3, a forward water ballast would be required for partial payloads and ferry missions. The concept would be similar to that used on the national SST program (B-2707-300) and that discussed for the Model 5-3 (Reference 1, P. 189). The airplane also contains an after body fuel tank for selective fuel management providing the capability to minimize cruise trim drag.

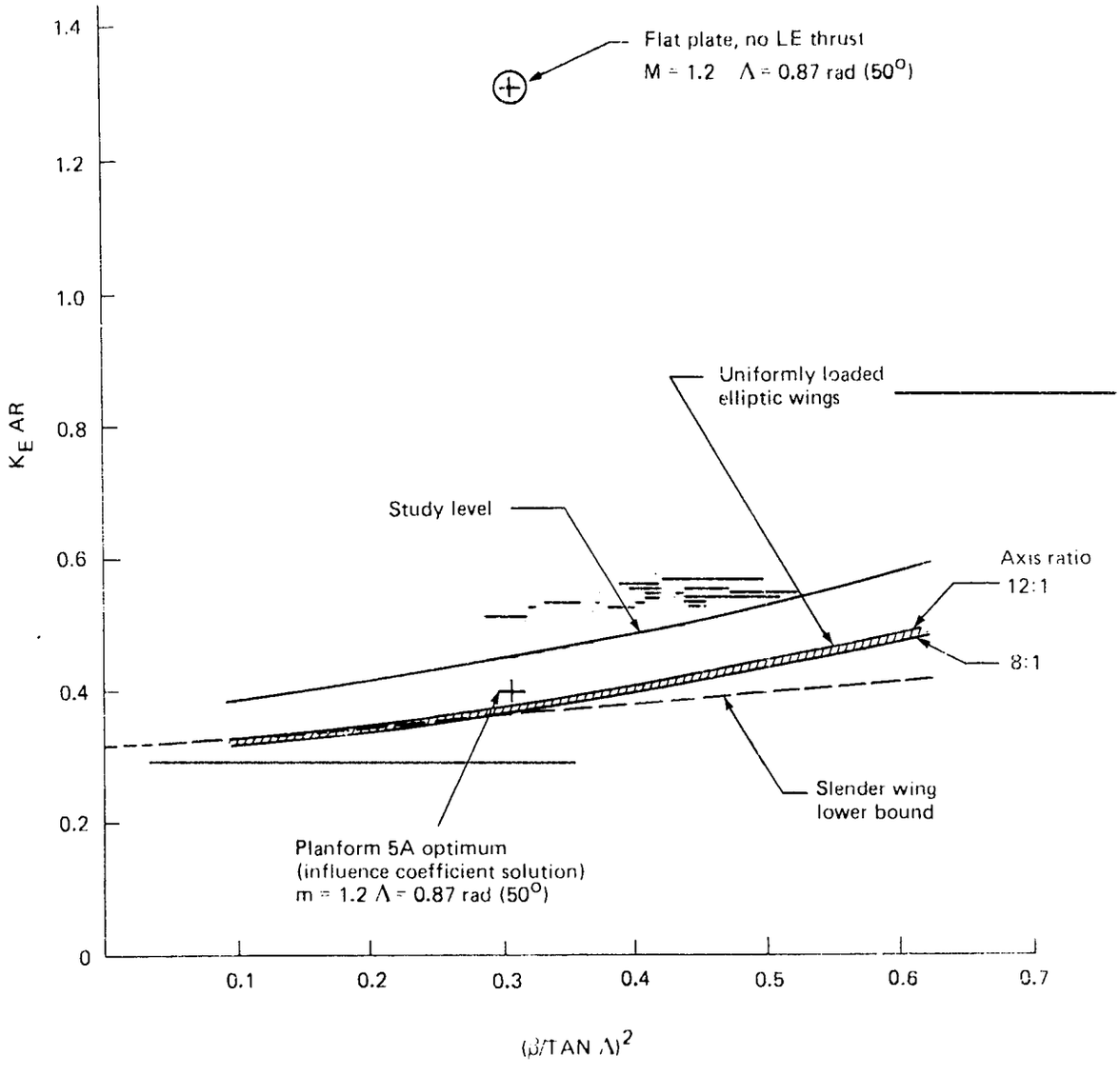

Figure 74 Oblique Wing Drag Due to Lift

Table 20 Model 5-7 Weight Statement

	Mass kg	Weight lb
Wing	30 890	68 090
Horizontal tail	1 020	2 260
Vertical tail	530	1 170
Body	25 560	56 350
Main landing gear	6 070	13 390
Nose landing gear	1 790	3 940
Nacelle and strut	8 260	18 200
Total structure	(74 120)	(163 400)
Engine	9 050	19 960
Engine accessories Engine controls Starting system	650	1 430
Fuel system	1 960	4 330
Thrust reverser (in nacelle)		
Total propulsion system	(11 660)	(25 720)
Accessory drive system	490	1 080
Instruments	480	1 050
Surface controls	2 790	6 150
Hydraulics	1 810	3 980
Pneumatics	660	1 450
Electrical	1 810	3 980
Electronics	1 390	3 070
Flight provisions	430	950
Passenger accommodations	5 570	12 280
Cargo handling	750	1 660
Emergency equipment	340	740
Air conditioning	1 810	4 000
Anti-icing	1 330	2 930
Auxiliary power unit	610	1 350
Water ballast system	110	250
Total fixed equipment	(20 380)	(44 920)
Exterior paint	90	200
Options	1 130	2 500
Manufacturer's empty weight	(107 380)	(236 740)
Standard and operational items	5 140	11 330
Operational empty weight	(112 520)	(248 070)
Maximum taxi weight	195 040	430 000

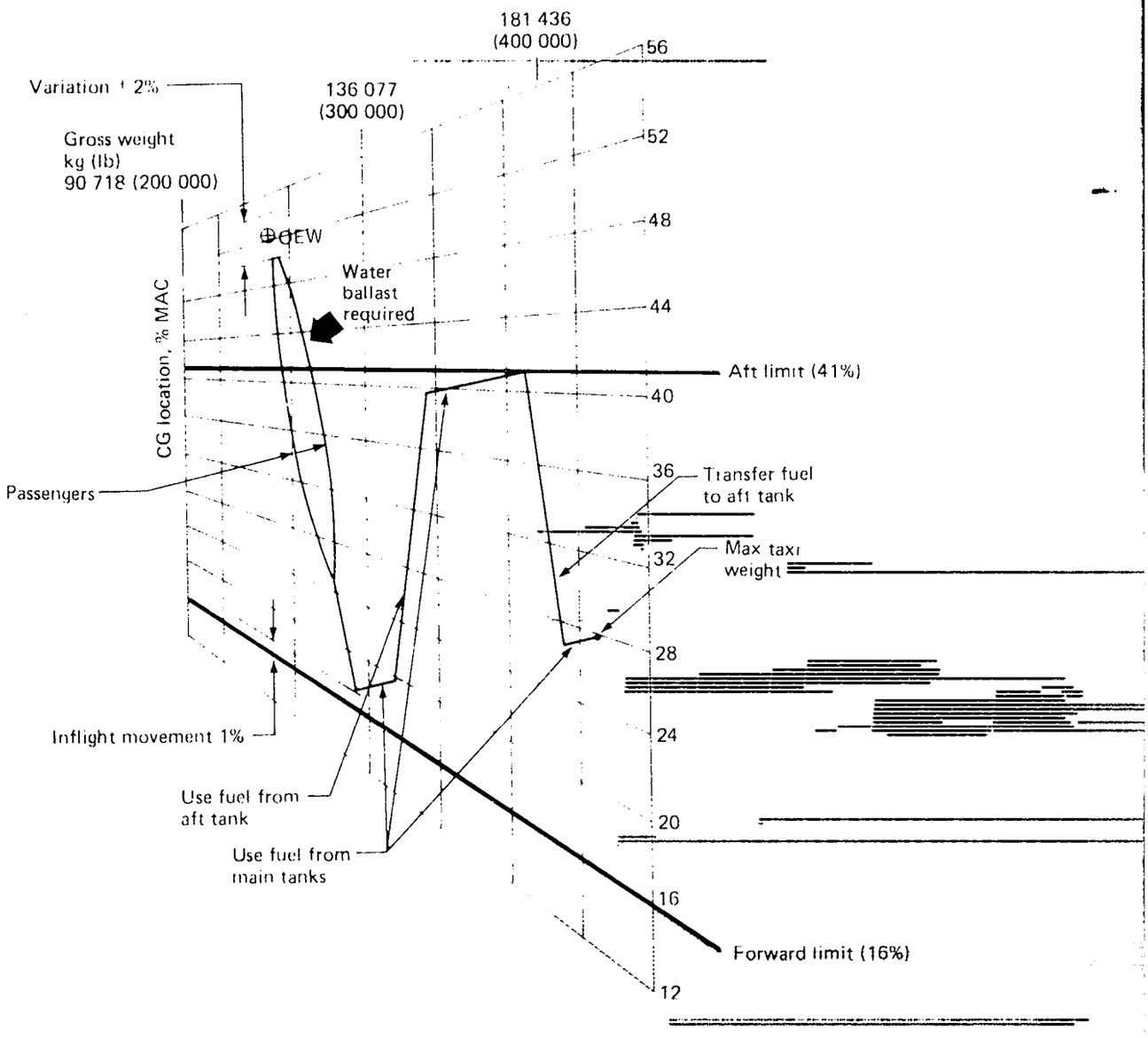

Figure 75 Model 5-7 Balance Diagram

8.4.4 PERFORMANCE AND NOISE

The performance and noise characteristics of the Model 5-7 are summarized in Table 18. The Model 5-7 performance is identical to that given for the sized BPR = 2 configuration in Section 6.10, except at low speed. The low-speed aerodynamic characteristics of the Model 5-7 were revised as described in Section 8.4.1. The improved lift-drag ratios led to a reduction in noise and minor changes in speed and field length.

Note that maximum taxi weight (Table 20) differs from TOGW (Table 18) in the allowance for fuel burned during warm up and taxi.

9.0 TRADE AND SENSITIVITY STUDIES

Trade and sensitivity studies have been conducted to find the percent change in TOGW and block fuel for changes in airplane technology level, design range, and engine noise treatment.

The effect on cycled TOGW and block fuel for uncycled changes in cruise SFC, drag, thrust and OEW are shown in Figure 76. Since the airplanes were sized to constant thrust/weight ratio (T/W) = 0.328 and W/S = 141, uncycled OEW changes had the greatest cycled effect on TOGW. Cruise drag had the greatest effect on cycled block fuel. This was due to a 10 percent loss in lift/drag ratio resulting from increased $C_{D_{min}}$ and reduced C_L due to a lower cruise altitude, with the remainder of fuel burned increase caused by the scaling to the larger airplane size (+6.6 percent SLST and S_W).

Design range trades are shown in Figure 77. Changes in design range of 10 percent resulted in changes in TOGW and sea level static thrust (SLST) of 6 percent with increasing ranges yielding slightly higher trade slopes. The change in block fuel with design range was steeper, with ±10 percent range resulting in a 14 percent increase in fuel burned. This is the result of cycled increases in engine size +6 percent, L/D CRUISE +1 percent, with relative increments in ground, climb, and reserves increasing with engine size. Traded noise was almost independent of range.

The effect of additional acoustical treatment (Reference 1, p. 151) on TOGW and block fuel is shown in Figure 78. At FAR 10 traded noise, TOGW is increased 4 percent and block fuel is increased 4-1/2 percent.

The noise levels estimated for the study aircraft represent noise reductions that can be achieved when 1976 noise technology is qualified for airplane hardware for a 1985 design freeze. The most significant possible reductions in Figure 78 are for sideline noise. On takeoff climbout, the benefits of extensive noise reduction treatment are offset by the lower altitudes achieved and higher thrust required. This is the result of lower installed thrust with increased noise treatment. The altitude, noise treatment, and thrust required will also significantly affect the noise at cutback. For the oblique-wing design, cutback power below 50 percent of maximum thrust significantly reduces jet noise, allowing much lower traded noise levels than with continuous takeoff power. On approach, maximum noise reduction also depends on airframe noise reduction once engine noise is four EPNdB lower than the peripheral lining values. At the present time, it appears that traded noise levels can be improved most with emphasis on approach noise reduction of engine and airframe components. Changes in future FAR-type noise requirements, applicable when this airplane might enter service around 1990+, may still require a balanced noise component approach.

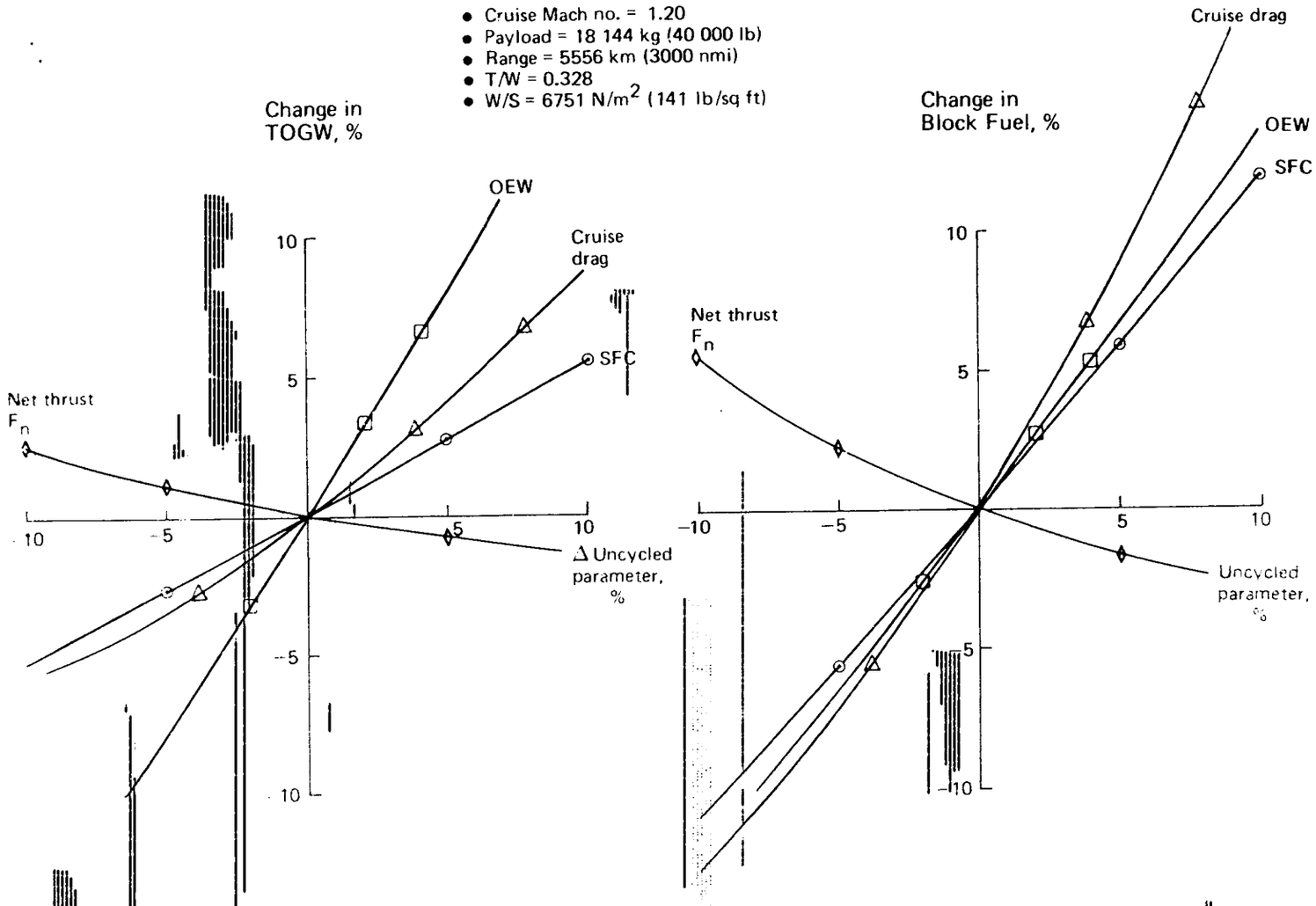

Figure 76 Gross Weight and Block Fuel Sensitivities—Model 5-7

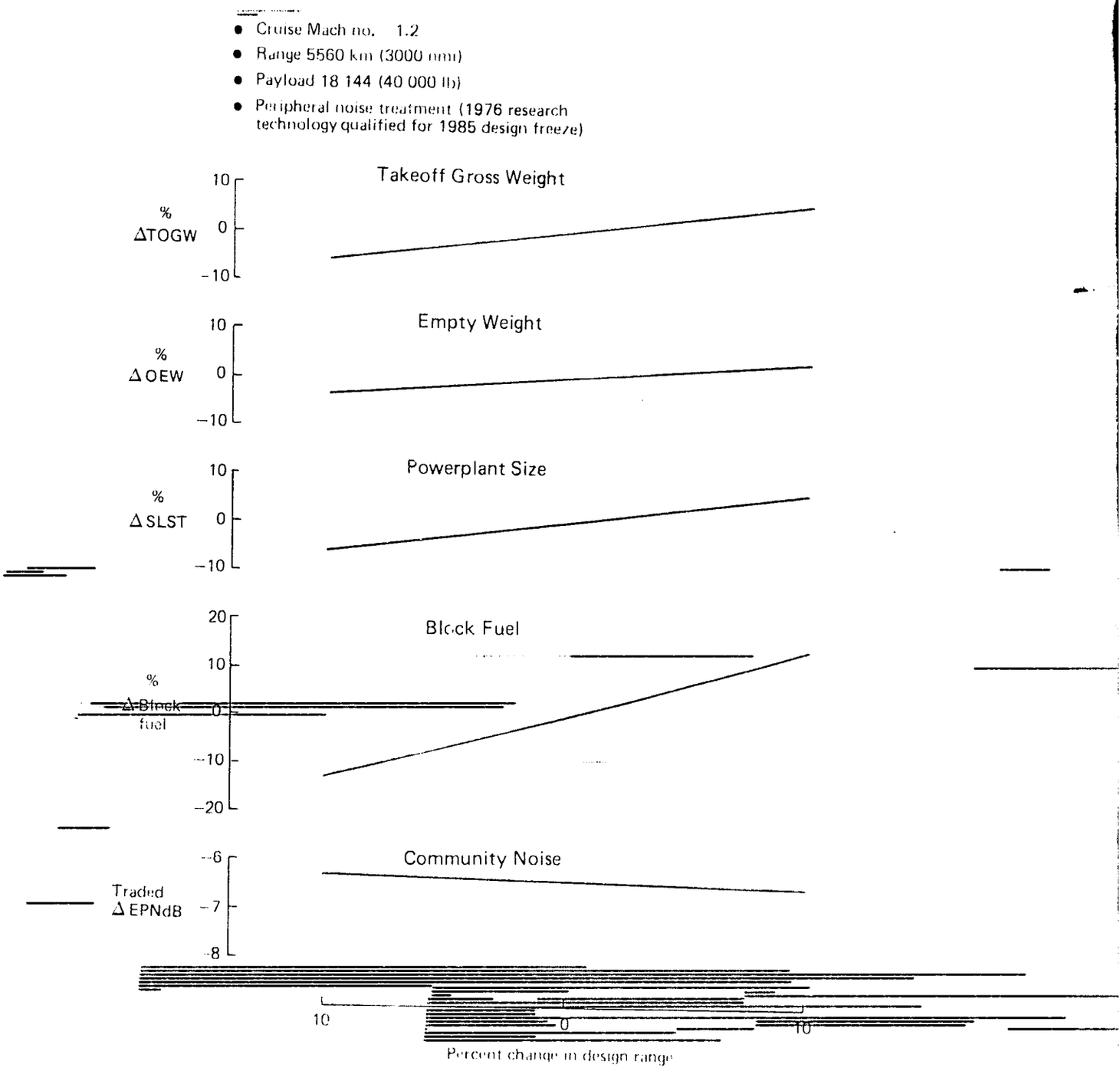

Figure 77 Range Sensitivity Model 5-7-BPR = 2

- Cruise Mach no. = 1.2
- Range 5560 km (3000 nmi)
- Payload 18 144 kg (40 000 lb)

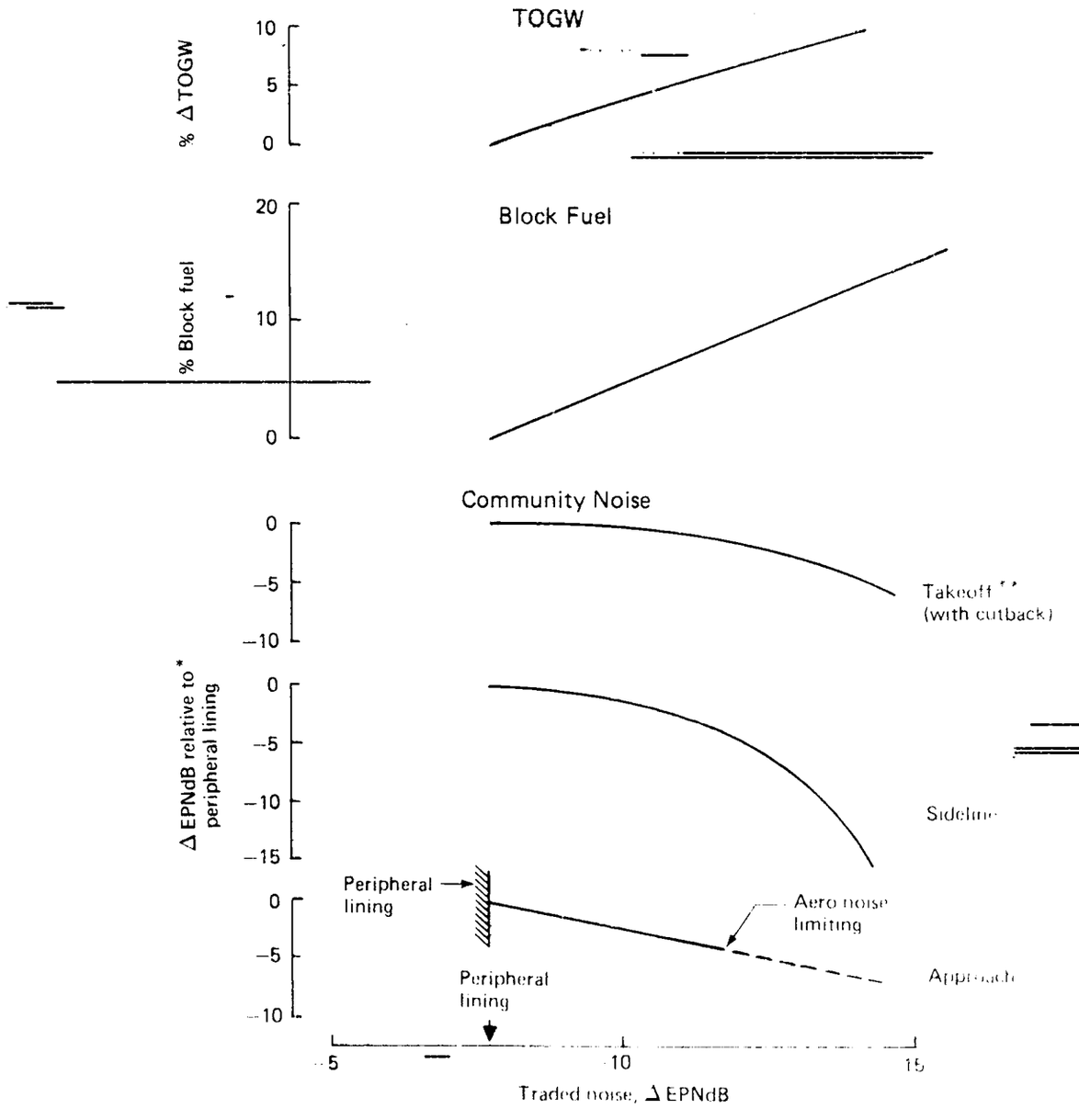

* 1976 research technology qualified for 1985 design freeze

** Oblique wing allows thrust cutback below 50% takeoff power

Figure 78 Noise Trades Model 5-7 BPR 2

10.0 EXPERIMENTAL DATA ANALYSIS

10.1 DATA SOURCES

NASA (Ames Research Center) has conducted a number of wind tunnel tests on oblique-wing models. Most of the data has been published in References 12 to 17, without analysis. Reference 18 contains comparisons of theoretical predication and experimental data for a low aspect ratio (AR = 6, Λ = 0) oblique wing. Agreement is generally good.

In the course of the present study, some analysis was conducted of experimental data (Reference 17) obtained from a wind tunnel model (Figure 79) derived from the Boeing Model 5-3 integrated body/nacelle configuration. The wing has a 12 percent NACA 3612-02.40 airfoil section and the same aspect ratio as the Model 5-7 (13.47), but is more highly tapered. A configuration with pod-mounted engines, and a clean body reference model (Figure 80) were also tested. The model was blade-mounted (Figure 81). The data was corrected for blade-interference using data obtained with an image mount. Corrections for internal drag and base pressure were applied. The Reynolds number was 19.7×10^6 m (6×10^6 ft) and boundary-layer trip strips were used.

The results of this analysis are discussed later in this section.

10.2 OPTIMUM SWEEP

Figure 82 shows experimental values of $(L/D)_{max}$ as a function of the wing sweep for Mach numbers from 0.7 to 1.2. Let Λ_{opt} be the sweep angle that gives the highest value of $(L/D)_{max}$ at a given Mach number, and let $M_{N_{opt}}$ be the corresponding component of free stream Mach number (M) resolved normal to the leading edge.

$$M_{N_{opt}} = M \cos \Lambda_{opt} = \frac{M}{\frac{1}{\cos \Lambda_{opt}}}$$

Figure 83 shows $(1/\cos \Lambda_{opt})$ as a function of free stream Mach number. The length of the vertical bars represents the uncertainty in determining Λ_{opt}. A reasonably good fit is obtained by taking $M_{N_{opt}} = 0.68$, so that the optimum sweep is given by

$$\Lambda_{opt} = \cos^{-1}\left(\frac{0.68}{M}\right)$$

This leads to the following optimum sweep angles:

M	0 ⟶ 0.68	0.8	0.9	1.2
Λ_{opt}	0	0.56 rad (32°)	0.72 rad (41°)	0.96 rad (55°)

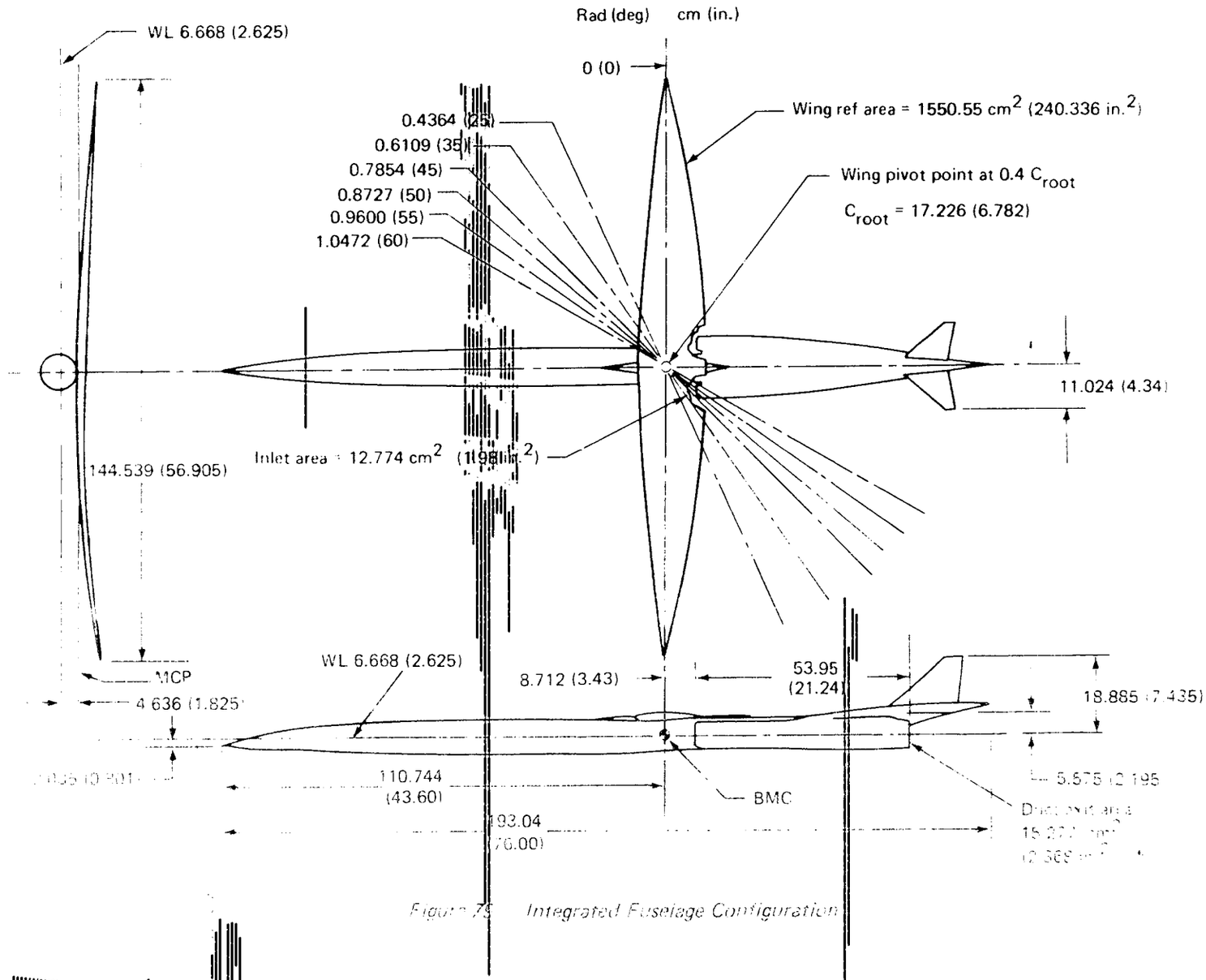

Figure 75 Integrated Fuselage Configuration

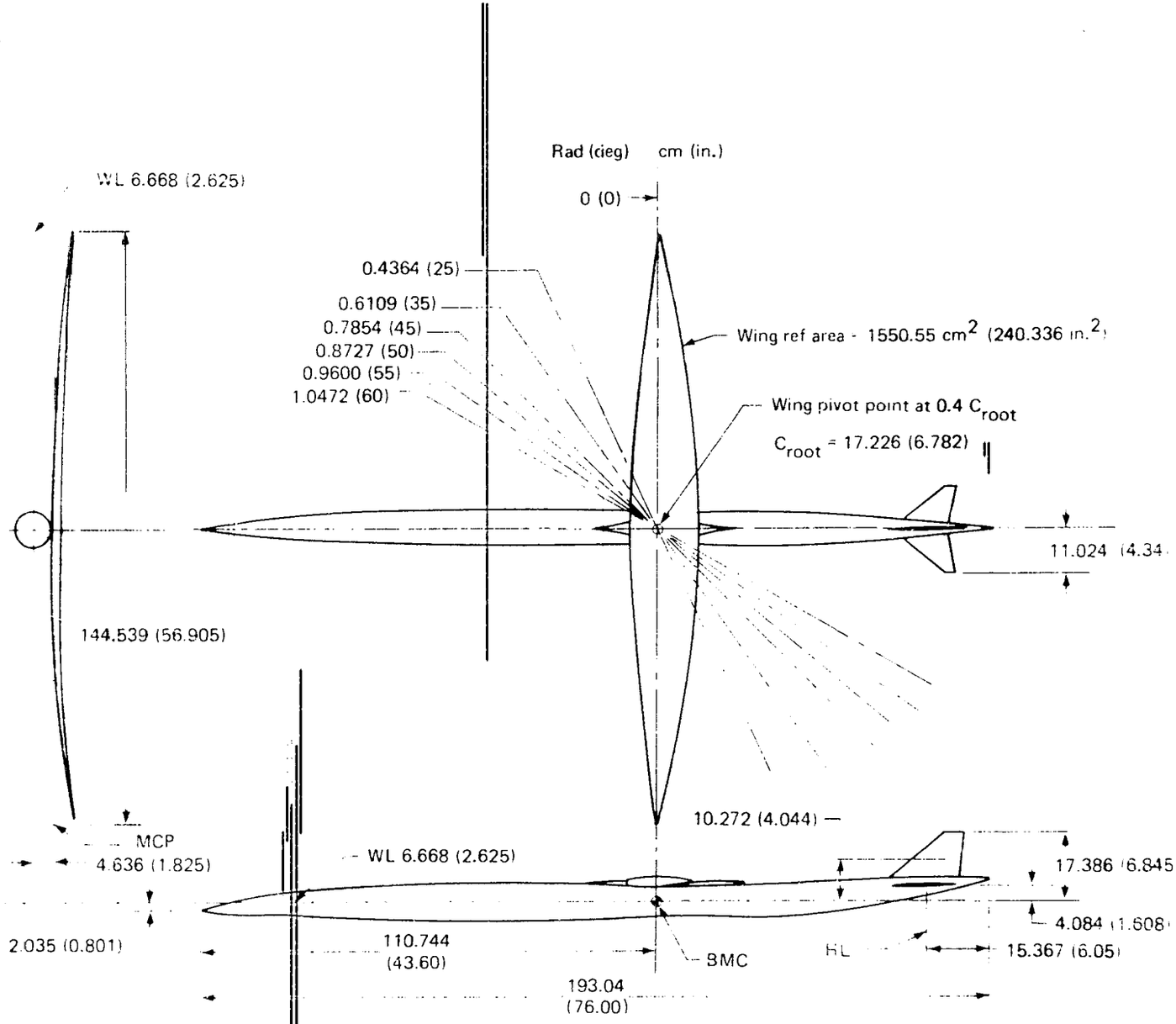

Figure 80 Clean Fuselage Configuration

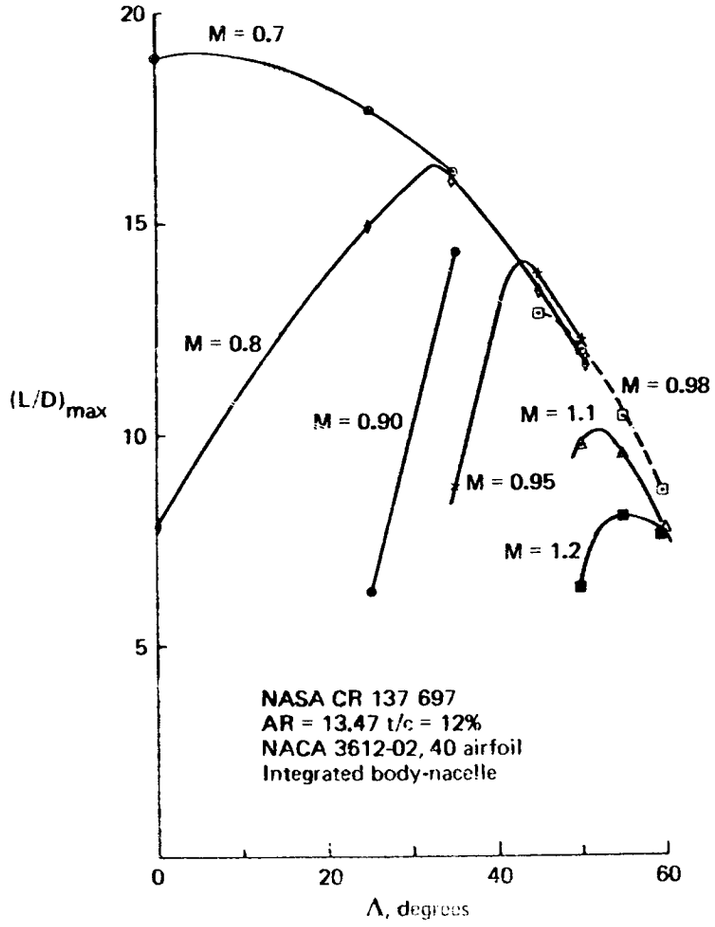

Figure 82 Maximum Lift/Drag Ratio from NASA Test Data

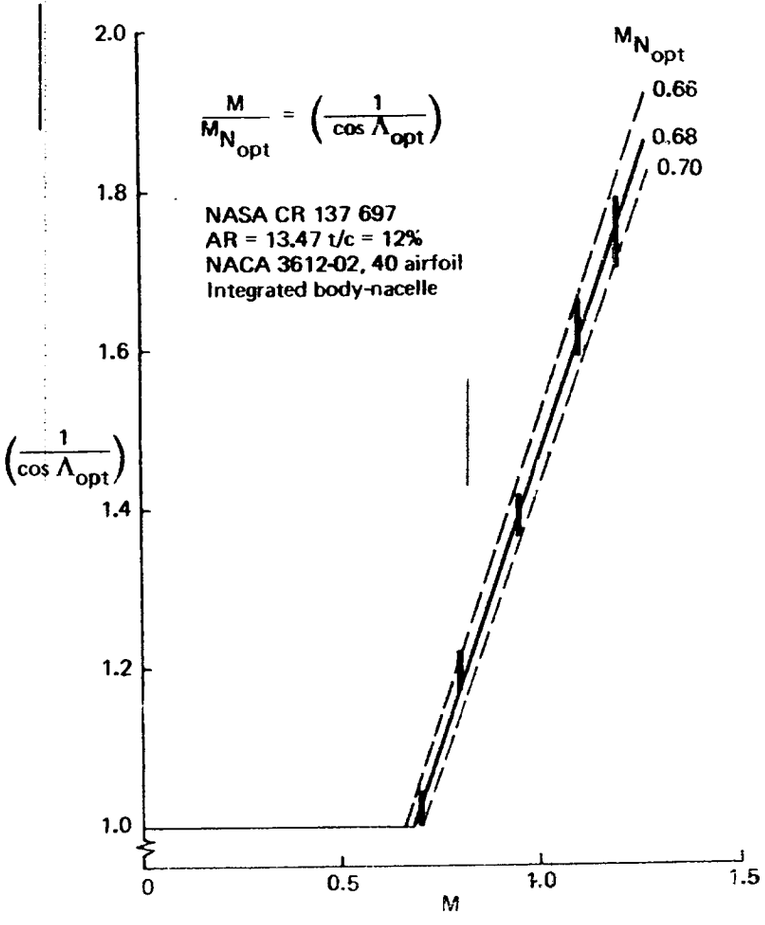

Figure 83 Sweep Selection

The sweep angles actually used in performance calculations were:

M	0 → 0.68	0.8	0.9	1.2
Λ_{opt}	0	0.61 rad (35°)	0.72 rad (41°)	0.87 rad (50°)

At M = 0.8, experimental data is available at Λ = 0.61 rad (35°) and lift/drag ratio is close to the optimum. Following cruise sweep selection studies described in Reference 1 and Section 7, which gave $M_{N_{opt}}$ = 0.75, 0.87 rad (50°) sweep was selected at M = 1.2. The relatively low value of $M_{N_{opt}}$ derived from the experimental data may be due to the airfoil section (a conventional NACA 4-digit series, with design lift coefficient equal to 1.3) or may be associated with low Reynolds numbers on the short outer wing chords.

10.3 SUBSONIC DRAG DUE TO LIFT

The drag polars presented in Section 7.4.1 were estimated using the leading edge suction approach described in Reference 8.

Figure 84 shows effective leading edge suction factors found from the experimental data of Reference 17 using the expression:

$$s = \frac{C_L \, TAN(\alpha - \alpha_0) - \left(C_D - C_{D_{SYM}}\right)}{C_L \, TAN(\alpha - \alpha_0) - (C_L^2 / \pi AR)}$$

C_L, C_D and $(\alpha - \alpha_0)$ were obtained directly from the experimental data. Model $C_{D_{SYM}}$ was found by adding estimated wing skin friction and profile drag to the drag of the body and empennage, measured near zero lift. (At subsonic speeds the measured body empennage drag is about 30 percent higher than estimated. This is discussed in the following section).

Note that "s" is a measure of how closely drag due to lift approaches the minimum value $C_L^2/\pi A$, and is influenced by a number of parameters (camber, twist, profile drag) in addition to the leading edge thrust force.

The peak values of "s" (90-95 percent) are in the range expected under full-scale conditions and have therefore not been corrected for Reynolds number effects.

All the experimental data was obtained tail on. The values of "s" have not been corrected for the presence of the horizontal tail because the effect is estimated to be small (1-2 percent).

Airplane drag due to lift was found using the expression

$$\Delta C_{D_{LIFT}} = \left\{ C_L \, TAN(\alpha - \alpha_0) - s \left[C_L \, TAN(\alpha - \alpha_0) - (C_L^2 / \pi AR) \right] \right\}$$

where

$$\alpha - \alpha_0 = C_L / C_{L_\alpha}$$

NASA CR 137697
R No. = 6 x 10^6/ft

AR = 13.47
LE radius = 2% chord

Symbol	M	Λ rad (deg)	RN_{LE}
●	0.6	0	42 000
+	0.8	0.61 (35)	34 400
×	0.8	0.70 (45)	29 700
⊙	0.9	0.79 (45)	29 700

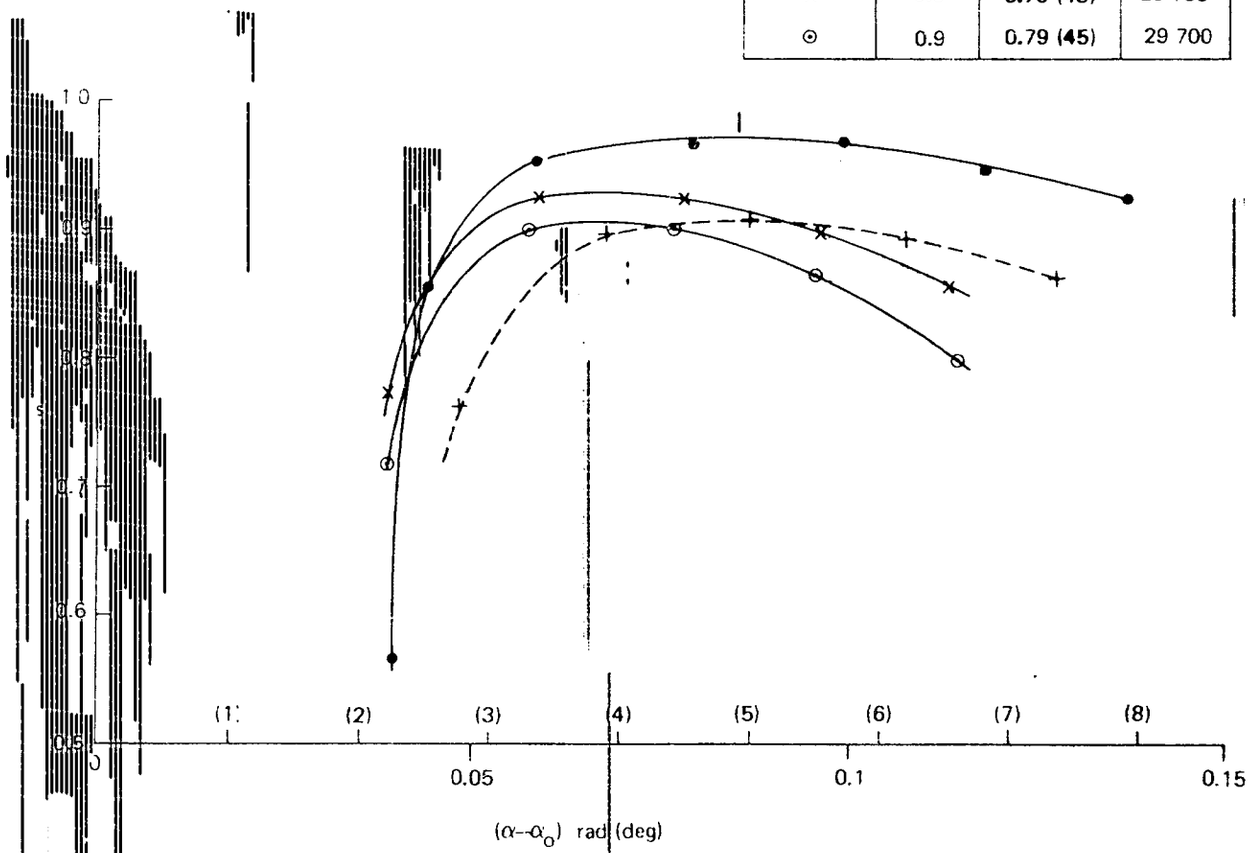

Figure 84 Effective Leading Edge Thrust Factor

The lift slope, C_{L_α}, was obtained from Figure 85, which shows experimental data from Reference 17 compared to a modified form of an empirical expression derived by Polhamus (Reference 19).

The experimental values generally agree quite well with predictions at low speeds, but fall below the predicted values when Mach number normal to the leading edge exceeds the optimum ($\underline{M}$ = 0.68). This suggests the onset of shock-induced separation.

The values of C_{L_α} used for calculating subsonic drag polars are:

M	0.5	0.8	0.9
Λ	0	0.61 rad (35°)	0.73 rad (41°)
$C_{L_\alpha}/a_0 \cdot AR \cdot COS^2 \Lambda$	0.0722	0.0925	0.1000
C_{L_α}/radian	5.85	5.03	4.6

10.4 SUPERSONIC LIFT/DRAG RATIO

A brief investigation has been carried out to understand the poor lift/drag ratios measured at supersonic speeds ($L/D_{max} \approx 8$ at M = 1.2, Figure 82).

Figure 86 shows the drag of the clean and integrated configurations measured wing-off, near zero lift. At M = 1.2, the measured drag of the clean configuration is about 40 percent greater than estimated. This is difficult to understand because experience has shown that the drag of such configurations can be well predicted. It is suspected that the blade mount system is responsible.

At Mach numbers below 1.1, the integrated body has slightly higher drag than the clean configuration. This would be expected because the integrated body has greater wetted area. However, the difference increases rapidly at Mach numbers greater than 1.05. Adding the wing increases the discrepancy between the two configurations, particularly between M = 1.1 and 1.2.

A possible explaination is that spillage is occurring through a normal shock located ahead of the inlet. A large increase in drag did occur when duct flow was reduced by a screen (Figure 86).

Note also that the model uses a bounday-layer diverter rather than the auxiliary inlet system proposed for the airplane (Section 6.7), so that air diverted over the top of the inlet will be forced into a narrow channel between body and wing, possibly causing choking.

The lift/drag ratios measured during this test are not considered to represent the potential of an oblique-wing transport and have not been used in the airplane analysis.

$$\left(\frac{C_{L_\alpha}}{a_0 \, AR \cos^2 \Lambda}\right) \qquad \frac{1}{2 + \sqrt{4 + (AR \cos \Lambda)^2 \left[1 + (M \cos \Lambda)^2\right]}}$$

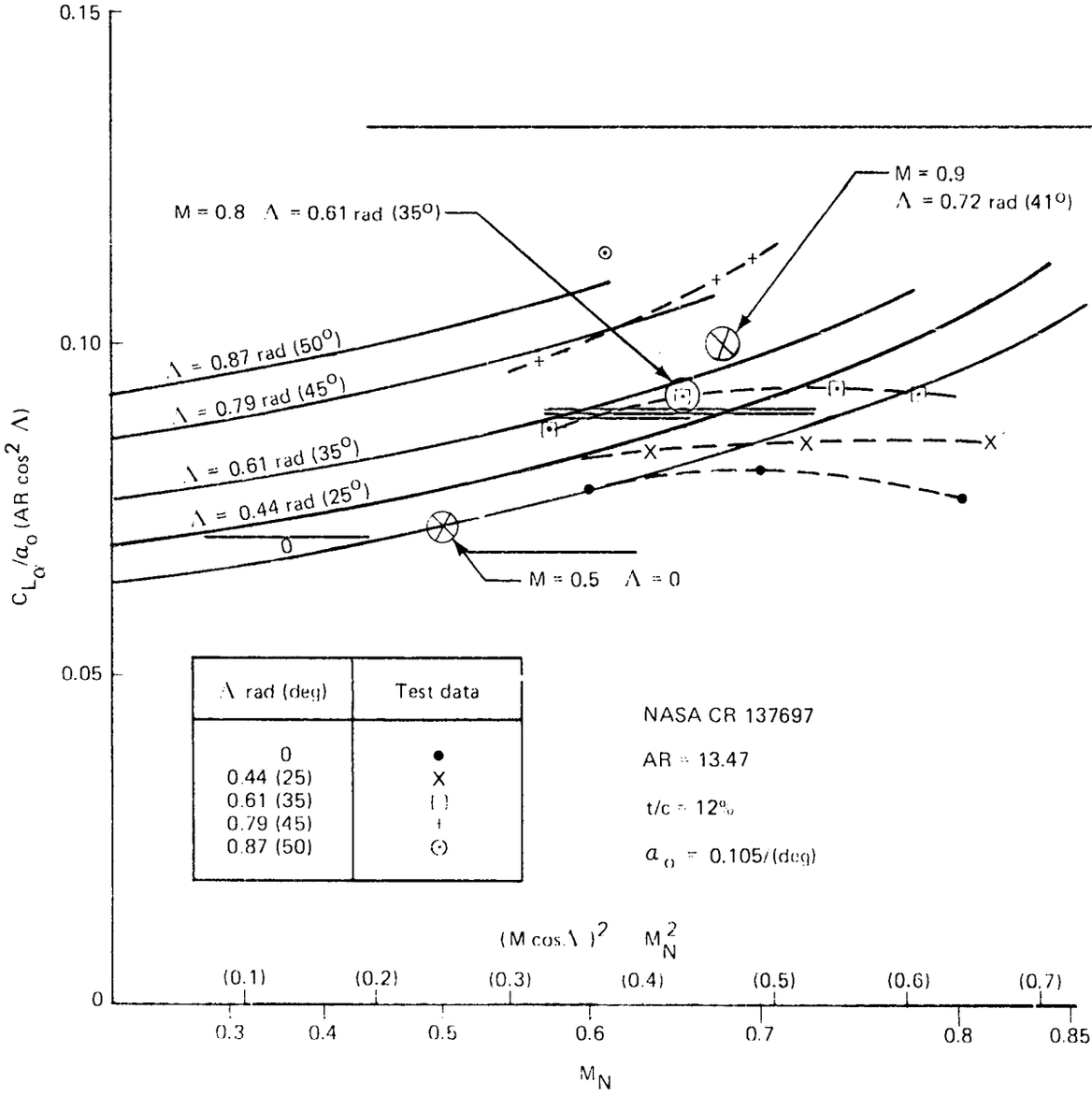

Figure 85 Oblique Wing Lift Slope

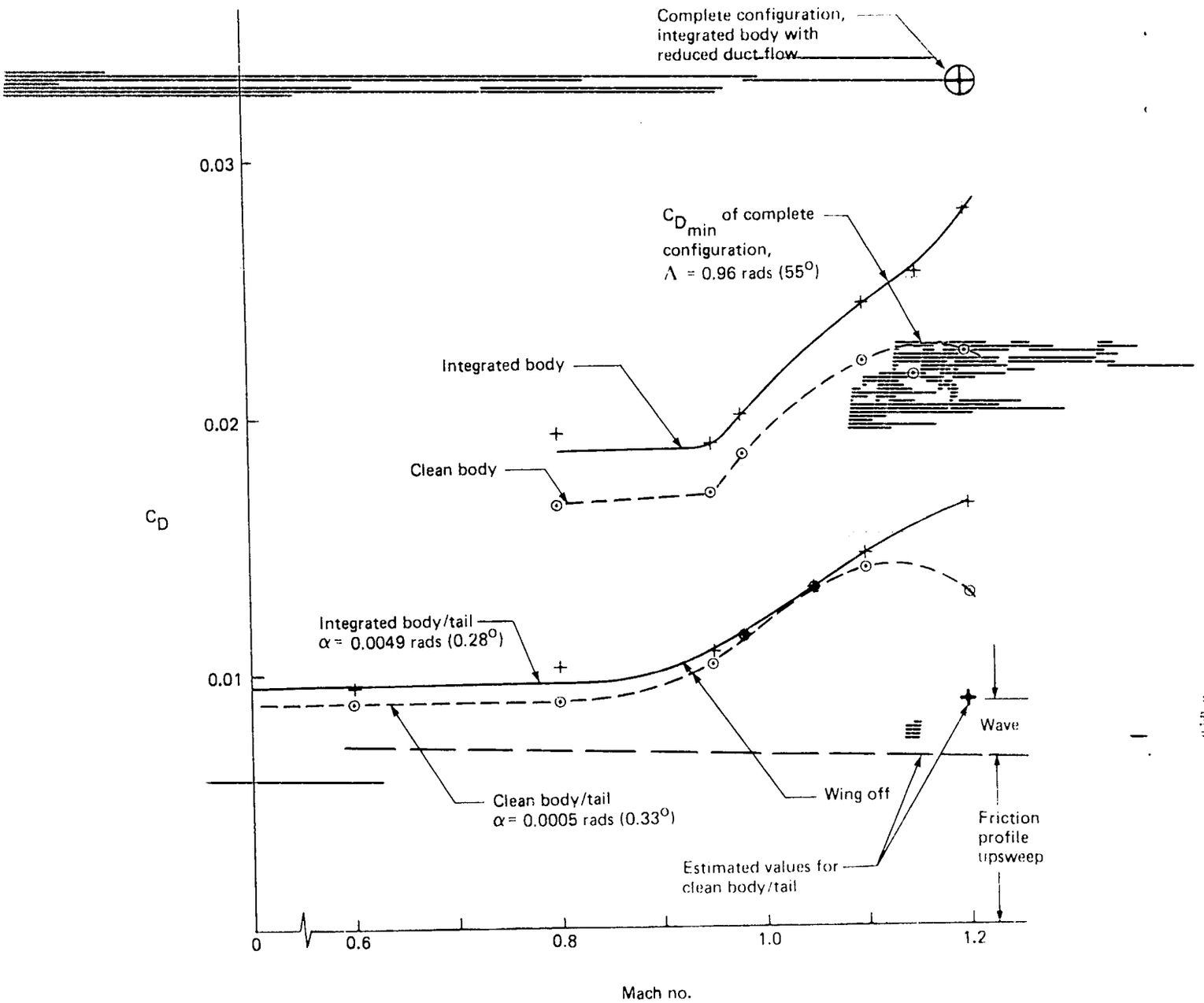

Figure 86 *Comparisons of Minimum Drag Coefficient*

10.5 SUPERSONIC DRAG DUE TO LIFT

Experimental data from the clean-body model has been used to check the drag-due-to lift factors used in airplane analysis that are based on adjusted theoretical results (Sections 4.1.2 and 8.4.2).

Figure 87 shows a comparison of experimental results with an envelope drag polar, given by

$$C_D = C_{D_{SYM}} + K_E C_L^2$$

$C_{D_{SYM}}$ has been found by adding estimated wing skin friction and wave drag to the measured drag of the clean-body tail (Figure 86). The envelope drag-due-to-lift factor (K_E) was obtained in the manner used during airplane analysis (Figure 74–Study Level).

The data shown in Figure 87 confirm that study level of drag due to lift is reasonable, at least for sweep angles of 55° and lift coefficients less than 0.25. It was not possible to carry out a similar check for the selected airplane flight condition ($M = 1.2$, $\Lambda = 0.87$ rads (50°), $C_L = 0.34$) because clean-body test data is not available for this condition.

M = 1.2 Λ = 0.96 rad (55°) Cylindrical Body

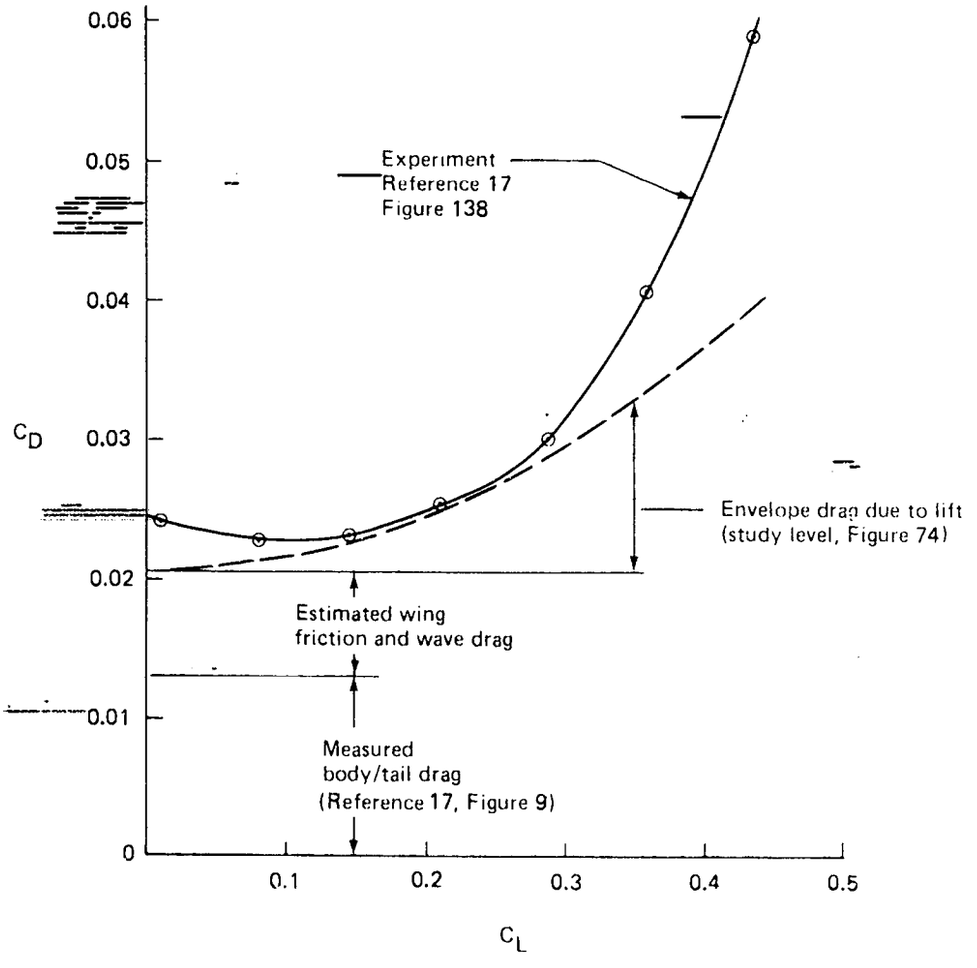

Figure 87 Supersonic Drag Comparison

11.0 CONCLUSIONS AND RECOMMENDATIONS

The variable sweep oblique-wing concept is technically feasible and is the best configuration for flight at moderate supersonic Mach numbers. It is lighter, quieter, and more fuel efficient than comparable symmetric configurations. The concept is very versatile, combining excellent low-speed and noise characteristics with transcontinental boom-free supersonic flight and possibly cruising over water at speeds up to about M = 1.6.

The single-pivot oblique wing appears structurally more efficient than the conventional, dual-pivot variable sweep wing.

Major characteristics of the oblique-wing transport are:

- High aspect ratio, tapered wing with composite structure, pivoted at 25 - 30 percent chord
- Teflon-coated, turntable-type pivot
- Bypass ratio 2 engines, aft mounted, integral with the body
- Bicycle (nonrotating) landing gear
- Probable requirement of a full-time stability augmentation system permitting reductions in horizontal and vertical tail size, uncoupling longitudinal, lateral, and directional modes and providing acceptable dynamic characteristics

Additional research and development is recommended in the following areas.

Economic and operational studies are needed to determine the operating costs and characteristics of the oblique-wing transport relative to subsonic and supersonic transports.

Aircraft designed to cruise at higher supersonic Mach numbers should be investigated in combination with variable cycle engines. Such aircraft have potential for efficient overwater flight at moderate supersonic speeds (M = 1.5 - 1.6), combined with boom-free transcontinental supersonic flight.

The aerodynamic design of the wing and the integration of the powerplant should be developed using theoretical and experimental methods.

Aerodynamic studies and response calculations should be carried out to develop ways to reduce aerodynamic cross coupling and to better understand the stability augmentation system requirements.

A subscale model of the pivot and portions of the wing and body support structure should be built. This model would be used to investigate producibility of the pivot and the effects of wing and body structural deflections.

A subscale demonstrator aircraft would provide valuable data in many areas, including:

- Manned flight evaluation of handling and ride qualities
- Takeoff and landing characteristics of nonrotating aircraft
- Correlation of analytic and wind tunnel results with flight data to provide confidence in aerodynamic prediction techniques for future oblique-wing design programs

12.0 REFERENCES

1 Kulfan, R. M., et al: *High Transonic Speed Transport Aircraft Study-Final Report*, NASA CR-114658, 1973.

2 Kulfan, R. M., et al: *Study of the Single-Body Yawed-Wing Aircraft Concept*, NASA CR-137483, May 1974.

3 Smith, R. L.; Jones, R. T.; and Summers, J. L.: *Transonic Wind Tunnel Tests on an F8 Airplane Model Equipped with 12% and 14% Thick Oblique Wings*, NASA TM X-62,478.

4 Jones, R. T.: *The Spanwise Distribution of Lift for Minimum Induced Drag of Wings Having a Given Lift and a Given Bending Moment*, NACA TN 2249.

5 Sommer, S. G. and Short, B. J.: *Free Flight Measurements of Turbulent Boundary Layer Skin Friction in the Presence of Severe Aerodynamic Heating at Mach Numbers from 2.8 to 7.0*, NACA TN 3391.

6 Smith, J. H. B.: *Lift/Drag Ratios of Optimized Sleved Elliptic Wings at Supersonic Speeds*, Aeronautical Quarterly, August 1961.

7 McCloy, R. W.: *The Fundamentals of Supersonic Propulsion*, Boeing Document D6A-10380-3.

8 Henderson, W. P.: *Studies of Various Factors Affecting Drag Due to Lift at Subsonic Speeds*, NASA TN D-3584.

9 Jones, R. T.: *Reduction of Wave Drag by Antisymmetric Arrangement of Wings and Bodies*, AIAA Journal, Vol. 10, No. 2, February 1972.

10 Woodward, F.; LaRowe, E.; and Love, J. E.: *Analysis and Design of Supersonic Wing-Body Combinations, Including Flow Properties in Near Field, Part I and II*, NASA CR-73107, 1967.

11 Sotomayer, W. A. and Weeks, Thomas M.: *A Semi Empirical Estimate of Leading Edge Thrust for a Highly Swept Wing in Supersonic Flow*, AFFDL-TM-76-63-FXM

12 Graham, L. A.; Jones, R. T.; and Boltz, F. W.: *An Experimental Investigation of an Oblique-Wing and Body Combination at Mach Numbers Between 0.60 and 1.40*, TM X-62,207, December 1972, NASA

13 Graham, L. A.; Jones, R. T.; and Boltz, F. W.: *An Experimental Investigation of Three Oblique Wing and Body Combinations at Mach Numbers Between 0.60 and 1.40*, TM-X 62,256, April 1973, NASA

14 Hopkins, E. J.; Meriwether, F. D.; and Pena, D. F.: *Experimental Aerodynamic Characteristics of Low-Aspect Ratio Swept and Oblique Wings at Mach Numbers Between 0.6 and 1.4*, TM-X-62,317, November 1973, NASA.

15 Smith, R. C.; Jones, R. T.; and Summers, J. L.: *Transonic Wind Tunnel Tests of an F-8 Airplane Model Equipped with 12 and 14 Percent Thick Oblique Wings*, NASA TM X-62,478, October 1975.

16 Smith, R. C.; Jones, R. T.; and Summers, J. L.: *Transonic Lateral and Longitudinal Characteristics of an F-8 Airplane Model Equipped with an Oblique Wing*, NASA TM X-73,103, March 1976.

17 Black, R. L.; Beamish, J. K.; and Alexander, W. K.: *Wind Tunnel Investigation of an Oblique Wing Transport Model at Mach Numbers Between 0.60 and 1.4*, NASA CR-137697, July 1975.

18 Hopkins, J. F. and Levin, A. D.: *Study of Low Aspect Ratio Swept and Oblique Wings*, Journal of Aircraft, Vol. 12, No. 8, August 1975.

19 Spencer, B. J., Jr.: *A Simplified Method for Estimating Subsonic Lift-Slope at Low Angles of Attack for Irregular Planform Wings*, NASA TM X-525.